

AD 675181

AFFDL-TR-67-192
VOLUME I

ESTABLISHMENT OF AN UNSYMMETRICAL WAKE TEST CAPABILITY FOR AERODYNAMIC DECELERATORS

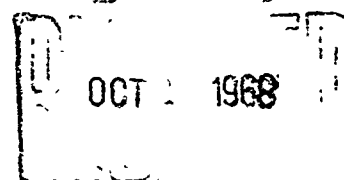
VOLUME I. TEST VEHICLE DESIGN MODIFICATION

DANIEL W. HENKE
Goodyear Aerospace Corporation

TECHNICAL REPORT AFFDL-TR-67-192, VOLUME I

AUGUST 1968

This document has been approved for public
release and sale; its distribution is unlimited.



AIR FORCE FLIGHT DYNAMICS LABORATORY
AIR FORCE SYSTEMS COMMAND
WRIGHT-PATTERSON AIR FORCE BASE, OHIO

Reproduced by the
CLEARINGHOUSE
for Federal Scientific & Technical
Information Springfield Va 22151

AFFDL-TR-67-192
Volume I

NOTICES

When Government drawings, specifications, or other data are used for any purpose other than in connection with a definitely related Government procurement operation, the United States Government thereby incurs no responsibility nor any obligation whatsoever; and the fact that the Government may have formulated, furnished, or in any way supplied the said drawings, specifications, or other data, is not to be regarded by implication or otherwise as in any manner licensing the holder or any other person or corporation, or conveying any rights or permission to manufacture, use, or sell any patented invention that may in any way be related thereto.

This document has been approved for public release and sale; its distribution is unlimited.

Copies of this report should not be returned unless return is required by security considerations, contractual obligations, or notice on a specific document.

STI	WHITE SECTION	<input checked="" type="checkbox"/>
DOC	BUFF SECTION	<input type="checkbox"/>
UNCLASSIFIED		<input type="checkbox"/>
IDENTIFICATION		
.....		
DISTRIBUTION/AVAILABILITY CODES		
DIST.	ANAL. and/or SPECIAL	
1		

ABSTRACT

The results of wind tunnel investigations, analyses, and preliminary design efforts performed in order to show the feasibility of accomplishing supersonic free flight tests of deployable aerodynamic decelerators in the wake of an unsymmetrical forebody are described in this volume. The results show that the simulation of the wake of a nonaxisymmetric lifting body is feasible and practicable by integrating inflatable aft-appendages on an Arapaho C test vehicle and that the resultant modified vehicle retains the same test capabilities as the basic Arapaho C. The modified vehicle design also includes modifications required for compliance with Eglin AFB/Eglin Gulf Test Range safety criteria. Included are recommendations for further vehicle modifications that would improve the test capabilities of the basic Arapaho C test vehicle. A vehicle mockup was constructed to demonstrate feasibility of the approach and to preclude major assembly and actuation interference problems.

(The distribution of this abstract is unlimited.)

AFFDL-TR-67-192
VOLUME I

**ESTABLISHMENT OF AN UNSYMMETRICAL WAKE TEST
CAPABILITY FOR AERODYNAMIC DECELERATORS**

VOLUME I. TEST VEHICLE DESIGN MODIFICATION

DANIEL W. HENKE

This document has been approved for public
release and sale; its distribution is unlimited.

FOREWORD

The work described in this report was performed by Goodyear Aerospace Corporation (GAC), Akron, Ohio, under USAF Contract AF33(615)-3595. The contract was initiated under Project 6065, "Performance and Design of Deployable Aerodynamic Decelerators," Task 606507, "Aerodynamic Decelerator Free-Flight Performance at High Mach Numbers." The program was administered by the Air Force Flight Dynamics Laboratory, Air Force Systems Command, Wright-Patterson Air Force Base, Ohio. Mr. W. R. Pinnell and Mr. C. A. Babish III, (FDFR), were project engineers.

The work covered in this report was initiated on 1 March 1966 and completed on 15 October 1966. The report was submitted in March 1968.

This volume does not cover all of the program's primary objectives. The investigation and analyses of aerodynamic decelerator performance in supersonic wake flow fields is covered in Volume II. Volume III contains a tabulation of wake survey and body surface pressure data obtained from wind tunnel tests conducted in support of this program.

The authors and contributing personnel of Goodyear Aerospace Corporation were R. J. Manzuk, project engineer; D. W. Henke, assistant project engineer; I. M. Jaremenko, wake analysis; J. J. Dean, Jr., vehicle design and modification; F. A. Pake, aero-thermo analyses; Dr. A. D. Topping, structural analyses; and numerous other Goodyear Aerospace personnel who contributed to the various supporting tests and analyses.

The contractor's report number is GER-13528.

Acknowledgement is made of the conscientious support of the Arnold Engineering Development Center, von Karman Facility (VKF), Supersonic Branch, during the wind tunnel tests. Special recognition is given to Mr. A. W. Myers, VKF project engineer, for his cooperation during the test series.

Publication of this report does not constitute Air Force approval of the report's findings or conclusions. It is published only for the exchange and stimulation of ideas.



GEORGE A. SOLT, Jr.
Chief, Recovery & Crew Station Branch
Vehicle Equipment Division
AF Flight Dynamics Laboratory

TABLE OF CONTENTS

<u>Section</u>	<u>Title</u>	<u>Page</u>
I	INTRODUCTION	1
	1. Program Objectives.	1
	2. Design Requirements	1
II	WIND-TUNNEL TEST EQUIPMENT AND INSTRUMENTATION.	5
	1. General	5
	2. Wind-Tunnel Description	5
	3. Models and Support System	5
	4. Instrumentation.	5
III	SIMILARITY ANALYSIS OF ASYMMETRIC WAKES BASED ON EXPERIMENTAL RESULTS	11
	1. Introduction	11
	2. Vehicle Configurational Selection.	11
	3. Flow Fields around Vehicles	11
	4. Wake Flow Field Structure.	14
	5. Wake Flow Field Similarity	14
	6. Results of Criteria Analysis	17
	7. Similitude Conclusions	33
IV	DESIGN INVESTIGATION	39
	1. Basis for Design Changes	39
	2. Aerodynamic Analyses	39
	<u>a.</u> Nature of Data Collected	39
	<u>b.</u> Static Stability	40
	<u>c.</u> Static Stability Margin.	44
	<u>d.</u> Vehicle Drag Investigation.	46
	<u>e.</u> Despin Analysis	46
	3. Thermodynamic Analyses	50
	<u>a.</u> Objectives	50
	<u>b.</u> Pressure Distribution.	50
	<u>c.</u> Critical Heating Analysis	50
	4. Vehicle Modifications	58
	<u>a.</u> Recommended Modifications	58
	<u>b.</u> Sequencing.	58
	<u>c.</u> Test Item Stowage Volume	64
	<u>d.</u> Recovery System Location.	64
	<u>e.</u> Despin System	66
	<u>f.</u> Flare Deployment.	66

AFFDL-TR-67-192
Volume I

<u>Section</u>	<u>Title</u>	<u>Page</u>
	g. Flare Inflation	70
	h. Test Decelerator Deployment	73
	i. Test Item Retention	80
	j. Vehicle Diameter	80
	k. Data Acquisition	80
	l. Recovery	84
5.	Vehicle Structural Analysis	87
	a. Stress Analysis.	87
	b. Mass Properties Data.	96
6.	Inflatable Appendage Design	96
	a. Design Considerations.	96
	b. Design Approaches	105
	c. Selected Approach	105
	d. Flare Stress Analysis.	105
	e. Materials Investigation	116
7.	Auxiliary Equipment	118
	a. Refurbishment	118
	b. Aerospace Ground Equipment	118
V	FULL-SCALE MOCKUP.	123
	1. Contract Requirements	123
	2. Objectives	123
	3. Compliance Assurance	123
	4. Mockup Problems and Necessary Corrections	123
	a. Vehicle	123
	b. Skirt Assembly	126
VI	SUMMARY OF RECOMMENDED VEHICLE CHANGES	129
	1. EUREKA Requirements Implementation	129
	2. Vehicle Capability Improvement	129
	a. General	129
	b. Radar Beacon	129
	c. Recovery.	131
	d. Pressure Measurements.	131
	e. Flotation.	131
VII	CONCLUSIONS	133
<u>Appendix</u>		
I	SEQUENCE CIRCUIT ANALYSIS	135
II	APPENDAGE STRESS CALCULATION DATA	143
III	CHECKOFF LIST.	149

AFFDL-TR-67-192
Volume I

<u>Appendix</u>	<u>Title</u>	<u>Page</u>
IV	VIEWS OF MOCKUP CONFIGURATION	155
V	ENGINEERING DRAWINGS.	183
	LIST OF REFERENCES	195

(Reverse is blank)

LIST OF ILLUSTRATIONS

Figure	Title	Page
1	EUREKA Test Vehicle Capabilities Envelope.	2
2	Forebody Model Details	6
3	Wake Survey Probe Details	9
4	Pressure Distribution on Modified Arapaho C	12
5	Pressure Distribution on Blunted Elliptical Cone	13
6	Flow Field Nomenclature at High Speeds	15
7	Mach Number Variation in Asymmetric Wake ($M_{\infty} = 2$ and 3; $Y/D = Z/D = 0.15$)	19
8	Mach Number Variation in Asymmetric Wake ($M_{\infty} = 4$ and 5; $Y/D = Z/D = 0.15$)	20
9	Mach Number Variation in Asymmetric Wake ($Y/D = 0.379$; $Z/D = 0.607$)	21
10	Total Pressure in Asymmetric Wake versus Y/D ($M_{\infty} = 2$, $Re_{\infty}/in. = 0.37 \times 10^6$)	23
11	Total Pressure in Asymmetric Wake versus Z/D ($X/D = 1$ and 2, $M_{\infty} = 2$, $Re_{\infty}/in. = 0.37 \times 10^6$)	24
12	Total Pressure in Asymmetric Wake versus Z/D ($X/D = 3, 5$, and 8, $M_{\infty} = 2$, $Re_{\infty}/in. = 0.37 \times 10^6$)	25
13	Total Pressure in Asymmetric Wake versus Y/D ($M_{\infty} = 5$, $Re_{\infty}/in. = 0.49 \times 10^6$)	26
14	Total Pressure in Asymmetric Wake versus Z/D ($M_{\infty} = 5$, $Re_{\infty}/in. = 0.49 \times 10^6$, $X/D = 1$ and 2)	27
15	Total Pressure in Asymmetric Wake versus Z/D ($M_{\infty} = 5$, $Re_{\infty}/in. = 0.49 \times 10^6$, $X/D = 3, 5$, and 8)	28
16	Static Pressure Variation in Asymmetric Wake ($Y/D = 0.15$)	29
17	Base Pressure Variation in Asymmetric Wake	30
18	Dynamic Pressure Variation in Asymmetric Wake ($Y/D = Z/D = 0.15$)	31
19	Dynamic Pressure Variation in Asymmetric Wake ($Y/D = 0.37$, $Z/D = 0.607$)	32

AFFDL-TR-67-i92
Volume I

<u>Figure</u>	<u>Title</u>	<u>Page</u>
20	Mach Number Correlation Parameter for Similitude Deviation (Y/D).	34
21	Mach Number Correlation Parameter for Similitude Deviation (Z/D).	35
22	Asymmetric Near-Wake Flow Mean Similitude Deviation versus Mach Number	36
23	P_b/P_∞ versus Reynolds Number for Basic Arapaho C with Blunted Nose Cone	41
24	P_b/P_∞ versus Reynolds Number for Basic Arapaho C and Modified Arapaho C-1	42
25	Flow Classification by Empirical Reference	43
26	Selection of Farthest Forward Center-of-Pressure Location.	45
27	Nose Drag Differential of Spike versus Blunted Nose	47
28	Flare Drag Differential Axisymmetric versus Asymmetric Flares	47
29	Vehicle Drag.	48
30	Predicted Vehicle Drag for Recommended Modified Arapaho C	49
31	Estimated Pressure Distribution over Modified Arapaho C-1.	51
32	Trajectories for Two Test Points in Support of Thermal Analysis.	53
33	Cold Wall Heat Flux Rate in Turbulent Flow	54
34	Cold Wall Heat Flux Rate in Turbulent Flow (Mach 6; 200,000 ft).	56
35	Temperature Rise with Time on EUREKA Inflatable Appendage	57
36	Geometric Details of Elliptical Flared Appendage	58
37	EUREKA Electrical Load versus Time Electrical System	63
38	Recovery Parachute Deployment	65
39	Flare Deployment Sequence	67

<u>Figure</u>	<u>Title</u>	<u>Page</u>
40	Placement of FLSC	68
41	Flare Cover Loading at Ejection	69
42	Appendage Inflation System	71
43	EUREKA Appendage Inflation Parameters	73
44	Deployment of Basic Arapaho C Test Decelerator	74
45	Deployment of EUREKA Test Decelerator	75
46	Deployment Data	77
47	Repositioning Sequence	81
48	Data Acquisition System.	83
49	Radar and Radio Beacon.	85
50	EUREKA Flight Test Camera View Angles.	86
51	Profile of Modified Arapaho C Test Vehicle	88
52	Opening Shock Loading Characteristics	89
53	Loads on Modified Arapaho C Test Vehicle	91
54	Test Item Container Aft Flange Loading (Boost Conditions)	93
55	Tensiometer Beam Stress Analysis (Section A-A)	97
56	Tensiometer Beam Stress Analysis (Sections 2-2, 3-3, and 4-4).	98
57	Beam Support Fitting Stress Analysis.	99
58	Test Item Container Cover Stress Analysis (Launch Conditions).	100
59	Test Item Container Cover Stress Analysis (Test Item Deployment).	101
60	Inflatable Appendage Designs.	106
61	Longitudinal and End Views of Elliptical Frustrum	108
62	Cross Section of Midpoint of Elliptical Frustrum	111
63	Base Support Loading Diagram	114

AFFDL-TR-67-192
Volume I

<u>Figure</u>	<u>Title</u>	<u>Page</u>
64	Despin Plumbing Changes	125
65	Skirt Assembly Leakage Locations	126
66	Flare Shape Deviation	127
67	Spacing of Wave-Guide Cavity Antennas	130
68	Sequencing Circuit	137
69	Line Resistance Diagram	139
70	Component Installation (Starboard View)	156
71	Component Installation (Port View)	157
72	Component Installation (Top View)	158
73	Component Installation (Bottom View)	159
74	Flare Module Inner Construction	160
75	Flare Cover (Aerodynamic Fairing)	161
76	Mockup Assembly (Front View)	162
77	Mockup Assembly (Rear View)	163
78	Mockup Assembly (Side View)	164
79	Flare Cover Jettison	165
80	Uninflated Flare	166
81	Inflated Flare (1 PSI)	167
82	Test Item Deployment	168
83	Test Item Unpackaged	169
84	Test Item Line Stretch	170
85	Test Item Repositioning	171
86	Recovery Parachute Deployment	172
87	Recovery Parachute Line Stretch	173
88	Internal View (Cameras Exposed)	174
89	Flare with 1-psi Inflation Pressure (Top View) . .	175

AFFDL-TR-67-192
Volume I

<u>Figure</u>	<u>Title</u>	<u>Page</u>
90	Flare with 2-psi Inflation Pressure (Top View) . .	176
91	Flare with 5-psi Inflation Pressure (Top View) . .	177
92	Flare with 2-psi Inflation Pressure (Side View) . .	178
93	Flare with 3 1/2-psi Inflation Pressure (Side View)	179
94	Flare with 5-psi Inflation Pressure (Side View) . .	180
95	Flare with 3 1/2-psi Inflation Pressure (End View).	181
96	Flare with 5-psi Inflation Pressure (End View) . .	182

LIST OF TABLES

<u>Table</u>	<u>Title</u>	<u>Page</u>
I	Range of Uncertainties	7
II	Wake Survey Test Conditions Summary	8
III	Static Stability Test Conditions Summary	10
IV	Recommended Vehicle Modifications	59
V	Pyrotechnic Devices	60
VI	Sequence of Events	62
VII	Sequence Firing Current Summary	64
VIII	Circuits Affected by Fuse Resistor Incorporation. . .	65
IX	FM/FM Data	82
X	FM/PAM Data (Channel 22)	84
XI	Weight Estimate for Stress Check	92
XII	EUREKA Flight Vehicle Weight/Balance Variation with Programmed Sequencing.	102
XIII	Weight and Balance Comparison of Basic C and Modi- fied C	102
XIV	Weight/Balance Summary (Items Removed in Redesign)	103
XV	Weight/Balance Summary, Items Added in Redesign .	104
XVI	Critical Pressure Computation.	107
XVII	Seam/Cloth Test Results	117
XVIII	Refurbishment Parts List	119
XIX	Aerospace Ground Equipment List	121
XX	Pyrotechnic Device Circuit Characteristics	141
XXI	Calculate Functions of ϕ	144
XXII	Calculated θ Values for Corresponding ϕ 'S	145
XXIII	Calculation Results of ψ	146

AFFDL-TR-67-192
Volume I

<u>Table</u>	<u>Title</u>	<u>Page</u>
XXIV	Hoop Stress Calculations	146
XXV	Hoop Stress Calculation Summary	147

LIST OF SYMBOLS

WAKE SIMILARITY ANALYSIS (Section III)

C = speed of sound, fps

D = forebody base diameter, ft

f_n = function of

$K_{X,Y,Z}$ = nondetermining criteria

$K_1 \dots K_n$ = determining criteria

K' = correlation parameter

l = body length, ft

M_L = local Mach number

M_∞ = free stream Mach number

P = pressure, psi

P_b = base pressure, psi

P_{t_2} = pitot pressure (total pressure immediately behind shock wave), psi

P_{t_∞} = free stream stagnation pressure, psi

P_∞ = free stream static pressure, psi

q = dynamic pressure, psi

$Re_\infty/\text{in.}$ = free stream Reynolds number per inch

V = velocity, fps

X = downstream direction and distance, ft

Y = vertical direction and distance, ft

Z = lateral direction and distance, ft

σ_i = singular similarity deviation

$\bar{\sigma}$ = mean similarity deviation

AERODYNAMIC ANALYSIS (Section IV, Item 2)

A_b = forebody base area, sq ft

C_D = vehicle drag coefficient

C_{D_1} = basic Arapaho C drag coefficient

C_{D_2} = Arapaho C with nose cone drag coefficient

C_{D_3} = modified Arapaho C-1 drag coefficient

C_M = pitching moment coefficient

C_{M_α} = change in pitching moment coefficient with angle of attack

C_N = normal force coefficient

C_{N_α} = change in normal force coefficient with angle of attack

D = vehicle reference diameter, ft

dp/dt = spin deceleration, deg/sec²

F = thrust, lb

I_R = vehicle roll moment of inertia, slug-sq ft

M_∞ = free stream Mach number

P_b = base pressure, psi

P_∞ = free stream static pressure, psi

Re = Reynolds number

T = torque, ft-lb

t = time, sec

W_0 = initial spin rate, deg/sec

W_1 = final spin rate, deg/sec

X_{cp} = location of center of pressure in longitudinal direction, ft

x = moment arm, ft

α = vehicle angle of attack, deg

ϕ = vehicle angle of roll, deg

THERMODYNAMIC ANALYSIS AND VEHICLE MODIFICATION (Section IV, Item 3 and Section IV, Item 4)

A = area, sq ft

a = acceleration, ft/sec²

C_D = drag coefficient

C_P = pressure coefficient

c = specific heat, Btu/lb F

D = diameter, ft

D_o = nominal diameter, ft

E = energy, ft-lb

F = force, lb

g = gravitational constant, ft-lbm/lbf-sec²

h = convective heat transfer coefficient, Btu/hr-sq ft-F

h_r = recovery of adiabatic wall enthalpy, Btu/lb

h_w = wall enthalpy, Btu/lb

k = thermal conductivity, Btu/hr-ft-F

KE = kinetic energy, ft-lb

m = mass, slugs

M_∞ = free stream Mach number

n = ratio of specific heats

P = peak thruster force, lb

AFFDL-TR-67-192
Volume I

Pr = Prandtl number

p = pressure

q = dynamic pressure, lb/sq ft

\dot{q}_w = heat flux rate, Btu/sq ft-sec

R = gas constant, ft-lbf/lbm - R

Re = Reynolds number based on length

Re_θ = Reynolds number based on momentum thickness

r = radius, ft

T = temperature, F or R

T_i = nodal temperature, F or R

T_i' = new nodal temperature, F or R

T_{aw} = adiabatic wall temperature, F or R

T_{cw} = cold wall temperature, F or R

T_s = space temperature, F or R

t = time, sec

u = local velocity, fps

v = velocity, fps; or volume, cu in.

w = weight, lb

\dot{w} = weight flow rate, lb/sec

x = distance, ft

ϵ = emissivity

μ = viscosity, lbm/ft-sec

ρ = density, lbm/cu ft

σ = Stefan-Boltzmann constant = $(0.173 \times 10^{-8}$
Btu/hr-sq ft-R⁴)

AFFDL-TR-67-192
Volume I

Subscripts

- a = conditions in appendage
- B = conditions in reservoir
- w = conditions at wall
- ∞ = free stream conditions
- 1 = conditions at boundary layer edge or initial conditions
- 2 = secondary conditions

VEHICLE STRUCTURAL ANALYSIS (Section IV, Item 5)

- A = area, sq in.
- c = moment arm, in.
- d = diameter, in.
- E = energy, ft-lb
- E_y = modulus of elasticity, psi
- F_A = axial force, lb
- f_b = bending stress, psi
- f_{br} = bearing stress, psi
- f_c = compressive stress, psi
- f_{cy} = compressive yield stress, psi
- f_v = shear stress, psi
- I = moment of inertia, in.⁴
- I_{NA} = moment of inertia about neutral axis, in.⁴
- m = mass, slugs
- M.S. = margin of safety

AFFDL-TR-67-192
Volume I

M_{\max} = maximum bending moment, in. -lb

M_{ult} = ultimate bending moment, in. -lb

P = load, lb

R = reaction at beam ends, lb

r = radius, in.

T = thrust, lb

t = thickness, in.

V = velocity, fps

w = weight, lb

\bar{x} = distance measured from c. g., in.

α = angular acceleration, rad/sec²

η = lateral component of test item opening shock load, lb

θ = taper angle, deg

μ = Poisson's ratio

APPENDAGE DESIGN(Section IV, Item 6)

a = length, in.

b = elliptical semimajor axis

d = length of conical frustrum, in.

E = modulus of elasticity, psi

$E(k)$ = elliptic integral

f = stress, psi

f_b = bending stress, psi

f_c = compressive stress, psi

f_h = hoop stress, psi

f_m = meridional stress, psi

h = elliptical semiminor axis

I = moment of inertia, in.⁴

$j = \sqrt{EI/P}$, in.

$k = \sqrt{b^2 - h^2} / h$

L = ellipse circumference, in.

M = bending moment, in.-lb

P = axial load, lb

p = differential pressure, psi

R = radius, in.

R_i = reaction at inner beam end, lb

R_o = reaction at outer beam end, lb

r_i = inner radius, in.

r_o = outer radius, in.

S = distance along ellipse, in.

w_i = distributed load per inch at inner beam end, lb/in.

w_o = distributed load per inch at outer beam end, lb/in.

x, y, z = reference coordinates

α = angle between tangent to ellipse and its major axis, deg

β = taper angle of meridian, deg

γ = half angle of circular arc, deg

δ = deflection, in.

θ = arctan (x/y), deg

ϕ = ellipse parameter angle, deg

$\psi = \pi/2 - \theta + \alpha$, deg

SECTION I

INTRODUCTION

1. PROGRAM OBJECTIVES

Under the AFFDL-sponsored Aerodynamic Deployable Decelerator Performance Evaluation Program (ADDPEP) reported in Reference 1, Good-year Aerospace Corporation designed, developed, and manufactured the Arapaho C free-flight test vehicle capable of testing a variety of decelerator types in supersonic flight regimes. The C vehicle, in the purely ballistic type classification, generates a symmetrical wake that is typical of such bodies of revolution. Extensive free-flight and wind-tunnel testing of supersonic deployable aerodynamic decelerators in the wakes of symmetrical forebodies has given the Air Force much insight into the drag and stability performance characteristics of decelerators in such flow fields. However, there has been relatively little research to evaluate and/or predict accurately the performance of those same decelerators in the wake of an unsymmetrical forebody (typified by the lifting class of re-entry vehicles presently under investigation).

Because of the limitations of wind-tunnel testing, the Air Force Flight Dynamics Laboratory (AFFDL) recognized the need for development of a flight test capability in order to properly evaluate the performance of decelerators in unsymmetrical wakes. Therefore, AFFDL sponsored the Establishment of an Unsymmetrical Wake Test Capability for Aerodynamic Decelerators (EUREKA) program to develop this capability. One of the primary objectives of the EUREKA program was to investigate the feasibility of modifying the Arapaho C test vehicle to provide an unsymmetrical free flight test capability. Only the investigations and analyses to achieve this objective are presented in this volume, while the remaining objectives are reported in Volumes II and III. The investigation and analyses of aerodynamic decelerator performance in supersonic wake flow fields is covered in Volume II. Volume III contains a tabulation of body surface and wake pressure data obtained from wind-tunnel tests.

2. DESIGN REQUIREMENTS

Based on prescribed free flight capability requirements and unsymmetrical wake simulation criteria, the following test vehicle configuration and supporting equipment requirements were established.

1. The test vehicle weight will be less than 450 lb at initiation of test item decelerator deployment.
2. The vehicle will be capable of achieving test item deployment points within the flight test envelope depicted in Figure 1.
3. The structural integrity of the basic Arapaho C will be maintained.

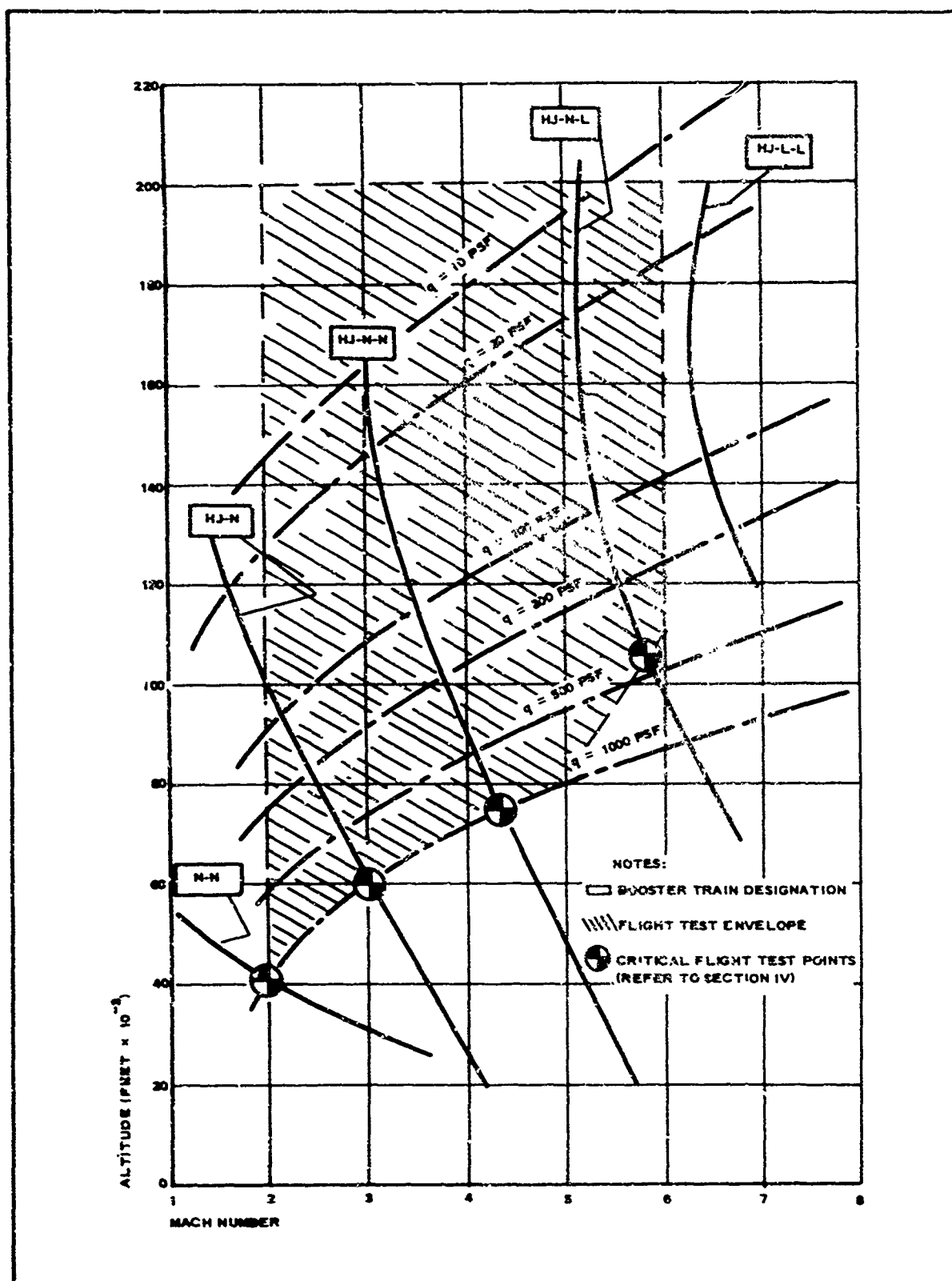


Figure 1 - EUREKA Test Vehicle Capabilities Envelope

4. All inflatable appendages incorporated for wake modification will be deployed and fully inflated prior to test item deployment.
5. The feasibility of deploying and erecting the appendages in less than 0.3 sec will be determined.
6. The test item will be deployed aft of the modified-in-flight vehicle parallel to the flight path.
7. A minimum test item stowage volume of 0.5 cu ft will be provided.
8. The test vehicle will be stable from launch through test item inflation, and the vehicular roll rates will not exceed 20 deg per second during the test item deployment and inflation sequence.
9. The positive deployment and inflation of the recovery system will not be interfered with by either the appendages or the test item decelerator.
10. The maximum projected diameter of the basic Arapaho C vehicle will not be exceeded.
11. The test data acquisition and transmission capabilities and overwater recovery capability of the basic Arapaho C will be retained in the modified vehicle.
12. The test item will be retained through vehicle impact.
13. The modified vehicle will comply with the Eglin AFB/Eglin Gulf Test Range safety criteria.

This volume contains complete descriptions of and conclusions resulting from wake analyses, vehicle stability analyses, vehicle design tradeoff studies, aero/thermo studies, and structural analyses conducted in order to determine the feasibility of modifying the Arapaho C test vehicle to provide the test capabilities and design requirements listed above. Also included is a description of a mockup of the inflatable appendage design that evolved from the preliminary design analysis.

SECTION II

WIND-TUNNEL TEST EQUIPMENT AND INSTRUMENTATION

1. GENERAL

All wind-tunnel tests in support of the EUREKA program were conducted in the 40-in. supersonic tunnel A of the von Karman Gas Dynamics Facility (VKF), AEDC. Two series of tests were required for support of the test vehicle feasibility investigation.

The first series, WT-I, was conducted to establish the stability of and flow field properties around two basic Arapaho C models and the modified Arapaho C. The second series, WT-II, was a wake survey of the near and middle wake regions of two basic Arapaho C models, the modified Arapaho C model, and the blunted elliptical cone model.

2. WIND-TUNNEL DESCRIPTION

Tunnel A is a continuous, closed-circuit, variable-density wind tunnel with an automatically driven, flexible plate-type nozzle and a 40- by 40-in. test section. The tunnel operates at Mach numbers from 1.5 to 6 at maximum stagnation pressures from 29 to 200 psia, respectively, and stagnation temperatures up to 300 F ($M_{\infty} \leq 6$). Minimum operating pressures are about one-tenth of the maximum at each Mach number.

3. MODELS AND SUPPORT SYSTEM

The forebody models are shown in detail in Figure 2. Configuration 1 is a 0.182-scale model of the basic Arapaho C test vehicle. Configuration 2 is identical to Configuration 1 except for the nose probe that was replaced with a blunted nose cone. Configuration 3 is the modified version of the Arapaho C vehicle, having an elliptical flare in place of the conical flare cylinder used on Configurations 1 and 2. Configuration 4 is an elliptical cone with an axisymmetric blunted nose cone identical to Configurations 2 and 3. Configuration 4 represents the target vehicle whose wake is to be simulated by the wake of the modified Arapaho C.

For the static stability tests, the models were sting mounted from the rear. The stings were fitted to a movable horizontal sector that has an angular travel of 20 deg in the horizontal plane and, with a straight sting, provides model angles in pitch or yaw of -5 to +15 deg.

For the wake survey tests, the models were mounted to a horizontal wall-to-wall strut having constant chord and constant thickness.

4. INSTRUMENTATION

Model force measurements were made with a six-component, moment-type, strain-gage balance supplied and calibrated by VKF. Before the test, loadings in a single plane and combined static loadings were applied to the balance, which simulated the range of model loadings anticipated for the test. The range of uncertainties listed in Table I corresponds to

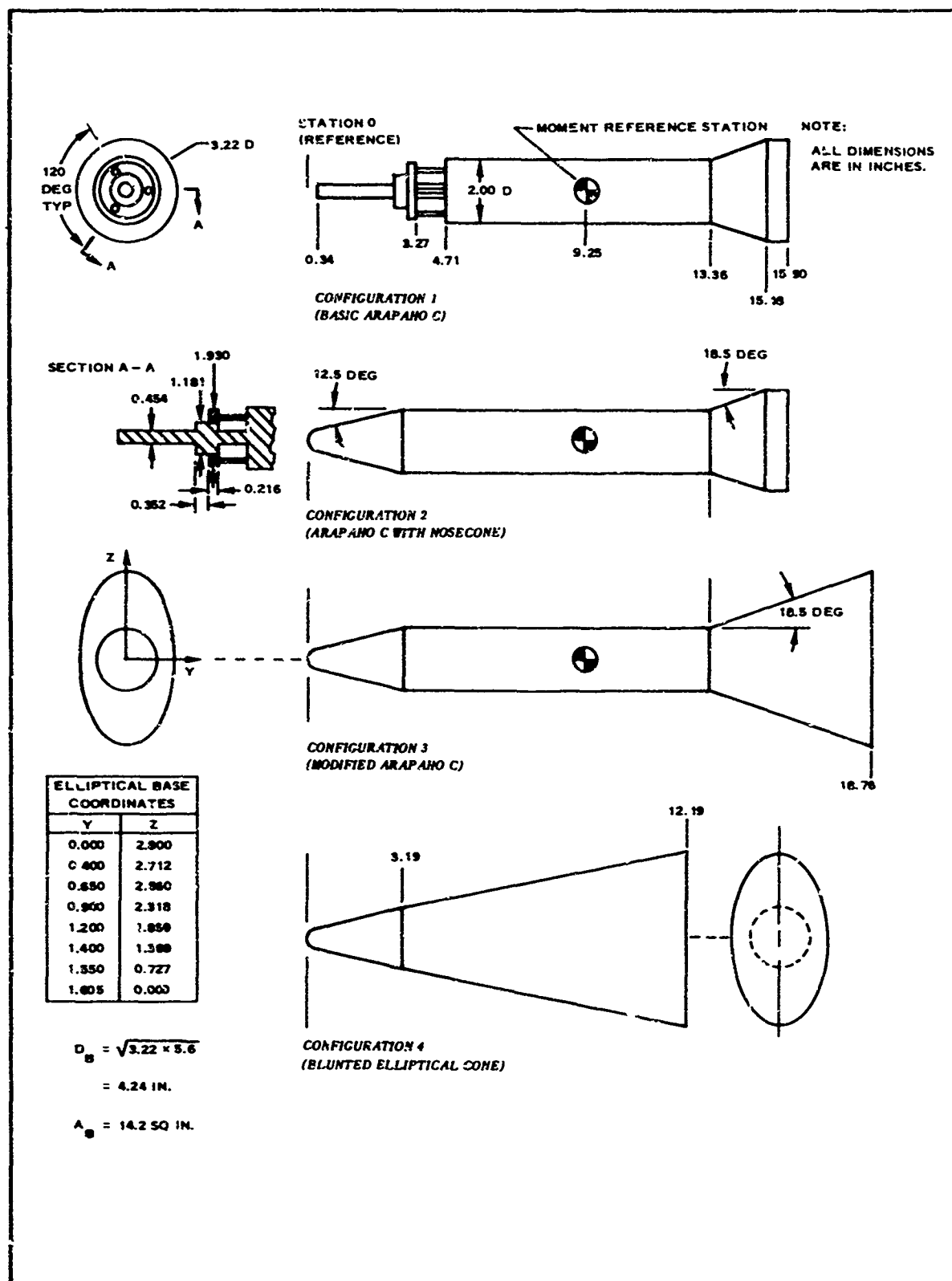


Figure 2 - Forebody Model Details

TABLE I - RANGE OF UNCERTAINTIES

Balance component	Design load	Range of static loadings	Range of uncertainties
Normal force (lb)	150	± 2 to ± 60	± 0.03 to ± 0.12
Pitching moment (in. -lb)	690	± 10 to ± 150	± 0.20 to ± 0.60
Side force (lb)	75	± 2 to ± 39	± 0.03 to ± 0.18
Yawing moment (in. -lb)	345	± 5 to ± 80	± 0.20 to ± 0.90
Rolling moment (in. -lb)	60	± 24 to ± 48	± 0.05 to ± 0.10
Axial force (lb)	75	5 to 25	± 0.07 to ± 0.12

the difference between the applied loads and the values calculated with the balance equations used in the final data reduction. The minimum uncertainties given are for loads up to about 10 percent of the maximum applied and are for loadings on the particular component only (no combined loading interaction effects). The maximum uncertainties are for combined loadings.

From calibration results, the maximum variation of tunnel centerline Mach number is about ± 0.5 percent and the angle-of-attack setting is considered accurate to within 0.1 deg. The tunnel stilling chamber temperature is considered to be accurate to ± 3 R. The tunnel stilling pressure, p_0 , was measured with transducers of 5-, 15-, 30-, 60-, 150-, and 300-psid (pounds per square inch, differential) capacity that are considered accurate to within 0.3 percent of full-scale capacity.

The model base pressures were measured with 1-, 5-, and 15-psid capacity transducers, referenced to a near vacuum, that are also considered accurate to within 0.3 percent of the transducer capacity. The lowest base pressures were encountered at the low Reynolds number test conditions at $M_\infty = 5$. At these test conditions, base pressures were in the order of 0.008 psia. The 0.3-percent accuracy of a 1-psid transducer could then introduce errors of approximately ± 37.5 percent of the measured values.

The local wake pitot and static pressures were measured with transducers of the same capacity as those used for base pressure measurement. Again the lowest pressures and, therefore, the greatest inaccuracies, were encountered at the minimum pressure test conditions at $M_\infty = 5$. Combined errors in the local static and pitot pressures may introduce inaccuracies of 0.2 M at $M_L = 1.0$. The inaccuracy in this case was determined using maximum errors in pressure measurements, assuming the local static pressure equal to free stream static pressure and being measured with a 1-psid transducer and the pitot pressure measured with a 5-psid transducer. Making these same assumptions at free stream Mach numbers of 4, 3, and 2 and at the minimum pressure condition, inaccuracies in measuring a local Mach number of 1.0 are 0.11, 0.06, and 0.03 M_L , respectively. At the high pressure conditions for these tests,

the accuracy of measurement at $M_{\infty} = 5$ and $M_L = 1.0$ is increased by approximately a factor of four. The lower Mach number test cases reflect a similar accuracy increase at the high pressure test conditions.

Table II lists the test conditions for the wake survey tests. The errors incurred in the measurement of the local static pressures (which are approximately equal to the free stream static pressure) caused by the inaccuracy of a 1-psid transducer appear in the third significant digit, except for the $M_{\infty} = 5$ case. The total pressure, being higher than the static pressures, should then reflect a higher degree of accuracy.

TABLE II - WAKE SURVEY TEST CONDITIONS SUMMARY

Configuration	M_{∞}	$Re_{\infty}/in. \times 10^6$	Total pressure (psia)	Static pressure (psia)	Total temperature (R)	Rake X/D stations
Modified Arapaho C and blunted elliptical cone	2	0.05	2.8	0.36	581	1, 2, 3, 5, 7, 8 for all test points
	2	0.365	19.0	2.43	582	
	3	0.058	5.9	0.17	583	
	3	0.50	43.0	1.17	582	
	4	0.09	13.5	0.09	583	
	4	0.50	73.0	0.46	583	
	5	0.13	30.5	0.058	585	
	5	0.50	133.0	0.251	631	

The wake survey rakes used in these tests were of a cruciform design with multiple probes, making it possible to obtain complete wake profiles at each X/D station without lateral or vertical movement of the rake. The spacing of the pitot probes was one-tenth the diameter of the axisymmetric forebody base. The pitot and static port locations are shown schematically in Figure 3 in their respective positions behind an elliptical forebody base.

5. TEST CONDITIONS

Table II summarizes the test conditions for the wake survey tests which were completed in support of the wake similarity analysis. Table III presents the test conditions for the static stability tests of the various forebody configurations. The results of these tests are discussed in detail as required in applicable sections of this report. Tabulated wake survey data are presented in Volume III of this report. The complete compilation of experimental data from these wind-tunnel tests may be obtained from AFFDL by request.

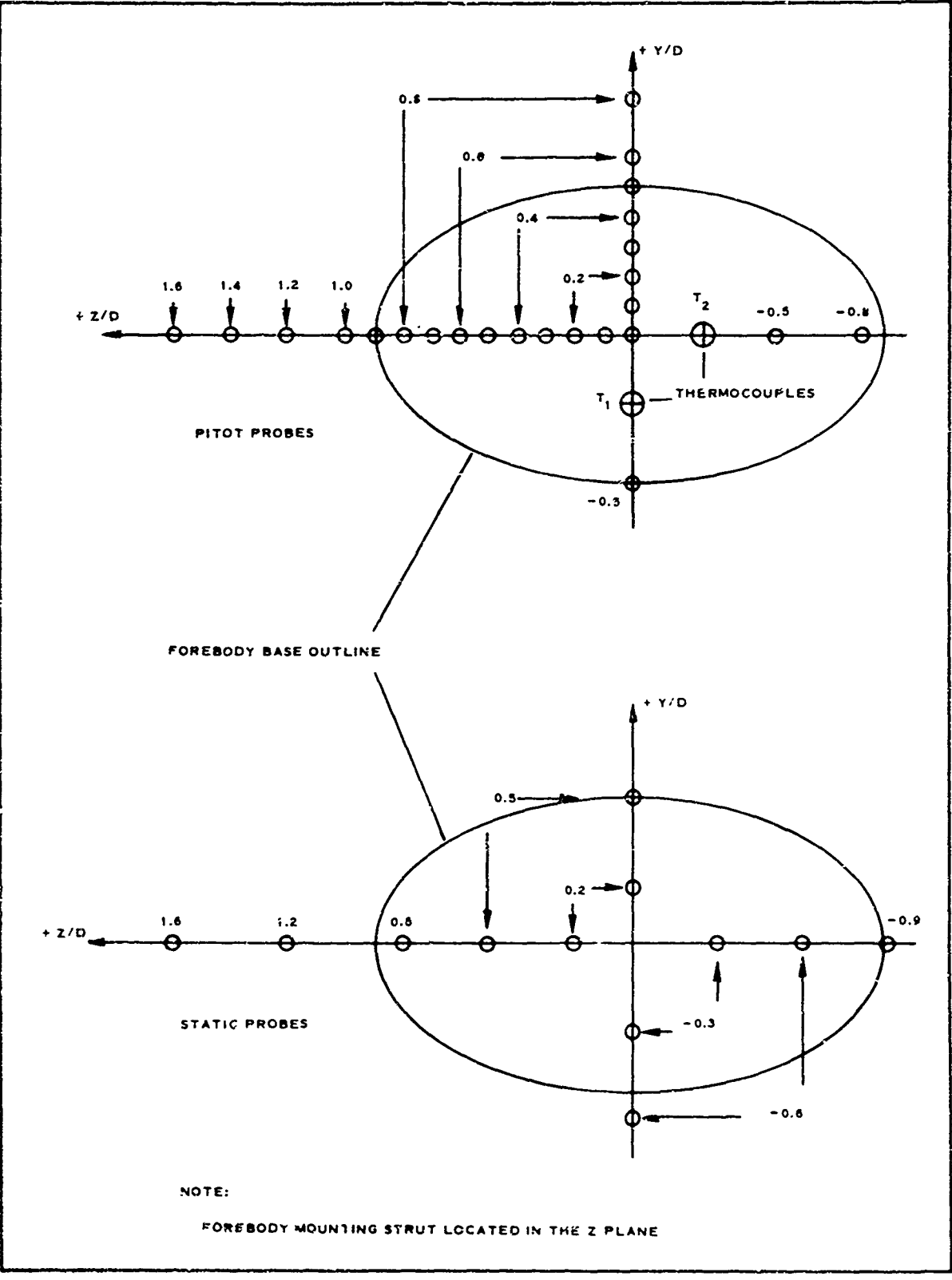


Figure 3 - Wake Survey Probe Details

TABLE III - STATIC STABILITY TEST CONDITIONS SUMMARY

Configuration	M_{∞}	$Re/\text{inch} \times 10^{-6}$		Vehicle angle of attack (deg)	Angle of roll (deg)	
		Minimum	Maximum			
Modified Arapaho C	2.5	0.04902	0.5157	-5 to 15, in 1/2-deg increments from -2 to +2	0, 22.5, 45 and 90 at each angle of attack	
	3.0	0.03608	0.5099			
	4.0	0.03665	0.5037			
	5.0	0.05174	0.4896			
Arapaho C with blunted nosecone	2.5	0.04932	0.5164	-5 to 15, in 1/2-deg increments from -2 to +2	Axisymmetric vehicles, no roll required	
	3.0	0.03727	0.5081			
	4.0	0.03705	0.5072			
	5.0	0.05115	0.5453			
Basic Arapaho C	2.5	0.04783	0.5134	-5 to 15, in 1/2-deg increments from -2 to +2		
	3.0	0.03810	0.5154			
	4.0	0.03987	0.4248			
	5.0	0.05089	0.2407			

SECTION III
SIMILARITY ANALYSIS OF ASYMMETRIC WAKES
BASED ON EXPERIMENTAL RESULTS

1. INTRODUCTION

Along with determining the feasibility of modifying the Arapaho C test vehicle, it was necessary to determine if the modified test vehicle could adequately simulate the wake of a lifting body. An experimental investigation was conducted in order to determine similarities in the wakes of two vehicles with elliptical aft ends. The two vehicles investigated were a modified Arapaho C and a blunted elliptical cone as shown in Figure 2.

2. VEHICLE CONFIGURATIONAL SELECTION

For the selection of two configurations with asymmetry in the Y-Z plane exhibiting a similarity in flow fields in their wakes, consideration was given to the following parameters:

1. Fore- and aft-body geometry
2. Fineness ratio
3. Wetted area
4. Volume to $2/3$ power
5. Fluid mechanics of the flow

These considerations were important to obtain a similarity of stream functions and associated boundary layers.

3. FLOW FIELDS AROUND VEHICLES

The streamline deflection defines the flow field in general and, assuming inviscid flow models, the following qualitative features appear for each vehicle.

Initial compression behind the main bow shock of the modified Arapaho C-1 is followed by the expansion at the cone shoulder, continuing along the cylindrical midbody until the region of flare influence is reached. Separation phenomenon from here on is felt along the flare until the final separation-expansion into the base region. These phenomena are illustrated by the pressure distributions along the X-Y axes obtained in the wind tunnel (see Figure 4).

Similar initial compression behind the main bow shock of the blunted elliptical cone and expansion at the shoulder is followed by a moderate expansion-compression with no perturbations to inhibit the separation prior to reaching the base region. Again, pressure distributions along the X-Y axes indicate the correctness of prediction (see Figure 5).

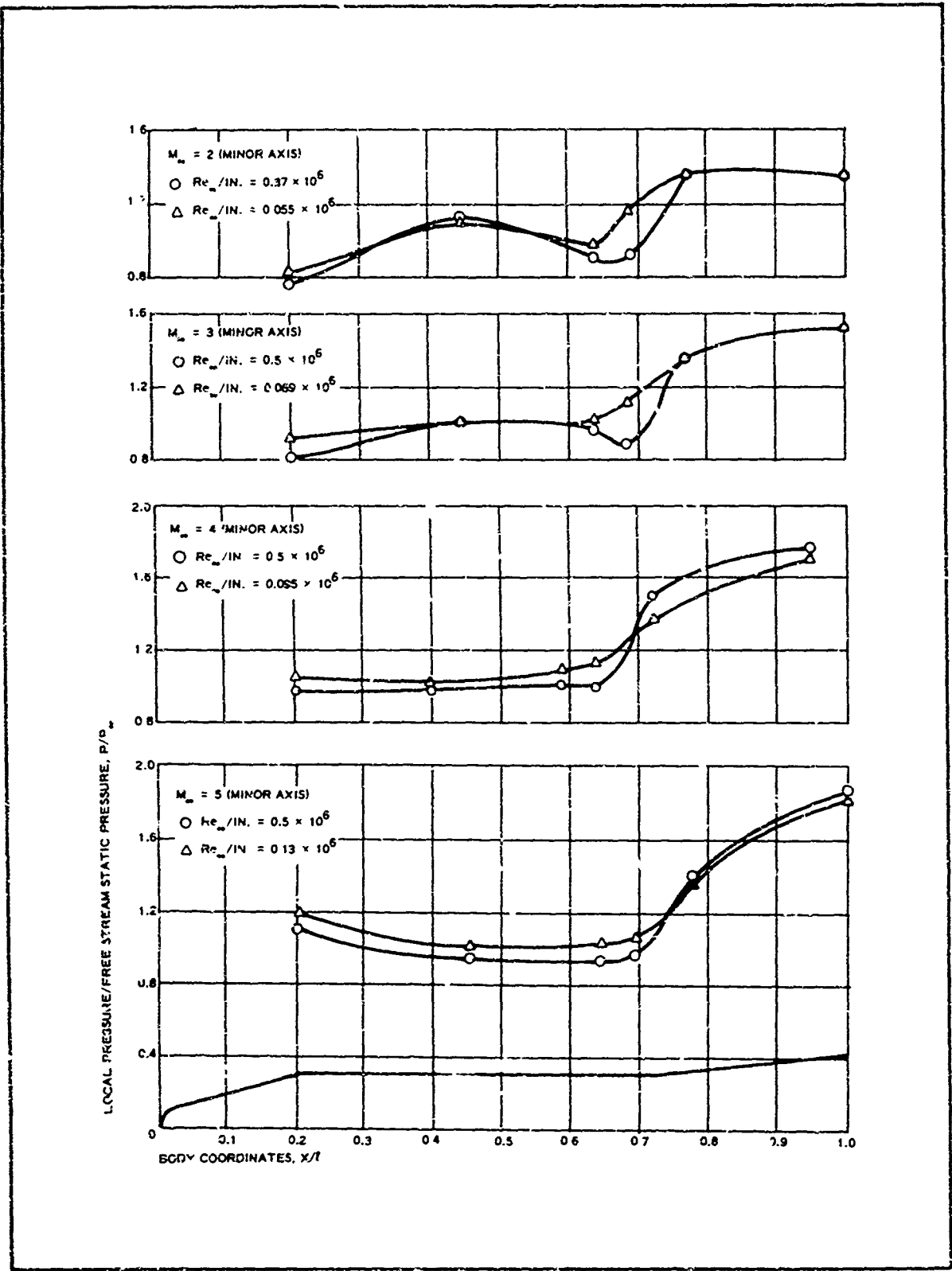


Figure 4 - Pressure Distribution on Modified Arapaho C

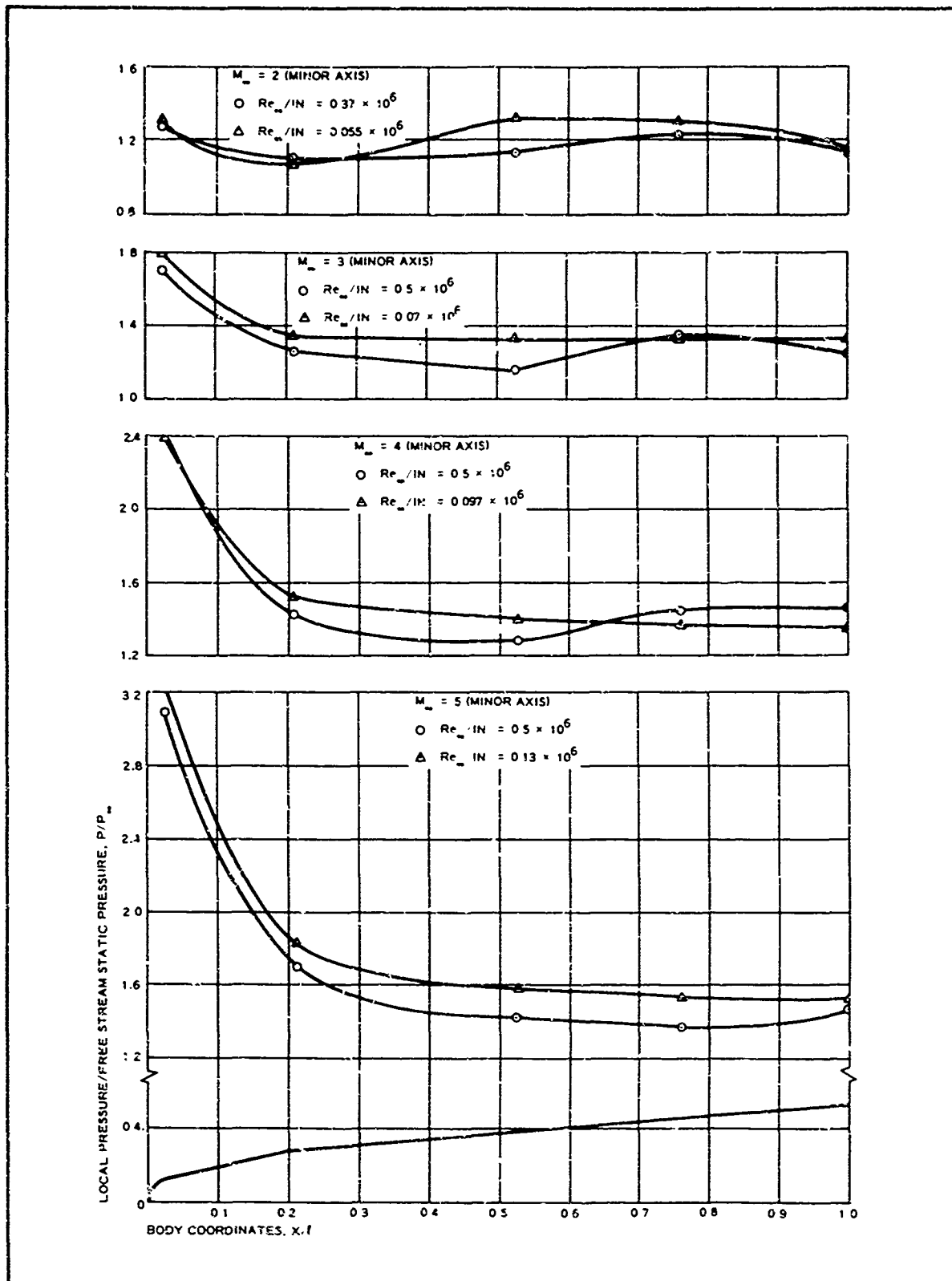


Figure 5 - Pressure Distribution on Blunted Elliptical Cone

At the base of the Modified C vehicle, flow streamlines expand through a larger deflection angle than with the blunted elliptical cone and diverge more from the free stream direction. The Mach number increase at separation is expected to be larger, hence, the boundary layer structure of a free-shear layer will be distorted, and deviations from the Prandtl-Meyer theory predictions are introduced.

In the case of the blunted elliptical cone, the streamlines are closer to being parallel to the free stream flow direction after the expansion. Then, the boundary layer structure of the free-shear layer is nearly preserved, and the predicted Prandtl-Meyer values are closer to reality.

The influence of the three-dimensional nature of the flow present around the elliptical surface (principal and crosswise components) makes the boundary layer thinner at the major axis and thicker at the minor axis. The flow from higher pressure gradients to lower ones creates additional vorticity at the base of both vehicles and into the near wake.

The flow lateral profiles in the near wake have an elliptical shape that, after being propagated further downstream, degenerates into a circular shape. The mechanics of this readjustment is such that the magnitudes of flow parameters (local velocities and pressures), which are lower initially at the major axis, accelerate in the downstream direction and at higher rates at the major axis than at the minor axis. Eventually, the rates approach each other, and the point of convergence will indicate the presence of a circular profile.

4. WAKE FLOW FIELD STRUCTURE

The flow field structure in a wake is shown in Figure 6 (from Reference 2). There are areas in this structure that are of special interest to the present analysis. One area is the base region where the important wake-forming processes take place. This region is easily influenced by the presence of other bodies.

The experimental results indicate that the rake's presence distorts the flow in varying degrees in the $X/D \leq 3$ downstream range, and the corresponding data should be considered with caution. Another region of interest is the position of the neck since the decelerator performance is influenced by it. For the configurations and test conditions of this program, the $2 \leq X/D \leq 5$ range defines the limiting boundaries of the neck locations.

The wake flow fields are considered to be turbulent with a viscous edge region extremely difficult to define. As the Mach number increases, the influence of the inviscid supersonic outer wake is increasing. The inner viscous wake is mostly supersonic.

5. WAKE FLOW FIELD SIMILARITY

Similarity, or physical similarity, is defined as the phenomena describing two events when the properties of one event can be obtained from the prescribed properties of the other event by a simple conversion. Then

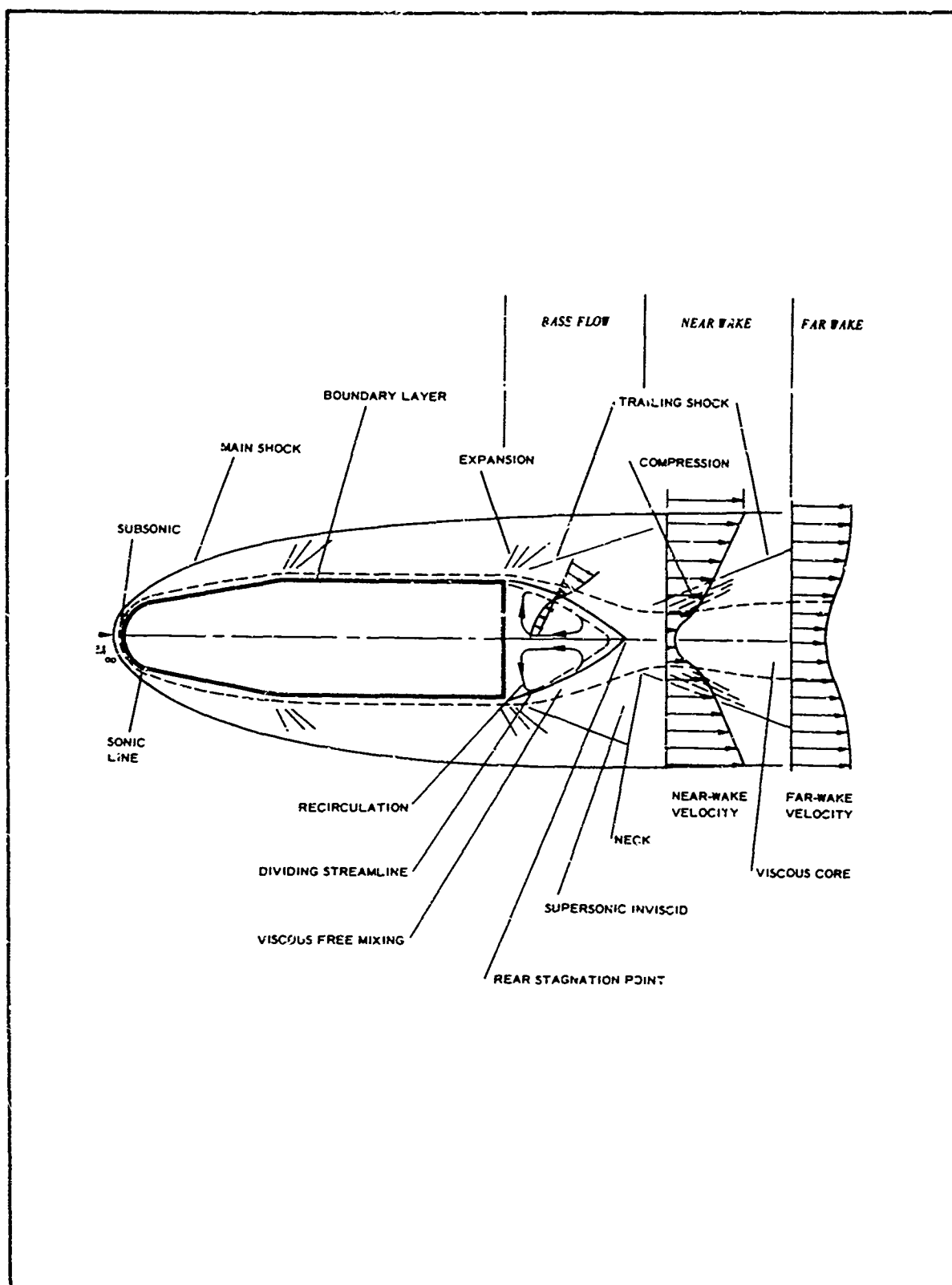


Figure 6 - Flow Field Nomenclature at High Speeds

if all nondimensional variables (nondimensional combinations of dimensional quantities) are equivalent, the events are similar. Similarity is defined by similitude criteria that take into consideration:

1. Uniqueness of a class of physical events
2. Uniqueness of a singular member of a class
3. Admittance of a difference in scale magnitudes for similar events

The similitude conditions that must be held in considering similar physical events in a wake are:

1. System invariance of basic variables
2. Similitude of all physical parameters
3. Initial uniqueness and stability of flow fields
4. Similitude of boundary conditions

In practical application, these criteria and conditions can not be fulfilled, and the question of the permissible magnitude for a deviation is introduced. Therefore, the criteria equation in general form is:

$$K_{X, Y, Z} = f_1 \dots f_n(K_1, K_2, \dots K_n) \quad (1)$$

where

$$K_{X, Y, Z} = \text{nondetermining criteria and} \\ K_1 \dots K_n = \text{determining criteria.}$$

The only determining criterion considered in this analysis is the Mach number (V/C), and the nondetermining criteria are the Mach number variations along the X, Y, Z axes in the wake, or

$$\begin{aligned} K_X &= f_1(M_L/M_\infty) \\ K_Y &= f_2(M_L/M_\infty) \\ K_Z &= f_3(M_L/M_\infty) \\ K_G &= f_4(M_L) \end{aligned} \quad (2)$$

The auxiliary nondetermining criteria are the normalized pitot, static, and dynamic pressures along a given set of cartesian coordinates. The initial free-stream similitude conditions for both vehicles are summarized in Table II. For similitude along the X, Y, Z axes, the following

ranges of cartesian coordinates (normalized by dividing them by the hydraulic diameter of 4.24 in.) were considered:

$$1 \leq X/D \leq 8 ,$$

$$0 \leq Y/D \leq 0.7 ,$$

and

$$0 \leq Z/D \leq 1.6 .$$

The experimental data used to define the similarity of the flow fields in a wake are influenced by the following experimental deficiencies.

1. Rake design (the configuration and volume occupied thereby) - The presence of the rake changes the structure of the normal wake flow. These changes were observed mostly in the $X/D \leq 3$ range.
2. Supporting strut (constant chord, straight, of a double-wedge-like profile, mounted at the mid-body) - The strut generates strong two-dimensional shock waves and a clearly discernible wake of its own. The shock wave interactions (three-to-two-dimensional, notably at a root-chord body) may affect the vehicle wake at the major axis, but are not understood at this time. Possible situations may involve either a strut-wake deflection or swallowing. Deflection will not influence the mass flow relations in the inner viscous wake, but swallowing (even partial) will affect the instrumentation readings.
3. Instrumentation outputs - These outputs are missing for some points, while at other points, the values are of questionable magnitudes. Preliminary evaluation of the static rake calibration indicates that data taken at lower stagnation pressure for each Mach number will have a lower accuracy for static pressures and local Mach numbers. Data reduction procedures that use the square of the Mach number will magnify these uncertainties in values.

6. RESULTS OF CRITERIA ANALYSIS

The analysis of the similarity of wake structures behind the two elliptical base vehicles is based on the experimental data. The method of analysis follows the principles of the similarity criteria stated above. Thus, if the Mach number is considered the determining criterion for similarity, its variation pattern along the major (Z) and minor (Y) axes at a given position (X) for each vehicle indicates the similarities in the wake flow fields of both. This search for similarity is applied for two regions of

the wake: the viscous inner wake in the Y-Z plane at the normalized coordinate station of $(Y/D, Z/D) = 0.15$ and the inviscid outer wake at the coordinate stations of $Y/D = 0.379$ and $Z/D = 0.607$. The latter stations are selected to coincide with the projected edges of the base, and they also indicate the approximate boundary for the viscous inner wake. This determining criterion is presented in Figures 7 through 9 as plots of the normalized ratios for each set of similar initial conditions (M_{∞} , $Re_{\infty}/in.$) for both vehicles. From these figures, the following generalized conclusions can be drawn.

1. Both vehicles indicate similar histories in developing local Mach numbers in the downstream direction.
2. The local Mach number ratios are higher at the minor axis initially, but rates of growth (recovery) are lower within the observable range (up to $X/D = 8$) as compared with those at the major axis.
3. The wake flow field profiles within the observable region are definitely elliptic in the viscous wake and more pronouncedly so at $M_{\infty} = 2.0$ conditions.
4. All profiles indicate gradual degeneration into a circular profile that will occur downstream of the observable range ($X/D > 8.0$).
5. In the viscous region under observation ($1 \leq X/D \leq 8$), the local Mach number never recovers to the free stream condition.
6. In the viscid-inviscid boundary region, the histories of local Mach number ratios again are similar for both vehicles.
7. The high Mach number ratios at $1 \leq X/D \leq 3$ region are more pronounced at the minor axis. Similar conditions are less pronounced at the major axis, which is in the plane of the supporting strut.
8. The changes of rates of recovery of Mach number ratios are smaller, but levels are higher due to viscid-inviscid mixing and dissociation.
9. At the $M_{\infty} = 2$ condition, the Mach number ratios represent the average readings that are outside of the viscous core. Hence, the streamlines are more of a planar nature, without shape discontinuities in direction.
10. At the $M_{\infty} = 5$ condition, the flow and local Mach numbers are influenced by the wake trailing (recompression) shock that tends to modify the typical histories shown at the $M_{\infty} = 3$ and 4 conditions in Figure 9.

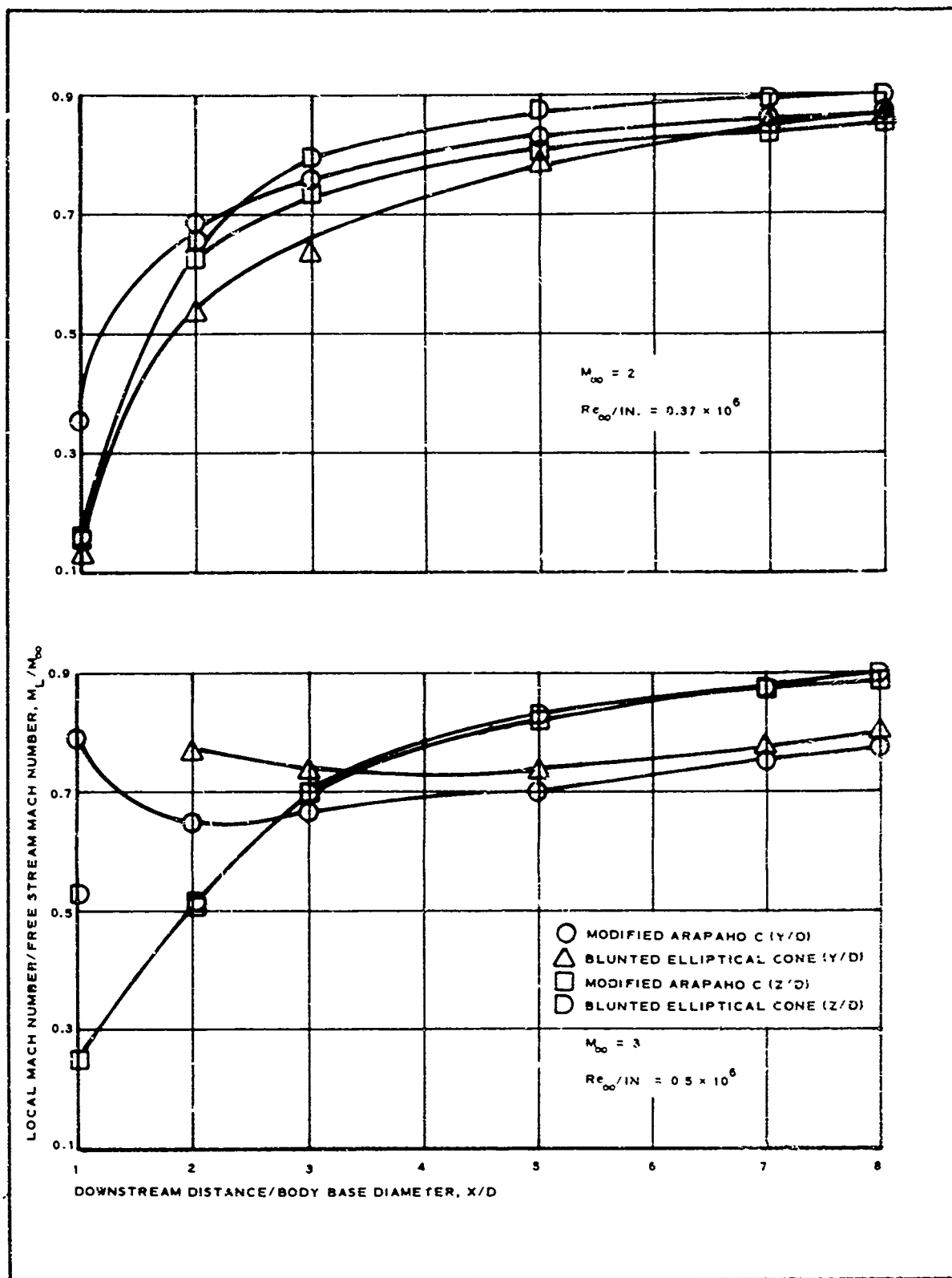


Figure 7 - Mach Number Variation in Asymmetric Wake
($M_\infty = 2$ and 3; $Y/D = Z/D = 0.15$)

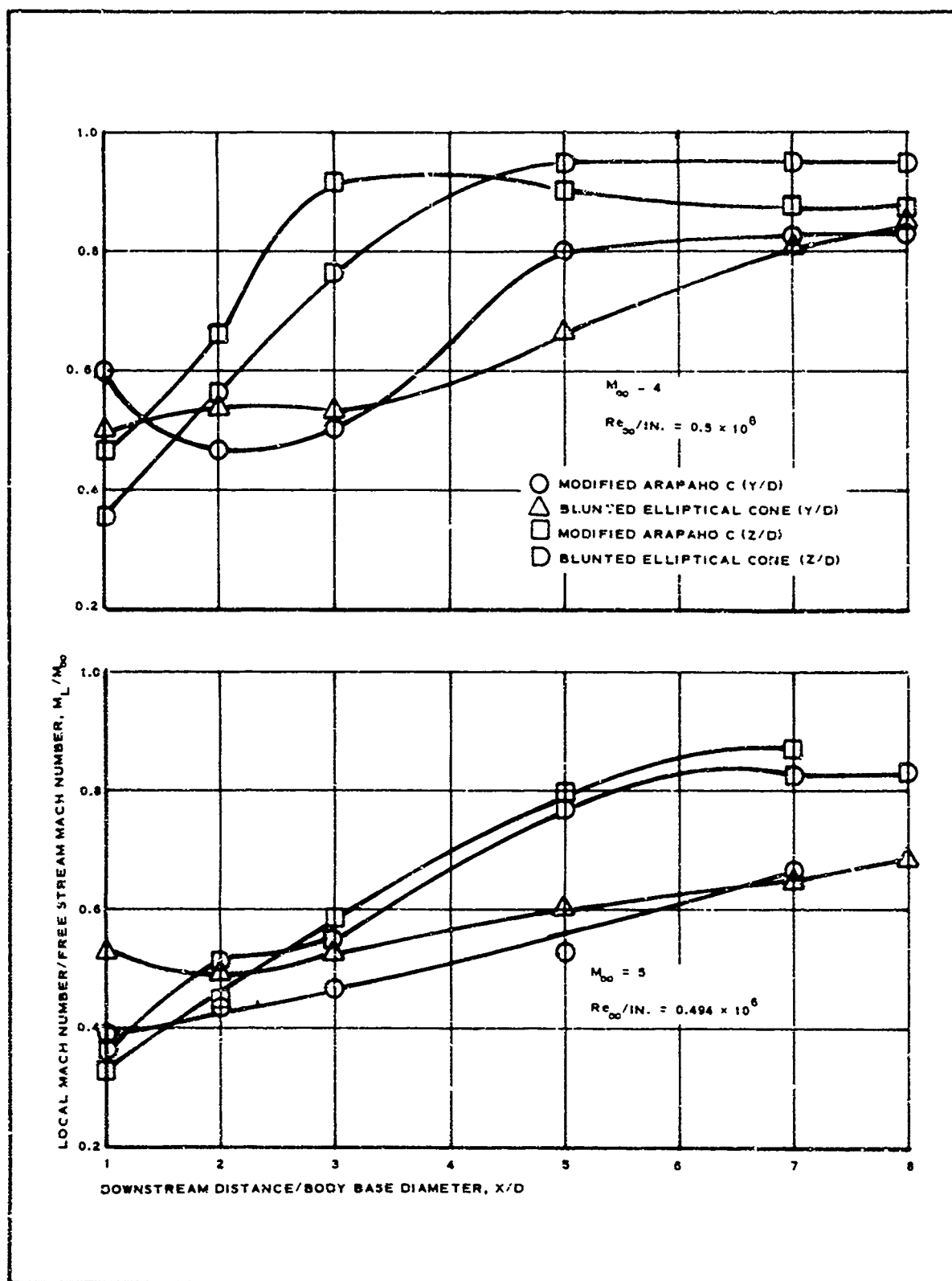


Figure 8 - Mach Number Variation in Asymmetric Wake
($M_\infty = 4$ and 5; $Y/D = Z/D = 0.15$)

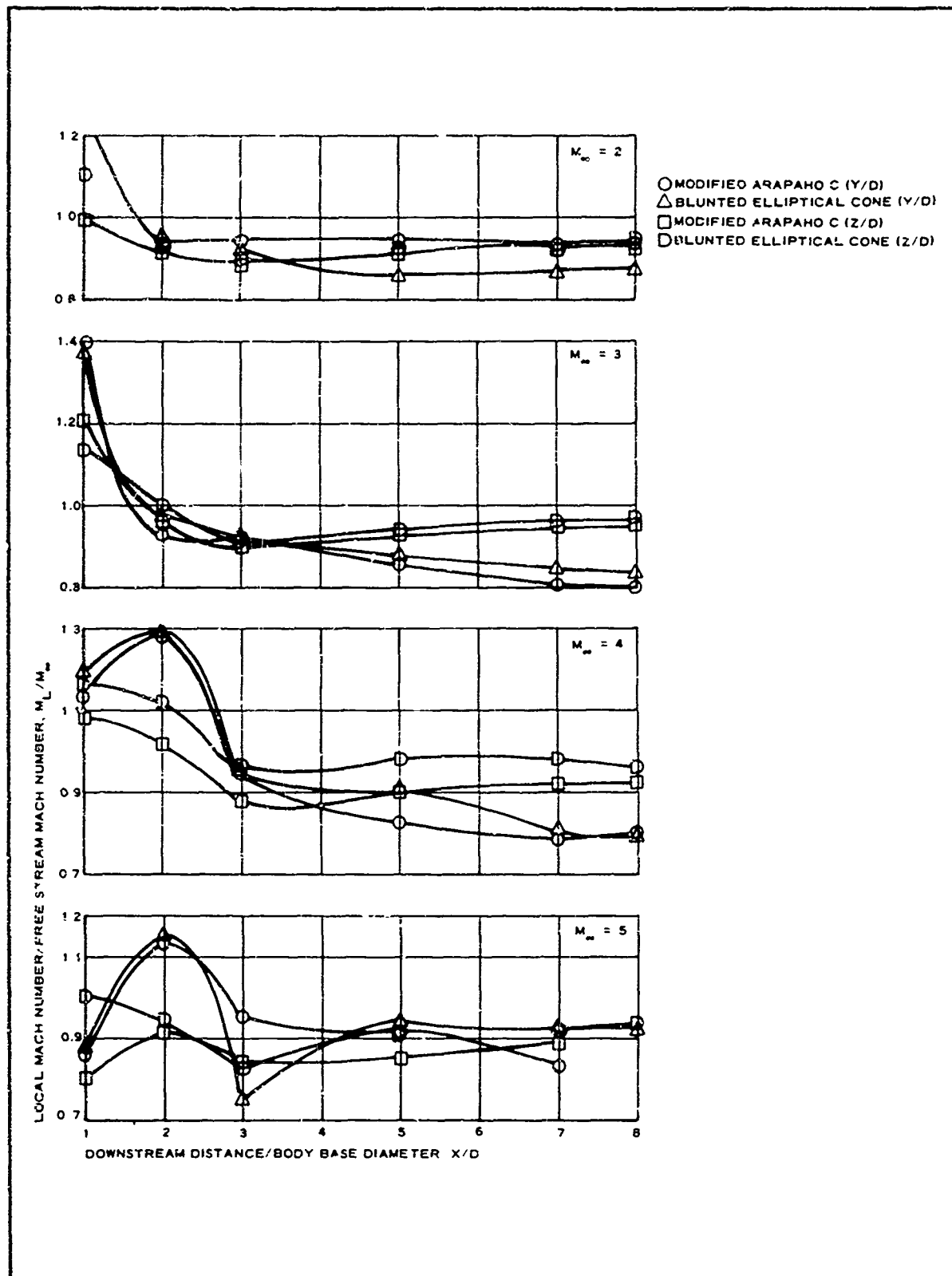


Figure 9 - Mach Number Variation in Asymmetric Wake
($Y/D = 0.379$; $Z/D = 0.607$)

Further analysis considered the auxiliary nondetermining criteria that were defined so because their variations were already expressed by the Mach number values. The parameters under consideration were the normalized profiles for pitot, static, base, and dynamic pressures at a given set of cartesian coordinates identical for both vehicles. The data are presented in Figures 10 through 19. The free stream conditions at Mach numbers two and five are discussed in more detail because they represent the boundaries of the flow envelope where the basic properties can be expected to fluctuate.

Mach number-two flow conditions are presented in Figure 10, which shows the wake development in the axial direction along the minor axis. At $1 \leq X/D \leq 3$, the pitot pressure variations are similar in shape, but the magnitudes in the inner viscous wake are not equivalent. The agreement is close in the vicinity of the wake centerline, with the growth for both vehicles proceeding at similar rates. At $X/D = 5$, curves flatten out as expected. However, behind the modified C vehicle, the curve has a convex shape, while behind the blunted elliptical cone, the curve is concave. The pitot pressure and velocity recovery in the wake along the minor axis is more energetic behind the modified C vehicle than behind the blunted elliptical cone. The comparison along the major axis at $X/D = 1$ in Figure 11 indicates almost complete similarity at the corresponding locations in the viscous wake behind both vehicles. At $X/D > 1$, the recovery of profiles behind the modified C vehicle is lagging as compared with the profile recovery behind the blunted elliptical cone. The analysis of the pitot pressure recovery profiles was done for the higher Reynolds number only, but similar variations were indicated at the lower number.

Figure 16 gives the static pressure variation in the asymmetric wake as a function of axial distance along the minor axis. The shapes and magnitudes for both vehicles are almost completely similar for each Reynolds number. The static pressures are higher at lower Reynolds number by about 10 percent. The maximum static pressure is recorded at $X/D = 2$ (for both vehicles), which indicates the recompression, neck, and trailing shock locations in the wake.

The behavior of the static pressure in the wake is typical (i. e., lower in the base region, reaching a peak in the vicinity of the neck, then leveling off to the free stream value farther downstream). Figure 17 shows the effect of the rake on base pressure readings for both vehicles. The curves are similar, and the variation in magnitude within the Reynolds number range is not significant for each vehicle. The blunted elliptical cone, however, indicates higher base pressure, by about five percent, independent of the Reynolds number. The base pressure orifice is selected along the minor axis where the influence of the strut is at a minimum. The local dynamic pressure variations, shown in Figures 18 and 19 are similar to those for the local Mach number since the Mach number served as an input for the calculation of the dynamic pressure.

The Mach number-five flow conditions presented in Figure 13 indicates complete similarity for both wake profiles expressed by pitot pressures at $X/D = 1$. At $X/D = 2$ and 3, the profiles are similar in shape, but the blunted elliptical cone wake shows a higher magnitude for recovery

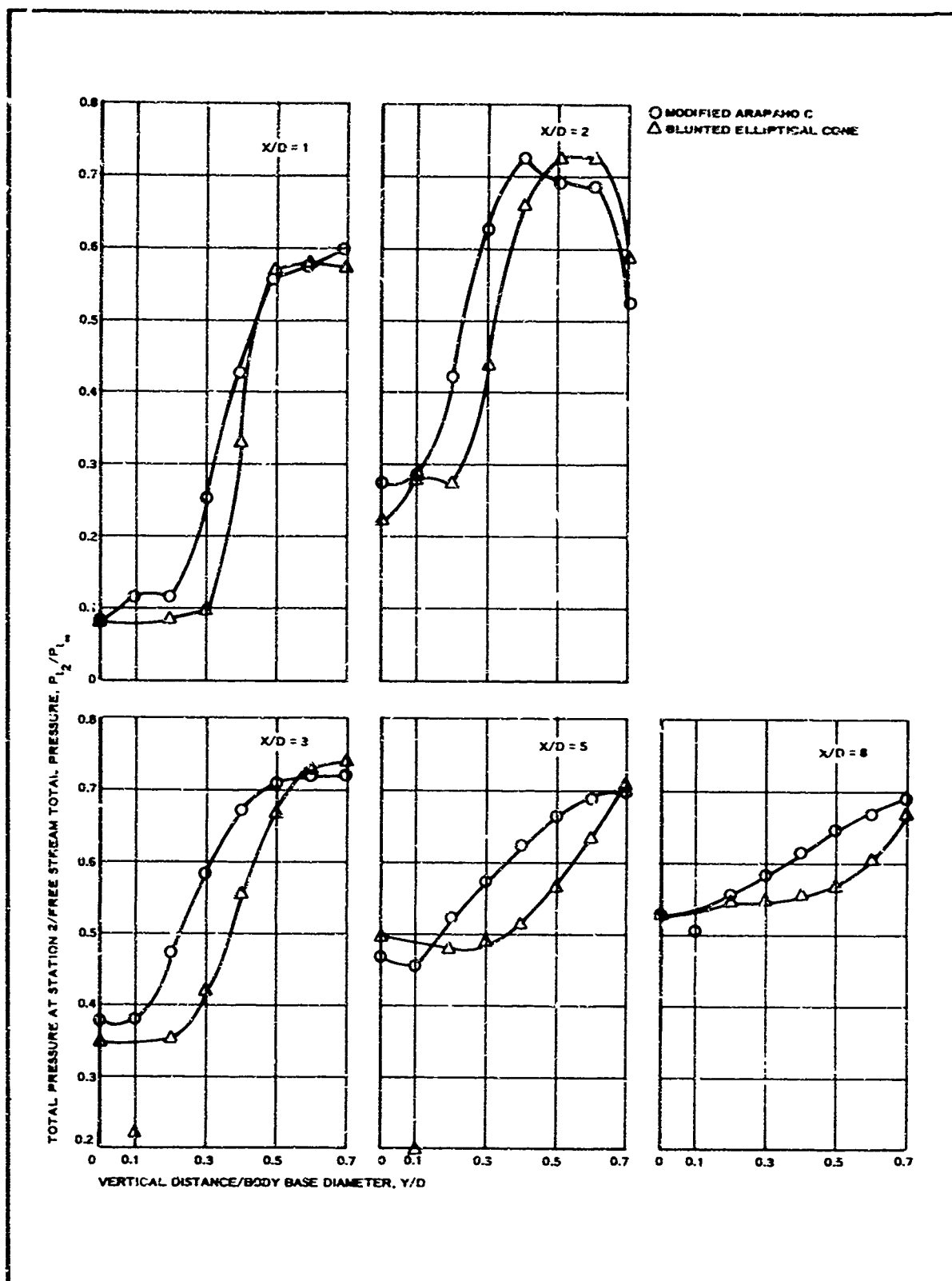


Figure 10 - Total Pressure in Asymmetric Wake versus Y/D
($M_\infty = 2$, $Re_\infty/in. = 0.37 \times 10^6$)

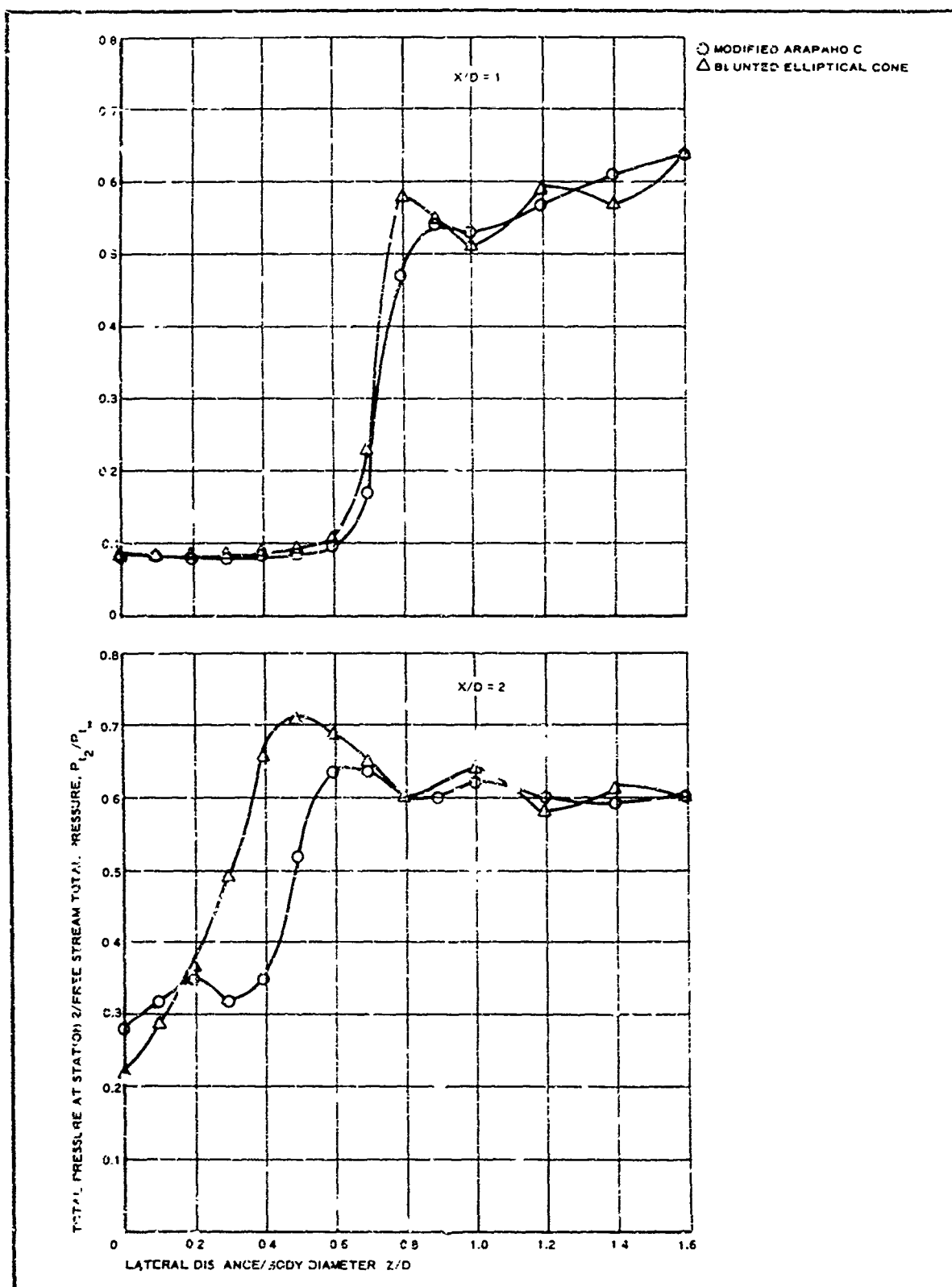


Figure 11 - Total Pressure in Asymmetric Wake versus Z/D
 ($X/D = 1$ and 2 , $M_\infty = 2$, $Re_\infty/in. = 0.37 \times 10^6$)

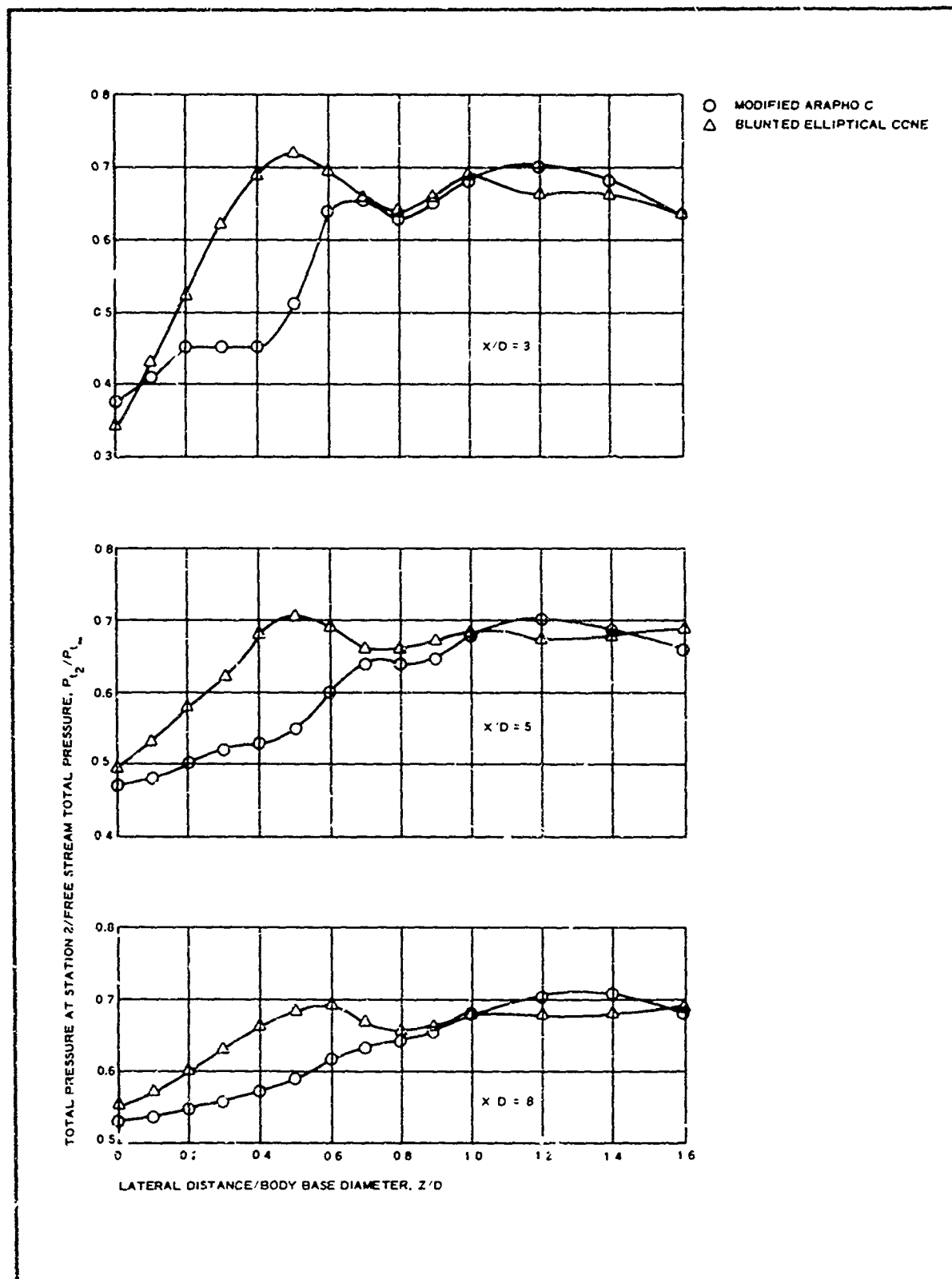


Figure 12 - Total Pressure in Asymmetric Wake versus Z/D
($X/D = 3, 5, \text{ and } 8, M_\infty = 2, Re_\infty/\text{in.} = 0.37 \times 10^6$)

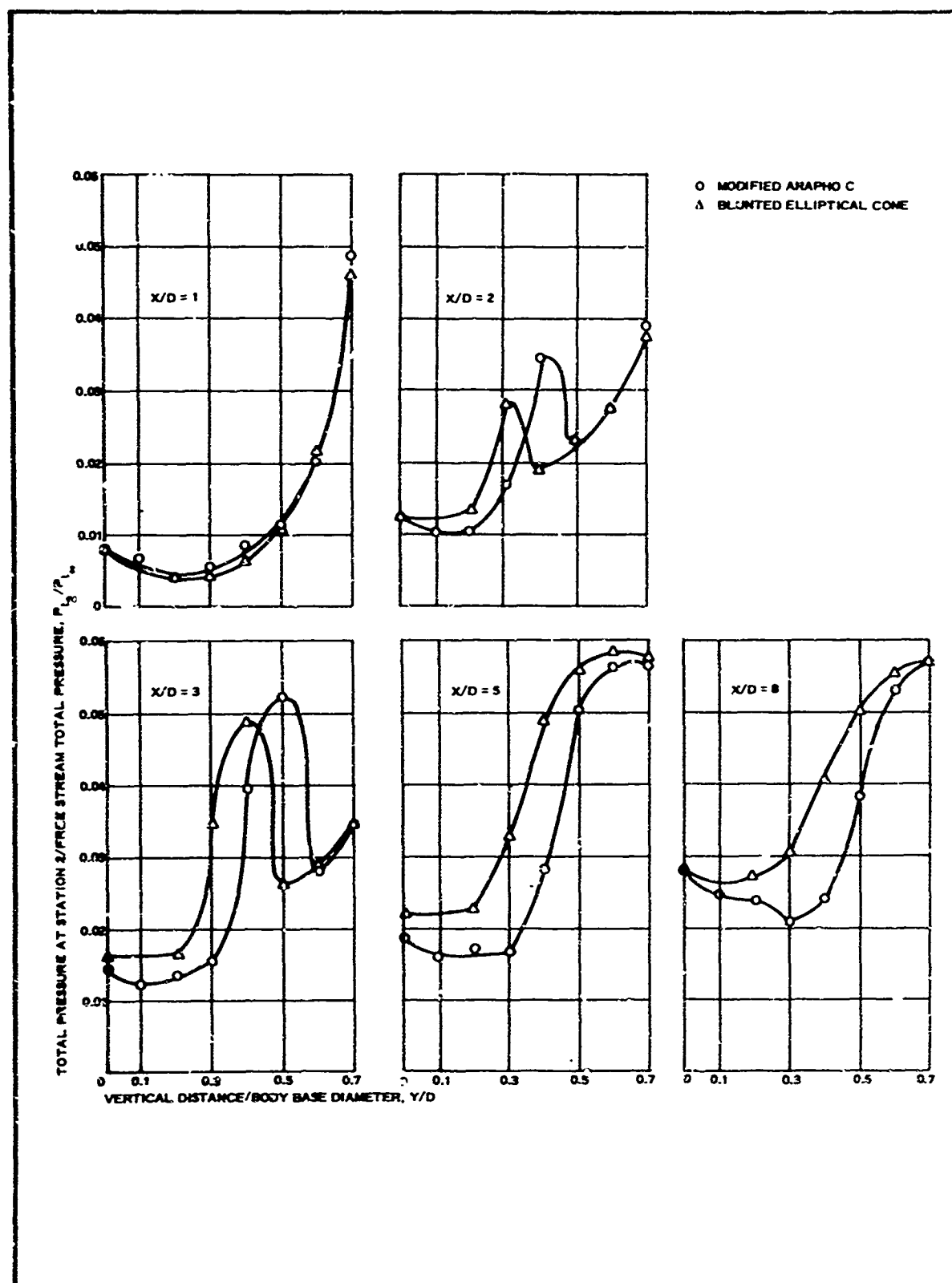


Figure 13 - Total Pressure in Asymmetric Wake versus Y/D
($M_{\infty} = 5$, $Re_{\infty}/in. = 0.49 \times 10^6$)

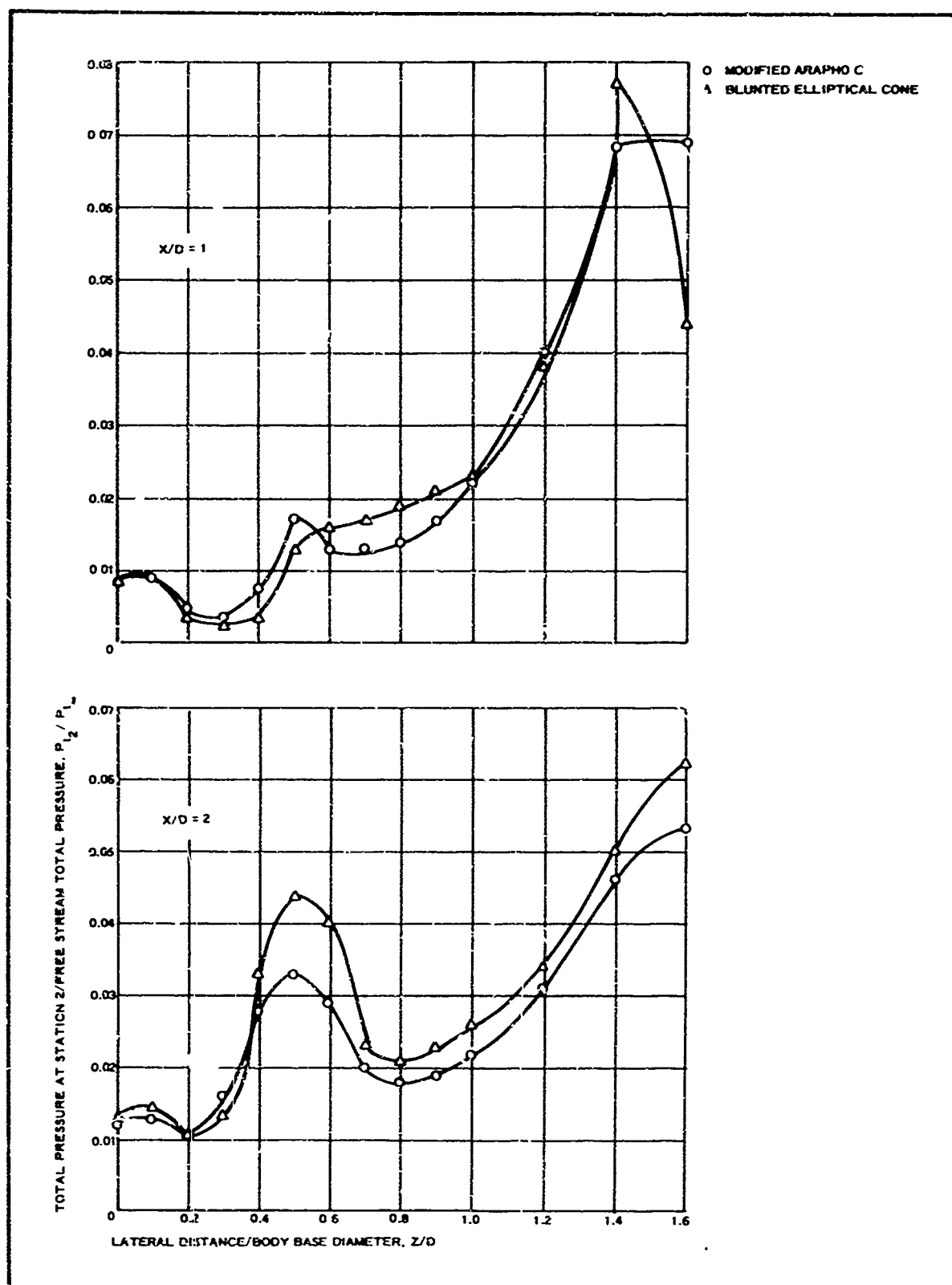


Figure 14 - Total Pressure in Asymmetric Wake versus Z/D ($M_\infty = 5$, $Re_{\infty}/in. = 0.49 \times 10^6$, $X/D = 1$ and 2)

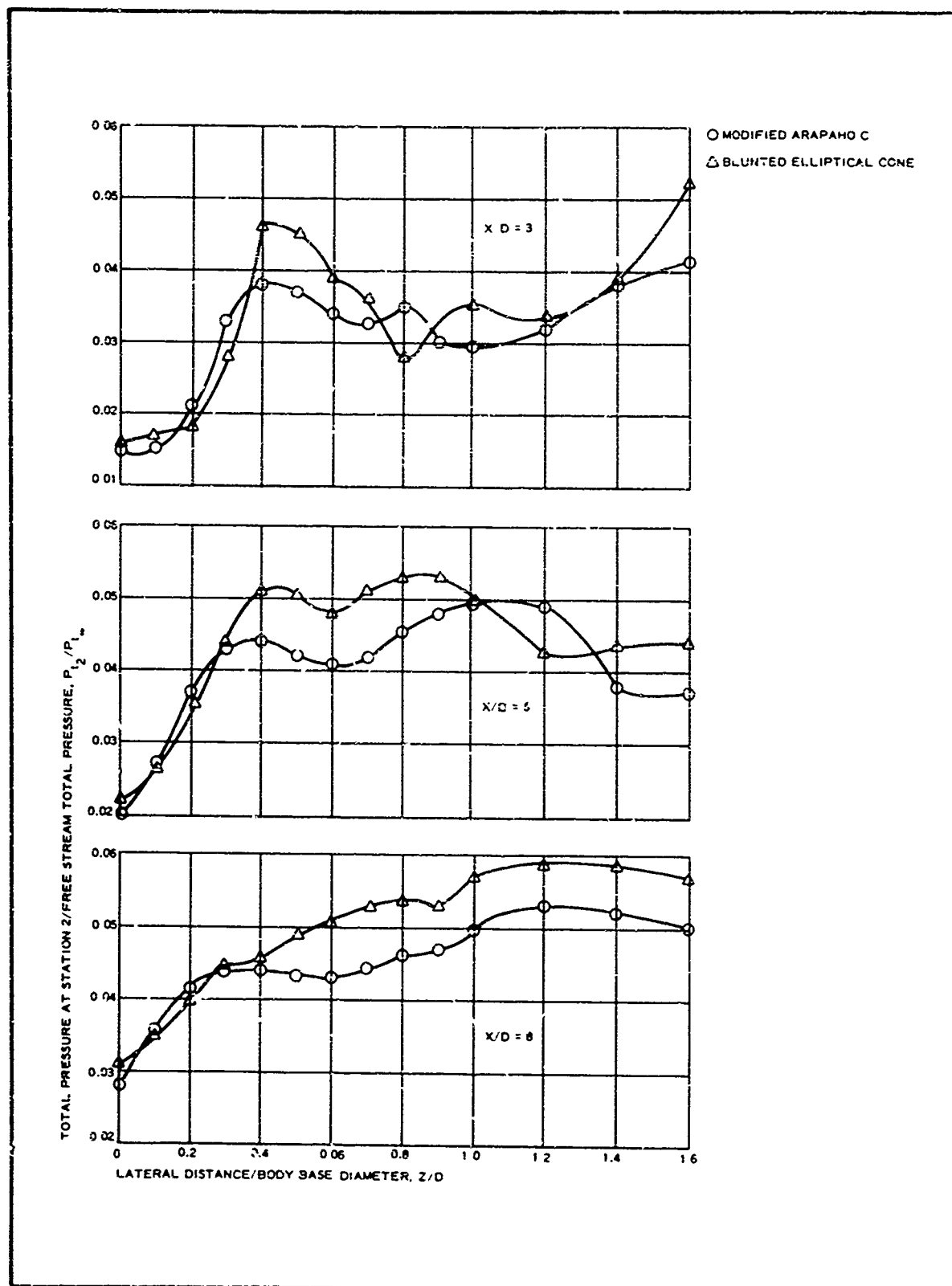


Figure 15 - Total Pressure in Asymmetric Wake versus Z/D ($M_\infty = 5$, $Re_{\infty}/in. = 0.49 \times 10^6$, $X/D = 3, 5$, and 8)

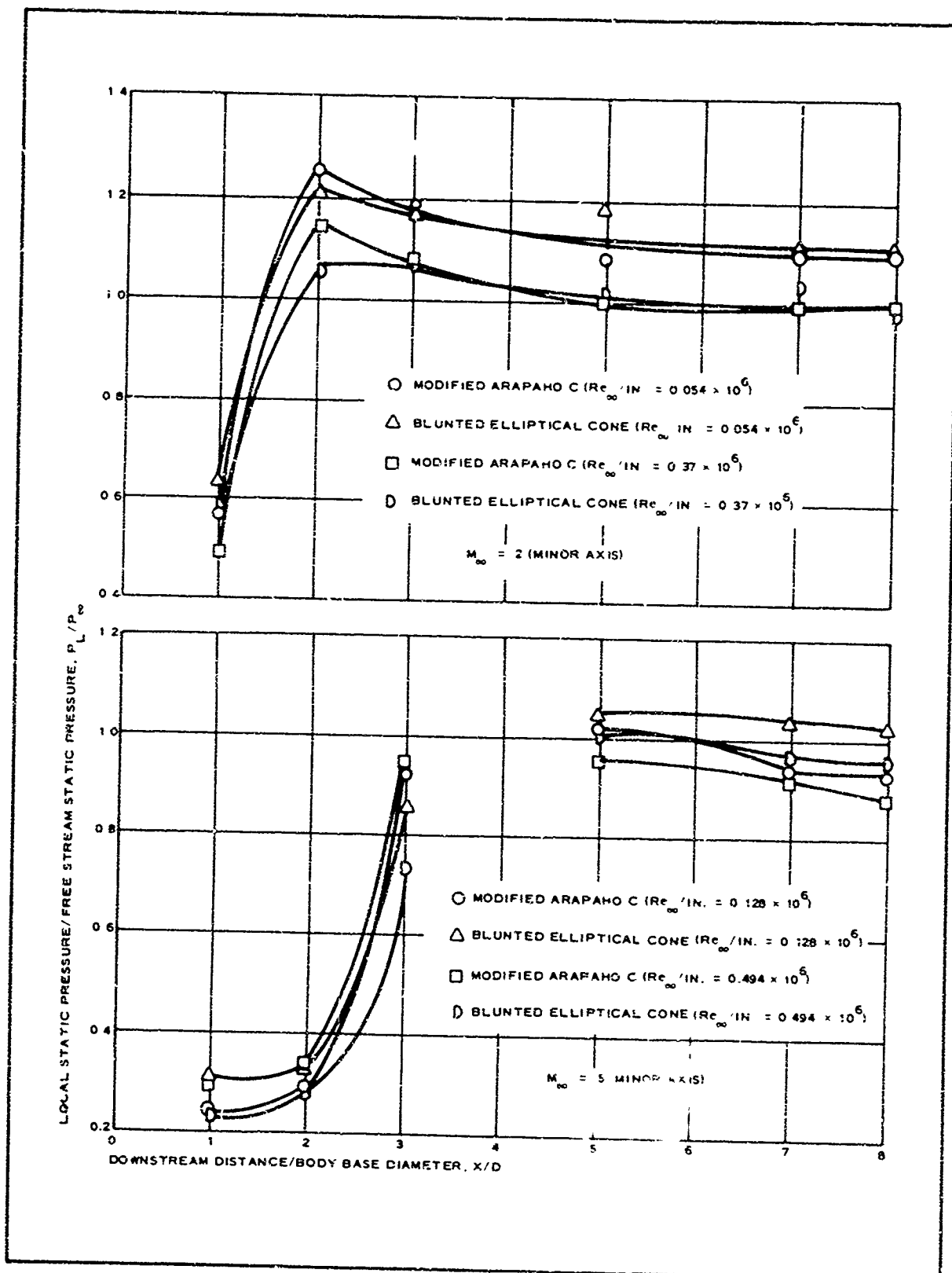


Figure 16 - Static Pressure Variation in Asymmetric Wake
($Y/D = 0.15$)

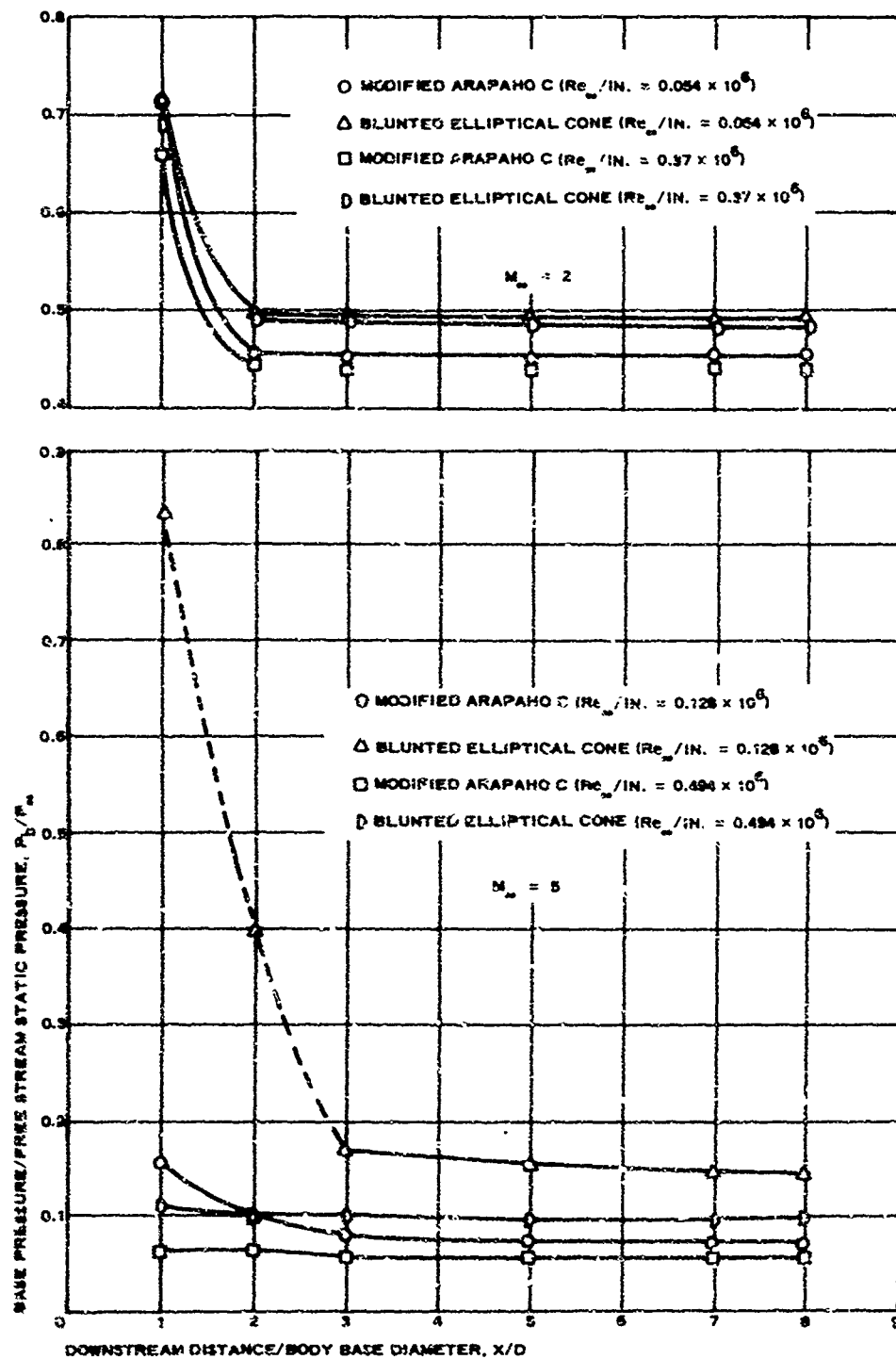


Figure 17 - Base Pressure Variation in Asymmetric Wake

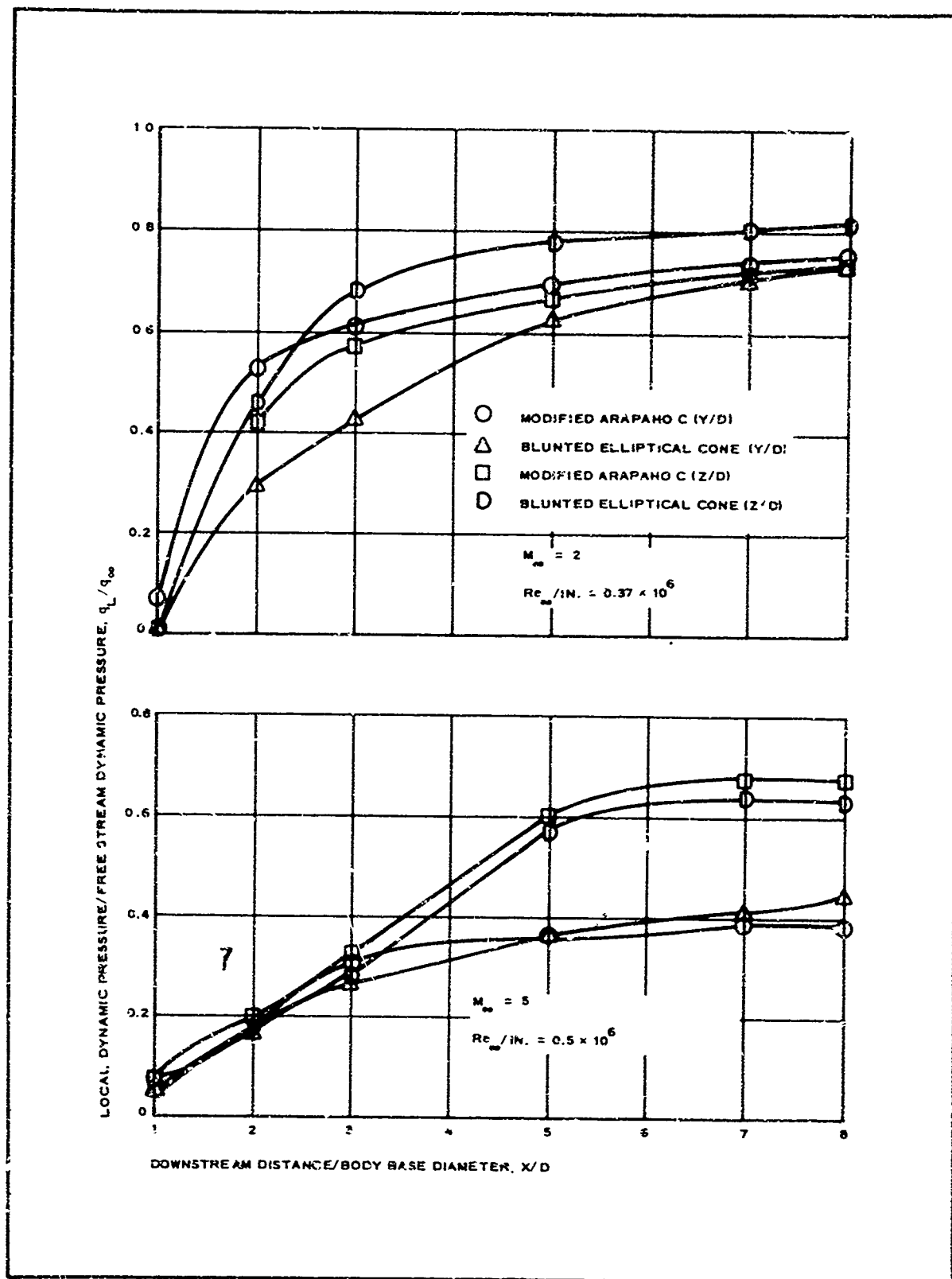


Figure 18 - Dynamic Pressure Variation in Asymmetric Wake
(Y/D = Z/D = 0.15)

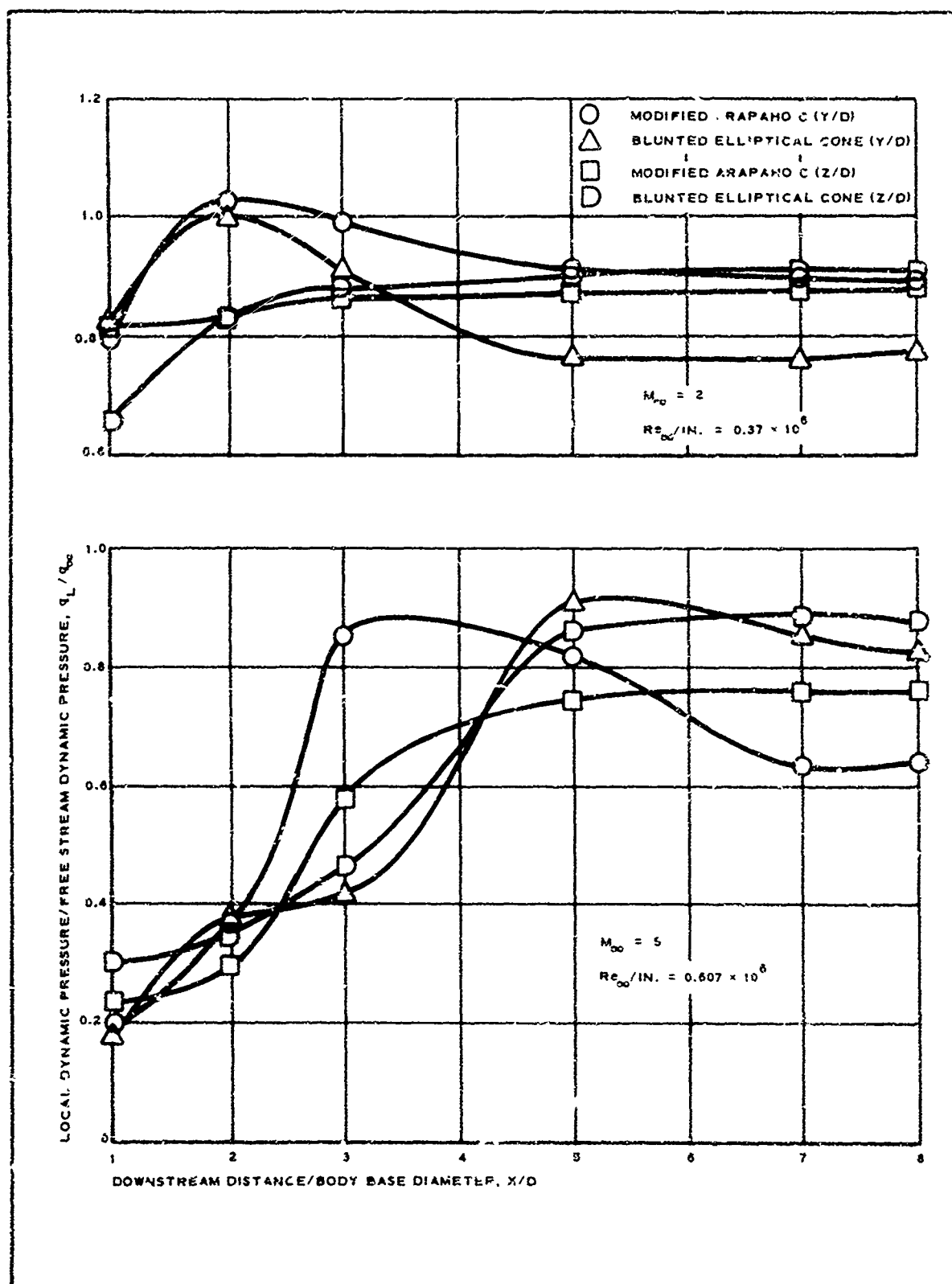


Figure 19 - Dynamic Pressure Variation in Asymmetric Wake
(Y/D = 0.37, Z/D = 0.607)

at each coordinate point along the minor axis in the inner wake. The same tendency prevails for both profiles at $X/D = 5$ and 8 .

The magnitudes are very close for values of Z/D up to 0.3 , at $1 \leq X/D \leq 8$ axial distance with the blunted elliptical cone's wake diverging upward at $Z/D = 0.4$ and remaining at a higher increment for the rest of the meaningful range.

The static pressure variation in the asymmetric wake (see Figure 15) shows a typical pattern of behavior, i. e., low values at the base region, rising to the free stream values at $X/D > 3$. The recompression region is indicated at $3 \leq X/D \leq 4$ location for both wakes.

Figure 17 gives the base pressure variation in the asymmetric wake along the minor axis. The pressures are low, suggesting that a cavity-type flow regime exists at the base. The blunted elliptical cone exhibits higher base pressures at lower and higher Reynolds numbers by about 50 percent.

7. SIMILITUDE CONCLUSIONS

In accordance with the principles stated in Item 5, the exactness of the similitude criteria can not be satisfied for practical applications, therefore, correlation parameters are introduced here to show the magnitude of a deviation from exact similitude. The correlation parameter K is defined as:

$$K' = \frac{\left(\frac{M_L}{M_\infty} \right)_{Y,Z}^{\text{Mod C}}}{\left(\frac{M_L}{M_\infty} \right)_{Y,Z}^{\text{R. E. C.}}} - 1. \quad (3)$$

Then K' can vary as:

$$K' = 0 \text{ (exact similitude),}$$

$$K' > 0 \text{ (positive deviation), and}$$

$$K' < 0 \text{ (negative deviation).}$$

The parameter K' is determined for each free stream Mach number condition at the following set of space coordinates:

$$X/D = 1 \text{ to } 3,$$

$$Y/D = 0.15; 0.379,$$

and

$$Z/D = 0.15; 0.607; 0.91.$$

The plots of K versus the axial location are given in Figures 20 and 21. The mean similitude deviation is then:

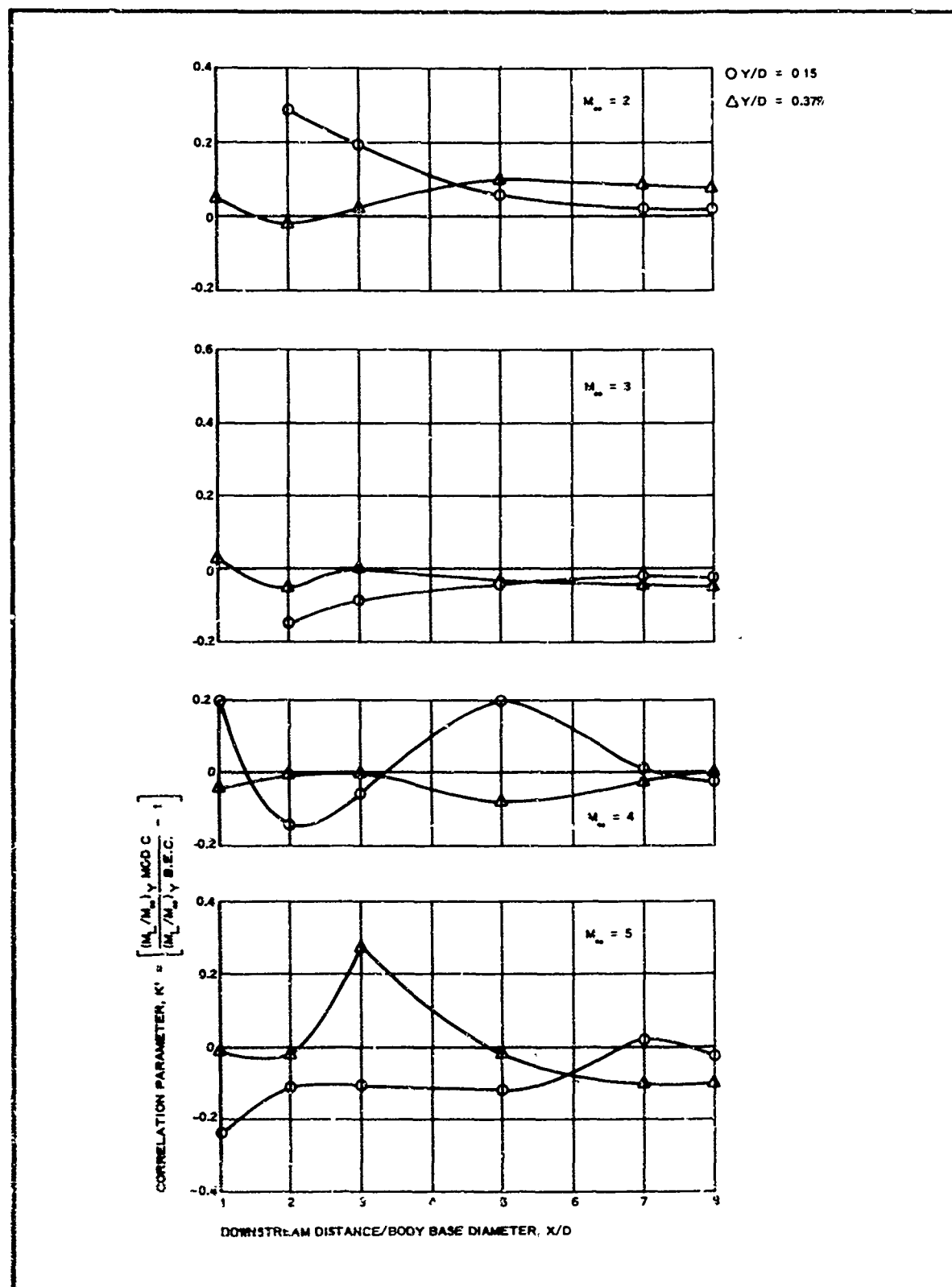


Figure 20 - Mach Number Correlation Parameter for Similitude Deviation (Y/D)

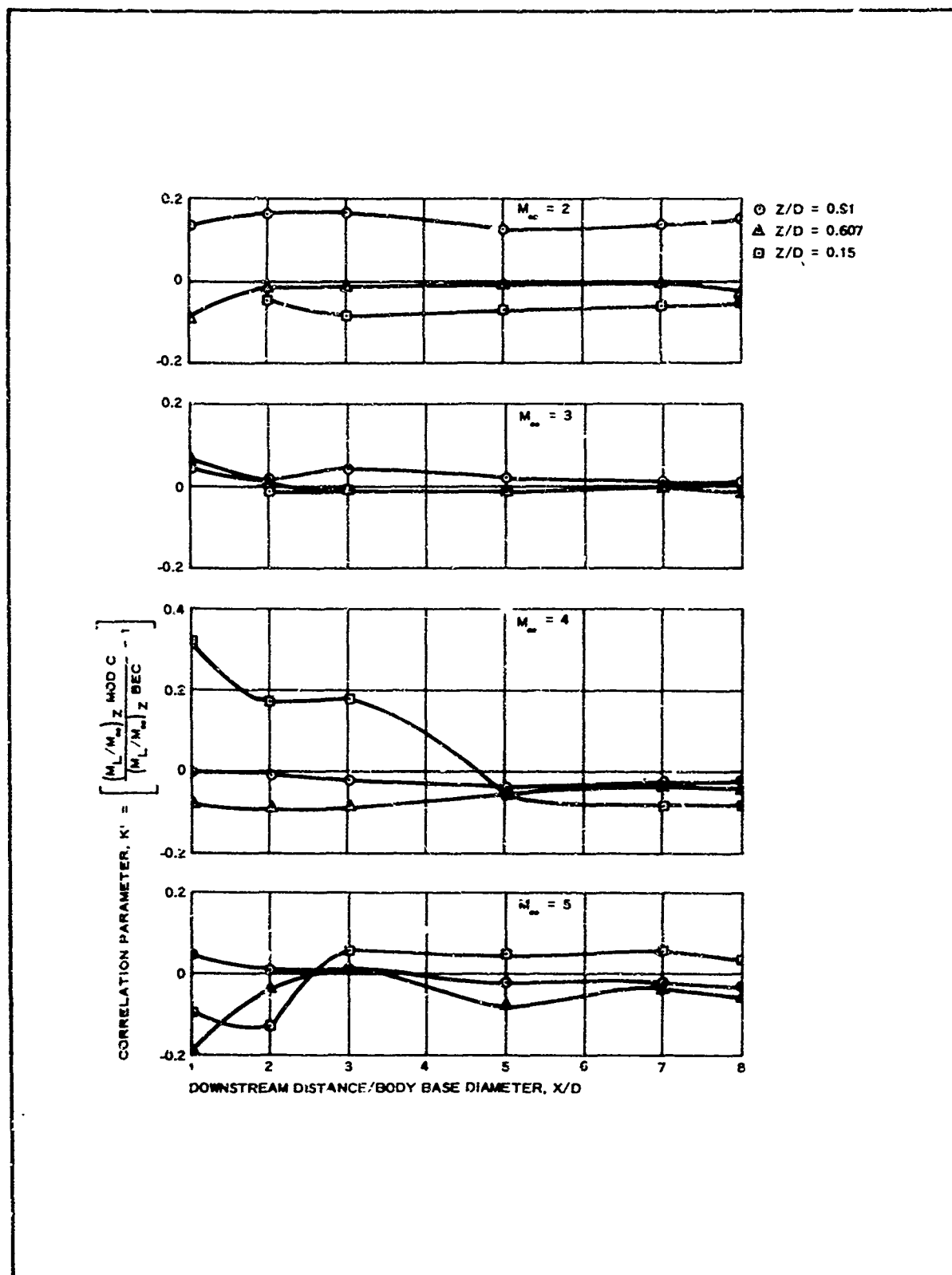


Figure 21 - Mach Number Correlation Parameter for Similitude Deviation (Z/D)

$$\bar{\sigma} = \frac{1}{n} \sum_{i=1}^n \sigma_i, \quad (4)$$

where

n = number of K' obtained, and

σ_i = value of K' at n_i .

The plot of mean similitude deviation versus free stream Mach number is shown in Figure 22, from which the following conclusions are reached:

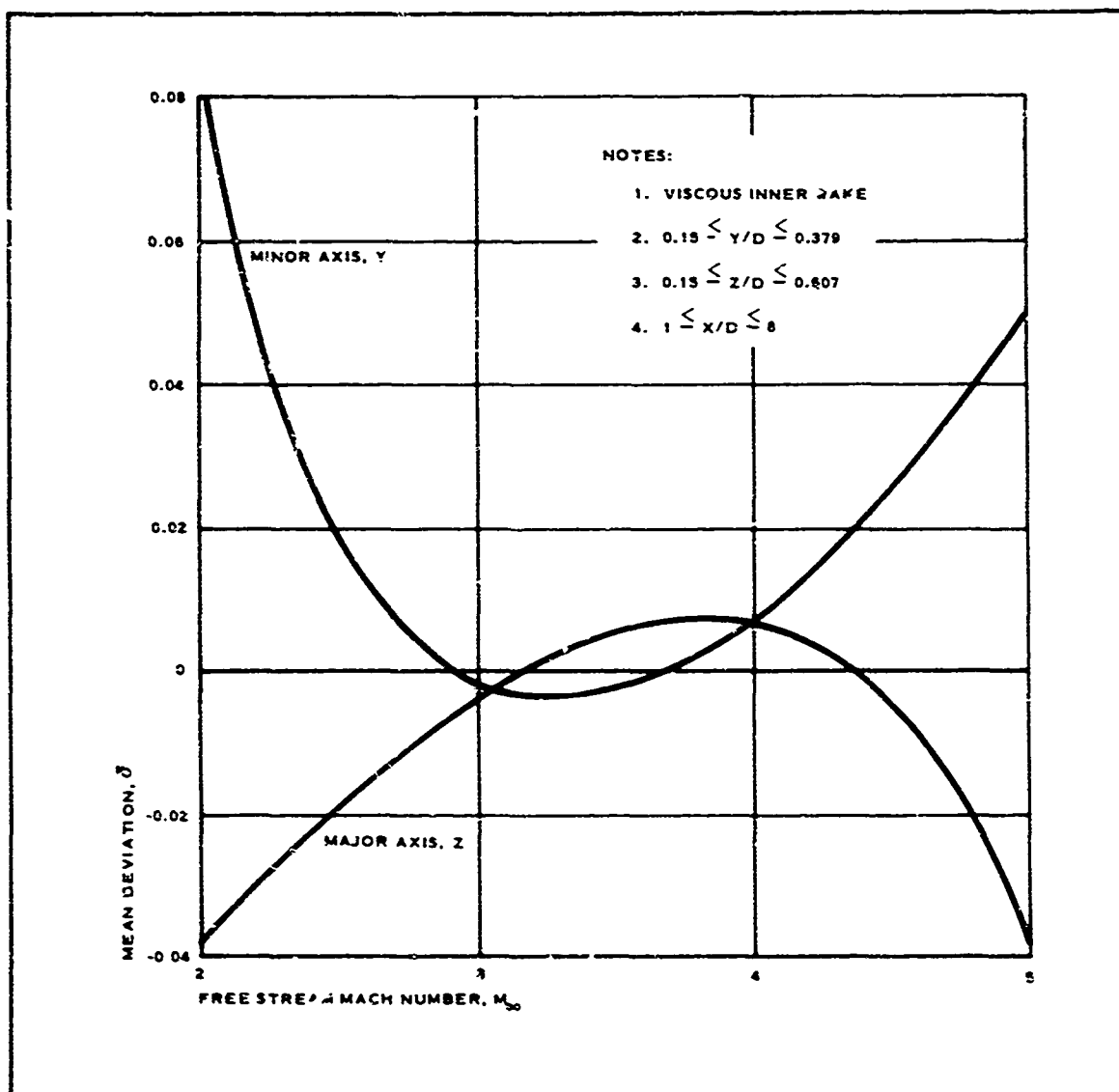


Figure 22 - Asymmetric Near-Wake Flow Mean Similitude Deviation versus Mach Number

1. The mean similitude deviation lies in the range of $(-0.038) \rightarrow (+0.080)$.
2. Similitude criteria are nearly satisfied at $M_\infty = 3$ and 4, where the range is $(-0.003) \rightarrow (+0.003)$.
3. The maximum deviation from the complete similitude is expected at $M_\infty = 2$, where the range is $(-0.038) \rightarrow (+0.080)$, followed by $M_\infty = 5$ condition, where the range is $(-0.036) \rightarrow (+0.050)$.
4. The similitude is positive at the minor axis (except at $M_\infty = 3$) and negative at the major axis (except at $M_\infty = 4$) for the modified C vehicle; the directions are reversed for the blunted elliptical cone.

Analysis of the auxiliary nondetermining criteria, the normalized pitot, static, and dynamic pressures for $M_\infty = 3$ and 4 test conditions in a way analogous to the $M_\infty = 2$ and 5 conditions presented herein, will lead to the same conclusions. This is the case because the inputs are interrelated through the basic similarity criterion, the Mach number. The experimental data for the $M_\infty = 3$ and 4 cases is presented in Volume III of this report.

As a final check on the two bodies for similarity, the momentum defect of the boundary layer at the base of each body was calculated. At $M_\infty = 2$, the results of the calculations (integrated solutions for the boundary layer equations) indicate that the boundary layer momentum defect of the modified C vehicle is 13.5 percent higher than that for the blunted elliptical cone vehicle at the lower stagnation pressure, and 12.15 percent higher at the higher stagnation pressure. The method for calculating the boundary layer momentum defect in computerized form was developed under this contract and is discussed in detail in Volume II.

SECTION IV

DESIGN INVESTIGATION

1. BASIS FOR DESIGN CHANGES

This section reports the findings of aerodynamic analyses, thermodynamic analyses, vehicular redesign studies, structural analyses, appendage design investigations, and auxiliary equipment selection endeavors, all of which contributed to the recommended flight-test vehicle selection summarized in Section VII. The findings aided in establishing the feasibility of reconfiguring the Arapaho C vehicle after booster separation to provide a flight test of a decelerator in the wake of a selected lifting body.

All design changes to the basic Arapaho C test vehicle are directly associated with the changes in aerodynamic shape required to adequately simulate the wake of the selected lifting body, based on the wake analyses of Section III. Consideration in this design investigation was given to:

1. Minimizing added test vehicle weight
2. Minimizing added volumetric allotments
3. Maximizing vehicle system reliability
4. Maintaining low refurbishment time and costs

2. AERODYNAMIC ANALYSES

a. Nature of Data Collected

Static stability and flow-separation survey testing was accomplished on three of the four bodies investigated under the EUREKA program: (1) basic Arapaho C, (2) Arapaho C with blunted nose cone, and (3) modified Arapaho C (see Figure 2). This WT-I test series was oriented toward determining the force/moment histories of those bodies at Mach numbers from 2.5 through 5.0 at angles of attack from -5 to +15 deg throughout a relatively broad range of Reynolds numbers ($0.05 \times 10^6/\text{in.}$ to $0.5 \times 10^6/\text{in.}$, as compatible with wind-tunnel limitations). Shadowgraphs were taken simultaneously with force/moment measurements in order to permit visualization of flow separation and transition over the forebodies.

The static-stability data proved useful later in the wake analyses by providing drag data that were indicative of the total integrated momentum defect in the vehicle wake. These data proved most useful in the development of wake calculation methods.

Program aerodynamicists also investigated vehicular drag characteristics, determined center-of-pressure locations for use in selecting a suitable cg location (static-stability margin), and analyzed the adequacy of the design system as applied to the modified Arapaho C flight-test vehicle.

b. Static Stability

Vehicular static stability comparisons were made in order to determine the influences of the two nose configurations and two base geometries tested in the WT-I series.

General trends of all three vehicles were to generate an increasingly negatively sloped C_{M_α} (change in pitching moment coefficient with angle of attack) with increasing Mach number throughout the Reynolds number regime, as was expected with flared vehicles. The basic Arapaho C and the modified C-1 were statically stable over the entire range of free stream parameters tested. The Arapaho C with nose cone, however, was seen to be statically unstable at Mach numbers 2.5 and 3 under high Reynolds number conditions. This peculiar phenomenon led to an examination of the Arapaho C with and without the blunted nose cone in order to determine the cause of the variations in vehicle stability. Figures 23 and 24 were plotted and compared with Hoerner's reference plot from Reference 3 shown in Figure 25, as a means of supplementing the shadowgraphs in determining the nature of the flow over and behind the bodies, with due consideration given to the differences in forebodies represented by WT-I data and the reference material. The curve shapes and shadowgraphs indicated that the vehicles were in the transitional-to-turbulent regime almost exclusively, with a remote possibility of being laminar at the Mach-5, extremely low Reynold's number. Shadowgraphs revealed that little or no flow separation occurs at the high Reynolds numbers on the Arapaho C with nose cone. Evidently, at Mach numbers 4 and 5 and high Reynolds number, static stability of the C plus nose cone vehicle was ascertained by the high-magnitude resultant forces acting on the axisymmetric tail-flare. However, even at the highest Reynolds number investigated, the flow at lower Mach numbers was insufficiently energetic to stabilize that vehicle.

Because the basic Arapaho C was stable under the same conditions at which the C plus nose cone was unstable and the only difference in the two vehicles was nose geometry, the logical choice was to investigate characteristics that could easily affect stability, and in turn are most susceptible to upstream flow signatures.

The WT-I shadowgraphs revealed that at Mach numbers 2.5 and 3 and high Reynolds numbers, the flow over the basic C vehicle was highly separated. For low Reynolds numbers, the flow over both the basic C and C plus nose cone vehicles also were separated throughout the Mach number envelope. The results of the investigation showed that flow separation produced a pressure distribution over the vehicles in which a greater force is generated at a point downstream of the vehicle moment center than for the unseparated flow case. Thus, even though the separation causes a reduction of forces felt by the tail flare, the summation of local forces multiplied by their respective moment arms yields a moment of greater magnitude than that produced under unseparated flow conditions. The resultant moment generated by the separation flow was sufficiently large to stabilize both vehicle configurations. The conclusion was made that regardless of nose shape, if separated flow exists over the vehicle, the Arapaho will be statically stable.

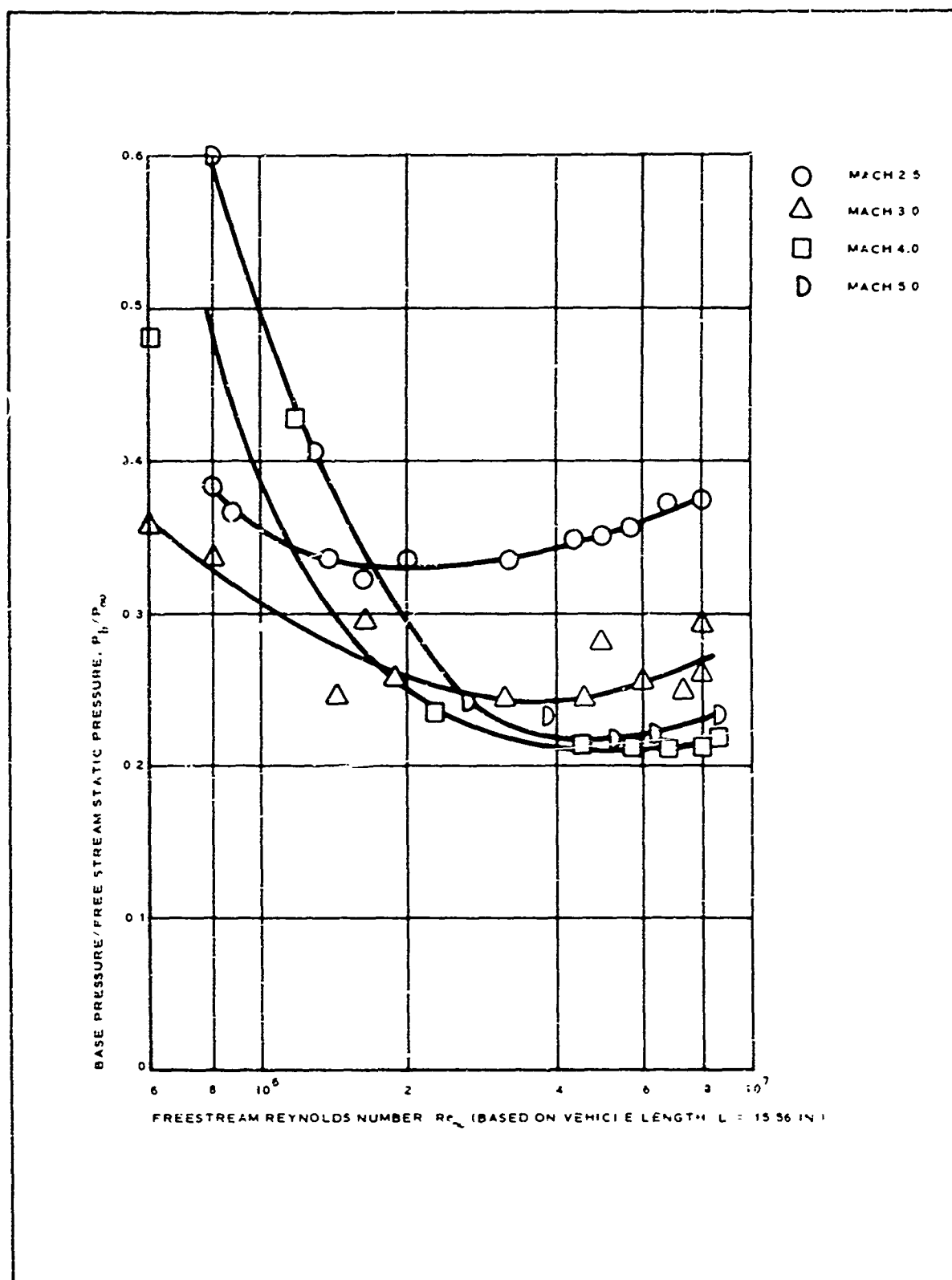


Figure 23 - P_b/P_∞ versus Reynolds Number for Basic Arapaho C with Blunted Nose Cone

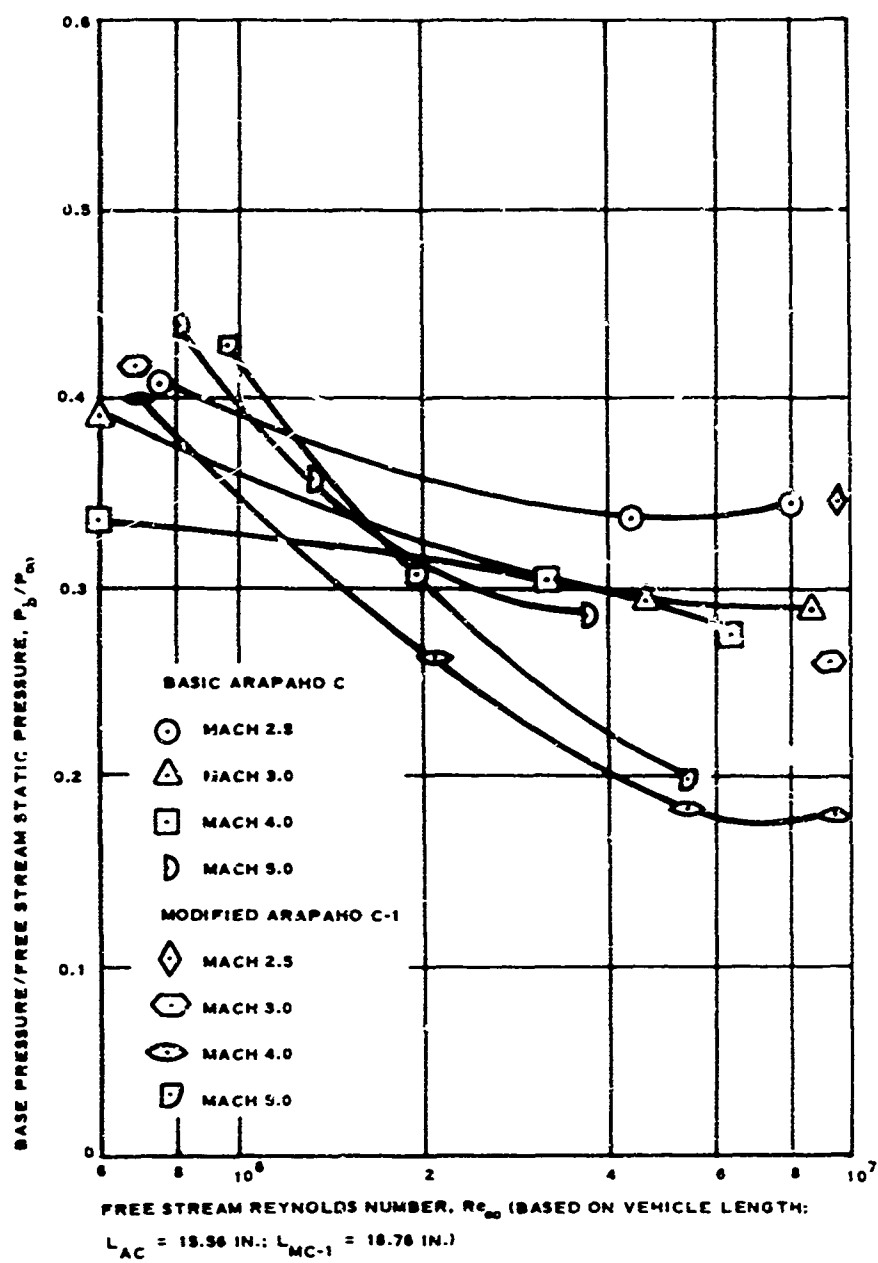


Figure 24 - P_b/P_∞ versus Reynolds Number for Basic Arapaho C and Modified Arapaho C-1

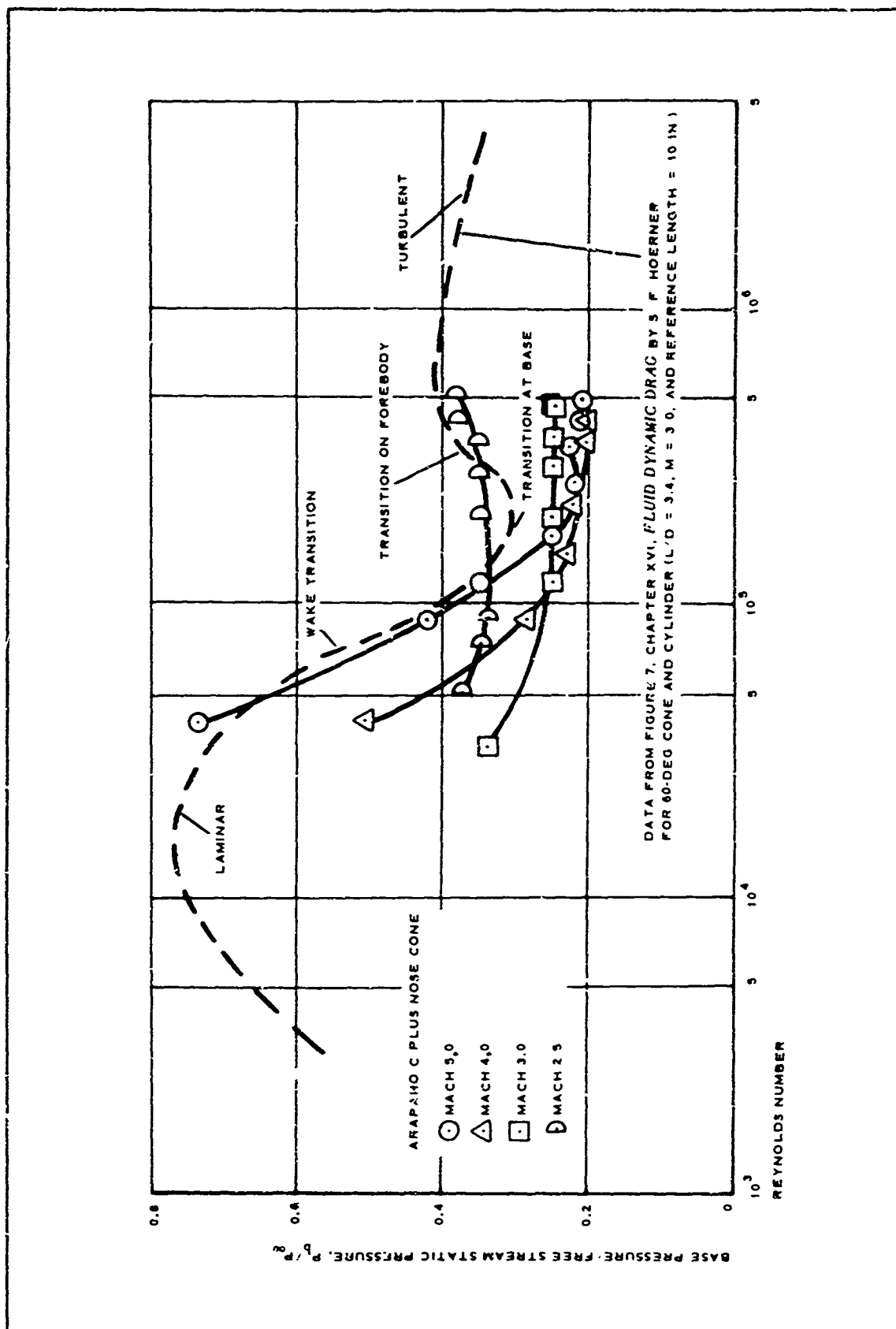


Figure 25 - Flow Classification by Empirical Reference

Investigation of the data gathered while testing the modified Arapaho C vehicle showed that the vehicle was inherently stable at all test conditions, primarily due to the relative enormity of the elliptical flare at its aft end. For reference purposes, Table III has been included earlier, indicating the conditions to which the vehicles were subjected during the static stability test series.

c. Static Stability Margin

An analysis was made to determine the maximum aft allowable center of gravity location that would still enable the modified Arapaho C vehicle to remain statically stable throughout its flight. This was accomplished by determining the center of pressure location that would occur the farthest forward during the flight.

The test vehicle was examined in three configurations:

1. Basic Arapaho C with extended cylindrical afterbody
2. Basic Arapaho C with the afterbody appendage covers jettisoned (immediately prior to appendage inflation)
3. Arapaho C with inflatable afterbody (modified Arapaho C)

By inspection of the three configurations, it was obvious that the configuration immediately prior to appendage inflation, presenting the "least-drag" profile, will produce the farthest forward center of pressure location during the flight.

Since the vehicle geometry just prior to appendage inflation is quite close to that of the Arapaho C wind tunnel test model, except for the partial cutout on the flight-vehicle configuration, the force results from the Phase I wind tunnel test program were used as a foundation for determining the center-of-pressure location. The wind tunnel results for the normal force coefficient, C_N , and moment coefficient, C_M , were modified slightly to account for the modified segment of the afterbody. The slopes of the variation of C_M and C_N with angle of attack were calculated so as to determine C_{N_α} and C_{M_α} , the normal force coefficient slope and moment coefficients slope and moment coefficient slope, respectively. The center-of-pressure locations then were determined as a function of Mach number for both the high and low Reynolds number cases.

The results for the limiting center-of-pressure location are shown in Figure 26. The figure indicates that the center of gravity is constrained forward of a location of 5.5 calibers from the vehicle nose to ensure static stability; the exact center of gravity location to be determined by the desired static margin, and the results of the vehicle design and structural analysis, as presented in Items 5 and 6 of this section.

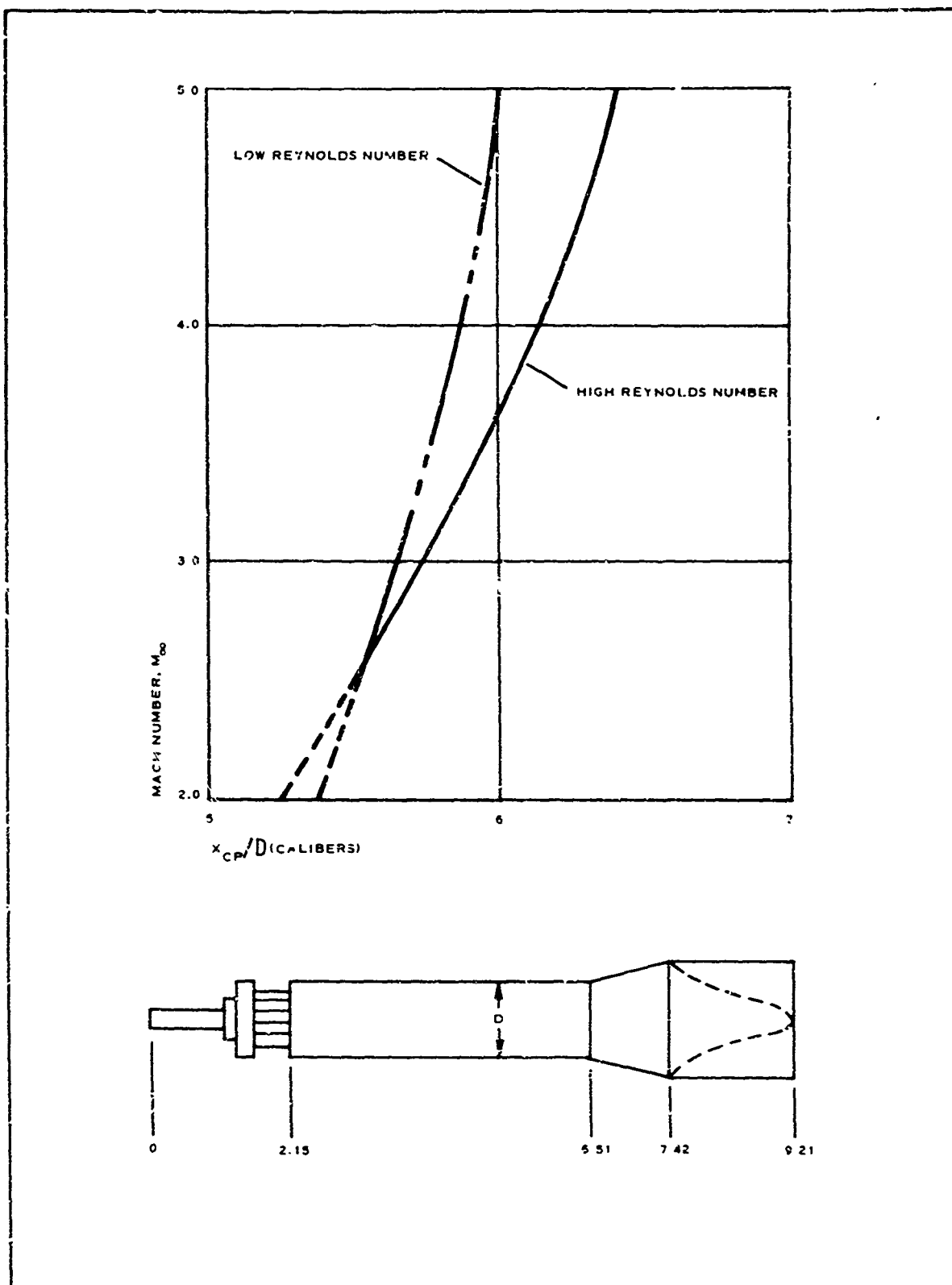


Figure 26 - Selection of Farthest Forward Center-of-Pressure Location

d. Vehicle Drag Investigation

A limited analysis was made to estimate the drag of the modified Arapaho C vehicle, since the wind-tunnel force tests were conducted on the modified Arapaho C vehicle with a nose cone, while the recommended flight-test vehicle is equipped with the basic Arapaho C's spike nose.

In order to determine the drag of the modified Arapaho C vehicle, the effect on vehicle drag of the removal of the nose cone was considered. This effect was accomplished by comparing wind-tunnel results for the basic Arapaho C without a nose cone and the Arapaho C with a nose cone. The resulting incremental drag due to the removal of the nose cone is shown in Figure 27 as a function of Mach number of both the high and low Reynolds number cases. The results of Figure 27 indicate that appreciable data scatter may be present in the wind-tunnel data. Therefore, a second (but related) method was also examined.

The incremental drag due to the difference between the elliptical and cylindrical flares was obtained by comparing the drag of the modified Arapaho C with nose cone to that of the basic Arapaho C with the nose cone. This incremental flare drag then was added to the drag of the basic Arapaho C to yield the resultant drag of the modified Arapaho C. The incremental flare drag curves are shown in Figure 28 and appear better behaved than the incremental nose drag curves of Figure 27. Figures 27 and 28 indicate that the incremental drag values are larger for the low Reynolds number case than for the high Reynolds number case. This relationship is in direct contrast to the trend shown by the total vehicle drag curves in which the drag is always greater for the high Reynolds cases. Figure 29 displays the total vehicle drag for the basic Arapaho C, the Arapaho C with the nose cone, and the modified Arapaho C with the nose cone, respectively.

Either incremental drag method discussed will yield the drag results for the modified Arapaho C shown in Figure 30, *i.e.*, the results of Figures 27 and 29C or Figures 28 and 29A. Figure 30 indicates that the drag of the modified Arapaho C is slightly higher for the low Reynolds number case as opposed to the results for the other three vehicles. The high Reynolds number drag curve appears to be very well behaved as is the low Reynolds number curve below Mach 4. Above Mach 4, the low Reynolds number curve exhibits a drag crossover similar to that shown in Figure 27.

Although the predicted drag coefficients for the modified Arapaho C are not exact, the methods used were the only realistic means available to predict the vehicle drag except for experimental testing.

e. Despin Analysis

Because of the contractual stipulation that the test vehicle shall not be spinning (roll-mode) in excess of 20 deg/sec at the test-item deployment initiation point, a cursory analysis was performed in order to ascertain that the despin system incumbent to the basic Arapaho C is adequate for roll negation of the modified vehicle. The despin event occurs on the

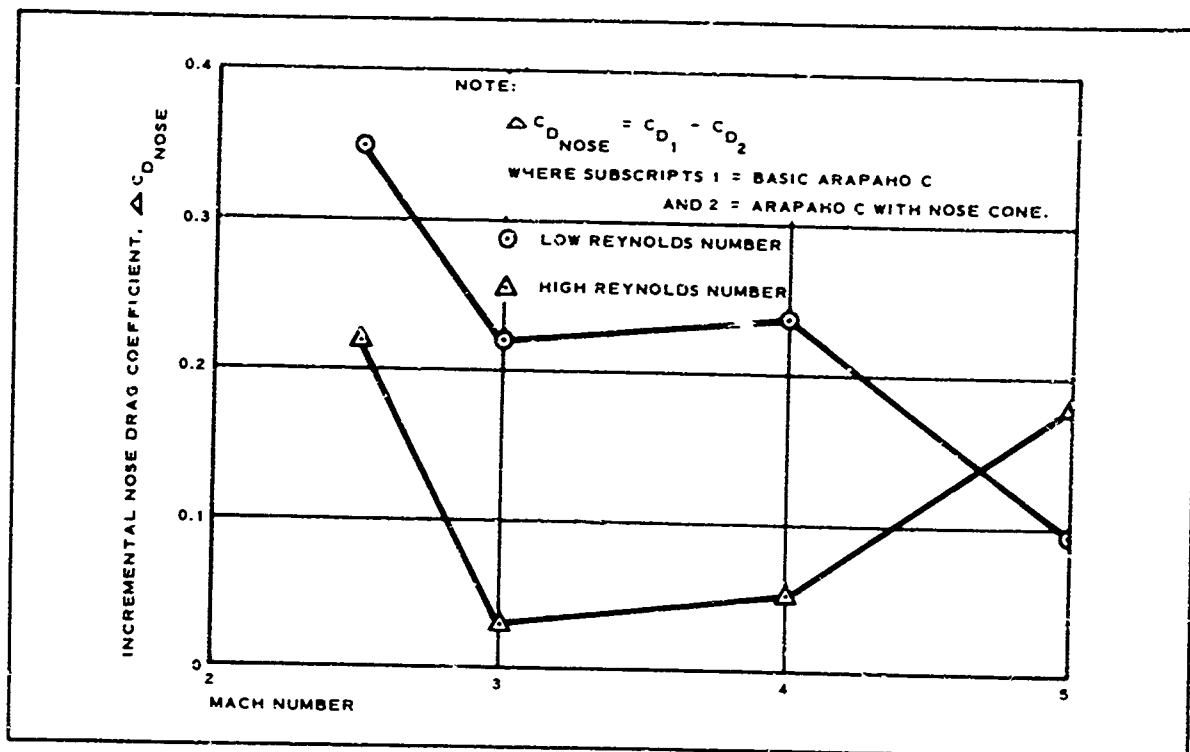


Figure 27 - Nose Drag Differential of Spike versus Blunted Nose

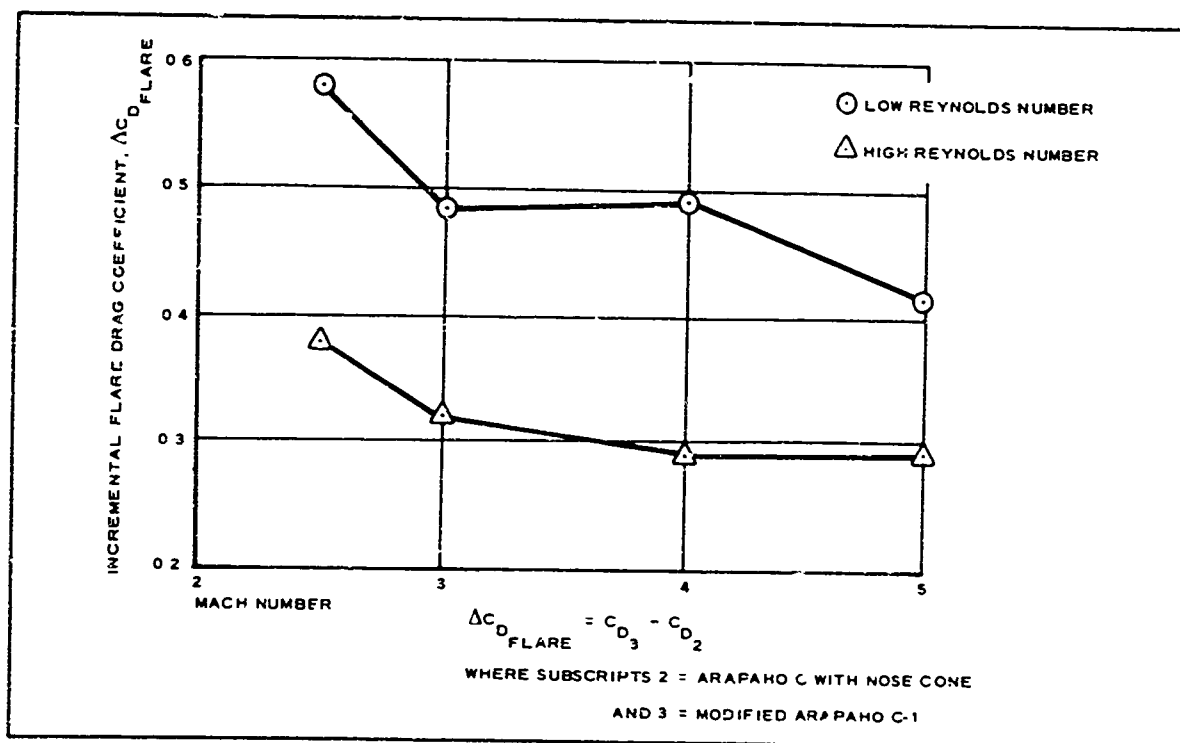


Figure 28 - Flare Drag Differential Axisymmetric versus Asymmetric Flares

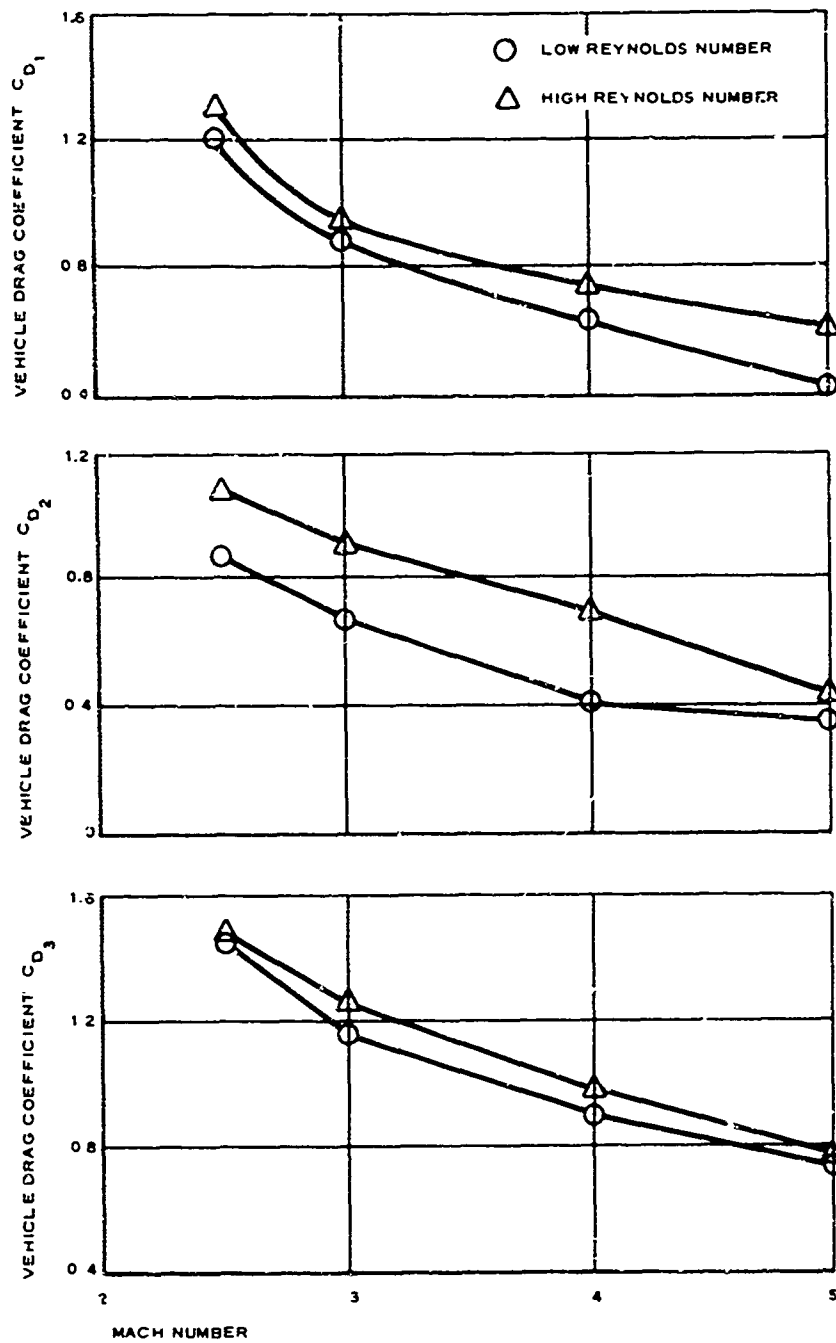


Figure 29 - Vehicle Drag

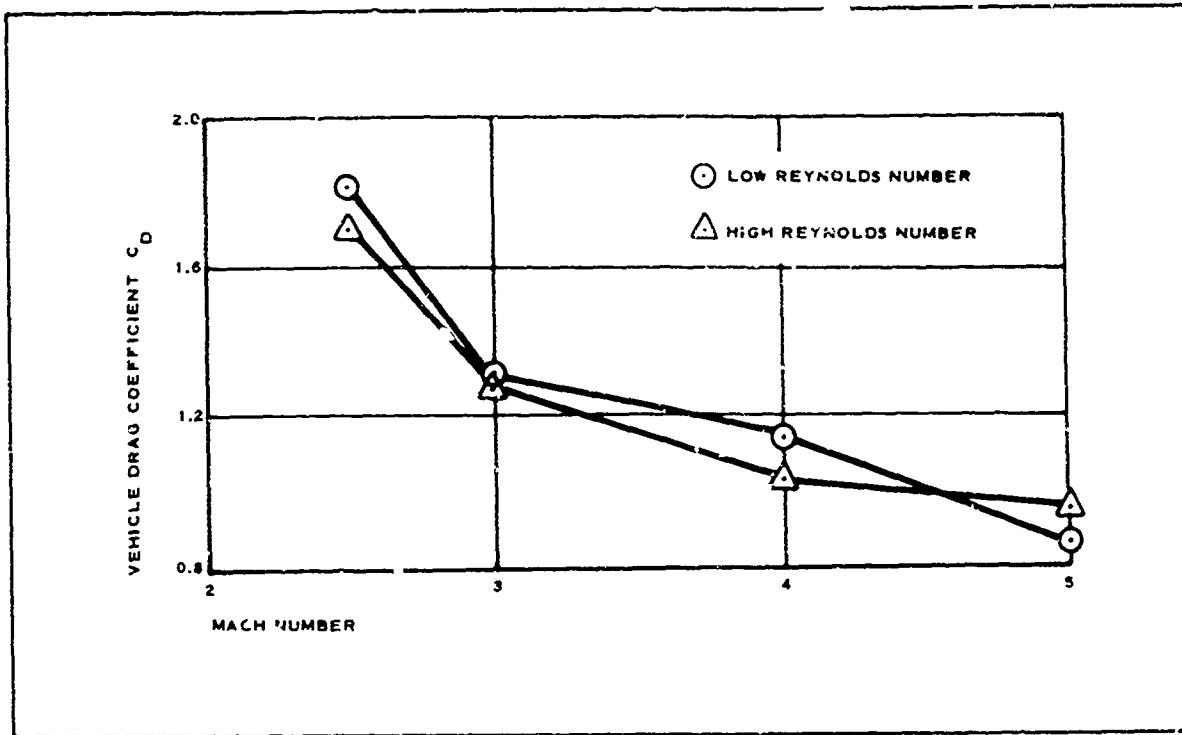


Figure 30 - Predicted Vehicle Drag for Recommended Modified Arapaho C

trajectory subsequent to booster separation, yet prior to jettisoning of the appendage covers.

The despin system design discussed in Item 4 of this section is such that two pairs of opposed-firing, oppositely oriented nozzles (each nozzle developing a 12.5-lb thrust) are located with the thrust axis of each nozzle lying at 0.67 ft from the vehicle's longitudinal axis. The system, as designed, develops a torque of:

$$T = F(\bar{x}) = 25 \times 0.67 = 16.75 \text{ lb-ft} . \quad (5)$$

The test vehicle investigated somewhat conservatively weighed 445 lb and had a roll moment of inertia of 2.37 slug-ft² (from Reference 4). The despin system's deceleration capability is then:

$$\frac{dp}{dt} = \frac{T}{I_R} = \frac{16.75}{2.37} = 7.07 \text{ rad/sec}^2 (405 \text{ deg/sec}^2) . \quad (6)$$

With the system propellant weight of 1.27 lb and nozzle flow rate of 0.153 lb/sec, the thrusting period of the system is 4.15 sec. If no overshoot in system despin occurs, the system is capable of despinning to 20 deg/sec from an initial spin rate of:

$$\begin{aligned}W_o &= \frac{dp}{dt} t + W_1 \\&= 405(4.15) + 20 \\&= 1680 \text{ deg/sec} \\&= 4.68 \text{ revolutions per second (rps)} .\end{aligned}\tag{7}$$

Should overshoot occur (as shown in prior system tests), necessitating despin thrust orientation reversal (switch nozzle sets), it is easily shown in a similar manner that even for 0.5-rps overshoot allowance, the system is capable of despinning to 20 deg/sec terminal spin rate from an initial rate of 4.5 rps.

3. THERMODYNAMIC ANALYSES

a. Objectives

Thermodynamic investigations on the recommended modified Arapaho C were made in order to assist in selection of inflatable appendage materials and in determining appendage inflation system parameters as a function of initial reservoir conditions. The critical test points portrayed in Figure 1 were selected on a critical heating basis.

b. Pressure Distribution

The pressure distribution over the flare configuration denoted as Mod C-1, tested in the WT-I and WT-II wind-tunnel series, was calculated for use in flare stress and thermal studies, using methods identical to that used in estimating the distribution over the basic Arapaho C in Reference 4. This distribution was shown to be conservatively high when empirical WT-II local pressure measurement data were superimposed on the estimates. Cone theory was used to determine pressure coefficients for the 18.5-deg conical angle major-axis plane and the 6.5-deg conical angle minor-axis plane. Figure 31 shows the estimated distribution used for the analyses, relative to the Mod C-1 forebody geometry.

c. Critical Heating Analysis

The addition of an inflatable appendage to the basic Arapaho C test vehicle required a consideration of the thermal effects on the material forming this surface, since aerodynamic heating rates on this surface may be significant in the Mach number range proposed for the flight-test program. This may be particularly so during the series of comparatively low altitude test flights that may be conducted, as shown in Figure 1.

The possible deployment test points at a Mach number 2 or 3 were eliminated from serious consideration, since the adiabatic wall temperature of the generated flow field at altitudes from 40,000 ft and upward lie within the capability of Nomex fabric material (≤ 600 F). However, the possible test points at a Mach number of 4.3 and 6 at altitudes of

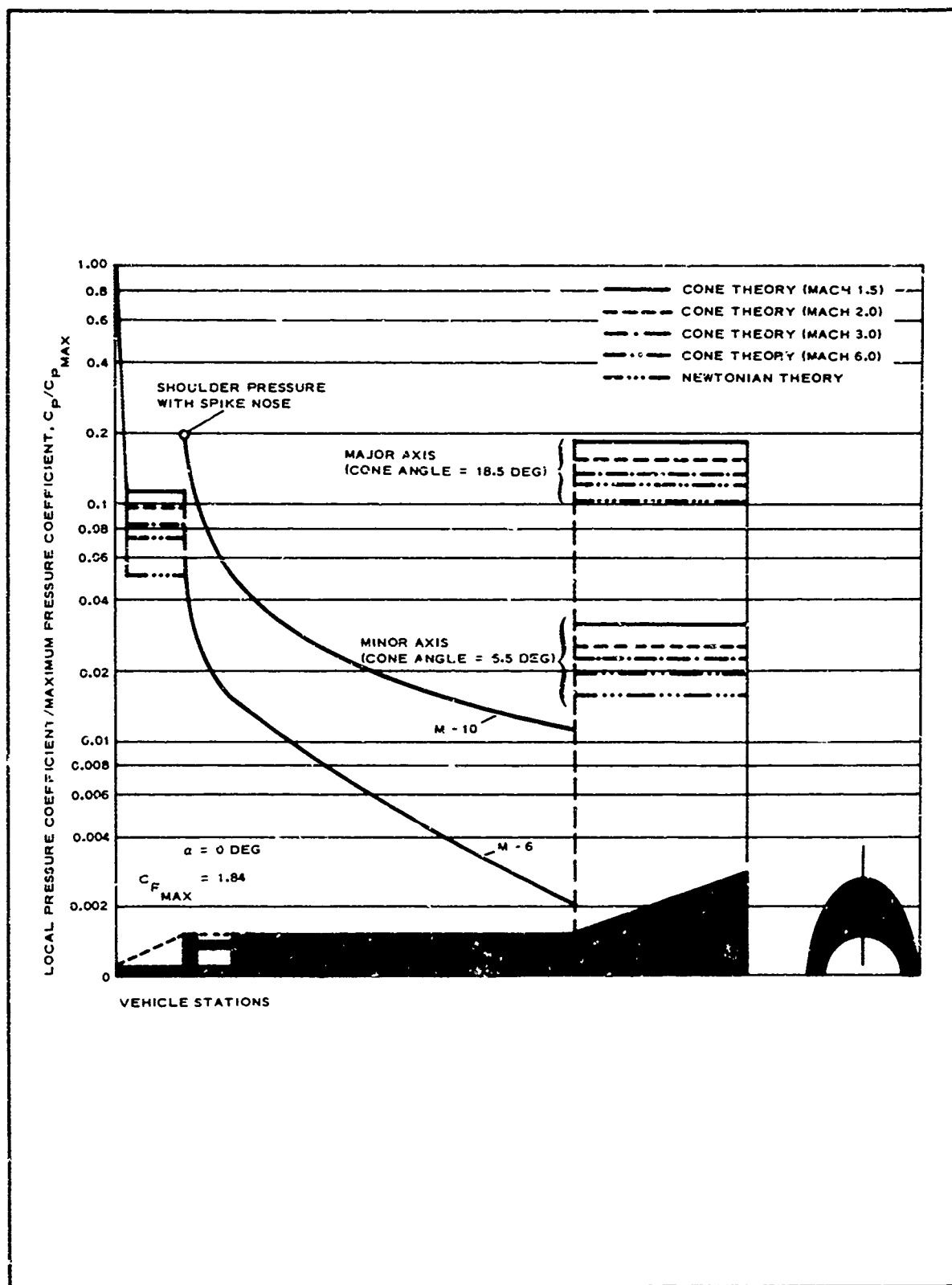


Figure 31 - Estimated Pressure Distribution over Modified Arapaho C-1

70,000 ft and 110,000 ft, respectively, generate adiabatic wall temperatures in excess of 600 F. It is these two points that were isolated for thermal analysis leading to specific material and coating selection.

In support of the thermal analyses, trajectories for these two isolated test points were calculated. The trajectories were based on equations of motion of a point mass involving two degrees of freedom. The trajectory calculation was begun from the instant of inflatable skirt deployment and inflation. The related positions in space were assumed to occur approximately one to two seconds prior to the deployment of the test item and did not include the influence of the drag of the test item. The trajectory for the Mach number 4.3 test point is shown in Figure 32A, while the Mach number 6.0 case is shown in Figure 33B. Of the two trajectory cases computed, the test point for a Mach number of 6.0 at 100,000 ft appeared to be more severe during both exit and entry flight since the flight extends over 300,000 ft of altitude before re-entering the sensible atmosphere at approximately the same velocity at which the initial test point was reached. At 60,000 ft after re-entry, the Mach number is about 5.6. In contrast, the trajectory for the Mach number 4.3 case does not carry over 300,000 ft. A maximum Mach number of 3.2 is reached at approximately 70,000 ft during descent for this case.

Looking at the aerodynamic heating aspects of these trajectories, a cold wall heat flux rate for both cases was calculated at a position one foot from the junction of the maximum flare angle (18.5 deg) and the cylindrical main body of the vehicle. The rates were based on a turbulent boundary layer existing over the flare during both exit and entry flight into the denser regions of the atmosphere. The assumption of a turbulent boundary layer was based on flat plate momentum Reynolds number calculations using the following equation suggested by Stetson (Reference 5):

$$Re_{\theta} = 0.695 \left(\frac{\rho_w \mu_w}{\rho_1 \mu_1} \right)^{0.114} \left(\frac{\rho_1 V_{\infty} x}{\mu_1} \right)^{0.5} \quad (8)$$

Boundary layer transition criteria is usually taken at $Re_{\theta} \approx 400$ to 600 for flow over a flat plate. Assuming that the flow over the cylindrical portion of the test vehicle is similar to flow over a flat plate, the resulting calculations showed that the momentum Reynolds numbers are well beyond the transition criteria range during the testing periods. Thus, it appeared reasonable to assume that these test points are in the turbulent boundary layer flow regime for purposes of heat flux rate calculations.

The cold wall heat flux rates for both trajectory cases are shown in Figure 33. The heat flux rates were calculated using the equation:

$$\dot{q}_w = \frac{0.0296}{(Pr^*)^{2/3} (Re^*)^{0.2}} (\rho^* u_1) (h_r - h_w) \quad (9)$$

which is representative of heat transfer to a flat plate in a high-speed turbulent boundary layer. The quantities with asterisks indicate evaluation

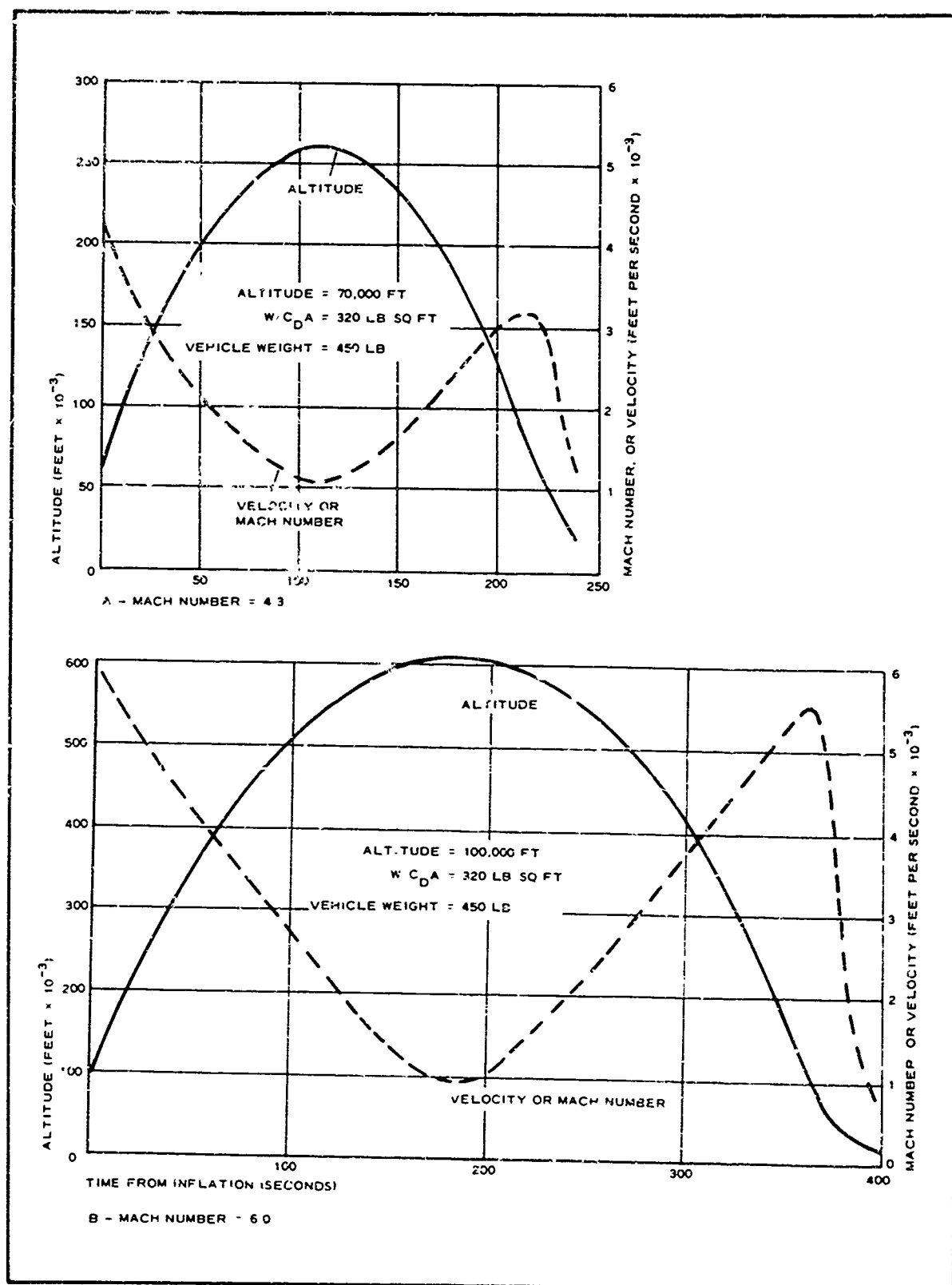


Figure 32 - Trajectories for Two Test Points in Support of Thermal Analyses

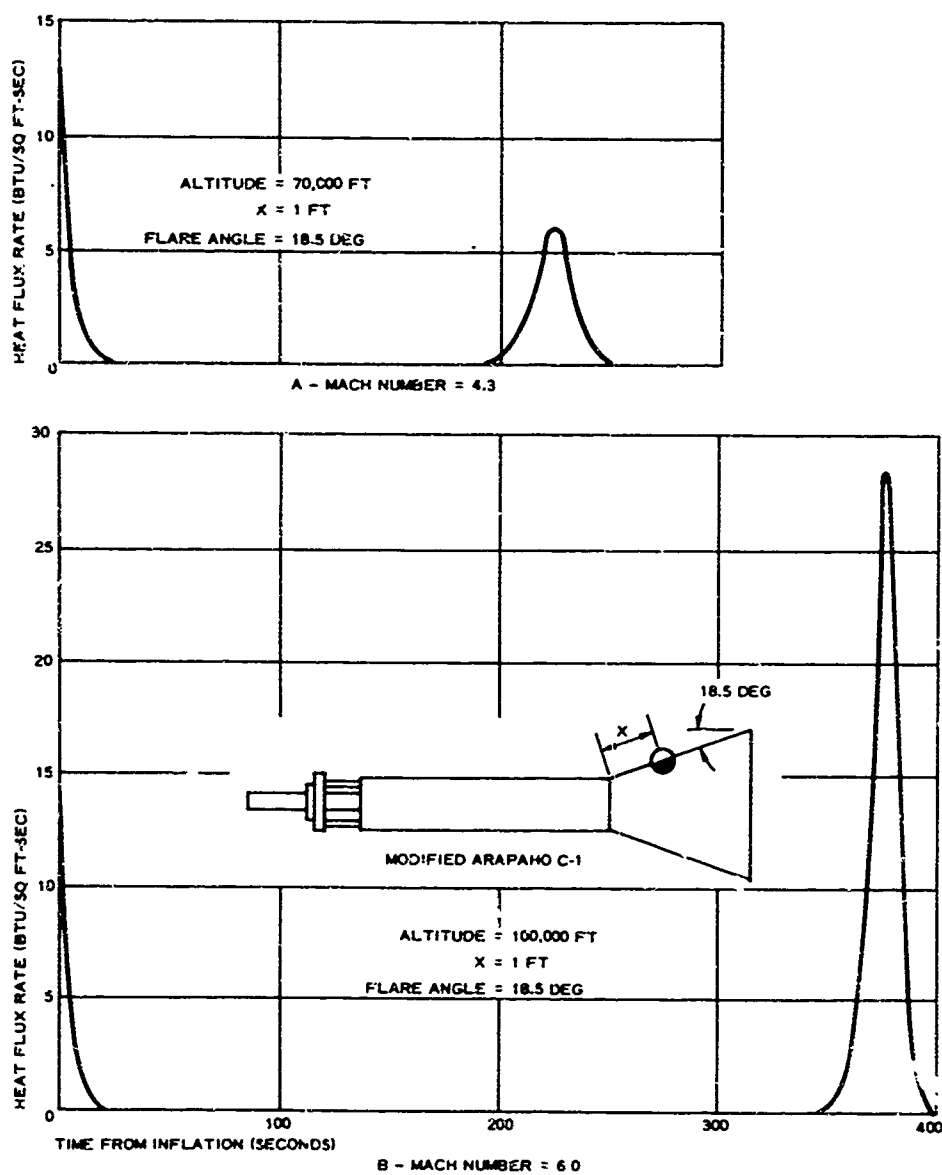


Figure 33 - Cold Wall Heat Flux Rate in Turbulent Flow

using reference enthalpy procedures. The heat flux calculations for the test point Mach number of 4.3 shows that the maximum heat flux rate is experienced immediately upon inflation of the appendage. A maximum heat flux rate of 13 Btu/ft²-sec is predicted to occur at this point, while during entry flight, a peak heat flux rate of 6 Btu/ft²-sec is reached. This latter rate reflects the trajectory path data that showed the test vehicle continually decelerating in the sensible atmosphere.

The maximum heat flux rate for the Mach number 6 flight occurs during re-entry. The heat flux rate variation with time of flight is shown in Figure 33B. A maximum rate of 15 Btu/ft²-sec is predicted at the point of inflation for this flight; however, during re-entry, the maximum heat flux rate to be expected is almost twice that expected during exit flight, reaching about 28 Btu/ft²-sec. Thus, it appears that the Mach-6 test flight at 100,000 ft will generate the most severe overall thermal exposure of the appendage material to aerodynamic heating.

One other interesting point in the test flight envelope that has not been mentioned thus far is the possible test point at a Mach number of 6 at 200,000 ft. Since the ambient pressure at this altitude has diminished considerably from the lower test point altitudes, the pressures acting on the appendage surface also have decreased considerably. Hence, the likelihood of aerodynamic heating at this particular test point can be considered negligible. However, during the re-entry phase, the aerodynamic heating rates will be of greater magnitude. In order to ascertain the magnitude of the heating rates, a trajectory path emanating from this test point was calculated and the heating rates to the appendage surface were appraised. These rates are shown in Figure 34. A peak rate of 48 Btu/ft²-sec is predicted for this re-entry case. This is almost twice as large as that predicted for the re-entry case where the Mach number is 6 at 100,000 ft. Thus, it appears that the most significant aerodynamic heating rates on the appendage will occur during the re-entry phase of the trajectory paths for any Mach 6 test flights.

On the basis of the aerodynamic heating potential at the appendage surface examined thus far, the lower heating rates predicted during the initial testing periods suggested that these be utilized to examine the appendage material for temperature rise. In particular, the heat flux rates generated by the Mach-6 deployment at 100,000 ft was apparently the most severe in the test point envelope; therefore, its effect on the appendage material should prove deciding for this series of test points. A one-dimensional transient heat conduction analysis for the temperature distribution in the appendage material was conducted using basically the partial differential equation for heat conduction in a slab:

$$\frac{\partial T}{\partial t} = \frac{\partial^2 T}{\partial x^2} \quad (10)$$

This equation was converted to a finite difference equation and put in the form of a heat balance, so that the heat-in minus the heat-out is equal to the heat-stored. For any *i*th layer, the heat balance can be written as:

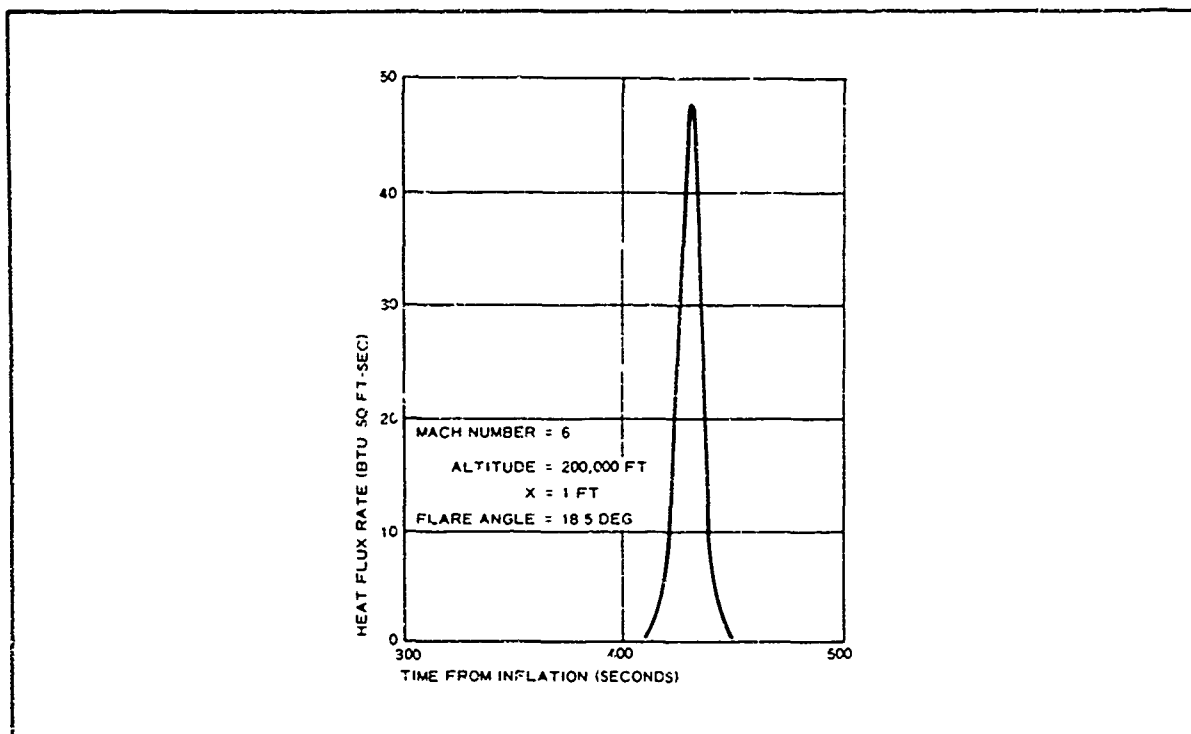


Figure 34 - Cold Wall Heat Flux Rate in Turbulent Flow
(Mach 6; 200,000 Ft)

$$\frac{k}{\Delta x} (T_{i-1} - T_i) - \frac{k}{\Delta x} (T_i - T_{i+1}) = \frac{\rho c (\Delta x)}{\Delta t} (T_i' - T_i) \quad (11)$$

At the outer surface:

$$h(T_{aw} - T_1) - \epsilon \sigma (T_1^4 - T_s^4) - \frac{2(T_1 - T_2)}{\frac{x_1}{k_1} + \frac{x_2}{k_2}} = \frac{\rho c \frac{\Delta x}{2}}{\Delta t} (T_1' - T_1) \quad (12)$$

At the inner surface, an adiabatic wall condition was specified; therefore, no heat crossed this boundary. The slab of appendage material was then divided up into a number of nodes and Equation 11 was used to balance the heat flow through these nodes. The convective heat input term into the outer surface in Equation 12 was modified to take into account the hot wall condition by operating on the cold wall heat flux rates in the following manner:

$$\dot{q}_w = h(T_{aw} - T_1) = \dot{q}_{cw} \left(\frac{T_{aw} - T_1}{T_{aw} - T_{cw}} \right) \quad (13)$$

These equations were solved simultaneously on a digital computer and the results are shown in Figure 35. The wall material was basically HT-72 Nomex fabric covered externally by a 25-mil layer of Dow-Corning 92-007, a flexible silicone ablative type of coating, and internally by

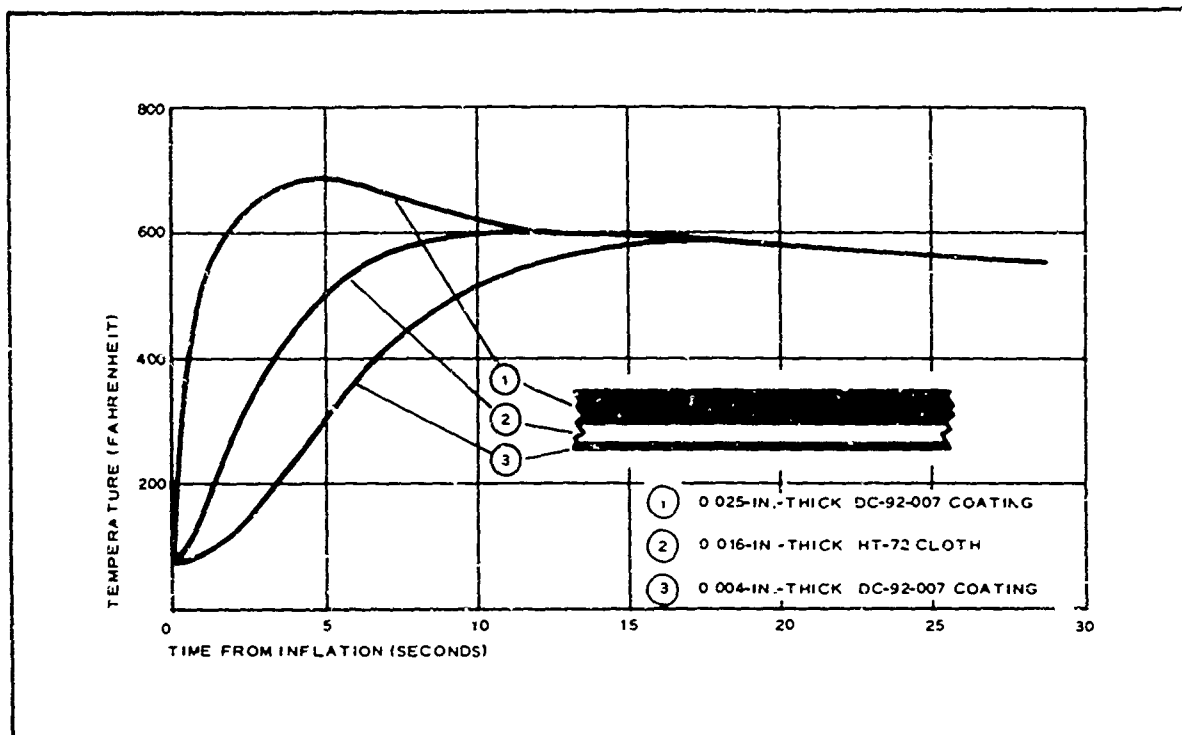


Figure 35 - Temperature Rise with Time on EUREKA Inflatable Appendage

4 mils of the same material. The results of the transient analysis showed that the outside surface temperature would rise to 780 F in four seconds. However, the thickness of the coating material is sufficient in keeping the Nomex material from reaching 600 F. As the heat flux rate decays with increasing altitude, cooling of the appendage takes place. After approximately four to five minutes of flight, the test vehicle re-enters the sensible atmosphere and again is exposed to aerodynamic heating.

Since the heat flux rates encountered during re-entry are much greater than those used in the exit flight heat conduction analysis presented above, undoubtedly, the temperature rise in the fabric appendage should be enough to raise the temperature of the fabric above 600 F. Other combinations, such as thicker Nomex cloth materials coupled with other types and thicknesses of coatings, were also analyzed using the outlined heat conduction analysis methods. Many of them showed potential for use as appendage material; however, their ability to be successfully packaged in the volume allotted was seriously questioned. As a result, further analysis of re-entry shielding and material requirements was discontinued.

In conclusion, the results of this thermal analysis show that the Nomex/-silicone-coating combination should be sufficient to absorb the aerodynamic heat loads predicted to occur at the appendage surface during and immediately after inflation and subsequent to test point occurrence. The geometric angle of the flare examined was 18.5 deg so that the results may be extrapolated to any of the other longitudinal surface geometries on the unsymmetrical appendage. In such a case, the shallower flare

orientation leads to lower heating rates, alleviating the temperature rise problem. However, the expected re-entry heat flux are two to three times as large as those used to thermally analyze the appendage material. The presently recommended appendage, therefore, is not expected to successfully survive the re-entry flight.

4. VEHICLE MODIFICATIONS

a. Recommended Modifications

The recommended test vehicle appendage, after analysis and wind-tunnel tests, was determined to be the elliptical flare configuration shown on Figure 36. The flare starts at Station 37.96 as an 11-in. diameter circle and changes into a shape closely approximating an ellipse. The flare configuration required changes to the Arapaho C vehicle chiefly in the region from Station 37.96 to Station 7.06. A list of vehicle design changes is given in Table IV.

b. Sequencing

(1) Sequence System Design Analysis

The Arapaho C vehicle's sequence system was reviewed to determine its compatibility with the EUREKA program. The requirement that the EUREKA vehicle meet the Eglin AFB range safety criteria makes it necessary that the vehicle employ 1-amp, 1-w, no-fire-for-5-min electro-explosive devices. This requirement involves a change to the Arapaho C

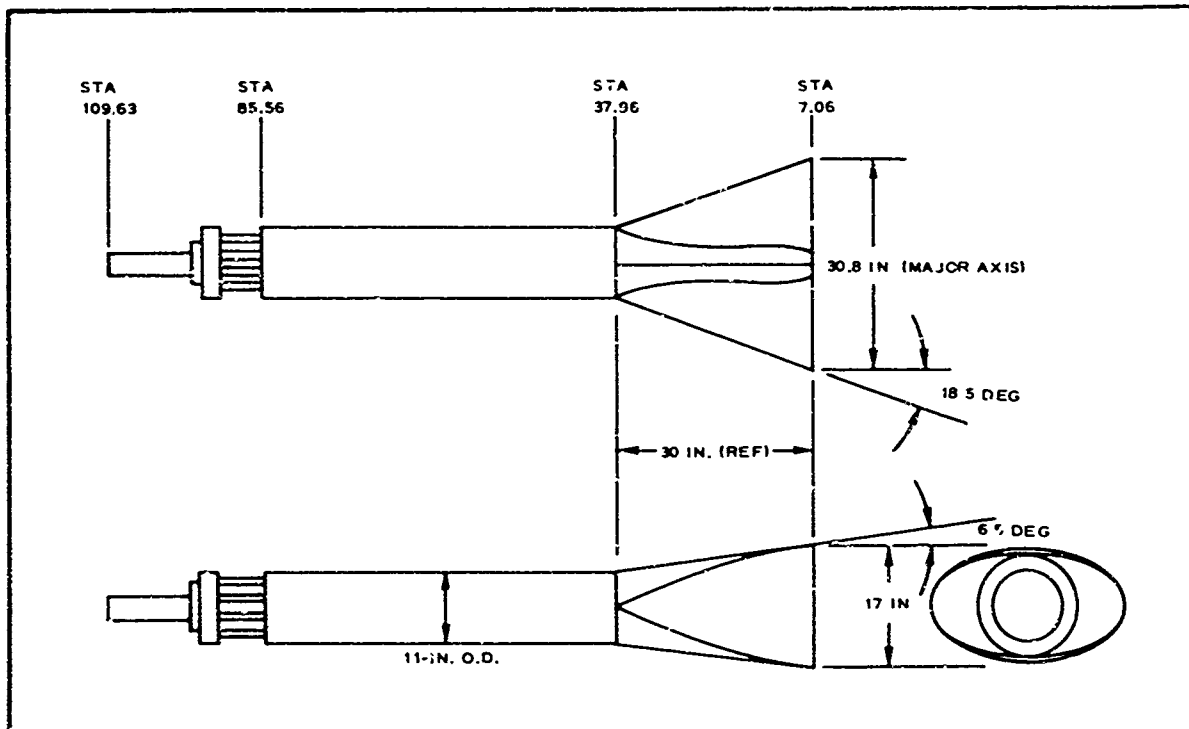


Figure 36 - Geometric Details of Elliptical Flared Appendage

TABLE IV - RECOMMENDED VEHICLE MODIFICATIONS

Modification	Reason
Relocate safe and arm receptacle	Interfered with installation of elliptical flare
Relocate lanyard switch	Interfered with installation of elliptical flare
Replumb despin system	Interfered with installation of elliptical flare
Redesign tensiometer beam	To permit separation and test item retention
Redesign test decelerator container	To provide packaging area for elliptical flare
Redesign test decelerator deployment	Container redesigned
Relocate aft pyrotechnic switches	Interfered with safe and arm receptacle and lanyard switch
Redesign recovery parachute clevis fitting	New test item container restricted parachute riser line installation
Addition of flare cover	Provide conical fairing during boost stages and to protect stowed elliptical flare
Addition of radar beacon battery pack	Battery cells in main battery pack used for sequence circuit
Redesign of main battery pack	Increase sequence circuit voltage
Incorporation of 1-amp, 1-w, no-fire, electroexplosive devices	Comply with new range safety criteria
Test decelerator retention capability addition	Design required

vehicle. It entails replacing many of the existing electroexplosive devices and also makes it necessary to supply more battery voltage to provide the 4.5 to 5.0 amp recommended fire current for the 1-amp, 1-w, no-fire devices. The Arapaho C vehicle's pyrotechnics are listed in Table V, and the suggested replacement devices also are shown in the table.

(2) Detonators

The replacement of the detonators for initiating the flexible linear-shaped charge offered various possibilities. These detonators are employed in final-stage booster separation and nose-probe separation. The Arapaho C vehicle uses DuPont X549D Minidets, which are miniature devices. They have proved to operate quite satisfactorily, however, they are not

TABLE V - PYROTECHNIC DEVICES

Arapaho C			EUREKA		
Description	Quantity	Vendor part number	Quantity	Vendor new part number	Comments
Dimple motors (actuate timers)	2	DM25N4, Hercules	2	DM43B0, Hercules	Physically interchangeable
Pyrotechnic switches (sequence control)	30	MS . . . CR Series, Atlas	34	MS . WRFRT Series, Atlas	Not physically interchangeable. Requires redesign of pyro switch boards
Detonators (booster separation)	2	X549D Minidet, DuPont	2	1DT123, Atlas	Not physically interchangeable
Cartridge (despin valve)	4	Part of Valve 1804-032-02, Conax	4	1DT123, Atlas	No change required
Squib (test item thrusters)	12	S-94, DuPont	2	IGN116, Atlas	Not physically interchangeable. New cartridge cap required
Detonators (nose probe separation ring)	2	X549D Minidet, DuPont	2	1DT123, Atlas	Not physically interchangeable
Cartridge (beam separation nut)	1	PC-10, Hi-Shear	1	1DT123, Atlas	No change required
Squib (recovery parachute)	4	S-94, DuPont	1	IGN116, Atlas	Not physically interchangeable. New cartridge cap required
Cartridge (latch pin puller)	4	Part of Pin Puller 1808-024-02, Conax	4	Part of pin puller GDC, Conax	Physically interchangeable
Cartridge (floatation balloon valve)	1	Part of Valve 1802-069-01, Conax	1	Part of pin puller GDC, Conax	No change required
Squib (flare cover thrusters)	0	No requirement	2	IGN116, Atlas	New EUREKA application
Cartridge (flare inflation valve)	0	No requirement	1	Part of valve, Conax	New EUREKA application

1-amp, 1-w, no-fire devices. The manufacturer was contacted to determine if a 1-amp, 1-w device in the Minidet version is available. The response of E.I. duPont & Co. was, "No," and they do not wish to develop such a device at this time. Another vendor, Atlas Chemical Industries, Inc., was contacted and although they have no such device at this time, they would develop it and charge for development. Atlas Chemical does have a larger version available in the 1-amp, 1-w version. Another company, Unidynamics/Phoenix Division, also has a 1-amp, 1-w, no-fire device that is larger than the Minidet. Both the Atlas and Unidynamics devices have similar electrical characteristics. Use of the larger size detonators will require a different configuration for the detonator installation. The Atlas version is listed in Table V as the suggested replacement item.

(3) Circuitry

Use of the 1-amp, 1-w, no-fire devices involved a complete circuit analysis of the sequence system to determine the correct battery voltage, current limiting resistances, and short circuit protection. These are all

critical factors in the proper sequencing and firing of electroexplosive devices. Additional events also have been incorporated in the sequence system to operate the elliptical flare deployment and inflation system.

Table VI lists the sequence of events for the EUREKA test flights. As shown on Table VI there are requirements for different sequences, depending upon the booster configuration and test point. In particular, the Honest John-Lance-Lance booster combination requires additional operations to separate the third-stage Lance when final-stage booster separation occurs at altitudes above 125,000 ft. For this condition, retrorockets are required to decelerate the final stage booster after separation.

The current pulses experienced on a typical test flight are shown in Figure 37. During ideal operation, the current pulses will be less than 100 msec in duration. In normal operation some of the electroexplosive device bridgewires can be expected to short after firing. This is particularly true for flexible linear-shaped charge detonators used for booster separation and nose-probe separation.

A circuit analysis was made to determine the sequence battery voltage required for the EUREKA system as a result of the 1-amp, 1-w criteria. The analysis also determined the values of sequence circuit current limiting resistors. The circuit analysis is presented in Appendix I. The sequence of calculated firing currents are summarized below in Table VII. The analysis shows that the sequence battery voltage should be 31.25 v. This voltage is obtained by using 25 cells at 1.25 v per cell, connected in series. The cells are the same as those used for the Arapaho C. The cells are of nickel and cadmium, Part Number S-113, manufactured by Sonotone Corporation.

(4) Circuit Isolation

The use of pyrotechnic switch contacts to open the circuit to the electroexplosive device bridgewires after firing has been maintained in the EUREKA program except for the flare cover thruster and flare inflation valve circuits. These two circuits were added for the EUREKA application. For circuit isolation, fuse resistors have been employed. Type FR fuse resistors, manufactured by International Resistance Company, appear to be suitable for this application.

Some advantages of the fuse resistor are that it:

1. Eliminates need for pyrotechnic switch in cases where the pyrotechnic switch is used only for circuit isolation
2. Combines current-limiting resistor function with fuse function
3. Only acts as a fuse if shorting condition exists
4. Requires no current to fire pyro switches; reduces complexity of sequence circuit

TABLE VI - SEQUENCE OF EVENTS

Activity	Actuation	Time (sec)	Operation	ADDPEP	EUREKA				
					HJ [®] -N	HJ [†] -N-N	HJ-N-L [‡]	HJ-L-L	HJ [§] -L-L
First-stage ignition	Ground initiated	T + 0	Fire igniter squib	x	x	x	x	x	x
Launch	Start timers	T + 0	Pull lanyard and actuate inertia switch	x	x	x	x	x	x
First-stage burnout	...	T + 5	...	x	x	x	x	x	x
Second-stage ignition	Ground initiated delay	T + 10	Fire igniter squib	x	.	x	x	x	x
Second-stage ignition	Cam 1	T + 15	Fire igniter squib	x	x
Second-stage burnout	...	T + 18	...	x	x	x	x	x	x
Second-stage separation	Interstage (automatic)	...	Fire separation nut	x	.	.	.	x	x
Final-stage ignition	Cam 1	T + 25	Fire igniter squib	x	x	x	x	x	x
Final-stage burnout
Final-stage separation	Cam 2	T + 32	Fire FLSC detonators	x	x	x	x	x	x
Retrorocket ignition	Cam 2, plus time delay	T + 32.5	Fire igniter squib	x	x
Pretest calibration on	Cam 3	T + 34	Operate relays	x	x	x	x	x	x
Despin on	Cam 3	T + 34	Fire explosive valve squib	x	x	x	x	x	x
Despin off	Cam 3, plus time to despin	T + 36	Fire explosive valve squib	x	x	x	x	x	x
Flare fairing ejection	Cam 3, plus 5-sec time delay	T + 39	Fire thrusters' squib	.	x	x	x	x	x
Flare inflation	Cam 3, plus 5.5-sec time delay	T + 39.5	Fire explosive valve squib	...	x	x	x	x	x
Cameras on	Cam 4	T + 41	Operate relays	x	x	x	x	x	x
Solenoids open	Cam 4	T + 41	Operate relay	x	x	x	x	x	x
Pretest calibration off	Cam 4 + <1 sec	T + 42	Operate relay	x	x	x	x	x	x
Test item deployment	Cam 4 + 1 sec	T + 42	Fire thruster squib	x	x	x	x	x	x
Post-test calibration	Cam 5	T + 71	Operate relay	x	x	x	x	x	x
Solenoid valves closed	Cam 6	T + 90	Operate relay	x	x	x	x	x	x
Camera power off	Cam 6	T + 90	Operate relay	x	x	x	x	x	x
Recovery enable	Cam 6	T + 90	Close timer switch	x	x	x	x	x	x
Beam release	Altitude baroswitch	At 11,000 ft, fire separation nut squib	...	x	x	x	x	x	x
Recovery parachute deployment and auxiliary flotation BALLUTE [§] deployment	Baroswitch plus 0.5 to 1 sec	Fire gas generator squib	...	x	x	x	x	x	x
Nose probe separation	Baroswitch plus 1.5 to 2 sec	Fire FLSC detonators	...	x	x	x	x	x	x
Activate salt water battery	Water impact (WI)	W1 + 0	.	x	x	x	x	x	x
Flotation canister latch plus	...	W1 + 0.5	Fire pin puller squib	x	x	x	x	x	x
Flotation balloon inflation	...	W1 + 0.5	Fire explosive valve squib	x	x	x	x	x	x
Radio beacon operation	...	W1 + 5	.	x	x	x	x	x	x
Dye marker dispensation	...	W1 + 3	Water soluble	x	x	x	x	x	x
Pinger operation	...	W1	Self initiating and sustaining	x

[®]HJ - Honest John

[†]N - Nike

[‡]L - Lance

[‡]For booster separation occurring at altitudes greater than 125,000 ft

[§]TM, Goodyear Aerospace Corporation, Akron, Ohio.



Figure 37 - EUREKA Electrical Load versus Time

TABLE VII - SEQUENCE FIRING CURRENT SUMMARY

Device	Firing current			Calculated firing current-circuit shorted condition (amps)
	Recommended firing current (amps)	Calculated firing current (amps)	Minimum fire current (amps)	
Dimple motor	5.0	5.40	3.5	3.90
Pyrotechnic switches	5.0	5.16	3.5	3.80
Final-stage igniter (Nike)	5.0	5.00	3.5	4.16
Final-stage booster separation	5.0	6.30	3.5	4.70
Despin valve	5.0	5.46	3.0	3.89
Test item thruster	4.5	5.70	3.6	4.35
Nose probe separation	5.0	6.30	3.5	4.70
Beam separation nut	5.0	5.38	3.5	3.86
Recovery parachute	4.5	6.56	3.6	5.25
Latch pin puller	5.0	5.40	3.0	3.87
Flotation balloon valve	5.0	5.40	3.0	3.04
Flare cover thruster	4.5	5.70	3.6	4.35
Flare inflation valve	5.0	8.20	3.0	...
Final-stage igniter (Lance)	4.5	4.80	3.5	3.79

It is recommended that the circuit isolator pyrotechnic switches that have been carried over from the Arapaho C be replaced with fuse resistors. The circuits affected are shown in Table VIII.

Elimination of eight pyrotechnic switches and eight associated limiting resistors could be achieved by the use of fuse resistors.

c. Test Item Stowage Volume

A minimum of one-half cubic foot is required for test item stowage. The preliminary design provides a cylindrical test item stowage compartment that is 11.5 in. in diameter and 13.5 in. long for a total stowage volume of eight-tenths cubic foot.

d. Recovery System Location

The Arapaho C recovery parachute container (see Figure 38A) is located in the aft part of the recovery section. Since the test item container was ejected during test item deployment, the recovery parachute was blasted out directly into the wake of the recovery section. The EUREKA vehicle

TABLE VIII - CIRCUITS AFFECTED BY FUSE
RESISTOR INCORPORATION

Circuit	Pyro switch reference design number *		Limiting resistor number associated with pyro switch ⁺	Limiting resistor number
	Sequence A	Sequence B		
Final-stage igniter	S2PT	S2PT	R109, R110	R39, R40
Final-stage separation	S3PT	S3PT	R113, R114	R49, R50
Test item thruster	S8PT	S8PT	R79, R88	R63, R64, R65, R66
Latch pin and flotation valve	S15PT	S15PT	R119, R120	R57, R58, R59, R60

* These devices are eliminated, one in each sequence.

⁺ These devices are replaced with fuse resistors.

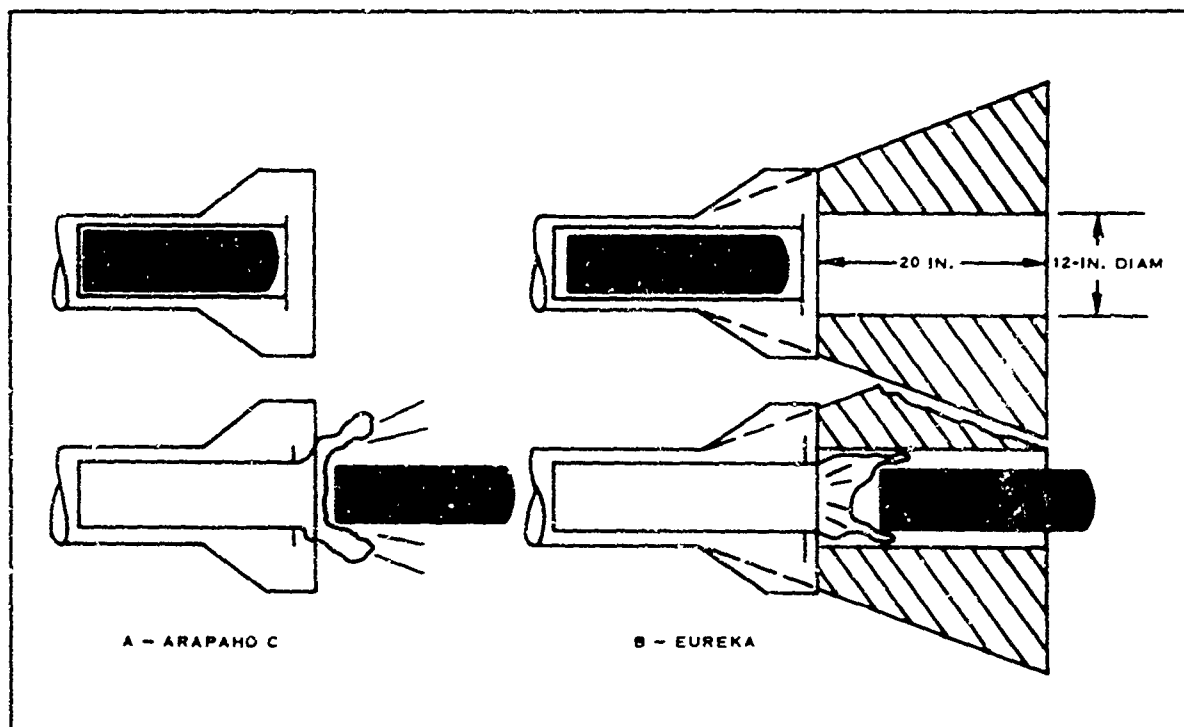


Figure 38 - Recovery Parachute Deployment

will have an additional shell behind the recovery section (see Figure 38B) because the test item container will remain with the vehicle.

The additional shell on the EUREKA vehicle has a 12-in. -diam by 20-in. - long smooth bore through which the recovery parachute pack (7.7 by 4.7 by 20 in.) travels before reaching the wake of the vehicle. This additional 20 in. should produce no adverse effects on recovery parachute deployment.

e. Despin System

The existing Arapaho C vehicle employs a despin system that operates prior to test item deployment after final-stage booster separation. A rate gyro aboard the vehicle opens the despin nozzles when the spin rate is greater than 20 deg/sec as mentioned in Item 2, e of this section. The addition of the elliptical shape in the flare area removed the hard structure that formerly held the nozzles. To maintain the present capability, it is necessary to relocate the nozzles so that the moment arm about the center of roll is the same.

The despin system for EUREKA will be operated after booster separation, but before ejection of the elliptical flare and the inflation of the elliptical flare. The changes in sequencing are shown below.

<u>ADDPEP sequence</u>	<u>EUREKA sequence</u>
Booster separation	Booster separation
Despin	Despin
	Flare cover ejection
	Inflation of elliptical flare
Test item deployment	Test item deployment

f. Flare Deployment

(1) Deployment Sequence

The elliptical flare will be deployed after the despin operation occurs. Deployment of the flare entails removal of the flare cover sections and then inflation of the elliptical flare. Removal of the flare cover is accomplished with two thrusters that eject the two half sections. The flare is inflated by explosively opening a valve that allows nitrogen gas stowed in a high-pressure reservoir to escape to the flare assembly. The sequence is shown schematically in Figure 39.

(2) Flare Cover Ejection, Alternate Consideration

Shaped charges and thrusters also were considered for flare deployment. The shaped charge method utilized a flexible linear-shaped charge (FLSC) that was installed between the butting edges of the two half-flare shells as shown in Figure 40.

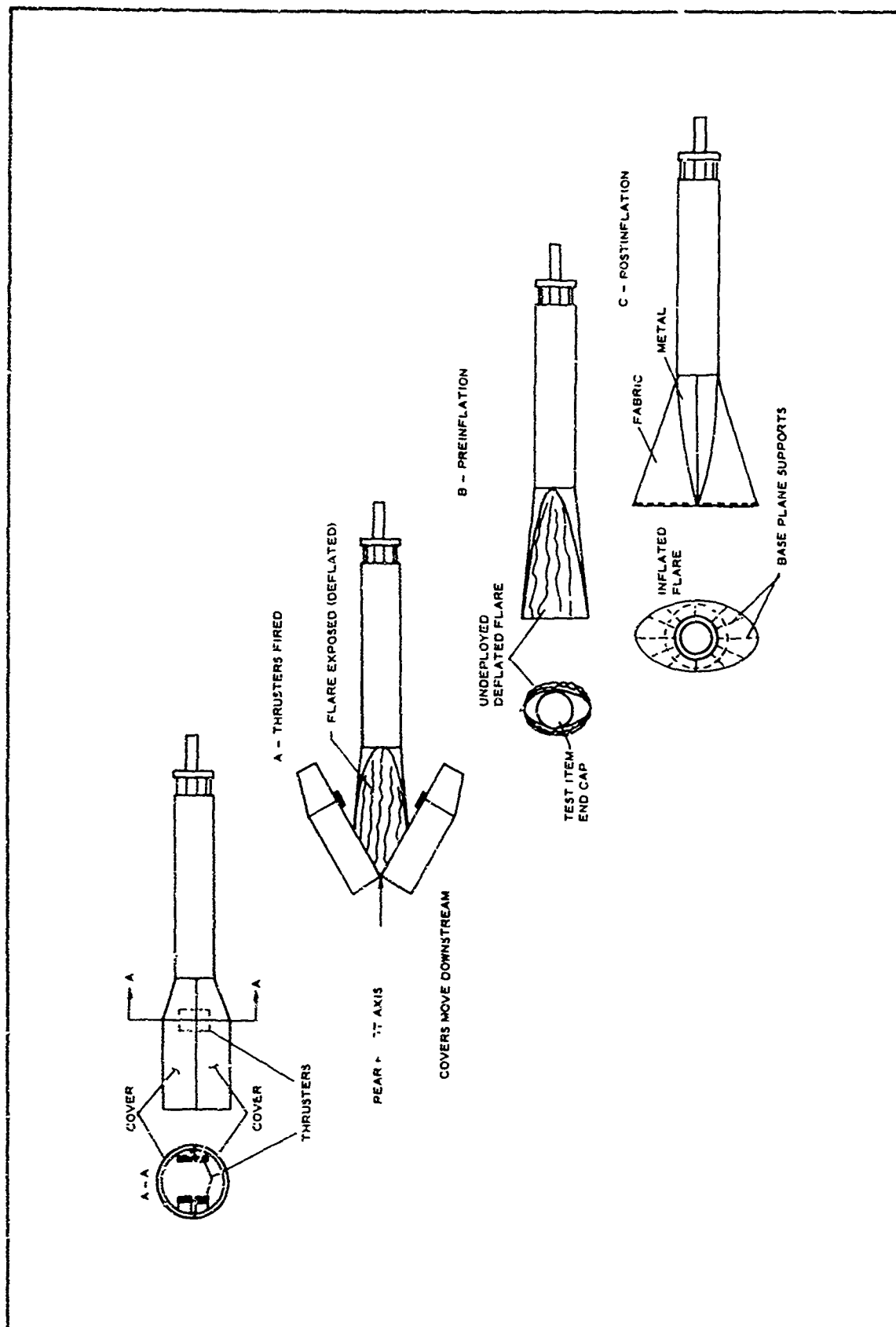


Figure 39 - Flare Deployment Sequence

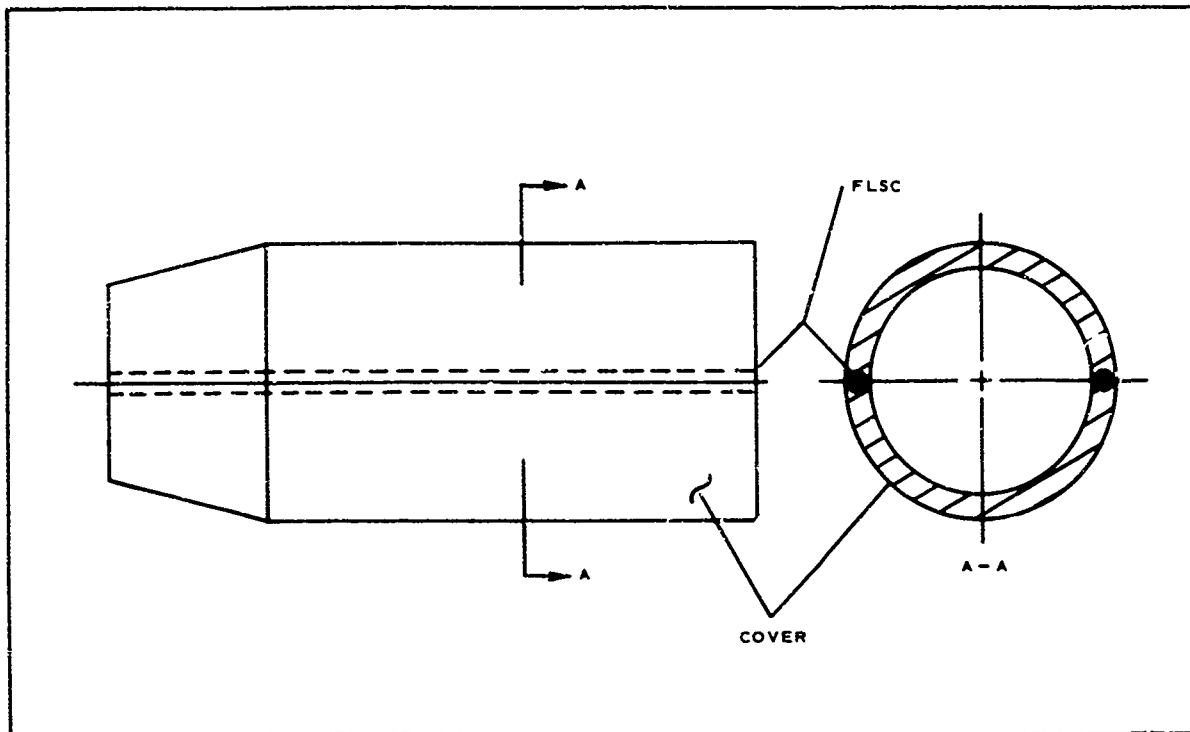


Figure 40 - Placement of FLSC

This method was discarded because the residue of the pyrotechnic explosion was not contained. Fragmentation could damage the skirt assembly fabric.

(3) Flare Thruster Calculations

Dynamic pressure at time of flare inflation was estimated to be a maximum of 2000 psf. This was obtained by using the $q = 1000$ -psf line as the test point regime and the worst test point on this line of Mach 3 at 60,000 ft. By assuming that flare inflation occurs three seconds prior to the test point and that the velocity is constant for this time span, the altitude at flare inflation then will be:

$$60,000 \text{ ft} - (3 \text{ sec} \times 3 \times 968 \text{ fps}) = 51,000 \text{ ft} .$$

At 51,000 ft, $p = 232.4$ psf. The dynamic pressure is then

$$\begin{aligned} q &= 0.7(232.4)(3)^2 \\ &= 0.7 p M^2 \\ &= 1460 \text{ psf} . \end{aligned}$$

A value of 2000 psf was used to be conservative.

The spike nose version of the C test vehicle would have a $C_p/C_{r_{\max}}$ of about 0.125 at $M_\infty = 3.00$ to 6.00 (see Reference 4). For $q = 2000$ psf, $P = 250$ psf, or 1.74 psi.

The flare cover geometry and loading are shown in Figure 41. Assuming that the differential pressure on the cylindrical portion of the flare is negligible and using a factor of safety of 1.5, the normal force on the flare is:

$$F_N = \left(\frac{11 + 18}{2} \right) \times 9.875 \times 1.74 \times 1.5$$

$$= 374 \text{ lb ultimate .}$$

Assuming the force on the flare is zero when $\theta = 18 \text{ deg } 30 \text{ min}$, the energy required per side is:

$$E = Fr\theta$$

$$= \frac{374}{2} \times \frac{24.05}{12} \times \frac{18.5}{57.3} .$$

The total energy per thruster is then 120.6 ft-lb.

A small amount of energy is required to break the shear screws at the thruster assembly. These shear screws serve an important purpose in

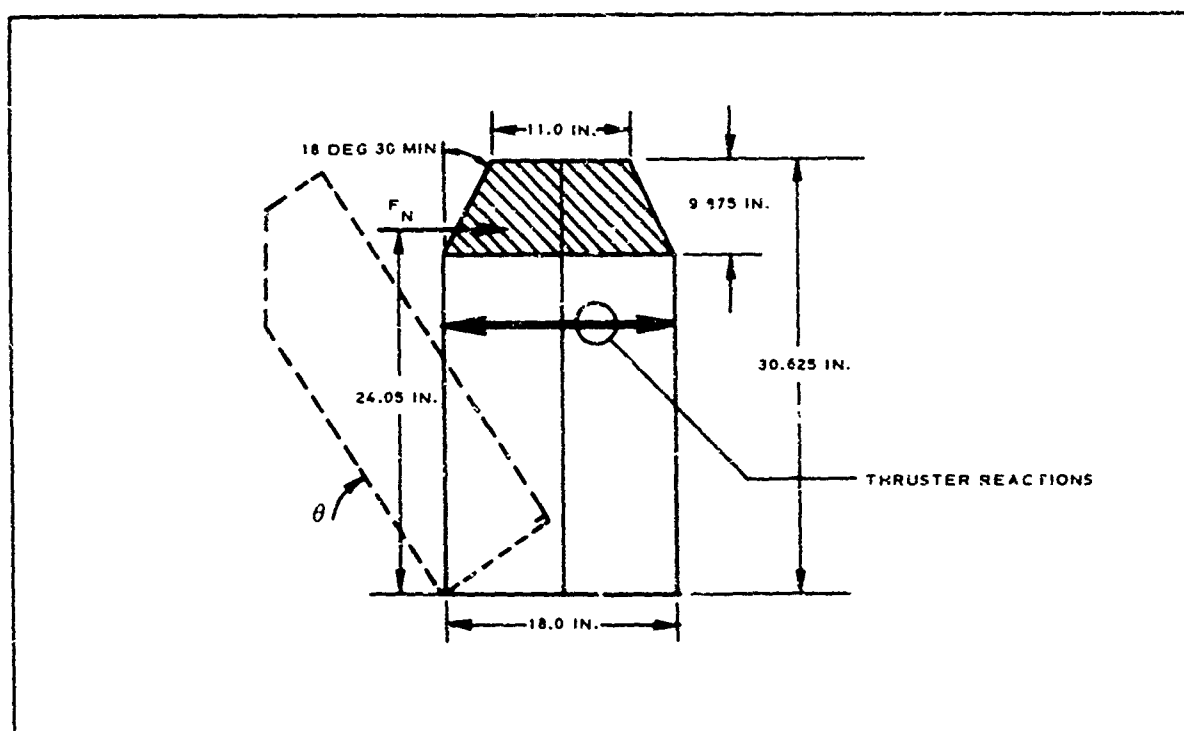
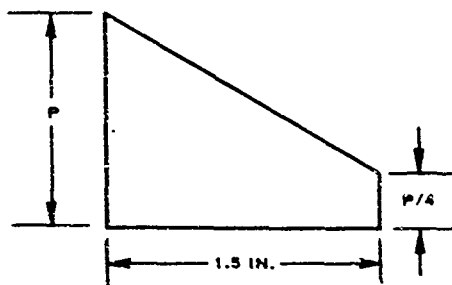


Figure 41 - Flare Cover Loading at Ejection

that they ensure pressure buildup in the thruster prior to breakage. The energy required to break these shear screws is negligible when compared to the total energy required for the thrusters and is, therefore, not considered in this analysis. With a stroke of 1.5 in. for the thruster and, assuming that the force at the end of the stroke is one-fourth that at the start, the maximum force required for the thruster is:



$$E = \left(\frac{5P}{8} \times \frac{1.5}{12} \right) = 120.6 \text{ ft-lb}$$

$$P = \text{peak force} = 1544 \text{ lb.}$$

g. Flare Inflation

The elliptical flare is composed of two separate modules that are joined together by an inflation manifold. Stored nitrogen passes through the explosive operated valve to a tee and then to each of the flare modules. The inflation system is shown schematically in Figure 42.

A study was conducted to determine appendage inflation system parameters as a function of initial reservoir conditions. The study was based on the expulsion of a gas stored in a pressure vessel through a sonic orifice into a fixed-volume receiver. In the case of the modified Arapaho C test vehicle, it is proposed to inflate the appendage using a fixed amount of gas, stored under high pressure, into a fixed volume container. Thus, once the inflation process is initiated, transient conditions exist in both the pressure vessel as well as in the fixed volume appendage receiver until equilibrium conditions are reached between the two reservoirs. As a result, the final state of the gas will depend largely on the changes in the gas properties in the storage vessel as the contained gas expands within the vessel, while the exit mass flow at sonic velocity depletes the amount remaining in the vessel. In addition, the gas properties in the fixed volume appendage reservoir changes due to accumulative addition of gas at conditions other than that already present.

The amount of gas expelled from the storage vessel under sonic flow conditions can be derived from the conservation of mass principle, isentropic flow relationships, and sonic velocity equation. This equation can be written as:

$$\dot{w} = \frac{dw}{dt} = \frac{A_t P_1 g n \sqrt{\left(\frac{2}{n+1} \right)^{(n+1)/(n-1)}}}{\sqrt{g n R T_1}} \quad (14)$$

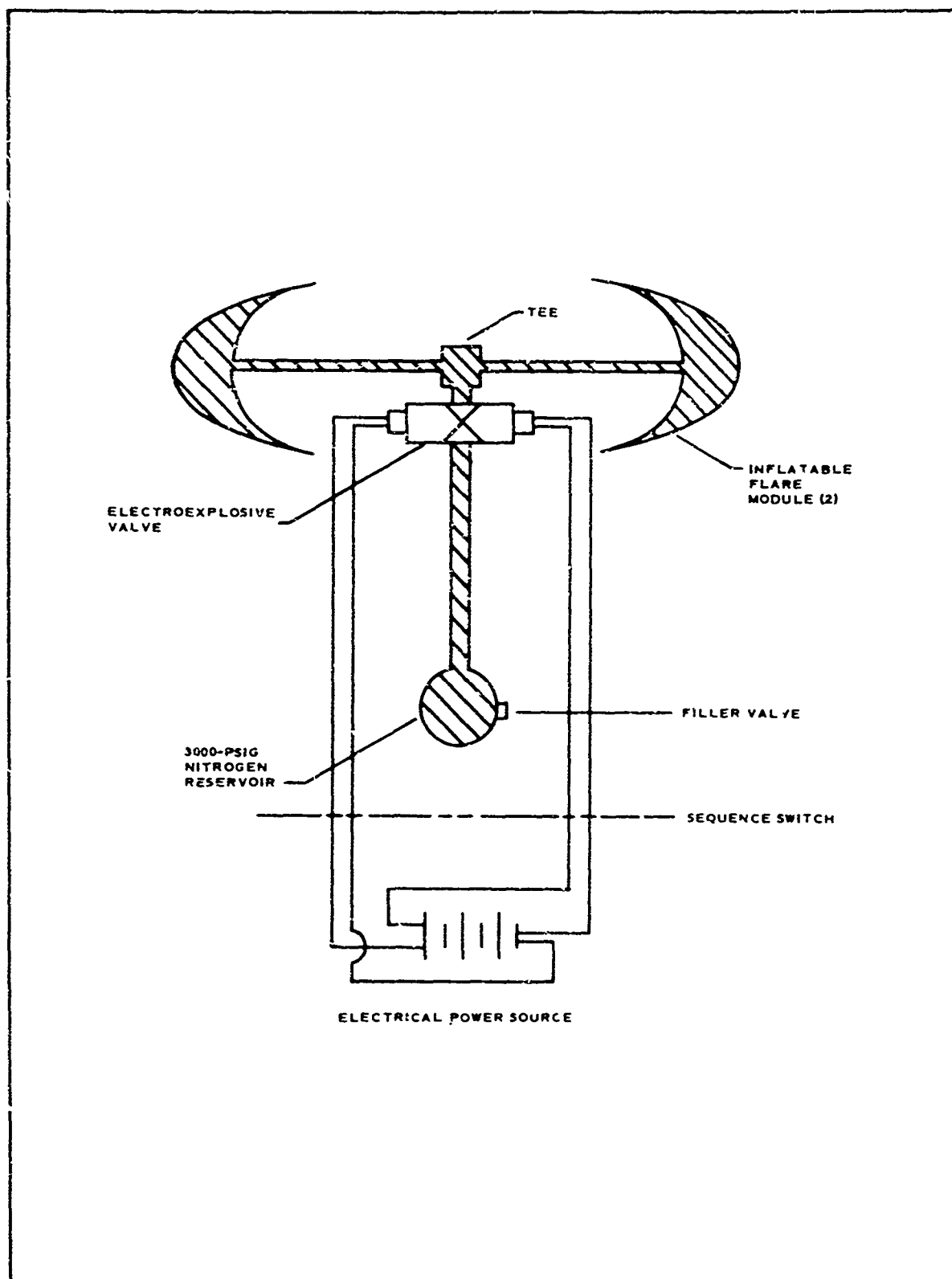


Figure 42 - Appendage Inflation System

If one considers very short time increments, then the weight of gas remaining in the storage vessel can be approximated by the following relationship:

$$W_B' = W_B - \Delta w, \quad (15)$$

while the change of weight of gas in the appendage is:

$$W_a' = W_a + \Delta w. \quad (16)$$

The new pressure in the storage vessel now may be calculated from the perfect gas law and the isentropic pressure-temperature relationship to yield the new pressure vessel gas properties.

The gas properties in the appendage volume then may be calculated on the basis of the weight of gas present. Using a heat balance between the weight of gas present and the weight of gas newly arriving, the temperature of the gas may be calculated from the following equation:

$$T_B = \frac{W_1 T_1 + W_2 T_2}{W_1 + W_2}. \quad (17)$$

The pressure in the bag also can be calculated using the perfect gas law.

If the inflation process is to take place over a short elapsed time period, it becomes quite evident that the process is highly transient. Thus, the analysis was conducted using a digitally computed iteration process. The results of the analysis particularly applicable to the appendage inflation process for the Arapaho C test vehicle are shown in Figure 43. The initial storage vessel gas properties were specified to be

$$p_1 = 3000 \text{ psi},$$

$$T_1 = 76 \text{ F},$$

and

$$V_1 = 4 \text{ cu in.},$$

while the receiver volume was estimated to be 1782 cu in. The gas to be used for inflation is nitrogen. The ratio of specific heats, n , remains to be identified. Based on experimental work conducted at Goodyear Aerospace on inflation systems of this type, this ratio n has been determined to approach 1.2 and was used in the analysis. The required pressure in the inflated appendage was specified by strength requirements to be 5.5 psi. The results of the analysis conducted for a series of orifice size diameters showed that this pressure may be attained quite readily from the storage vessel specified over elapsed time intervals from about 0.2 sec to about 4 sec. The orifice diameters vary from 5/32 to 1/32 in. for these elapsed times, respectively. The gas temperature in the appendage is quite cool and varies with the diameter of the orifice utilized.

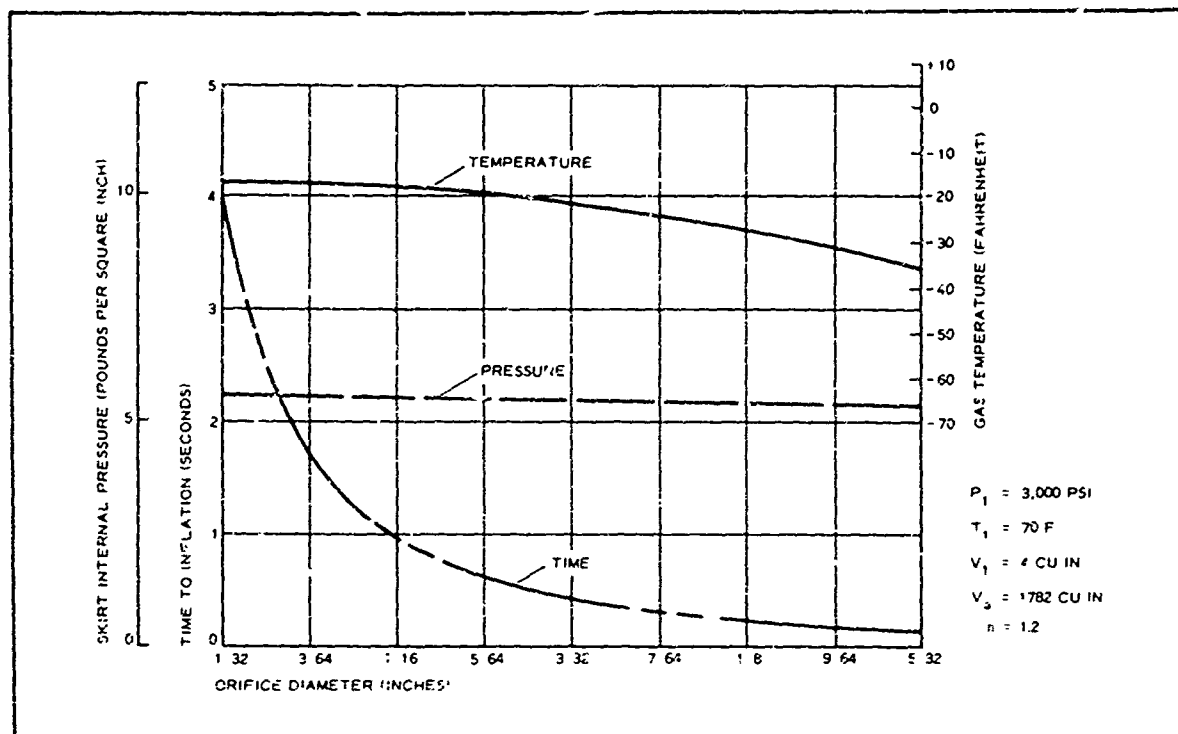


Figure 43 - EUREKA Appendage Inflation Parameters

The decrease in temperature of the gas in the appendage reflects directly the rapidly expanding gas in the storage vessel as the gas supply is depleted. From Figure 44, it appears to be feasible to inflate the appendage in the 0.3-sec time span specified in the subject contract by using an orifice diameter greater than 1/8 in.

h. Test Decelerator Deployment

(1) Variations in EUREKA Decelerator Deployment

The EUREKA test decelerator deployment differs from the Arapaho C test decelerator deployment. The difference is attributed to the special EUREKA considerations pertaining to the elliptical flare appendage. The Arapaho C test decelerator was deployed by using three thrusters to thrust the entire test decelerator container away from the test vehicle. This separation is shown in Figure 44. For the EUREKA, it was convenient to use the test decelerator container outer shell as the internal center member of the elliptical flare. The outer portion of the test decelerator container also is employed to stow the elliptical flare prior to inflation. Consequently, only the aft end of the EUREKA vehicle's test decelerator container is ejected in the EUREKA sequence. Only two thrusters are employed due to the decreased weight of the ejected parts. This decrease in weight of ejected parts can be related to the difference in weight between the Arapaho C test vehicle's decelerator container and the EUREKA vehicle's container end cap. Figure 45 depicts the EUREKA test item deployment.

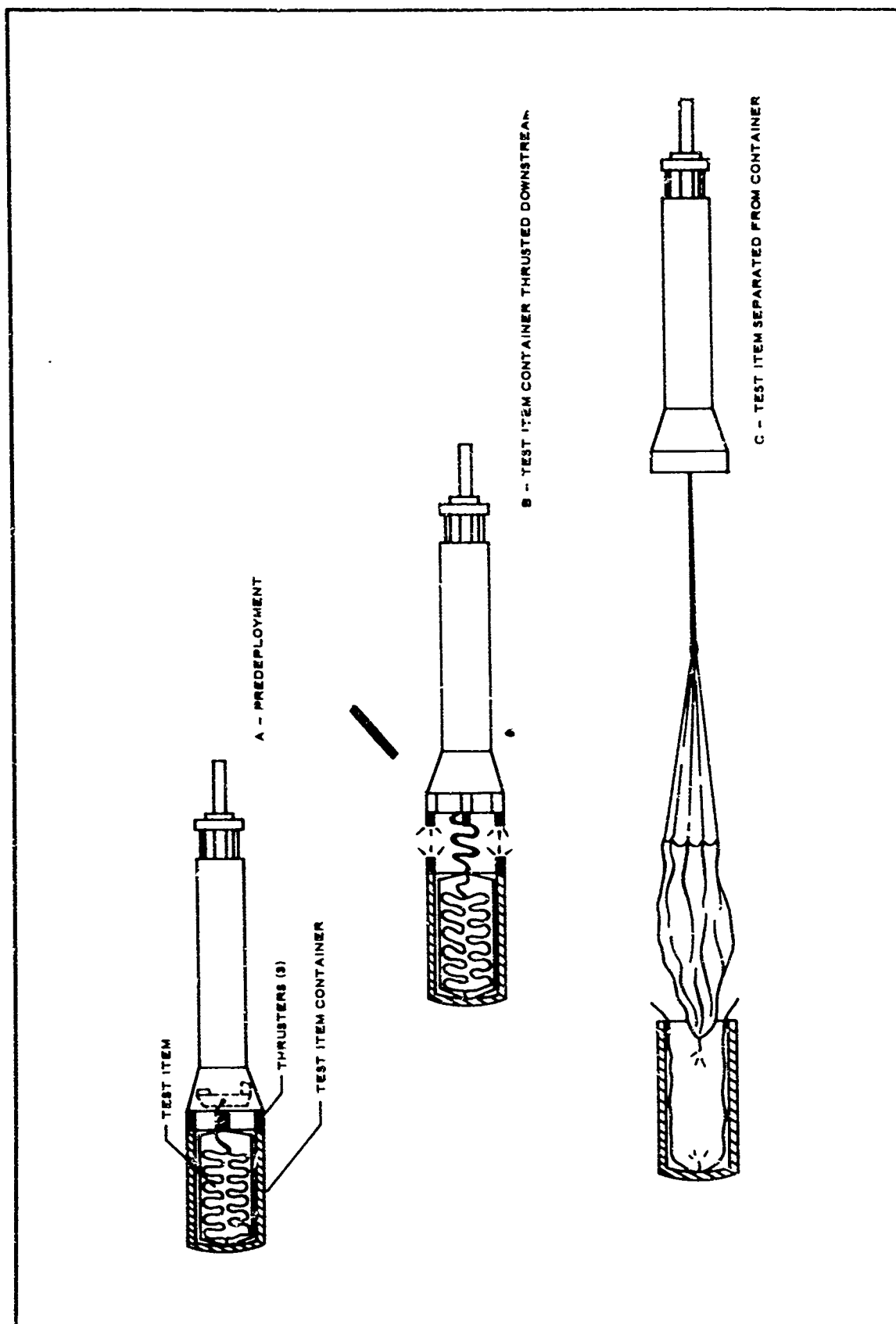


Figure 44 - Deployment of Basic Arapaho C Test Decelerator

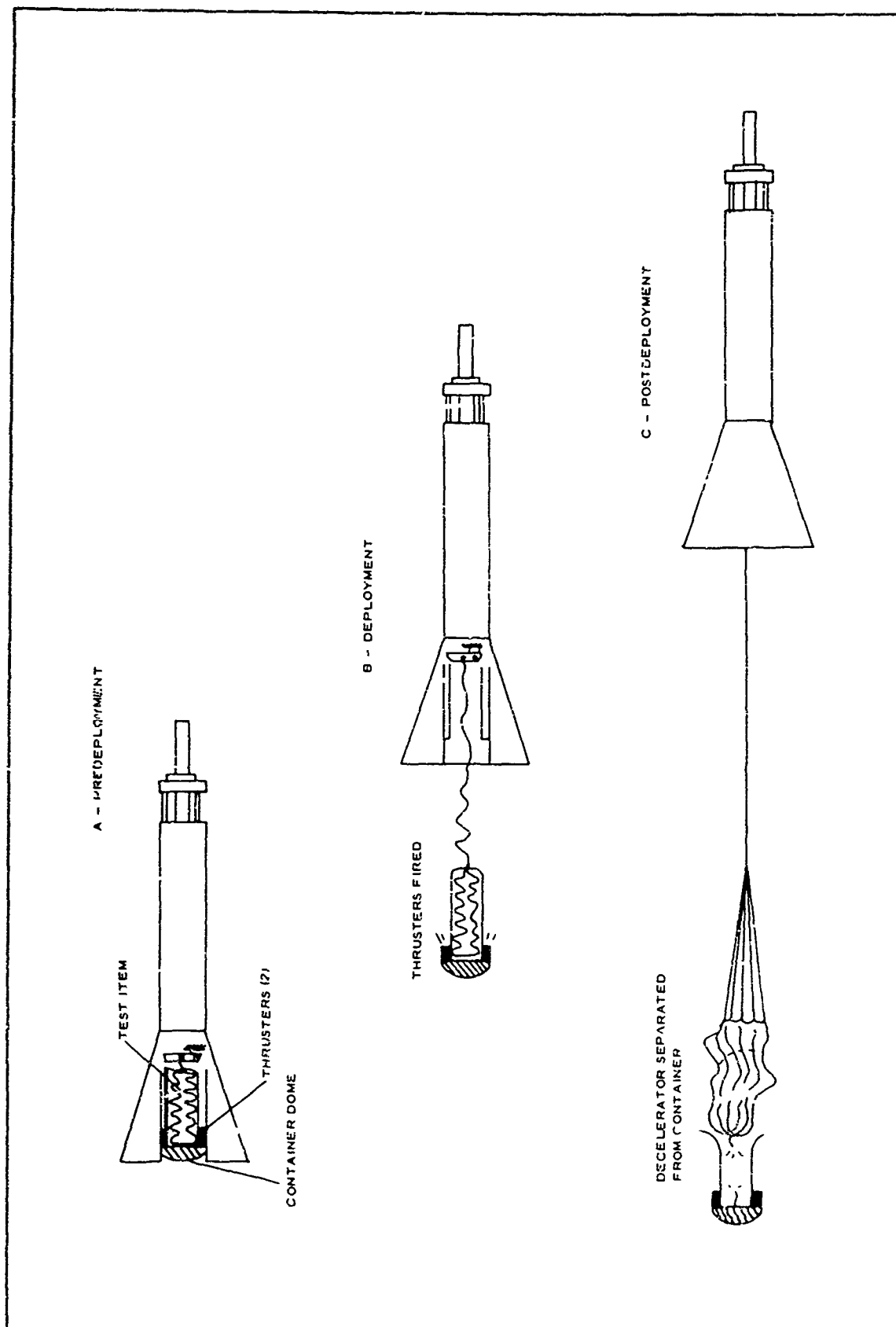


Figure 45 - Deployment of EUREKA Test Decelerator

(2) Alternate Methods for Test Item Deployment

In addition to the end cap thruster method for test item deployment, these alternates were considered:

1. Gas generator mortar
2. Drogue mortar
3. Ejection with three thrusters

The gas generator mortar method by which the test item would be blasted out was discarded because it will require a structure that interferes with subsequent deployment of the recovery parachute. The mortar also is not compatible with the present means for measuring shock and drag loads with the tensiometer.

The drogue method employs a mortared slug to pull out the test item. An intermediate drogue parachute that would be pulled out by the mortar slug may be required. The drogue parachute then would pull out the test item. This method was discarded because the weight of the mortar slug and its ejection mechanism approaches the weight and size of thrusters and the drogue parachute becomes a test item because it also has to operate in the test regime.

The use of three or more thrusters was discarded because as the quantity of thrusters increases, both the electrical circuit complexity and the input power requirements increase.

(3) Test Decelerator Deployment Calculations

To ensure that the decelerator is positively ejected from the test vehicle, additional energy must be imparted to the decelerator if the W/C_{DA} of the decelerator is greater than the W/C_{DA} of the vehicle (see Figure 46). At deployment, the W/C_{DA} of the decelerator was determined to be greater than the W/C_{DA} of the vehicle as follows:

$$\begin{aligned}\frac{W}{C_{DA}} (\text{vehicle}) &= \frac{405}{0.8 \times 2.86} \\ &= 177 \text{ psf ,}\end{aligned}$$

while

$$\begin{aligned}\frac{W}{C_{DA}} (\text{decelerator}) &= \frac{45}{0.1 \times 1.23} \\ &= 366 \text{ psf ,}\end{aligned}$$

using

$$\begin{aligned}F &= C_{DA} q A \\ &= ma ,\end{aligned}$$

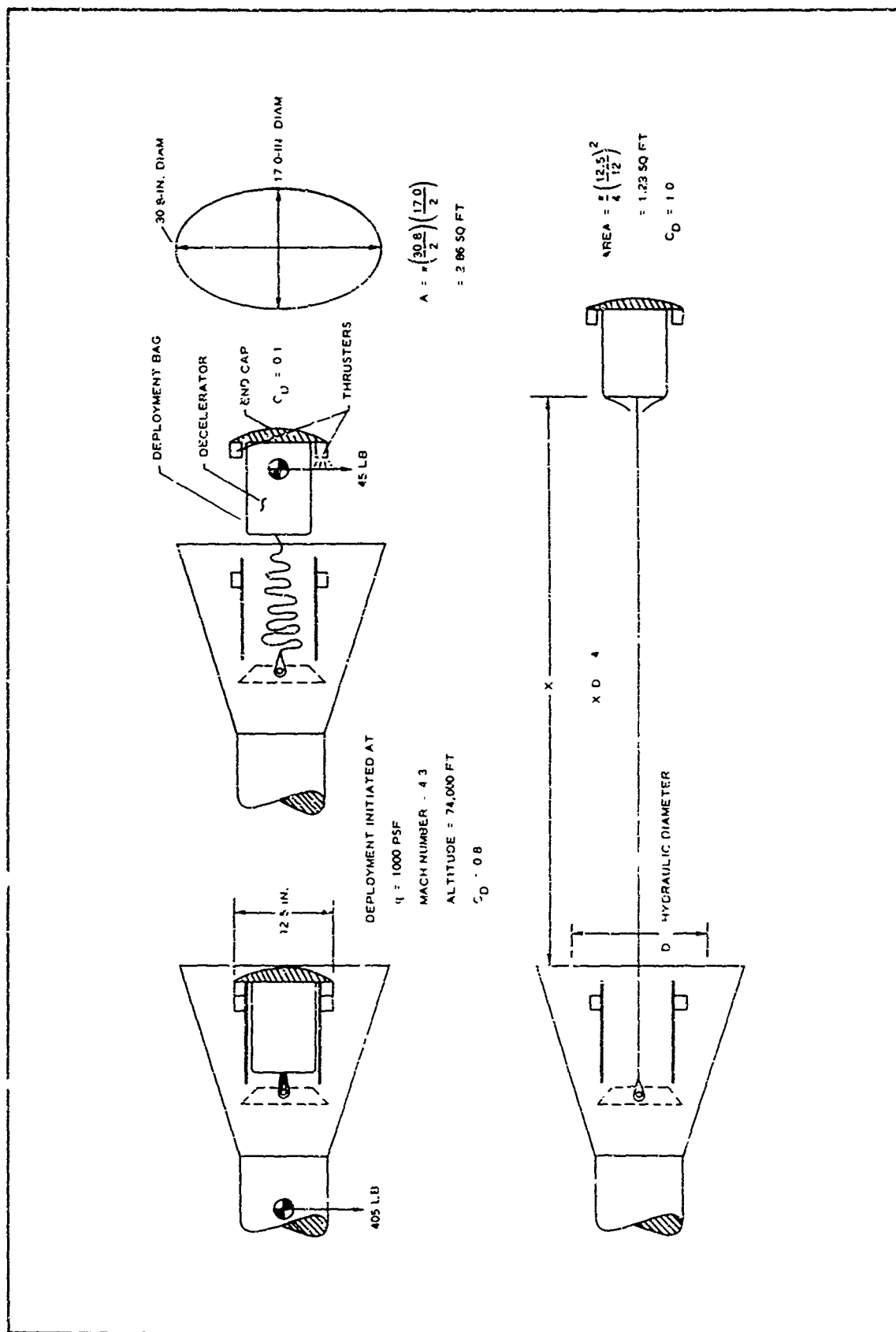


Figure 46 - Deployment Data

$$ma = C_D q A ,$$

$$(W/g)a = C_D q A ,$$

and

$$\begin{aligned} a/g &= C_D q A / W \\ &= q / (W / C_D A) . \end{aligned}$$

At deployment, the deceleration rates are:

$$\begin{aligned} \frac{a}{g} (\text{vehicle}) &= \frac{q}{\frac{W}{C_D A}} \\ &= \frac{1000}{173} \\ &= 5.65 \text{ g} ; \end{aligned}$$

$$\begin{aligned} \frac{a}{g} (\text{decelerator}) &= \frac{1000}{366} \\ &= 2.73 \text{ g} ; \end{aligned}$$

$$\begin{aligned} \Delta \frac{a}{g} &= 5.65 - 2.73 \\ &= 2.92 \text{ g} . \end{aligned}$$

Thrusters must impart initial velocity to the decelerator to overcome this differential of 2.92 g. Thrusters must act over a distance of $X/D = 4$ (where D = hydraulic diameter) to ensure that the decelerator package is aft of the base flow region of the wake. The hydraulic diameter is calculated by $D = \sqrt{4A/\pi}$. From Figure 82, the area of the elliptical base is 2.86 sq ft. The hydraulic diameter then is:

$$D = \sqrt{\frac{4(2.86)}{\pi}} = 1.91 \text{ ft} .$$

The total distance is then $X = 4D = 7.7 \text{ ft}$.

In calculating the energy required to overcome the 2.92-g differential for a distance of 7.7 ft, assuming that the vehicle is a stable platform, the initial velocity of the decelerator will be:

$$V^2 = 2 aX$$

$$\begin{aligned} V &= \sqrt{2 aX} \\ &= \sqrt{2(2.92)(32.2)(7.7)} \\ &= 37.4 \text{ fps.} \end{aligned}$$

The required kinetic energy input is:

$$K.E. = \frac{mV^2}{2} = \frac{45(37.4)^2}{32.2 \times 2} = 977 \text{ ft-lb.}$$

By applying a 100-percent margin of safety to ensure separation, then
K.E. = 1954 ft-lb.

Recalculating V for K.E. = 1954 ft-lb,

$$\begin{aligned} V &= \sqrt{\frac{2 K.E.}{m}} \\ &= \sqrt{\frac{2 \times 1954 \times 32.2}{45}} \\ &= 52.8 \text{ fps.} \end{aligned}$$

After the initial 7.7-ft separation, the decelerator package will be aft of the base flow region and is assumed to have a C_D equal to unity. At this time:

$$\begin{aligned} \left(\frac{\frac{q}{W}}{C_D A} \right)_{\text{decelerator}} &= \frac{1000}{45} \\ &= 27.3 \text{ g,} \end{aligned}$$

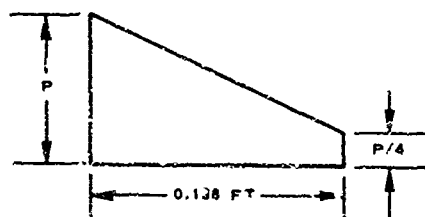
and

$$\begin{aligned} \left(\frac{\frac{q}{W}}{C_D A} \right)_{\text{vehicle}} &= \frac{1000}{405} \\ &= 5.65 \text{ g.} \end{aligned}$$

This difference in deceleration rates indicates that separation will be maintained.

As previously stated, this analysis was made assuming the vehicle to be a stable platform. An analysis of the system that takes into account any change in velocity of the test vehicle due to thruster firing would result in a kinetic energy input requirement slightly less than that obtained, assuming the vehicle to be a stable platform.

By using thrusters having a 2.25-in. (0.188-ft) stroke and assuming that the forces at the end of the stroke is one-fourth that at the start, the peak force required for the thrusters is:



$$E = \frac{5P}{8} \times 0.188 = 1954 \text{ ft-lb ,}$$

$$P = 16,620 \text{ lb .}$$

By using two thrusters, the peak force per thruster is 8310 lb. The strength of the shear pin for each thruster should also then be equal to 8310 lb to make certain that the required peak force has been generated within the thruster at the beginning of the thruster stroke.

i. Test Item Retention

The EUREKA vehicle has the requirement that the test item be retained, while the basic Arapaho C did not have this requirement. As a result, the Arapaho C released the parachute test items prior to recovery parachute deployment. The method employed to retain the test item must not interfere with subsequent deployment of the recovery parachute. Adequate clearance must be provided to ensure that the recovery parachute is not deployed into the test item canopy. The mode of retention shown in Figure 47 is that recommended for incorporation into the modified EUREKA test vehicle.

j. Vehicle Diameter

The maximum projected diameter of the existing Arapaho C vehicle was not exceeded in the preliminary design for the EUREKA program. The stowage area for the elliptical inflated flare, its actuation, and its erection hardware did not require an increase in maximum projected diameter.

k. Data Acquisition

(1) EUREKA Vehicle Capabilities

The EUREKA test vehicle retained the Arapaho C vehicle's capability for free-flight test data acquisition and transmission.

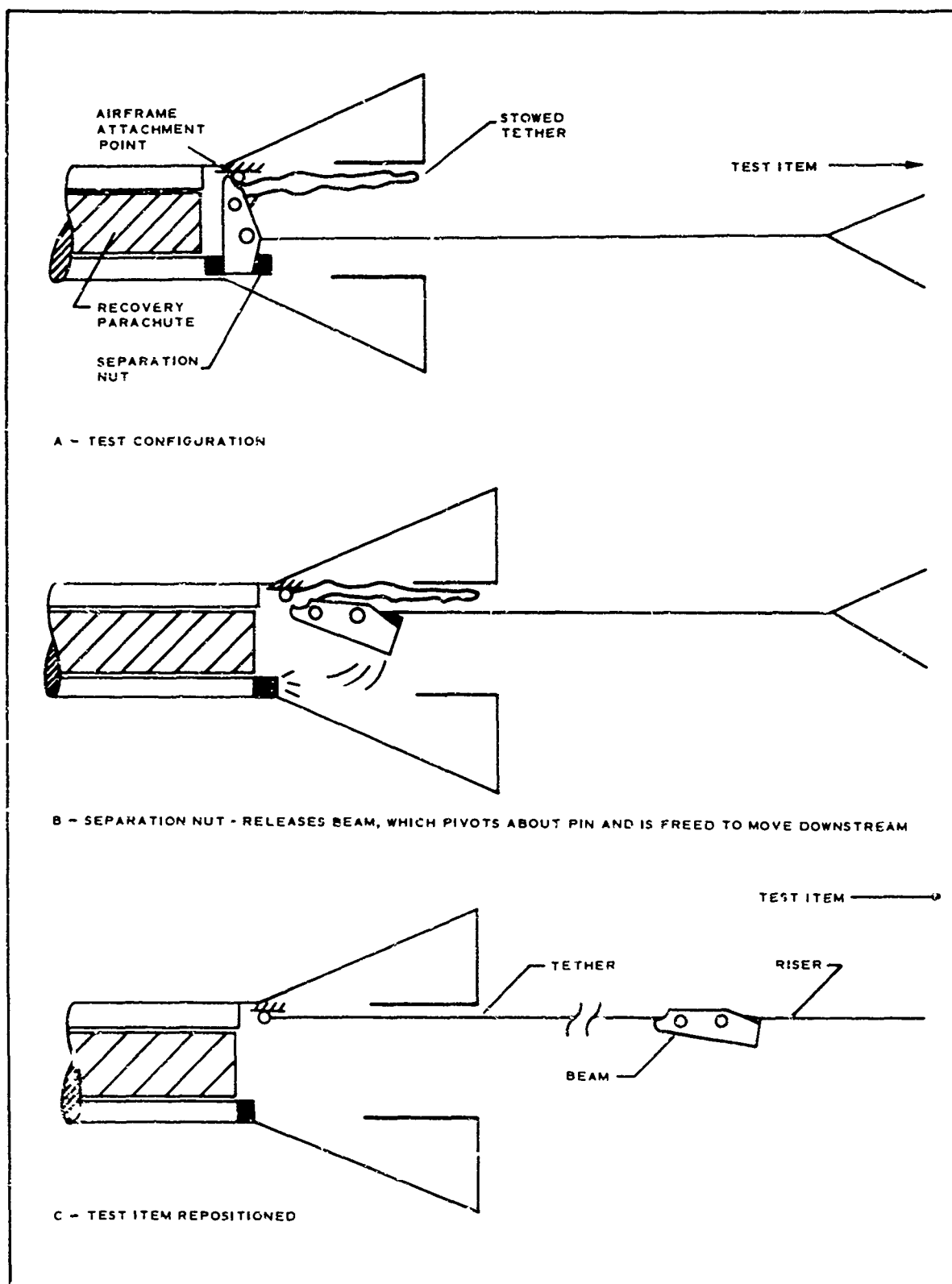


Figure 47 - Repositioning Sequence

(2) Telemetry Data

The Arapaho C vehicle telemetry system was retained for the EUREKA vehicle. Figure 48 represents a functional block diagram of the telemetry system. The system has seven information channels that provide continuous FM data. Tables IX and X list the data provided on each channel.

TABLE IX - FM/FM DATA

Data	Intermediate range instrumentation group, IRIG	Channel (KHz)	Voltage- controlled oscillator input voltage (mv)
100-KHz timing	11	7.35	0 to 20
Static pressure	12	10.50	0 to 20
Differential pressure	13	14.50	0 to 20
FM/PAM (see Table X)	14	22.00	0 to 20
Vehicle acceleration	15	30.00	0 to 20
Test item drag	16	40.00	0 to 20
Test item shock	18	70.00	0 to 20

Channel 14 provides 18 bits of information, each of which are commutated through on this IRIG channel. The information is listed in Table X.

(3) Radar Data

The vehicle has a C-band radar transponder to aid in tracking. Tracking radars will be used to determine the trajectory of the vehicle. Skin tracking will back up the beacon-tracking radar. Radar tracking will provide the following information:

1. Vehicle altitude versus time
2. Vehicle range versus time
3. Vehicle velocity

A block diagram of the vehicle's radar beacon system is shown in Figure 49.

(4) Photographic Data

The vehicle has two high-speed 16-mm cameras that provide color motion pictures of the test decelerator deployment, inflation, and operation.

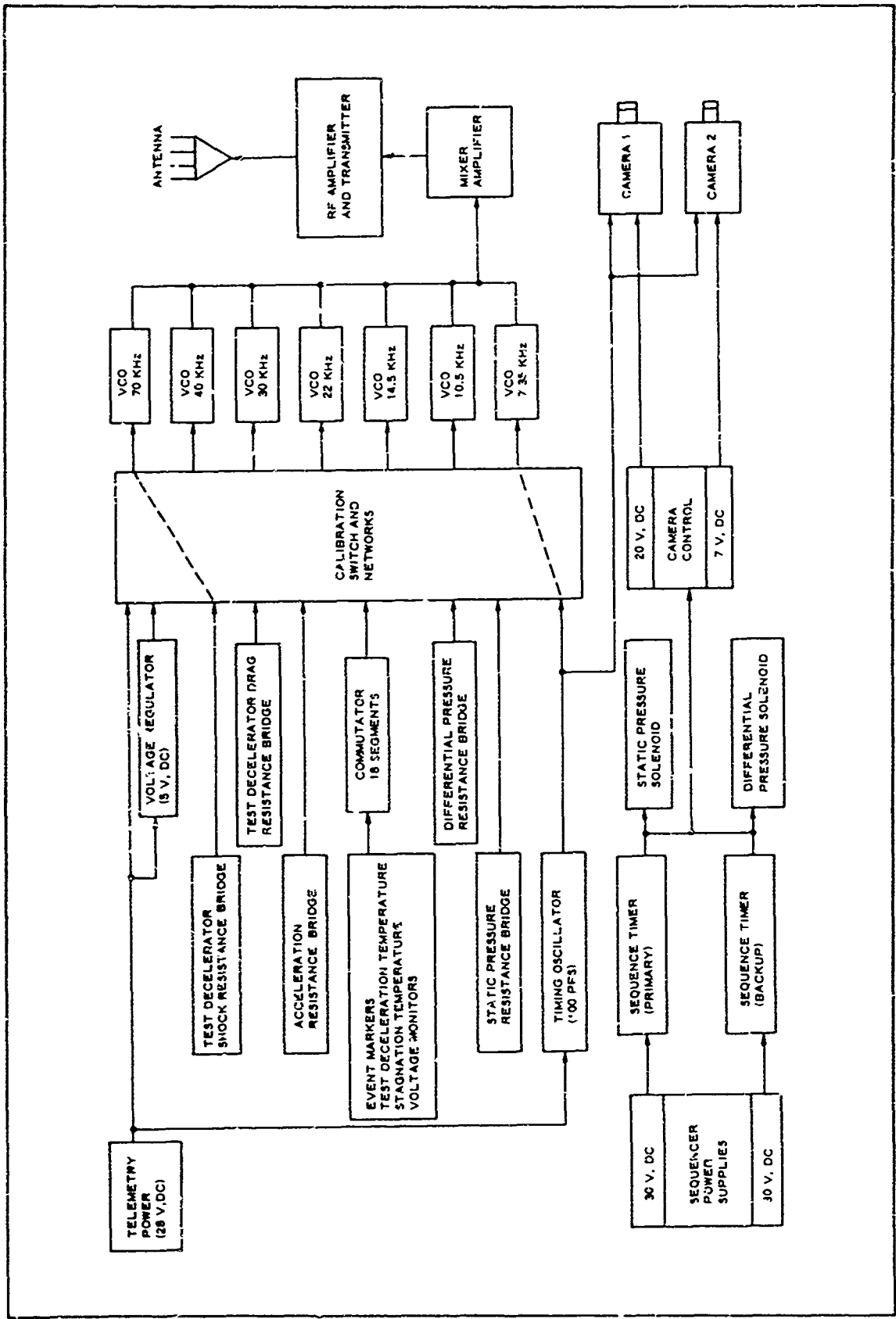


Figure 48 - Data Acquisition System

TABLE X - FM/PAM DATA (CHANNEL 22)

Segment	Function measured or monitored
1	Voltage monitor, 7-v, dc radar beacon
2	Voltage monitor, Sequence A
3	Thermocouple, nose
4	Voltage monitor, Sequence B
5	Thermocouple, test item
6	Current monitor, Sequence A
7	Thermocouple, test item
8	Current monitor, Sequence B
9	Thermocouple, test item
10	Ready to launch
11	Voltage monitor, 28 v, dc - telemetry
12	Event marker, probe jettison final stage separation
13	Event marker, recovery parachute test item deployment
14	Event marker, booster away
15	Thermocouple, test item
16	Thermocouple, test item
17	Sync pulse
18	Sync pulse

The cameras start one second prior to test item deployment and operate until 100 ft of film runs out. One camera runs at 200 frames per second for approximately 20 sec and the second camera runs at 700 frames per second for approximately 6 sec. The EUREKA vehicle can retain the same camera installation as used on the Arapaho C vehicle. The 16-mm motion picture cameras, manufactured by Photo-Sonics, Inc., are equipped with 13-mm f/3.5 lens. For the EUREKA, the field of view has been restricted by the inner core of the elliptical flare. Figure 50 illustrates the effect upon viewing the test decelerator. A four-foot-diameter test decelerator is shown deployed at an X/D of five calibers aft of the forebody.

1. Recovery

The preliminary designed EUREKA test vehicle will retain the same recovery system used on the Arapaho C vehicle. This system consists of a 9.35-ft D_0 recovery parachute, which is deployed at 11,000 ft, and an auxiliary flotation BALLUTE. The recovery parachute decelerates the vehicle to a velocity of 80 fps at water impact. Previous flight tests indicate that this recovery system may not be adequate for vehicle recovery

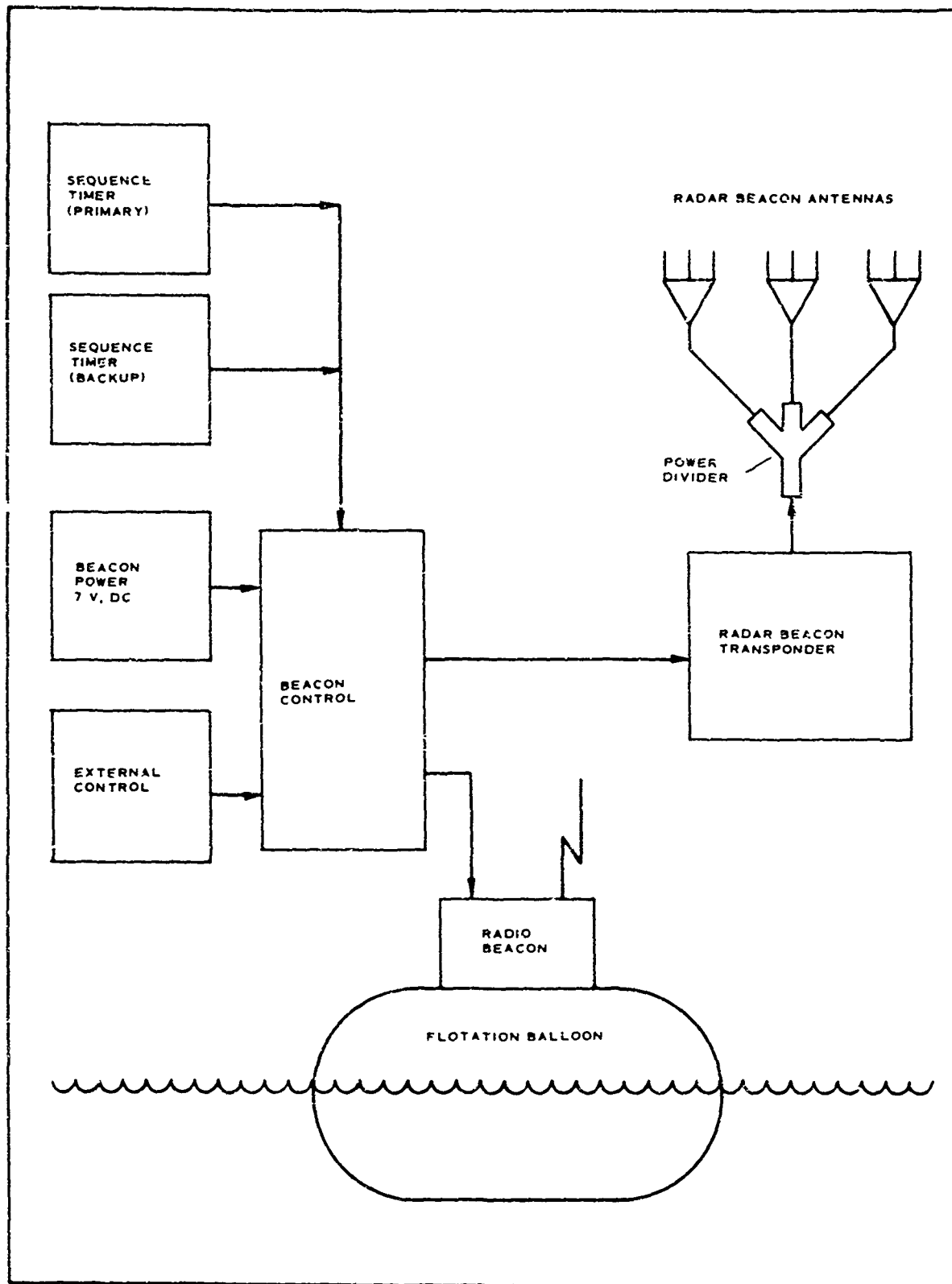


Figure 49 - Radar and Radio Beacon

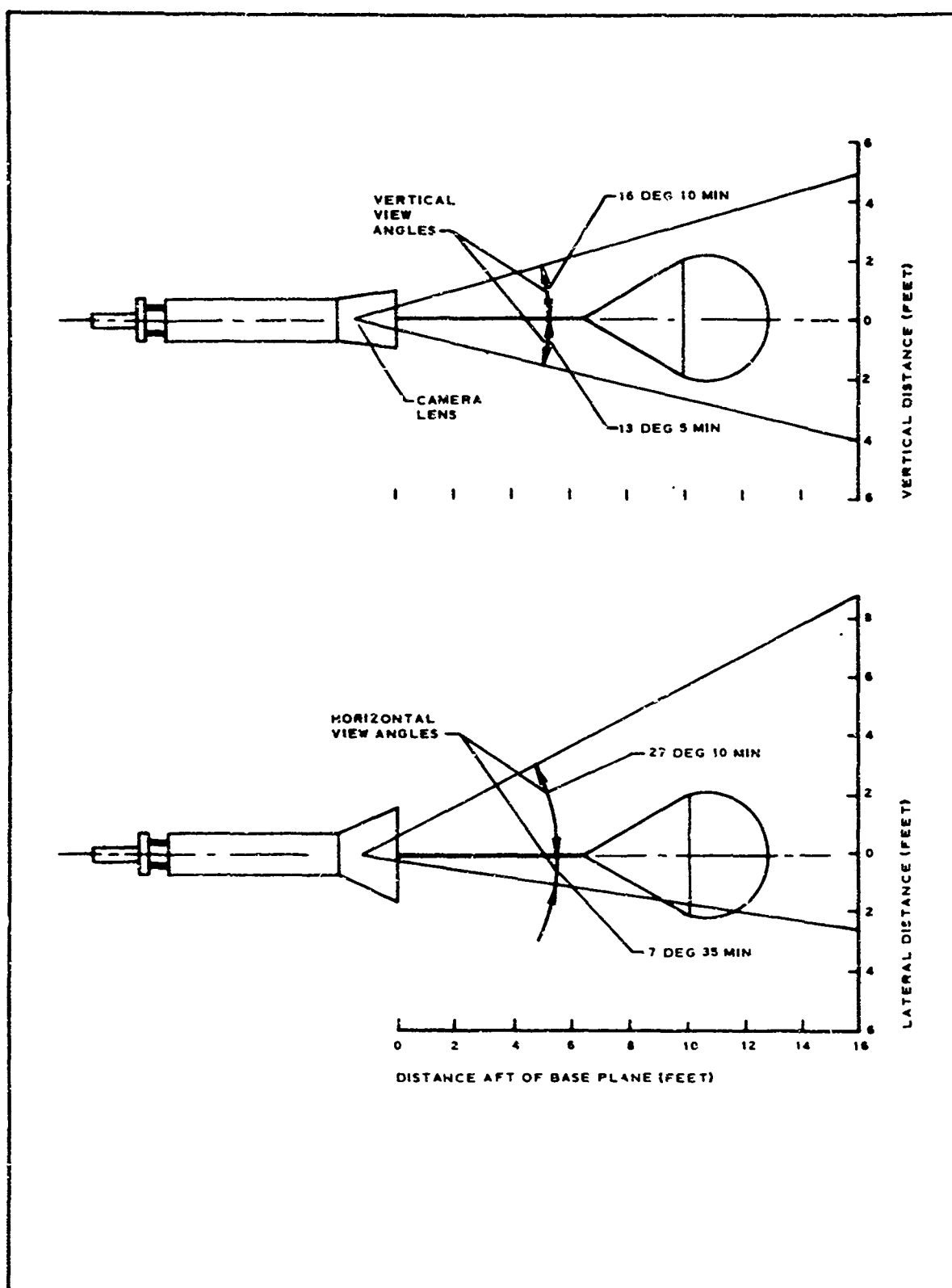


Figure 50 - EUREKA Flight Test Camera View Angles

in the high Mach number range of the test envelope. Redesign of the recovery system was not considered in the preliminary design investigation.

The main flotation system, which is activated by salt water batteries at water entry, has performed satisfactorily in previous flight tests and will be retained. The ultrasonic marker was removed for the preliminary design analysis. The marker, which was used for locating the vehicle in the event of flotation system failure, was attached directly to the tensiometer beam on the Arapaho C vehicle. This placement would not be suitable for the EUREKA configuration due to the possibility of damage during the test item repositioning sequence. The location of the marker will be dependent on the final design configuration. The addition of the marker upon finalization of the design does not appear to be a major problem area.

5. VEHICLE STRUCTURAL ANALYSIS

a. Stress Analysis

(1) General

The stress analysis of the recommended modified Arapaho C test vehicle covers loadings imposed by launching, ground handling, and test item deployment.

Figure 51 shows the modified sections in detail. Figure 52 is a compilation of loads imposed over the vehicle by a 100-g opening shock load produced by an imaginary test item acting through the tensiometer beam attached lug. This figure also portrays the limit shear and moment diagrams obtained from the aforementioned loading. Figure 53 shows the ultimate axial force and moment diagrams for the 100-g deceleration loading and the moment diagram for ground handling conditions. Previous test data indicate maximum recovery opening shocks in the order of 20 g's.

An estimate of the weight of components added to the test configuration of ADDPEP in arriving at the EUREKA configuration (to verify weight estimate used in load calculations) is given in Table XI.

The estimated weights and cg's for various stages are as follows:

<u>Stage</u>	<u>Weight</u>	<u>CG station</u>	<u>X_{cg}/d</u>
Launch	509*	47.3	N. A.
	487.97	47.46	
Despin	443.1*	52.9	5.16
Fairing off	416.47 [†]	53.7	5.08
Cover off	390.2	59.1	4.59
Test item out	389.97	56.44	4.84

* Based on 45-lb test item.

[†] 20-lb test item.

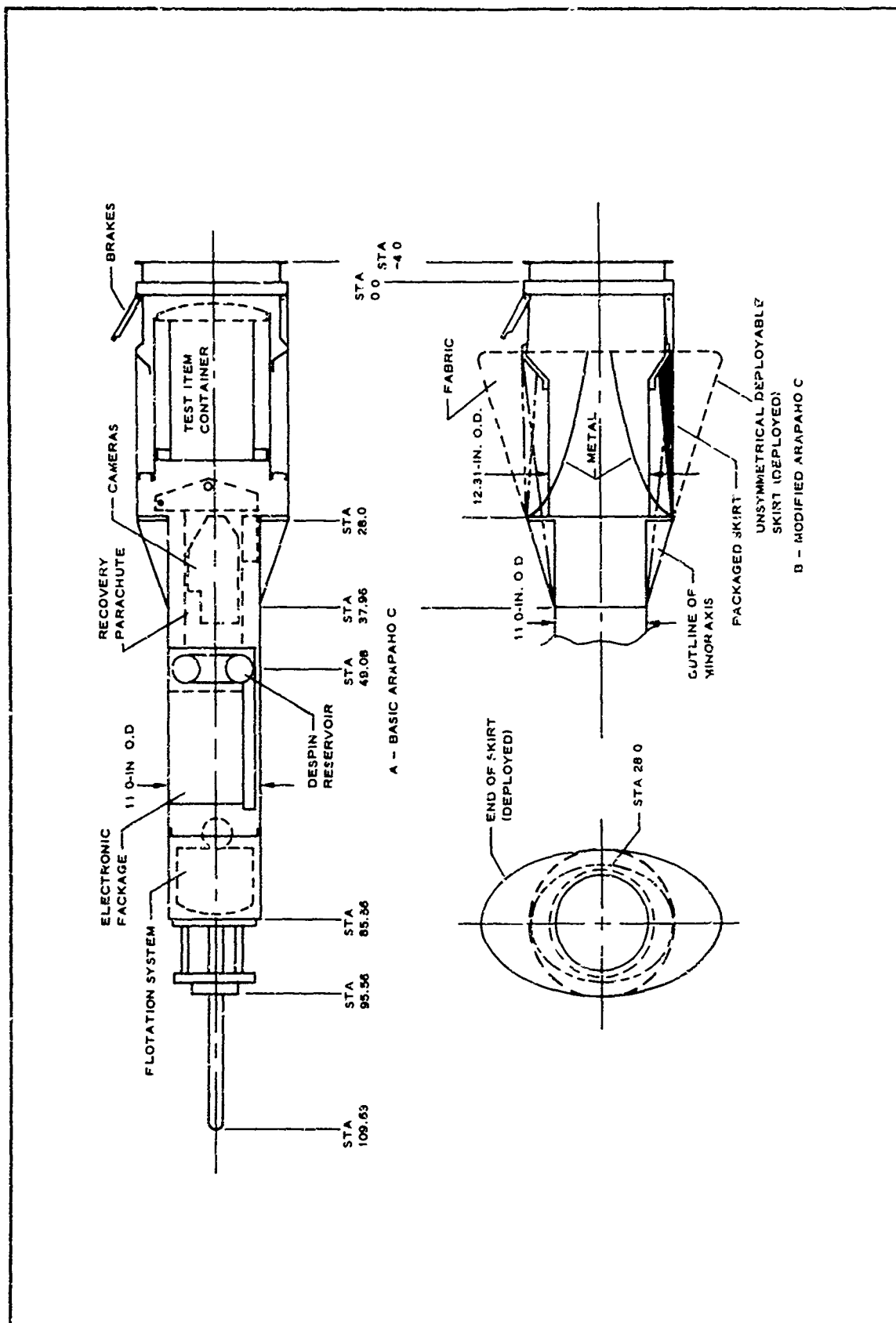
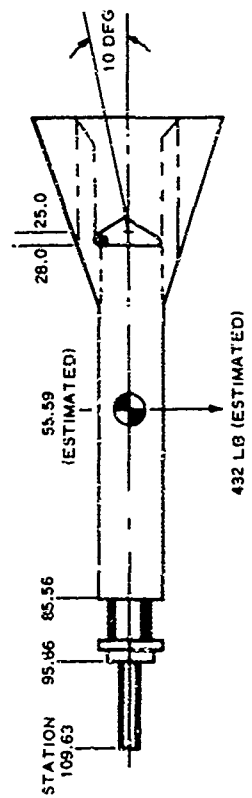


Figure 51 - Profile of Modified Arapaho C Test Vehicle

2

ESTIMATED TEST ITEM OPENING SHOCK OF 100 G'S = 43,200 LB (LIMIT)



ITEM	STATION											
	14.00	27.41	33.95	46.33	56.5	66.00	76.00	83.50	89.50	93.50	102.81	
W	60	41.2	53.6	58	22.4	46	34.4	43.3	10	27	30	
X	-41.59	-28.18	-21.64	-7.26	2.31	10.41	20.41	27.91	32.91	37.91	47.22	
Y W	1042	731	931	1007	493	799	597	752	174	469	521	
$\left(\frac{\pi}{386}\right)^{1/2} W$	1712	796	796	209	-57	-328	-482	-829	-228	-702	-972	
$W \sqrt{\left(\frac{g}{386}\right)^{1/2} W}$	2754	1527	1727	1236	436	471	115	-77	-52	-233	-451	

$T_{CG} = 43,200 \sin 10 \text{ DEG} (55.59 - 25.0) = 229,474 \text{ LB-IN.}; a = \frac{T}{I} = 264.8 \text{ RAD/SEC}^2$
 $I = \sum \frac{WX^2}{386} = 866.5 \text{ LB-IN.-SEC}^2; \eta = 100 \text{ G'S} \times \sin 10 \text{ DEG} = 17.365$

STATION (IN.)	LIMIT MOMENT (IN.-LB)	LIMIT SHEAR (LB)
102.81	0	-451
93.50	4,199	-684

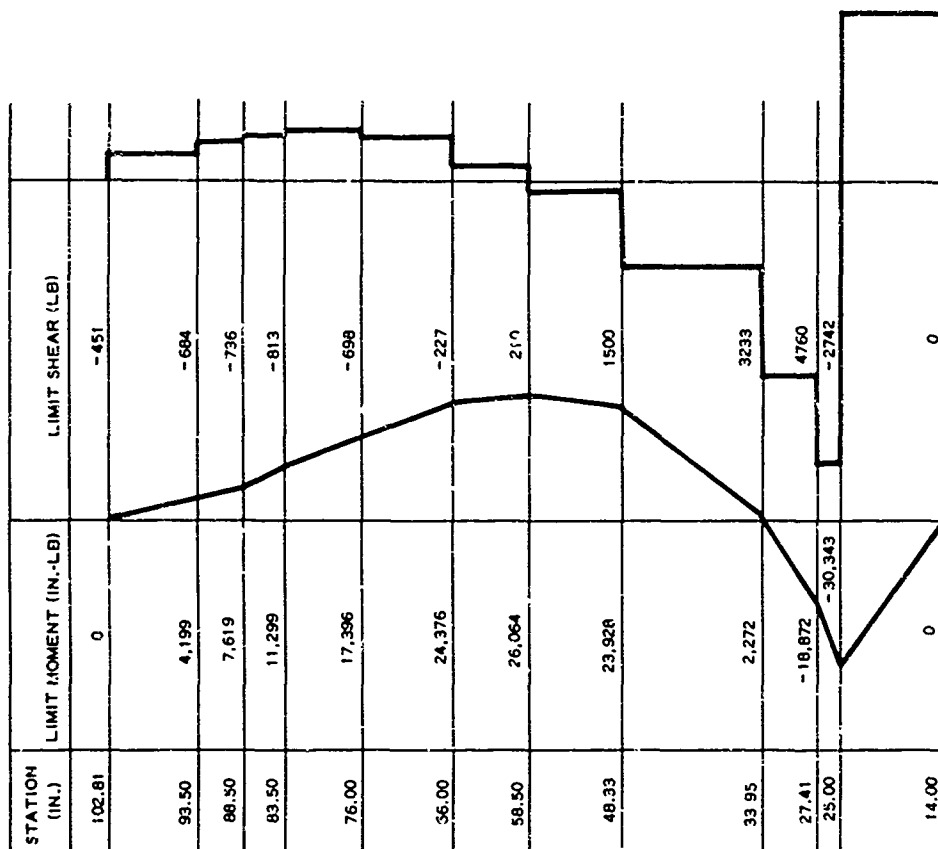


Figure 52 - Opening Shock Loading Characteristics

(Reverse is blank)

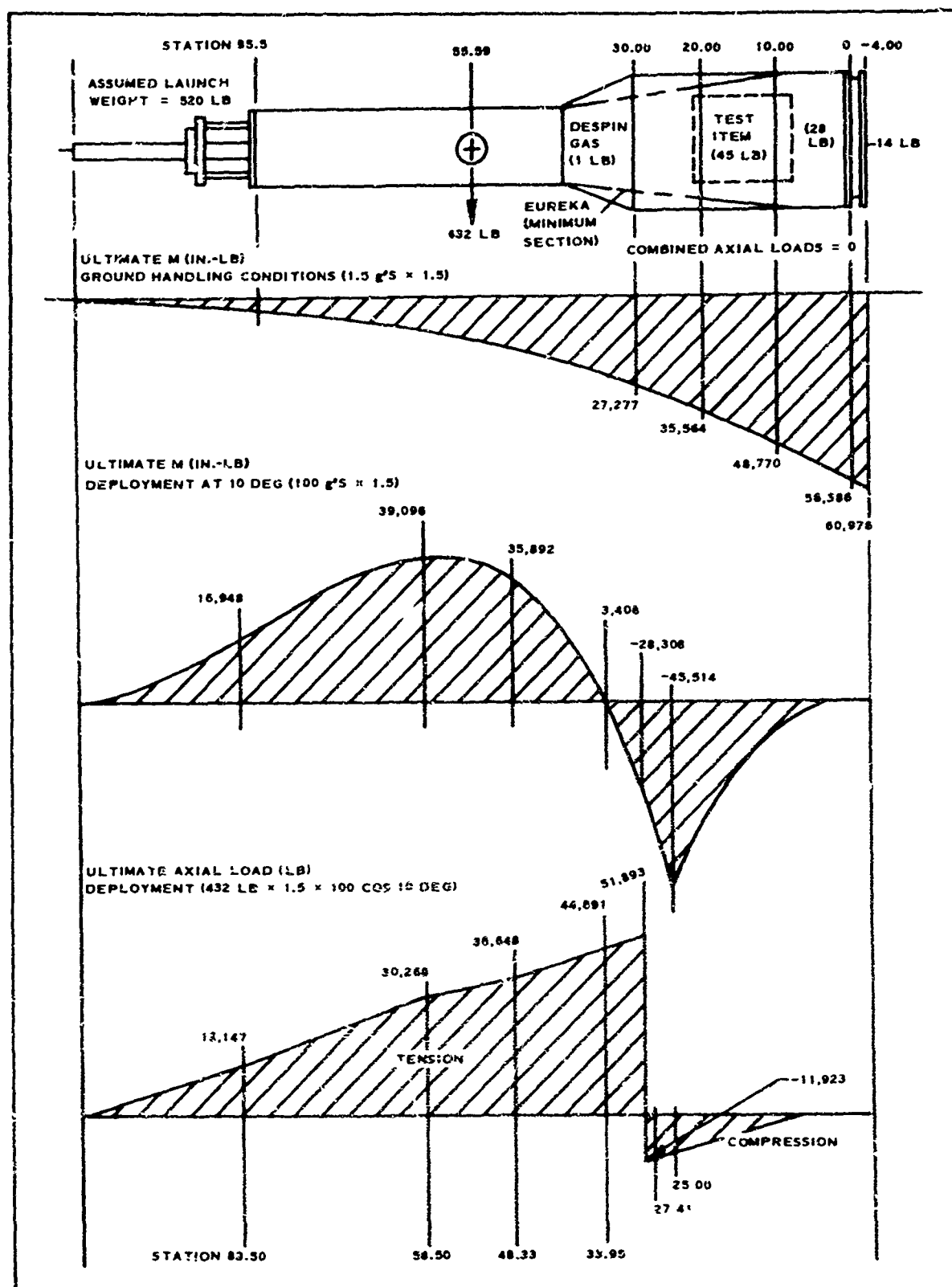


Figure 53 - Loads on Modified Arapaho C Test Vehicle

TABLE XI - WEIGHT ESTIMATE FOR STRESS CHECK

Item (size)	Weight (lb)	Station (in.)	WX (in. -lb)
Test configuration			
ADDPEP test (test configuration)	372.0	62.31	23,179.3
Inner shell (12-3/8-in. O.D. and 3/16 -in. thick by 20-in. length)	15.4*	17.10	263.3
Aft ring (12-3/8-in. I.D., 17.32-in. O.D., 3/16-in. thick)	7.8	8.50	66.3
Thrusters (two units plus mounting)	1.9	8.10	15.4
New bulkhead (decreased weight only)	-14.4	31.70	-456.5
Forward ablation (remove)	-9.9	31.00	-306.9
Bulkheads and skin (1/16-in. thick)	11.2	21.50	240.8
Printed circuit boards (move aft)	0	. . .	-48.0
Riser cable extension	1.8	20.00	36.0
Coated fabric plus attachments and stiffeners	2.9	14.40	41.7
Inflation bottle and lines	<u>1.5</u>	<u>22.00</u>	<u>33.0</u>
	390.2*	59.10	23,064.4
Launch configuration			
Net ablation (added weight)	22.9	23.30	510.7
Compartment lid	4.8	6.00	28.8
Thrusters plus attachment	3.1	6.10	18.9
Test item and bag	45.0	13.10	327.5
Separation ring	28.0	3.40	95.2
Adapter	14.0	-2.00	-28.0
Despin gas	<u>1.0</u>	<u>49.00</u>	<u>49.0</u>
	509.0	47.30	24,066.5

*The estimated weight of 432 lb used for load calculation was quite conservative. The weight reduction was primarily due to reduced bulkhead weight at Station 28, due to utilization of a better load path and the decision to jettison the ablation cone.

(2) Boost Loads

The maximum vertical launch load, assuming 40 g's acceleration and a factor of safety of 1.5, was calculated to be:

$$\text{Axial Force, } F_A = 520 \times 40 \times 1.5 = 31,200 \text{ lb.}$$

The loading of the 40-deg flange at the aft end of the test item container is shown in Figure 54.

At the forward end of the flange, the load per inch will be:

$$F/\text{in.} = \frac{F_A}{\pi d} = \frac{31,200}{12\pi} = 828 \text{ lb/in.}$$

At the aft end of the flange,

$$F/\text{in.} = \frac{31,200}{17\pi} = 584 \text{ lb/in.}$$

Checking the welds at the forward end of the flange of shear loads and assuming that the shear thickness of the weld is equal to the thickness of the flange material, the shear stress is:

$$f_s = \frac{P}{A} = \frac{828}{(2 \times 0.1875)} = 2210 \text{ psi.}$$

Therefore, the margin of safety for the flange is high. Considering the forces acting in the forward attachment ring, the axial force acting on the conical section tends to expand the section due to the Poisson effect. This expansion produces tensile stresses in the attachment ring. Assuming the attachment ring produces the only resisting force to stop this expansion, the tensile stress in the ring may be determined by equating the expansion of the conical section and the attachment ring. From Reference 6, the expansion in the conical section is constant throughout the section and can be evaluated from the equation:

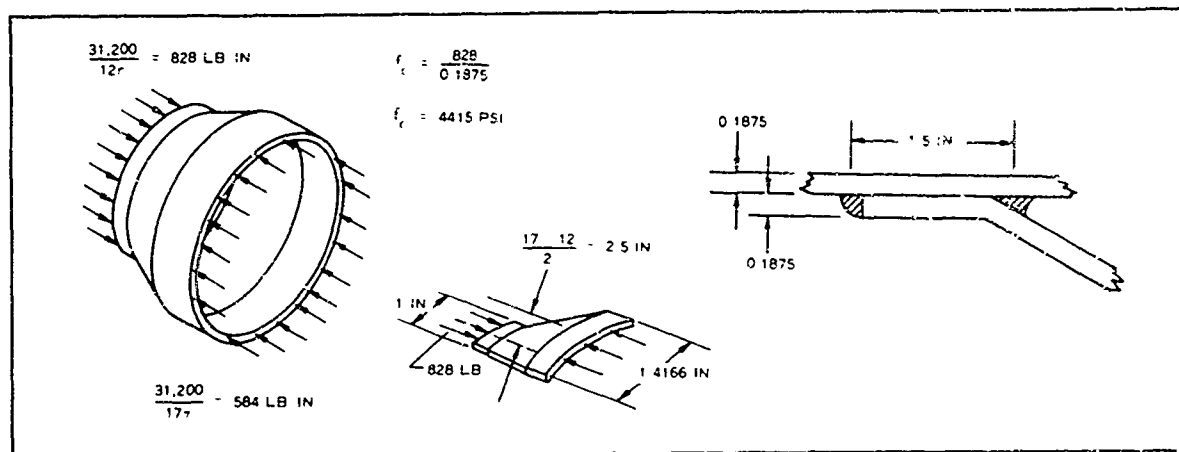


Figure 54 - Test Item Container Aft Flange Loading (Boost Conditions)

$$\Delta r = \frac{\mu F_A}{2\pi E_y t \cos \theta}$$

The expansion in the attachment ring is obtained by.

$$\Delta r = \text{strain} \times \text{radius} = \frac{fr}{E_y}$$

By equating the expansion and solving for the stress in the attachment ring,

$$f = \frac{\mu F_A}{2\pi r t \cos \theta} = \frac{(0.33)(31,200)}{2\pi(6)(0.1875)(0.766)} = 1902 \text{ psi.}$$

Therefore, the margin of safety is high.

Stresses at the aft end of the flange will be less due to the larger radius. The maximum load in the conical section of the flange will then occur at the forward end and will be equal to:

$$\frac{828}{\cos 40 \text{ deg}} = 1081 \text{ lb/in.}$$

Thus,

$$f_c = \frac{1081}{0.1875} = 5765 \text{ psi.}$$

Therefore, the margin of safety is high.

The severity of launch loads could be increased by considering wind shear and nonvertical launch loads. The wind-shear loads were found to be very low and therefore were not considered in this analysis. The limiting case for nonvertical launch loads would be a horizontal launch. As a conservative estimate, the vertical launch loads were combined with the ground handling loads and evaluated at the forward end of the aft flange.

From Figure 54,

$$M_{\max} = 48,770 \text{ in. -lb (ultimate).}$$

For a circular tube in bending,

$$f_{\max} = \frac{Mr}{I} = \frac{Mr}{\frac{\pi r^3}{2}}$$

therefore,

$$f_{\max} = \frac{M}{\pi r^2 t}$$

The maximum load per inch is then:

$$F_{\max}/\text{in.} = \frac{M}{\pi r^2}.$$

By adding the axial force loading,

$$F_{\max}/\text{in.} = \left(\frac{F_A}{2\pi r} \right) + \left(\frac{M}{\pi r^2} \right).$$

In considering the combination of boost and ground handling loads,

$$F_{\max}/\text{in.} = \frac{31,200}{2(6)\pi} + \frac{48,770}{\pi(6)^2} = 828 + 431 = 1259 \text{ lb/in.}$$

The most critical load is the load along the conical section, which then will be:

$$\frac{1259}{\cos 40 \text{ deg}} = 1640 \text{ lb/in.}$$

The stress in the conical section is then,

$$f_c = \frac{1640}{0.1875} = 8750 \text{ psi.}$$

Therefore, the margin of safety is high.

(3) Decelerator Deployment Loads

Considering the decelerator deployment shock loads, the critical portion is the attachment required for the splice at Station 28 of the tube with a 12.31-in. O. D. and a 0.312-in. wall thickness, therefore:

$$\text{Shear diameter} = 12.31 - 0.312 \approx 12 \text{ in.}$$

Using the ultimate critical loads and moments from Figure 54, the load at the maximum stress point will be:

$$F_{\max}/\text{in.} = \frac{P}{2\pi r} + \frac{M}{\pi r^2} = \frac{51,893}{2\pi(6)} + \frac{45,514}{\pi(6)^2} = 1376 + 402 = 1778 \text{ lb/in.}$$

Two rows of 24 rivets (1/4 A17ST) per row have an allowable load of

$$\frac{2 \times 1550}{12\left(\frac{\pi}{24}\right)} = 1974 \text{ lb/in. (ultimate).}$$

Thus,

$$\text{M. S.} = \frac{1974}{1778} - 1 = 0.11.$$

The critical loading in the tensiometer beam will be imposed by the test item opening shock. The shear and moment diagrams for the beam under these conditions is shown in Figure 55. The stress analysis of the beam is shown in Figures 55 and 56. The critical loading on the beam support fitting also will be imposed by the test item opening shock. The shear and moment diagrams and stress analysis for the beam support fitting are shown in Figure 57. The beam support fitting also is used to tether the recovery parachute riser line. The load imposed by the recovery parachute opening shock will not be as severe as the loads imposed by the test item opening shock.

The test item container cover was analyzed for two loading conditions. The first condition considered the load imposed by acceleration at launch and is shown in Figure 58. The second condition considered loads imposed during test item thruster firing. For test item deployment based on the estimated energy available in the powder charge (one-half the amount used in each of the three thrusters for the ADDPEP C vehicle), each thruster was assumed capable of a 10,000-lb thrust load for design. The stress analysis for this loading condition is shown in Figure 59.

The results of the stress analyses presented in this section indicate that structural integrity will be maintained in the modified vehicle.

b. Mass Properties Data

The calculated weight and balance data for the EUREKA vehicle are presented on Tables XII through XV. These weights differ slightly from the estimated weights used for the stress analysis. The stress analysis estimated weights are greater and therefore conservative.

One of the design requirements is that the vehicle weight at initiation of test deceleration deployment shall be less than 450 lb. The calculated weight indicates the vehicle weight will be 416.47 lb, which is well below the specified limit.

6. INFLATABLE APPENDAGE DESIGN

a. Design Considerations

The basic design task from which the inflatable flare assembly evolved had a variety of complications due to geometric constraints and the severe environment to which the inflated flare would be exposed during high Mach number, low-altitude flights. The basic objective of the appendage design effort was to develop a inflatable unit that would duplicate, as nearly as practically possible, the aerodynamic geometry of the flare tested in the WT-IIA wake survey series. Results of this wake survey test showed that the flare simulated the wake of the "target" blunted elliptical cone vehicle. In the deflated state, the flare was to be packageable in a minimal available volume that could not be enlarged by extending the external geometry of the test vehicle's launch configuration.

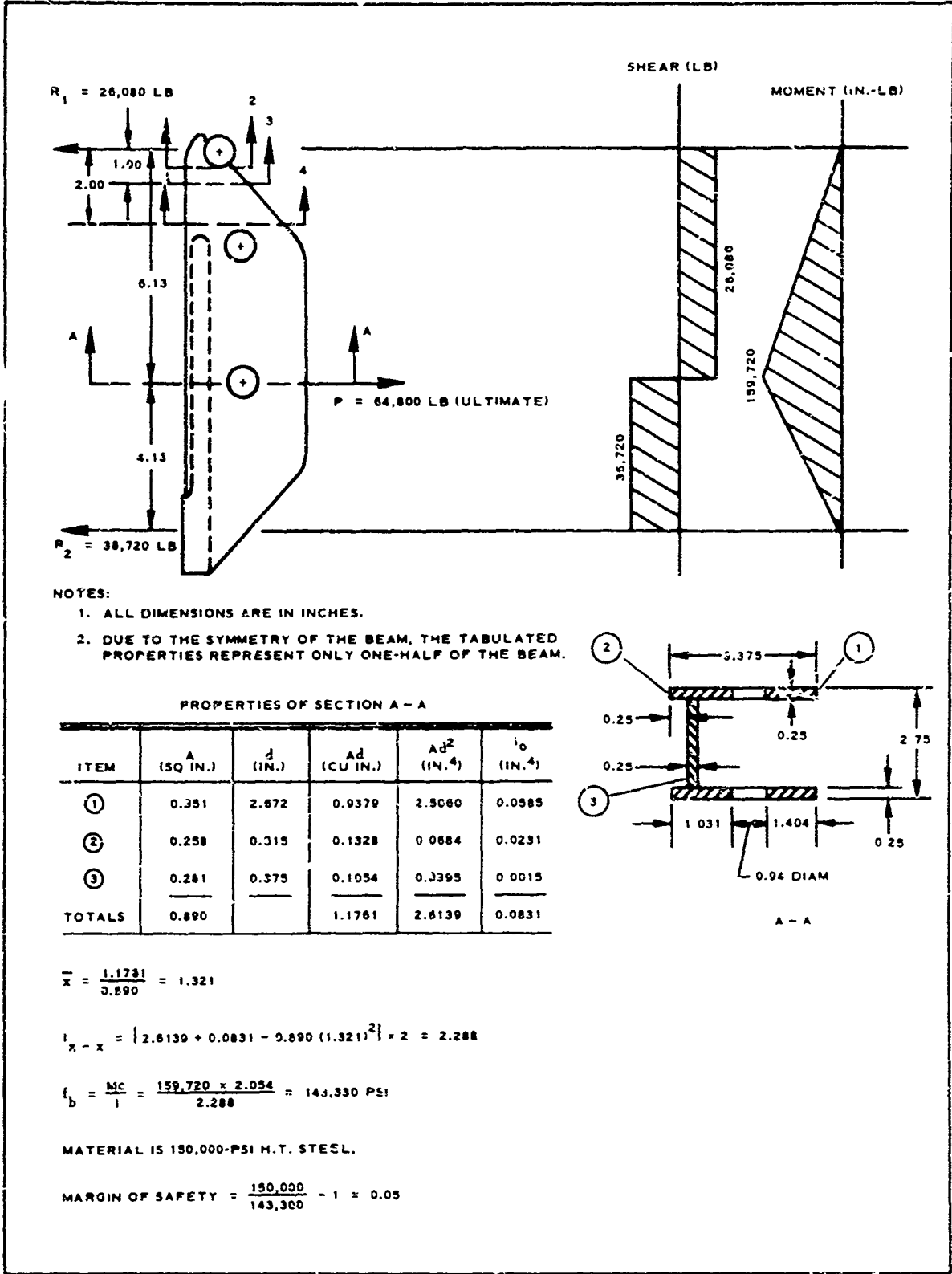


Figure 55 - Tensiometer Beam Stress Analysis (Section A-A)

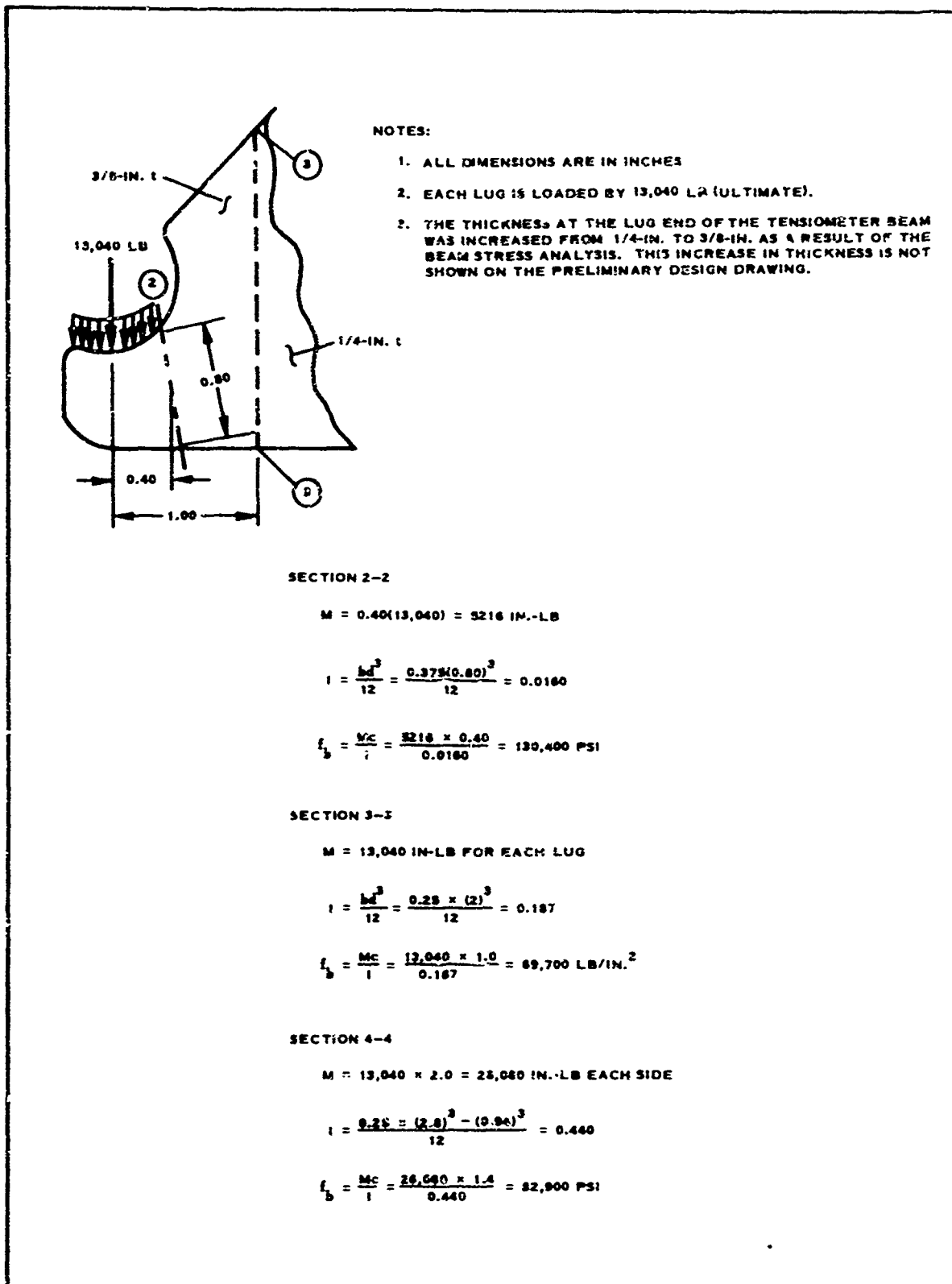


Figure 56 - Tensiometer Beam Stress Analysis (Sections 2-2, 3-3, and 4-4)

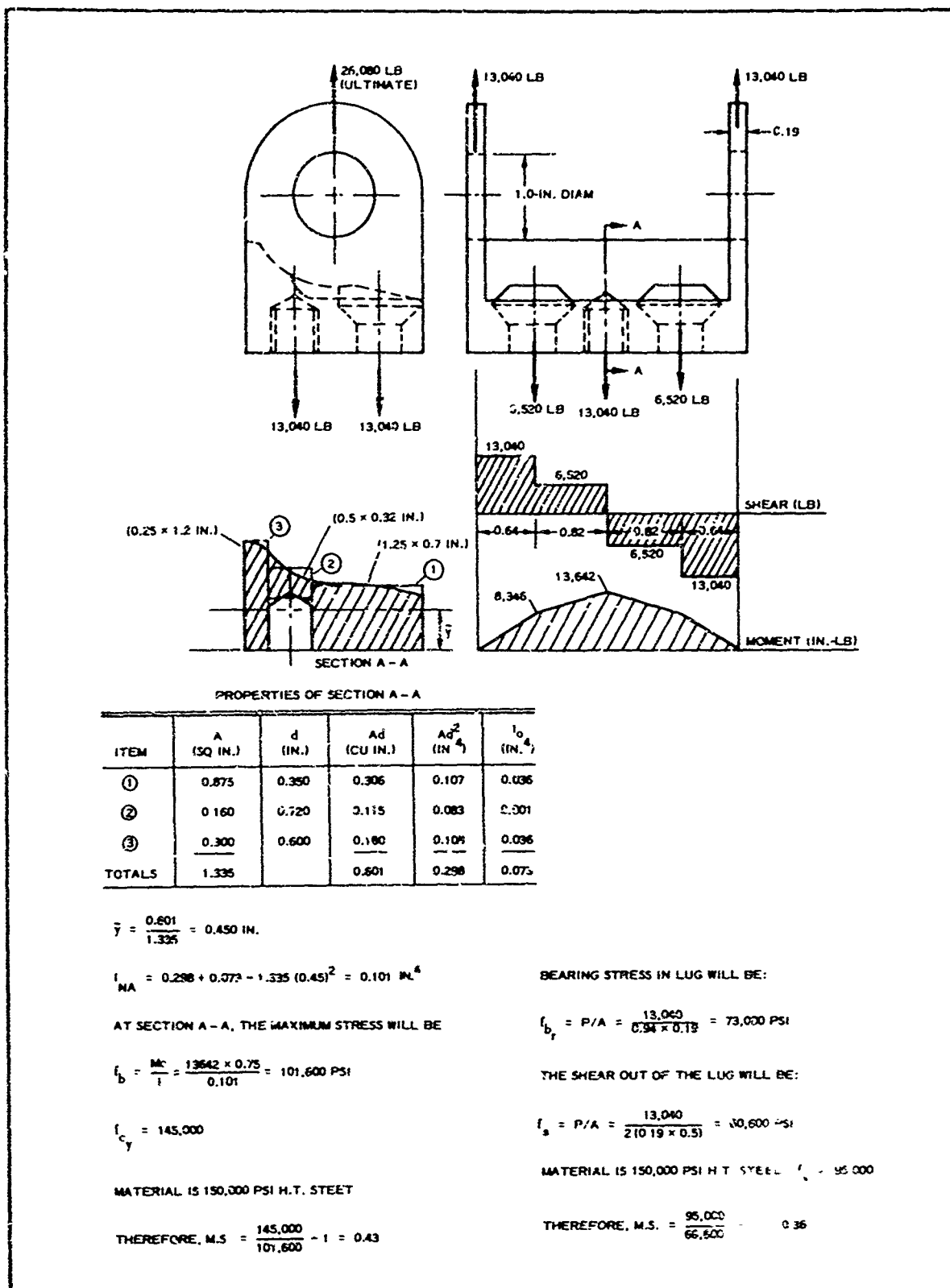
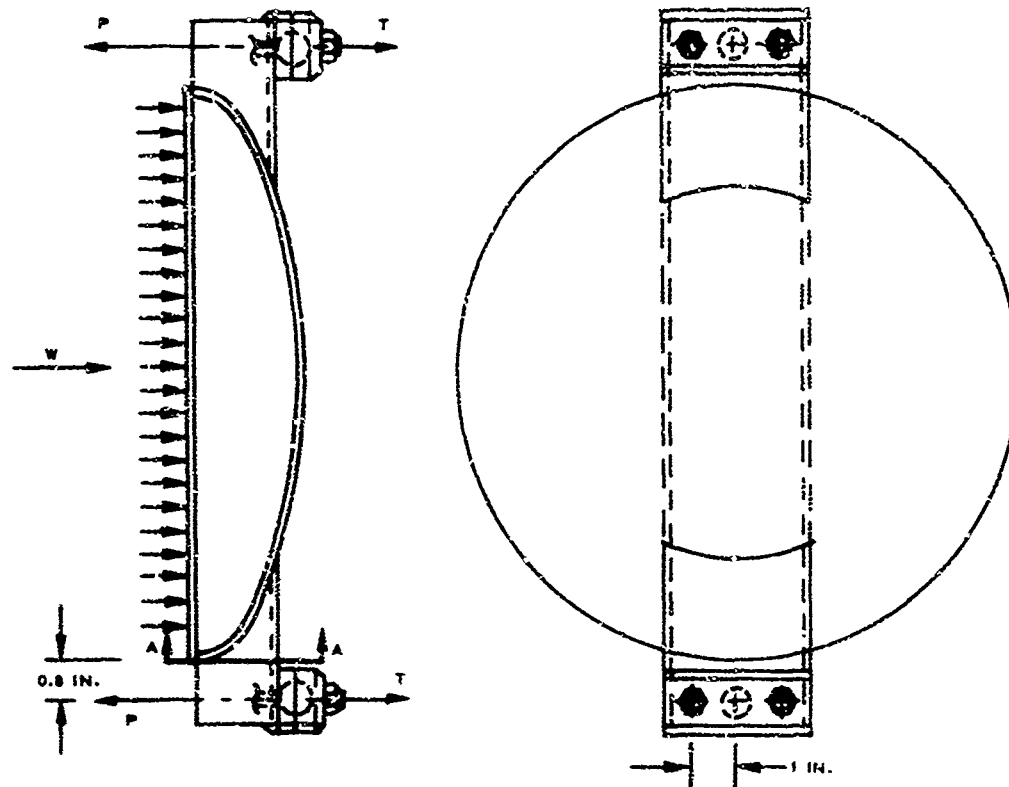


Figure 57 - Beam Support Fitting Stress Analysis



MAXIMUM ACCELERATION = $42 \text{ G'S} \times 1.5 = 63 \text{ G'S (ULTIMATE)}$
 ESTIMATED WEIGHT OF COVER = 5 LB
 ESTIMATED WEIGHT OF TEST ITEM = 45 LB (HIGHLY CONSERVATIVE)
 THRUSTER PISTONS = $\frac{3 \text{ LB}}{53 \text{ LB (TOTAL)}}$

ULTIMATE LOAD ON THRUSTER SHEAR PINS
 (TWO IN DOUBLE SHEAR) = $53 \text{ LB} \times 63 \text{ G'S} = 3339 \text{ LB (ULTIMATE)}$

DOUBLE SHEAR STRENGTH OF ONE PIN (7/32 - 1020 STEEL) = 2630 LB

THEREFORE, M.S. = $\frac{2630}{3339} - 1 = 0.57$

Figure 58 - Test Item Container Cover Stress Analysis
(Launch Conditions)

ANALYSIS OF THRUSTER RETAINER (HEADER BLOCK)
SECTION PROPERTIES AT C

ITEM	SIZE (IN.)	A (SQ IN.)	d (IN.)	Ad (CU IN.)	Ad ² (IN ⁴)	I _u (IN ⁴)
① (HEADER BLOCK)	5.8 × 1-1/4	0.7812	0.3125	0.2441	0.0763	0.0254
② (CHAMFER)	1/4 × 1/4	-0.0625	0.500	-0.0312	-0.0156	-0.0003
③ (HALF CIRCLE)	3/4	-0.2209	0.1592	-0.0352	-0.0056	-0.0022
TOTALS		0.4978		0.1777	0.0551	0.0229

$$\bar{y} = \frac{0.1777}{0.4978} = 0.357$$

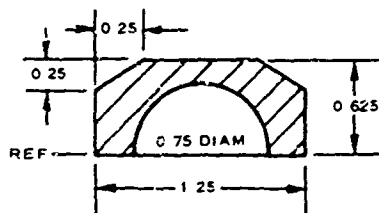
$$I_{NA} = 0.0551 + 0.0229 - 0.4978(0.357)^2 = 0.0146 \text{ IN}^4$$

$$\text{BENDING MOMENT} = 1 \text{ IN} \times 5000 \text{ LB} = 5000 \text{ IN-LB}$$

$$f_b = \frac{Mc}{I} = \frac{5000 \times 0.357}{0.0146} = 122,300 \text{ PSI}$$

MATERIAL IS 150,000 PSI H.T. STEEL

$$\text{THEREFORE, M.S.} = \frac{150,000}{122,300} - 1 = 0.23$$



ANALYSIS OF GUSSET SUPPORT FOR THRUSTER ATTACHMENT
SECTION PROPERTIES

ITEM	A (SQ IN.)	d (IN.)	Ad (CU IN.)	Ad ² (IN ⁴)	I _u (IN ⁴)
①	0.380	0.095	0.0361	0.0034	0.0011
②	0.688	1.095	0.7534	0.8250	0.0108
TOTALS	1.068		0.7895	0.8284	0.0119

$$\bar{y} = \frac{0.6113}{0.973} = 0.739$$

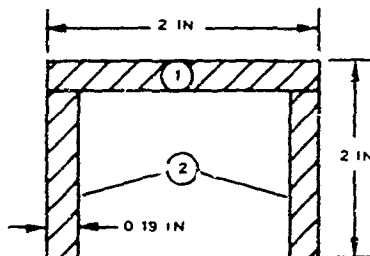
$$I_{NA} = 0.8284 + 0.0119 - 1.068(0.739)^2 = 0.2651 \text{ IN}^4$$

$$\text{BENDING MOMENT} = 0.8 \text{ IN} \times 10,000 \text{ LB} = 8,000 \text{ IN-LB}$$

$$f_b = \frac{Mc}{I} = \frac{8,000 \times 1.261}{0.2651} = 38,000 \text{ PSI}$$

MATERIAL IS 6061-T6 ALUMINUM

$$\text{THEREFORE, M.S.} = \frac{42,000}{38,000} - 1 = 0.11$$



SECTION A - A (FROM FIGURE 59)

Figure 59 - Test Item Container Cover Stress Analysis
(Test Item Deployment)

TABLE XII - EUREKA FLIGHT VEHICLE WEIGHT/BALANCE
VARIATION WITH PROGRAMMED SEQUENCING

Item	Weight (lb, calculated)	\bar{x} (in.)	M_x (in. -lb)
Launch configuration	487.47	47.46	23,134.5
Less booster adapter	-14.00	-2.00	+28.0
Less deceleration brake	-28.00	3.38	-94.6
Booster separation	445.47	51.78	23,067.9
Less despin gas	-1.00	49.08	-49.1
Test vehicle despin	444.47	51.79	23,018.8
Jettison flare cover and thrusters	-28.00	. . .	-655.4
Appendage inflation	416.47	53.70	22,363.4
Less test item	-20.00	15.00	-300.0
Less container dome	-6.50	8.00	-52.0
Decelerator test	389.97	56.44	22,011.4
Less tensiometer beam	-7.38	25.20	-208.5
Less tether	-0.70	19.50	-13.7
Reposition test item	381.89	57.06	21,789.2
Less recovery parachute	-7.98	34.44	-274.8
Recovery parachute deployed	373.91	57.54	21,514.4
Less probe assembly	-74.61	90.3	-6,737.3
Terminal descent	299.30	49.37	14,777.1
Less flotation canister	-5.60	81.78	-458.0
Flotation	293.70	48.75	14,319.1

TABLE XIII - WEIGHT AND BALANCE COMPARISON OF
BASIC C AND MODIFIED C

Item	W (lb)	\bar{x} (in.)	M_x (in. -lb)
EUREKA (launch configuration)	487.47	47.46	23,134.5
Basic C (launch configuration)	537.20	46.15	24,791.8
Items removed	-213.91	. . .	-4,003.9
Items added	164.18	. . .	2,346.6

TABLE XIV - WEIGHT/BALANCE SUMMARY (ITEMS REMOVED IN REDESIGN)

Part number	Item	W (lb)	\bar{x} (in.)	M_x (in.-lb)
530A002-011	Test item + container (45-lb test item)	-87.10	14.24	-1240.3
. . .	Retro rocket compartment	-44.20	-1.22	+53.9
. . .	Lance booster adapter section	-14.00	-8.7	+121.8
596-7327-101	Beam assembly	-4.82	25.8	-124.4
596-7342	Adapter ring	-11.93	26.0	-310.2
596-7355	Bulkhead	-6.20	27.3	-169.3
596-7323	Flare assembly	-14.71	32.9	-484.0
596-7564-103	Thrusters (3)	-7.59	25.2	-191.3
A37PS	Ultrasonic marker	-1.40	22.3	-31.2
596-7332	Hinge bracket	-1.40	26.2	-36.7
530A002-082	Beam latch assembly	-0.26	24.9	-6.5
530A002-188-3	Bolt and nut (MS20364-1216)	-0.63	26.2	-16.5
M479-1/596-7195	Switch and nut (relocate)	-0.50	25.7	-12.9
PT07A22555	Connector (relocate)	-0.15	25.7	-3.9
121EN27-2	Switch (relocate)	-0.15	25.0	-3.8
1337-5	Battery	(Included in marker)		
530A002-207	Fitting	-2.32	26.2	-60.8
530A002-188-1	Bolt and nut (AN364-1216)	-0.48	26.2	-12.6
. . .	Ballast to simulate nose cone	-16.07	9.18	-1475.2
	Total	-213.91		-4003.9

TABLE XV - WEIGHT/BALANCE SUMMARY,
ITEMS ADDED IN REDESIGN

Part number	Item	W (lb)	\bar{x} (in.)	M_x (in. -lb)
M479-1	Switch and nut	0.50	44.2	22.1
PT07A22-55S	Connector and bracket	0.15	44.2	6.6
121EN27-2	Switch	0.15	7.0	1.1
580A030	Beam	7.38	25.2	186.0
580A030	Beam hinge bracket	2.56	25.7	65.8
580A030	Aft ring container support	7.68	8.7	66.8
580A030	Test container shell	15.75	17.8	280.4
580A030	Test container dome	6.50	8.0	52.0
580A030	Microswitch bracket and actuation tab	0.19	9.0	1.7
580A030	Terminal boards	2.40	19.0	45.6
580A030	Tether cable assembly	0.70	19.5	13.7
580A030	Forward ring	7.58	27.5	208.5
580A030	Shell thrusters (2)	4.00	26.0	104.0
580A030	Dome thrusters (2)	4.00	7.0	28.0
590A030	Flare cover	22.00	22.7	499.4
580A030	Thruster support brackets	2.00	26.0	52.0
580A031	Inflatable appendage	15.32	. . .	293.4
580A031	Appendage pressure equipment	3.32	. . .	52.9
580A031	Booster adapter	14.00	-2.0	-28.0
580A031	Test item	20.00	15.0	300.0
580A031	Drag brake	28.00	3.38	94.6
	Totals	164.18		2346.6

Materials were selected that could be coated to retain internal pressurized gas, while withstanding the effects of aerodynamic heating, yet which were compatible with high density packaging requirements. A pressurization subsystem was designed that provided for preinflation gas storage as well as redundantly activated flare inflation at a pre-programmed time along the flight path. External filling means were provided. A mating of hard structure and flexible materials were accomplished to create a modular flare assembly that is easily removed for access to vehicle mounted components of other subsystems located in the same sector of the airframe. The unnatural target inflated shape was accomplished by strategic location of a minimum amount of rigid structure integrated into the assembly.

b. Design Approaches

The different approaches considered in initially designing the inflatable appendage are shown in Figure 60.

c. Selected Approach

The version selected for more intense analysis was a simplified compromise structure that eliminated the need for internal webbing. Not only did this structure enhance packageability, it also eliminated the lobed surfaces that digressed from the clean aerodynamic flare tested in the wind tunnel series. The selected design is shown in Goodyear Aerospace Drawing 580A031 (Appendix V), included as an attachment to this report.

d. Flare Stress Analysis

(1) General

The flare stress analysis was governed by the design constraints imposed upon the inflatable flare skirt assembly in flight, along with the requirement that the desired shape be maintained while inflated during the test period. In particular, the analysis substantiates the selection of materials and methods for structural support. The configuration analyzed was that shown in Goodyear Aerospace Drawing 580A031 in Appendix V.

The design loads were obtained from the pressure distribution information supplied in Item 3. a of this section and the flight envelope shown in Figure 1. From these sources of information, the critical pressures shown in Table XVI were calculated.

(2) Analytical Approach

The stress analysis of the skirt is first of all concerned with determining the stresses in a pressurized frustrum of an elliptical cross section. The frustrum, though tapered, is not conical, since the meridional elements do not meet in a common point. An external dynamic pressure distribution occurs that gives a maximum positive pressure at the ends of the major axis of the ellipse and is a function of the taper angle, β , of the meridian.

Since the skirt is a membrane except for two metal sheets of a symmetrical pattern at the extremities of the minor axis, the elliptical shape is maintained only at the bases of the frustrum, where it is fixed at the small end, and restrained at the other end by an array of tubular members intended to keep the base plane approximately flat. The center of the volume of the frustrum is a cylinder approximately equal in diameter to the minor axis of the ellipse at all cross sections.

The stresses in an elliptical cylinder with no center post are given by Stein in Reference 7, but only the hoop stresses are applicable here.

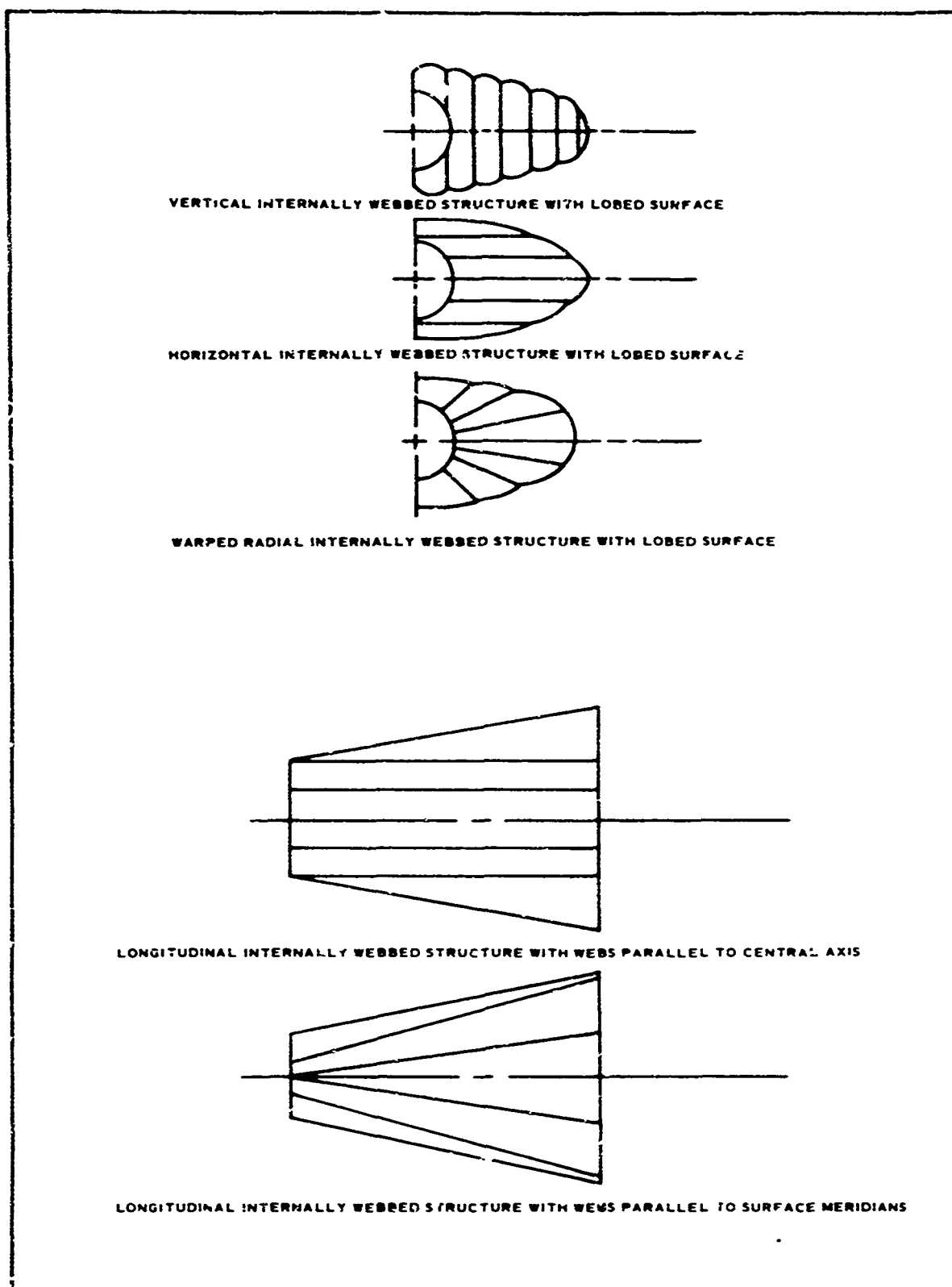


Figure 60 - Inflatable Appendage Designs

TABLE XVI - CRITICAL PRESSURE COMPUTATION

Condition	Altitude (ft)	Mach number	q (p.f)	Minor axis, $\alpha = 6.5$ deg			Major axis, $\alpha = 18.5$ deg			Estimated base p (psf)
				$C_p/C_{p_{max}}^*$	C_p	$C_{pq} = p_{-pa}$ (psf)	$C_p/C_{p_{max}}$	C_p	$C_{pq} = p_{-pa}$ (psf)	
1a	110,000	6.0	400	0.0195	0.0359	14.4	0.122	0.225	90	14.8
2a	75,000	4.3	1000	0.021	0.0386	38.6	0.129	0.238	238	74.0
3a	40,000	2.0	1000	0.025	0.0460	46.0	0.157	0.289	289	393.0
1	100,000	6.0	500	0.0195	0.0359	18.0	0.122	0.225	113	23.3
2	70,000	4.3	1200	0.021	0.0386	46.3	0.129	0.238	286	93.7
3	37,000	2.0	1200	0.025	0.0460	55.2	0.157	0.289	337	454.0

* From Reference 4, $C_{p_{max}} = 1.84$.

(3) Solution for Hoop Stress

In a circular cone (with no center support),

$$f_h = \frac{pr}{\cos \beta}$$

and

$$f_m = \frac{pr}{2 \cos \beta}.$$

It was assumed, for purposes of preliminary analyses, that the stresses in an elliptical cone are related to those in an elliptical cylinder (see Figure 62) in the same manner; i. e., the stresses are increased by the factor $\sec \beta$. However, a definition of β was needed; therefore, β was defined as $\tan \beta = a/d$.

From Figure 61, the generator, ϕ , can be seen to lie in a radial plane. Also, from Figure 62.

$$x = \frac{b}{2} \sin \phi, \quad (15)$$

$$y = \frac{h}{2} \cos \phi, \quad (16)$$

and

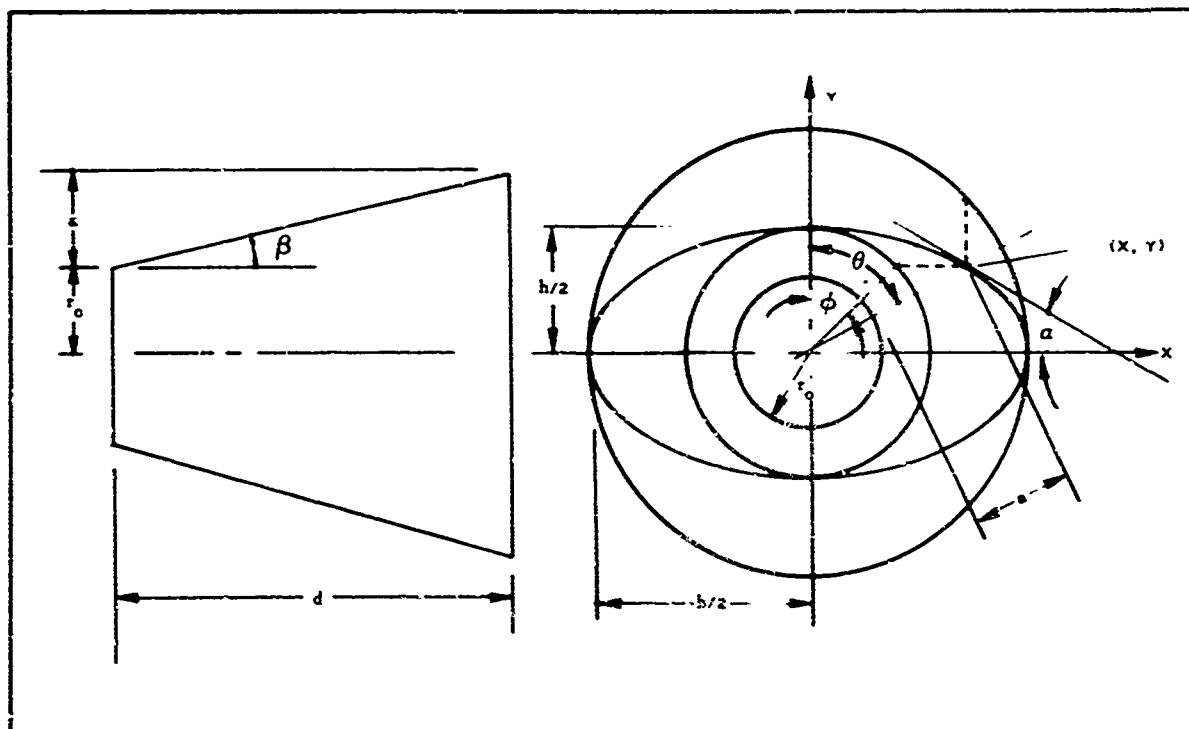


Figure 61 - Longitudinal and End Views of Elliptical Frustrum

$$\begin{aligned}(r_o + a)^2 &= x^2 + y^2 \\ &= \frac{b^2}{4} \sin^2 \phi + \frac{h^2}{4} \cos^2 \phi.\end{aligned}\quad (17)$$

At the large end, $b/2 = 15.40$ in. and, $h/2 = 8.50$ in. Therefore,

$$(r_o + a)^2 = 237 \sin^2 \phi + 72.2 \cos^2 \phi. \quad (18)$$

Varying ϕ in increments of 10 deg results in the trigonometric values shown in Table XXI, Appendix II, for the various functions of ϕ . With the values for the functions of ϕ established, the values for θ were determined. From Goodenear Aerospace Drawing 580A031,

$$r_o = 5.45 \text{ in.} \quad \frac{b}{h} = 1.812$$

$$d = 29.83 \text{ in.} \quad d^2 = 889.8$$

Using the same measurements of 10 deg for ϕ , Table XXII (Appendix II) was generated to arrive at corresponding values of θ .

Continuing on with the arithmetical process, values for θ then were determined for 10-deg incremental values of ϕ . These are shown in Table XXIII of Appendix II.

If Equations 15 and 16 are differentiated, then

$$dx = \frac{b}{2} \cos \phi d\phi,$$

$$dy = -\frac{h}{2} \sin \phi d\phi,$$

and

$$\frac{dy}{dx} = -\frac{h}{b} \tan \phi. \quad (19)$$

By definition,

$$\frac{x}{y} = \frac{b}{h} \tan \phi = \tan \theta, \quad (20)$$

so

$$\tan \phi = \frac{h}{b} \tan \theta$$

and

$$\frac{dy}{dx} = -\frac{h^2}{b^2} \tan \theta = \tan \alpha. \quad (21)$$

Tables XXIV and XXV (Appendix II) are a continuation of the trigonometric calculations employed in the determination of the hoop stresses. Table XXIV was obtained by interpolating approximately between $h/b = 0.5$ and $h/b = 0.75$ from Stein (Tables 3 and 4, pp 23 and 24, Reference 7). Table XXV was obtained by interpolating from Table XXIV for values of ϕ in 10-deg increments. As ϕ was varied from 0 to 90 deg, the data in Table XXV indicated that the hoop stress, f_h , will be a maximum at $\phi = 0$ deg and will be a minimum at $\phi = 90$ deg.

The required pressure to maintain a positive pressure differential is, for Condition 3 of Table XVI, equal to

$$p = 454 + 337 = 791 \text{ psfa} = 5.5 \text{ psia},$$

and referring to Table XXIV, the maximum hoop stress at the ends of the minor axis is

$$f_h = 8.55 p.$$

At this point of maximum hoop stress, there is a solid metal sheet, the stress does not change very rapidly with ϕ , and the metal extends only about 1.8 in. laterally from the minor axis. It is therefore only slightly conservative to take this as the maximum membrane stress. For $p = 5.5$ psi, $f_h = 47.0$ lb/in.

The fabric strength in both warp and fill at 600 F has been found to be 118 lb/in. (HT-72 Nomex). With a factor of safety of 2.0, the minimum margin of safety in the fabric is

$$\frac{118}{47.0 \times 2} - 1 = 0.25 \text{ (hoop direction)}.$$

However, the temperature at the point of this maximum stress is actually much less than 600 F, thus the margin of safety computed above is conservative.

(4) Meridian Stress

The maximum meridional stress obviously occurs at the ends of the major axis in the base plane. The load, R_o , is calculated at this point as 1.99 times the differential pressure, and is distributed over a 2.2-deg arc. The radius of the major axis at the base plane is 15.4 in., therefore the load is distributed over a length of

$$15.40 \left(\frac{2.2}{57.3} \right) = 0.592 \text{ in.}$$

The angle between R_o and f_m is 29 deg, so that the maximum meridional stress, f_m , is (for $p = 5.5$ psi):

$$f_m = \frac{1.99(5.5)}{0.592 \cos 29 \text{ deg}} = 21.1 \text{ lb/in.}$$

This maximum meridian stress is less than the maximum hoop stress calculated previously. The conditions half-way between the ends were of interest because the maximum deviations from the desired shape were expected to occur there.

As an approximation, it was assumed that the pressure differential is constant and also that the meridional stress does not affect the shape, so that a simple two-dimensional analysis was possible. The fabric will assume a circular cross section except where restrained by the metal side plates. The length of the original elliptical arc is needed. From Reddick and Miller (Reference 8), the circumference of an ellipse is

$$L = 4bE(k) \quad (22)$$

where

b = major semiaxis, and

$$k = \sqrt{(b^2 - h^2)} / b$$

At the midsection shown in Figure 62.

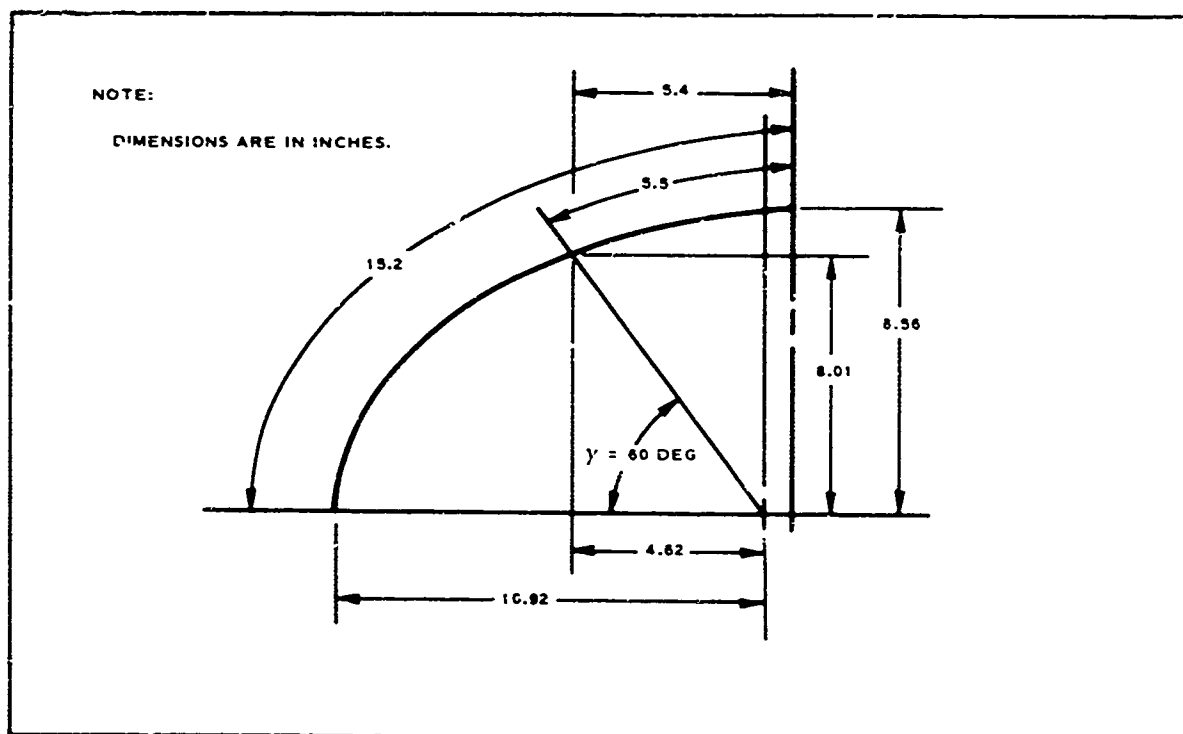


Figure 62 - Cross Section of Midpoint of Elliptical Frustum

$$b = \frac{15.40 + 6.43}{2} = \frac{21.83}{2} = 10.92 \text{ in. ,}$$

$$h = \frac{8.50 + 8.63}{2} = 8.56 \text{ in. ,}$$

$$k = \frac{\sqrt{10.92^2 - 8.56^2}}{8.56} = \frac{\sqrt{109.3 - 73.3}}{8.56} = \frac{6.00}{8.56} = 0.701 ,$$

and

$$\sin^{-1} k = 40.2 \text{ deg .}$$

From Dwight (Reference 9), $E(K) = 1.391$.

For a quarter ellipse, the arc length is:

$$10.92(1.391) = 15.2 \text{ in.}$$

From Figure 63, then:

$$\frac{x^2}{b^2} + \frac{y^2}{h^2} = 1 , \quad (23)$$

$$b^2 y^2 = b^2 h^2 - h^2 x^2 = h^2 (b^2 - x^2) \quad (24)$$

$$\begin{aligned} y^2 &= \frac{8.56^2}{10.92^2} (10.92^2 - 5.4^2) = \frac{73.3}{109.3} (109.3 - 29.2) \\ &= \frac{73.3(80.1)}{109.3} = 64.2 \end{aligned}$$

$$Y = 8.01 \text{ in.}$$

$$\text{Arc lengths} = 15.2 - 5.5 = 9.7 \text{ in.}$$

If this length becomes the arc of a circle, $9.7 = R\gamma$ and $8.01 = R \sin \gamma$;

$$\frac{\gamma}{9.7} = \frac{\sin \gamma}{8.01} \text{ or } 0.826 \gamma = \sin \gamma .$$

Trying $\gamma = 1.047$, $\sin \gamma = 0.866$, and $\gamma \cong 60 \text{ deg}$; then,

$$R = \frac{9.7}{1.047} = 9.27$$

or

$$R = \frac{8.01}{0.866} = 9.25$$

average = 9.26 ;

$$8.01(\cot 60 \text{ deg}) = 4.62 ,$$

$$5.4 - 4.62 = 0.78 ,$$

and

$$0.78 + 9.26 = 10.04 \text{ in.}$$

Deflection = $10.92 - 10.04 = 0.88 \text{ in.}$, or, normal to the meridian, $0.88 \cos 13 \text{ deg} = 0.835 \text{ in.}$ This is the largest deflection that can occur with a uniformly distributed differential pressure and, assuming that the higher pressures at the ends of the major axis are countered by the effects of the end restraints, is a good first approximation to the actual deflection.

If the length of the meridian is 21.4 in. and the deflected meridian is assumed to lie along a circular arc, the angular deflection, δ , is obtained from Reference 10.

$$0.835 = \frac{21.4}{2} \tan \frac{\delta}{4} ,$$

$$\tan \frac{(2\delta)}{4} = 0.0780 ,$$

$$\frac{\delta}{2} = 4.45 \text{ deg} ,$$

and

$$\delta = 8.9 \text{ deg} .$$

Here, δ is the angular change at either end of the skirt. At the aft (large) end, an increase in temperature and stress will result, but probably not so great as to reduce the minimum margin of safety, since the maximum stress at the end of the major axis is much lower than the maximum at the end of the minor axis, which is not affected. If proved necessary in detailed design analysis, some local increase in thermal coating thickness could be made as deemed fitting.

(5) Base Supports

At the "flat" end, the shape is maintained by small aluminum tubes spaced 2.2 deg apart with center lines intersecting at a common point. The longest, and most heavily loaded of these, lies in the plane of the major axis of the elliptical cross section, but is inclined to the axis plane by about 11 deg as shown in Figure 63. The tubes are simply inserted in pockets in the fabric. Mechanical stability is maintained by the outward pressure of the inflation gas, so the rods can be treated as simply supported beam columns. The longest tubes are assumed to be 0.25 in. O.D. with an 0.03-in. wall of 6061-T6 aluminum alloy. Let

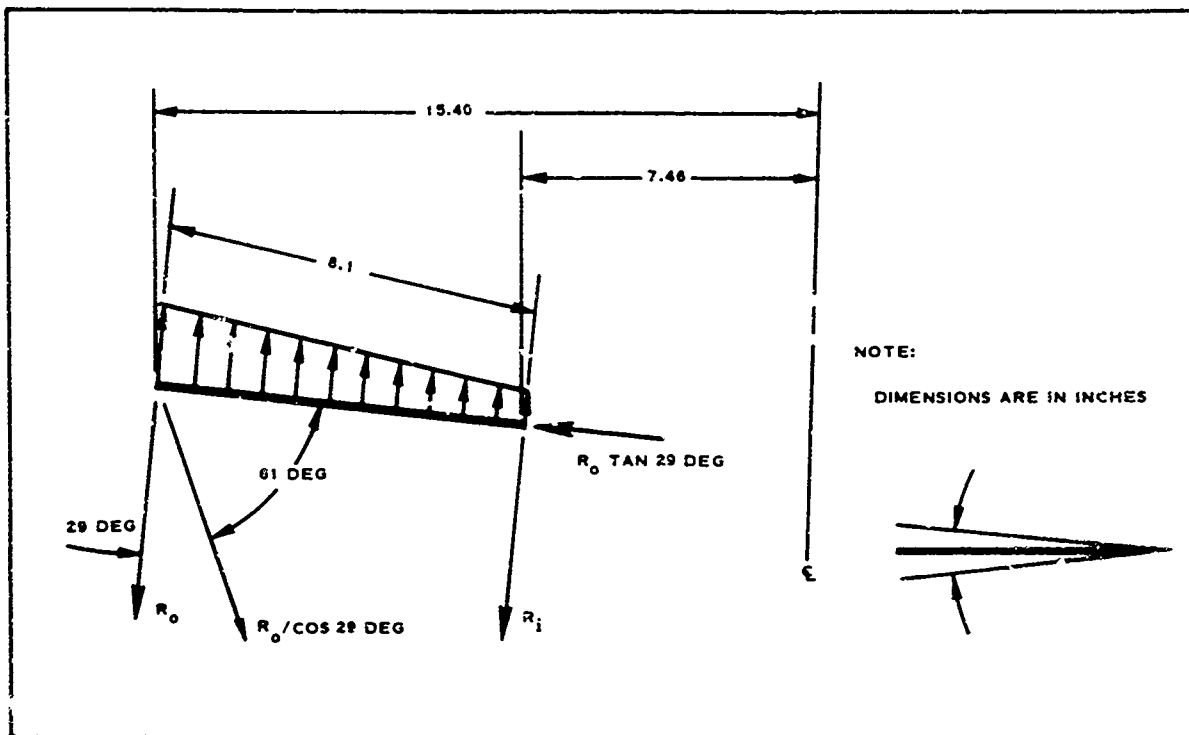


Figure 63 - Base Support Loading Diagram

$$E_y = 10 \times 10^6 \text{ psi}$$

and

$$I = \frac{(r_o^4 - r_i^4)}{4} = 0.785(0.000244 - 0.000083) = 0.000126 \text{ in.}^4$$

If the angle between rods is 2.2 deg,

$$W_o = 15.40 \frac{(2.2)}{57.3} p = 0.592 p.$$

For the maximum length,

$$W_i = 7.46 \frac{(2.2)}{57.3} p = 0.287 p;$$

$$\begin{aligned} R_i &= \frac{0.287(8.1)}{2} + \frac{(0.592 - 0.287)p(8.1)}{6} = 1.163 p + 0.412 p \\ &= 1.575 p; \end{aligned}$$

$$\begin{aligned} R_o &= \frac{0.592 p(8.1)}{2} - \frac{0.305 p(8.1)}{6} = 2.40 p - 0.412 p \\ &= 1.99 p. \end{aligned}$$

Check as follows:

$$\frac{(0.592 + 0.287)}{2} \ell_1 p = \frac{0.879(8.1)p}{2} = 3.56 p ;$$

$$R_o \tan 29 \text{ deg} = 1.99 p(0.565) = 1.125 p \approx \text{axial load, } P .$$

Assume limit load $p = 5.5$ psi; with F. S. $= 1.5$, $p = 8.25$ psi.

From Niles and Newell (Reference 11, pp 92 and 96):

$$M = C_1 \sin \frac{\psi}{j} + C_2 \cos \frac{\psi}{j} + f(w) , \quad (25)$$

using Cases 5 and 6 (or Cases 2 and 6). The maximum moment is not at midspan, but is very nearly so, therefore X is assumed to be $L/2$:

$$C_1 = \frac{W_1 j^2}{\tan \frac{L}{j}} - \frac{W_2 j^2}{\sin \frac{L}{j}} , \quad (26)$$

$$C_2 = -W_1 j^2 , \quad (27)$$

$$f(w) = W_1 j^2 \left(1 - \frac{X}{L}\right) + \frac{W_2 j^2 X}{L} , \quad (28)$$

$$W_1 = 0.592 p ,$$

and

$$W_2 = 0.287 p .$$

Since $p = 8.25$ psi,

$$j^2 = \frac{EI}{P} = \frac{(10 \times 10^6)(0.000126)}{(1.125)(8.25)} = 136 ,$$

$$j = 136 = 11.56 ,$$

$$C_1 = \frac{(0.592)(8.25)(136)}{\tan \frac{8.1}{11.66}} - \frac{(0.287)(136)(8.25)}{\sin \frac{8.1}{11.66}} = 295 ,$$

$$C_2 = -(0.592)(8.25)(136) = -664 ,$$

$$f(w) = 332 + 161 = 493 ,$$

and

$$\begin{aligned} M &= (295)\sin\left(\frac{4.05}{11.66}\right) + (-664)\cos\left(\frac{4.05}{11.66}\right) + 493 \\ &= (295)(0.340) + (-664)(0.940) + 493 \\ &= 100.3 - 624.2 + 493 \\ &= 31 \text{ in.-lb.} \end{aligned}$$

To obtain the bending stress,

$$f_b + f_c = \frac{mr_o}{I} + \frac{1.125 P}{\pi r^2 - \pi r_l^2} \quad (29)$$

and

$$\begin{aligned} f_{\max} &= \frac{(31)(0.125)}{(0.00125)} + \frac{(1.125)(8.25)}{3.14(0.125)^2 - 3.14(0.095)^2} \\ &= 30,700 + 450 \\ &= 31,150 \text{ psi.} \end{aligned}$$

The compression yield strength of 6061-T6 tubing [from Reference 12, p 3.260(b)] is 34,000 psi. The margin of safety is:

$$M.S. = \frac{34,000}{31,150} - 1 = 0.09.$$

There are some rods 0.18 in. in diameter, but the longest of these is about 4.0 in. The axial component is also reduced by a smaller taper angle of the skirt element at the side:

$$\begin{aligned} I &= \frac{0.785(0.18^4 - 0.15^4)}{16} = 0.785 \frac{(0.001050 - 0.000506)}{16} \\ &= \frac{0.000427}{16} = 0.0000267 \text{ in.}^4 \end{aligned}$$

or 0.212 times I for the 0.25-in. rod. Since the length is less than half the longest one checked above and both axial and distributed loads are smaller, it is unlikely that this tube is critical.

c. Materials Investigation

(1) Material Considerations

In accordance with the critical heating analysis in Item 3, c of this section, the HT-72 fabric selected therein was evaluated, prior to construction of the full-scale sectional mockup, in order to verify its suitability for use as a construction material in the EUREKA appendages. Considerations were given to the material's workability, coating compatibility,

adhesion characteristics, sewability, permeability, and strength. As indicated in Figure 35, the appendage surfaces are coated with Dow-Corning 92-007 silicone. For cloth-to-cloth and cloth-to-metal seams, Dow-Corning 92-018 adhesive was selected as being most suitable in combination with the coated Nomex cloth.

The cloth is rated by its manufacturer to have a room temperature strength of 397 lb/in. warp and 385 lb/in. fill. Its rated weight is 8.67 oz/sq yd for the 0.0166-in.-gage material selected. The coating selected (and the adhesive) were room-temperature-vulcanizing silicones, readily applied by manual brushing, and had favorable characteristics in the flare fabrication effort.

(2) Preparation Procedures for Laboratory Testing

Segments of the HT-72 fabric were coated with the 92-007 adhesive subsequent to treatment with A4094 primer. Four coats of the thermal-resistant silicone were applied to the representative exterior surface and two coats to the inner surface. A check subsequent to curing indicated complete lack of coat-to-coat adhesion. Other samples, coated in a multitude of different ways, exhibited no such deficiency. A review of the coating application history of the initial sample revealed that there was a period between coats during which the surfaces were exposed to a collection of grease, dirt, and dust contaminants. As a result of this discovery, the fabrication procedures now specify cleaning all silicone surfaces with acetone between coats if sufficient time lapses for a cure to start.

Initial seam samples, employing the 92-018 adhesive, failed seam-strength pull tests. Dow-Corning Corporation suggested that the high-gloss 92-007 adhesive surface be buffed prior to adhesive application. They also recommended that the 92-018 adhesive be thinned and applied directly to seaming surfaces, in lieu of the 92-007 undercoat, to achieve greater seam strength. Also provided was a reference related to metal surface preparation prior to mating with fabric.

(3) Laboratory Testing Results

Table XVII presents the results of high-temperature strength tests made

TABLE XVII - SEAM/CLOTH TEST RESULTS

Item	Coating	Adhesive	Temperature (F)	Strength (lb/in.)
Seams	92-007	92-018	300	92
Seams	92-018	92-018	300	141
Cloth (warp)	92-007	. . .	600	118
Cloth (fill)	92-007	. . .	600	118

prior to fabricating the flare mockup. Samples of material coated to a 4-to-1 exterior-to-interior thickness ratio were sewn and exhibited excessive machine drag such that stitch-spacing control was impossible. Samples coated to a 1-to-1 ratio proved compatible with machine sewing. From those samplings, it was determined that coatings in excess of the 1-to-1 ratio would have to be applied subsequent to unit fabrication.

Permeability tests on representative coated samples (performed on the Cambridge permeameter), with helium as the test gas, recorded average rates (unseamed cloth) of 7.3 liters per square meter per day. Subsequent to completion of the laboratory testing, a full-scale mockup was constructed. The evaluation of that unit is presented in Section V.

7. AUXILIARY EQUIPMENT

a. Refurbishment

The Arapaho C vehicle refurbishment parts list resulting from the modifications required for EUREKA is shown in Table XVIII. The EUREKA modifications have not appreciably affected the refurbishment requirements. Refurbishment time and costs have not been increased for the EUREKA Arapaho C test vehicle as recommended in this report.

b. Aerospace Ground Equipment

The assembly, test, and checkout equipment utilized for the ADDPEP Arapaho C vehicle can be employed with minor changes on the EUREKA modified Arapaho C vehicle. The vehicle handling dolly will require a modification to permit installation of the packaged skirt assembly and the flare cover onto the vehicle. The checkout panel will require a modification to incorporate provisions to check out the added sequence events for flare ejection and skirt inflation. Table XIX lists the aerospace ground equipment (AGE) requirements.

TABLE XVIII - REFURBISHMENT PARTS LIST

Name	EUREKA part number and vendor	Quantity	ADDPEP part number and vendor	Quantity
Flare cover	580A030	1	Not required	...
Decelerator brake assembly	596-7300-101	1	Not required	...
Nose spike assembly	596-7341-101	1	Not required	...
Frangible skin	530A002-209-1	1	Not required	...
Test item container	Not required	0	530A002-011-101	1
Test item container end cap	580A030	1	Not required	...
Balloon canister assembly	530A002-083-101	1	Not required	...
Balloon liner	530A002-205-101	1	Not required	...
Recovery parachute deployment cover	530A002-131-101	1	Not required	...
Recovery parachute deployment bag	596-7276	1	Not required	...
Ablation cover assembly	580A002-088-101	1	Not required	...
Aneroid barometric switch	9010-11, Aero Mech	2	Not required	...
Ultrasonic marker battery	B-37-5, Clevite	1	Not required	...
Dye marker	ALS-1, ACR Electronics	3	Not required	...
Salt water battery	EP 395, Eagle Picher	2	Not required	...
Film	16 MM, D100, 100 ft, Ansco	2	Not required	...
Lanyard ring	530A002-060-1	1	Not required	...
Cotter pin	MS24665-291	1	Not required	...
Guard	530A002-133-101	1	Not required	...
Striker	530A002-137-1	1	Not required	...
Connector	MS3116P8-4S	1	Not required	...
Explosive valve, flare inflation	New part	1	Not required	...
Dimple motor	DM43BO	2	DM25N4 Hercules	2
Explosive valve, despin	1804-013-01	2	DM25N4 Hercules	2
Explosive valve, flotation	1802-069-01, Conax	1	DM25N4 Hercules	1
Pin puller	GDC, Conax	1	1808-024-02, Conax	1
Thruster, test item	New part, Goodyear Aerospace	2	Goodyear Aerospace	3
Squib	IGN116, Atlas	2	S-94, Dupont	12
Thruster, flare cover	New part, Goodyear Aerospace	2	Not required	...
Squib	IGN116, Atlas	2	Not required	...
Detonator	IDT123, Atlas	4	X549D, Dupont	4
Cartridge, recovery parachute squib	IGN116, Atlas	2	S-94, Dupont	4
Pyro switch board, forward	New part	1	530A002-095-101	1
Contains pyro switches	MS-WRFR11 series, Atlas	14	MS---CRT1 series, Atlas	14
Pyro switch board, aft	New part	1	530A002-096-101	2
Contain pyro switches	MS---WRFR11 series, Atlas	8	MS---CRT1 series, Atlas	8
Pyro switch board, aft	New part	1	530A002-096-103	2
Contain pyro switches	MS---WRFR11, Atlas	8	MS---CRT1 series, Atlas	8
Separation nut	SN 2100-7, Hi-Shear	1	MS---CRT1 series, Atlas	1

AFFDL-TR-67-192
Volume I

Thrustor, flare cover	New part, Goodyear Aerospace	2	Not required	...
Squib	IGN116, Atlas	2	Not required	...
Detonator	IDT123, Atlas	4	X549D, Dupont	4
Cartridge, recovery parachute squib	IGN116, Atlas	2	S-94, Dupont	4
Pyro switch board, forward	New part	1	530A002-095-101	1
Contains pyro switches	MS-WRFRT1 series, Atlas	14	MS---CRT1 series, Atlas	14
Pyro switch board, aft	New part	1	530A002-096-101	2
Contain pyro switches	MS--WRFRT1 series, Atlas	8	MS---CRT1 series, Atlas	8
Pyro switch board, aft	New part	1	530A002-096-103	2
Contain pyro switches	MS--WRFRT1, Atlas	8	MS---CRT1 series, Atlas	8
Separation nut	SN 2100-7, Hi-Shear	1	MS---CRT1 series, Atlas	1
Cartridge	PC-10, Hi-Shear	1	MS---CRT1 series, Atlas	1
Flexible linear shaped charge	25 gr/ft, Ensign Bickford	6 ft	MS---CRT1 series, Atlas	6 ft
Flexible linear shaped charge	20 gr/ft, Ensign Bickford	6 ft	MS---CRT1 series, Atlas	6 ft
Propellant	M-9, Dupont	14 gr	MS---CRT1 series, Atlas	12 gr
Battery pack assembly, main	530A002-029	1	M-9, Dupont	1
Battery pack assembly, camera	530A002-097	1	596-7259	1
Battery pack assembly, radar	530A002-216	1	596-7259	1
Tensiometer strain link [†]	530A002-056	1	Not required	...
Hardware, nuts, screws, bolts	Miscellaneous	1 set	Not required	...
Pressure transducer, differential [†]	530A002-032	1	Not required	...
Pressure transducer, static [†]	530A002-034	1	Not required	...
Timer [†]	1060 DWB-180T-6PDT Raymond Engineering Laboratory	2	Not required	...
Potting compound [§]	RTV-11, G. E.	1 qt	Not required	...
Epoxy [§]	Epon 828	1 pt	Not required	...
Catalyst [§]	Versamid 125	1 pt	Not required	...
Sealing compound [§]	MIL-S-7502, Class B2	1/2 pt	Not required	...
Sealing compound [§]	MIL-S-7916	1/2 pt	Not required	...
Inflatable flare assembly [§]	580A031	1	Not required	...
Nitrogen [§]	GFE	1	Not required	...
			two 2-cu-ft, 3000-psi bottles needed to fill reservoir, same for both vehicles	

*New link may be required per test. Size of link is determined by expected loads for each particular tests. It is possible to use same link for several tests if the expected loads are similar.

†New pressure transducer required per test. Range of pressure transducer is determined by expected test regime. It is possible to use same pressure transducer for several tests if the test areas are similar.

‡The same timer can be used for several tests. However, for each test, the six cams on the timer will require resetting for proper sequencing of each test.

§ Bulk item.

¶ Required only if installed assembly is damaged.

(Reverse is blank)

B

TABLE XIX - AEROSPACE GROUND EQUIPMENT LIST

Item	Manufacturer	Model number
Telemetry indicator	Panoramic Electronics	TM1-1A
Telemetry indicator power supply	Panoramic Electronics	TMP-1A
Discriminator board selector	Data Control Lab	GND-2
Discriminator power supply	Data Control Lab	GFD-2
Differential dc voltmeter	John F. Fluke	801
FM receiver
Voltage regulator transformer
Decade capacitor box	Cornell Dublier	CDA5
Multimeter	Simpson	260
Oscilloscope	Tektronix	531
Plug-in unit	Tektronix	53/54B
Plug-in unit	Tektronix	CA
Plug-in unit	Tektronix	D
Plug-in unit	Tektronix	53B
Oscilloscope cart	Tektronix	500
Two-channel recorder	Brush Instruments	RL-202
DC amplifier	Brush Instruments	BI-928
Isolation transformer	Allied	PT62080
Megger	Biddle	. . .
Audio oscillator	Hewlett Packard	200CD
DC power supply	Sorenson	MR3215
DC power supply	Sorenson	MR3215
RMS voltmeter	Ballantine	320A
Wattmeter with five watts	Bird	43
Ignition circuit tester	Allegany Instrument	101-5BF
Differential dc voltmeter	John Fluke	801
Pneumatic test panel	Goodyear Aerospace	530A002-065
Battery test	Goodyear Aerospace	2
Test console	Goodyear Aerospace	530A004-001
Cable assembly	Goodyear Aerospace	530A002-059
Cable assembly	Goodyear Aerospace	530A002-070
Frequency counter	Berkeley	554B
Decade resistance box	General Radio	1432M
Multimeter	Simpson	260
Telemetry tester	Goodyear Aerospace	530A004-030
Oscillator tester	Vector	OVR-1
Dolly	Goodyear Aerospace	. . .

(Reverse is blank)

SECTION V

FULL-SCALE MOCKUP

1. CONTRACT REQUIREMENTS

In accordance with contractual requirements, a full-scale mockup of the recommended modified section of the test vehicle was constructed to demonstrate the feasibility of the approach and to preclude major assembly and actuation interference problems.

2. OBJECTIVES

The completed mockup, fabricated to Goodyear Aerospace Drawings 580A000 (Sheets 1 and 2 of Appendix V) and 580A031 (Sheets 1 and 2 of Appendix V), was inspected and evaluated for:

1. Proving installation feasibility and basic dimensional adherence
2. Demonstrating fairing separation, flare deployment, and inflation characteristics
3. Indicating noninterference during manual sequencing to the point of recovery parachute line stretch
4. Exhibiting accessibility to all components requiring prelaunch checkout
5. Evaluating major assembly and actuation interference problems

3. COMPLIANCE ASSURANCE

The completed vehicle mockup was evaluated using the checkoff list shown in Appendix III. The preliminary mockup drawing was not revised since the design was frozen and, in a few minor instances (such as despin plumbing), the final mockup assembly differs slightly from the preliminary drawing. The design deviations are noted in the footnotes to the list in Appendix III. Where possible, photographs were taken to document the mockup configuration and are presented in Appendix IV.

4. MOCKUP PROBLEMS AND NECESSARY CORRECTIONS

a. Vehicle

(1) Despin Nozzles

The method used to run the nitrogen from the fixed nozzle to the flare cover requires further work. The nozzle extension must not leak and yet be easily removed during flare cover ejection so that it will not

impair flare cover ejection. More development work is required to find a tight quick-disconnect fitting.

Two alternatives could be given further consideration and would eliminate the need for any removable nozzle extension (see Figure 64). The alternatives are as follows.

1. Relocate nozzles to aft end of test item container section.
2. Change sequence to remove flare cover prior to despin. The nozzles then need to extend only to the outer edge of the skirt assembly.

Relocation of the nozzles has the following disadvantages:

1. Increase in length of plumbing
2. Location of nozzles in the area of booster separation shaped charges
3. Increase in distance of despin plane from the vehicle cg, which increases chances of flat spin if any unbalance of reaction jets occurs

Changing the sequence so that despin will occur after flare cover removal eliminates the protection to the uninflated skirt assembly during despin. Of course, the skirt also could be inflated prior to despin, however, the vehicle despin characteristics would be changed with the skirt inflated. With the skirt inflated, the vehicle also has more drag and its capability of achieving the test point would be reduced.

(2) Electrical Component Thermal Protection

The aft section (also the test item housing) is used to mount electrical sequencing circuit component boards and wiring. If the inflatable skirt assembly is destroyed during re-entry due to extreme re-entry temperature conditions to which it is not designed, the circuit component boards and wiring will have to be protected from thermal damage. The mockup includes space to thermally insulate the component boards. Temperatures expected on the terminal boards and wiring could reach short-time temperatures of 2000 F. Use of teflon-insulated wire and a fiberglass cover over the component boards will be adequate.

(3) Inertia Switch Access

The inertia switch has been installed beneath the skirt assembly and flare cover. An access panel is required in both the skirt assembly (metallic part) and the flare cover to permit visual inspection of the switch status after final assembly. The Arapaho C had required only one access panel.

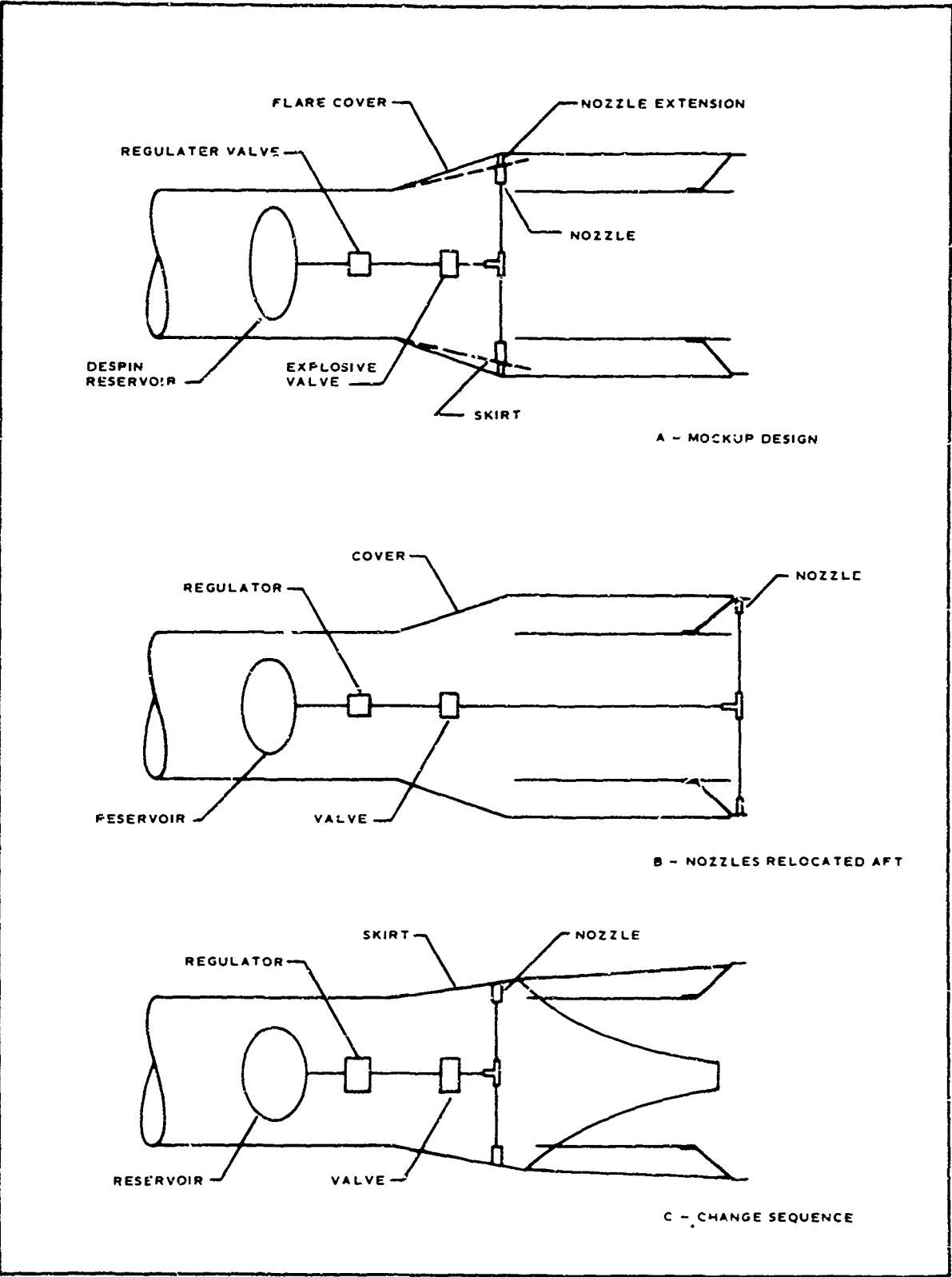


Figure 64 - Despin Plumbing Changes

b. Skirt Assembly

(1) Leaks

Leakage was evident at both lower aft edges of one of the skirt assembly sections (see Figure 65). As a temporary fix, caulking compound was injected into the skirt at the point of leakage. This leakage is not anticipated to be a problem in the manufacturing of flight articles.

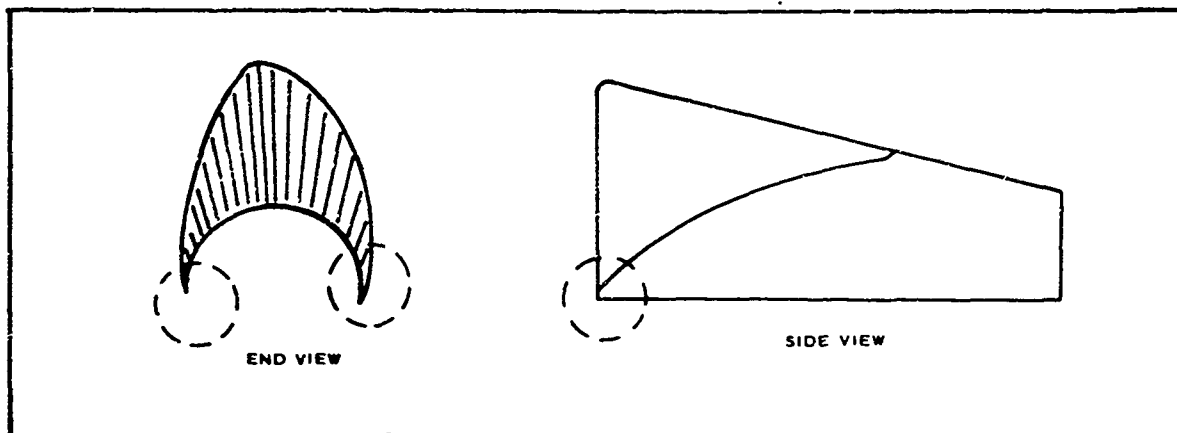


Figure 65 - Skirt Assembly Leakage Locations

(2) Appearance

The general appearance of the mockup skirt assembly, which has become a functional development model, would be improved with further development. The coating is streaky, and there are coated untrimmed thread ends visible. All the incorrect areas can be corrected on future models by better processing techniques and manufacturing control. The final design also should take into consideration any action that would improve and simplify construction techniques.

(3) Flare Inflation and Shape Tests

The flare was inflated and tested to determine its inflated shape. The internal pressure was increased in steps from 0 to 5 psig. At 1, 2, 3-1/2, and 5 psig, photographs were made of the flare assembly and are shown in Figures 89 through 96.

The design objective was to duplicate the shape of the wind-tunnel model tested during the WT-IIA wake survey. Inflation tests indicated that the mockup flare assembly did not exactly duplicate the wind tunnel model (see Figure 66). The reason for the slight deviations was the lack of internal webbing that allowed the fabric to move toward achieving a natural inflated shape. The amount of internal pressure did not appreciably affect the degree of deviation from the desired shape. The inflation tests did indicate that the inflated skirt assembly was quadrisymmetrical.

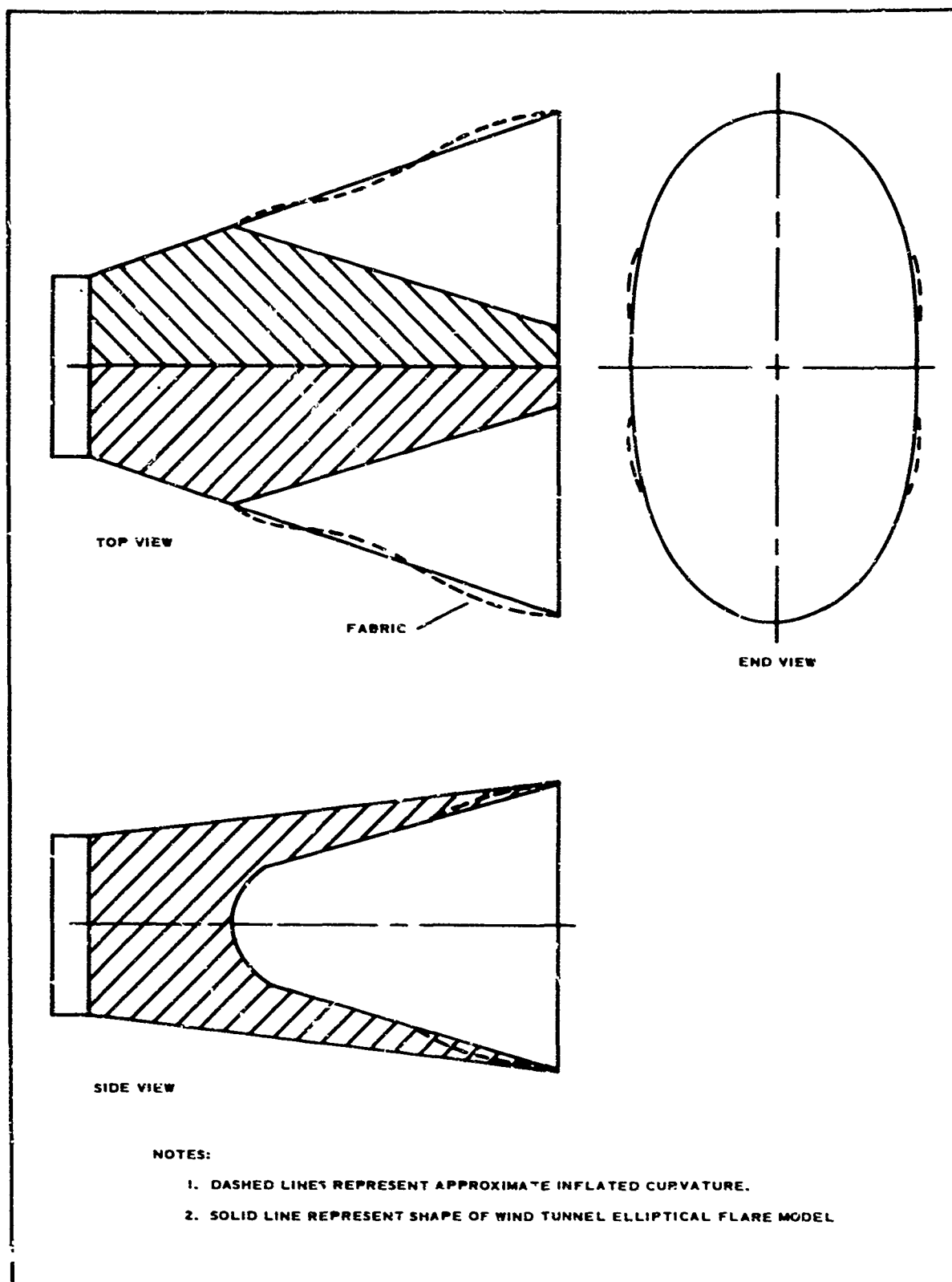


Figure 66 - Flare Shape Deviation

AFFDL-TR-67-192
Volume I

It may be possible, by redesigning the skirt assembly, to get closer to the wind tunnel model shape, but it is doubted that the exact shape can be achieved.

SECTION VI

SUMMARY OF RECOMMENDED VEHICLE CHANGES

1. EUREKA REQUIREMENTS IMPLEMENTATION

The modifications to the Arapaho C vehicle for the EUREKA program are listed on Table IV, shown on Goodyear Aerospace Drawing 580A030 (see Appendix V), and demonstrated on the mockup. The modifications are required for incorporation of the inflatable elliptical flare and range safety criteria. The modifications due to the inflatable flare included (1) relocation of components in the flare area, (2) incorporation of a new test item deployment method, (3) incorporation of flare inflation system, (4) installation of a flare cover and its ejection device, and (5) relocation of despin nozzles.

The modifications due to the range safety criteria for 1-amp, 1-watt, no-fire, electroexplosive devices required replacement of existing Arapaho C timer dimple motors, final-stage separation detonators, recovery parachute squibs, test item container thruster squibs, nose probe separation detonators, flotation latch pin squib, and pyrotechnic switches. Additional battery power also was required to properly fire the new electroexplosive devices.

2. VEHICLE CAPABILITY IMPROVEMENT

a. General

The results of high performance ADDPEP flights have indicated that the basic Arapaho C vehicle should be improved with respect to the following items to better ensure recovery from altitudes to 200 mi and velocities to Mach 11:

1. Radar beacon
2. Recovery system
3. Data acquisition
4. Flotation

The improvements are recommended to ensure radar beacon tracking and recovery system operation in the high Mach number (greater than Mach 4) flight regime. The data acquisition improvements are recommended to provide better static pressure data in the high altitude flight regime.

b. Radar Beacon

The Arapaho C radar system consists of a radar beacon transponder that transmits through a power divider into three wave-guide cavity antennas spaced at 120 deg on the vehicle shell as shown in Figure 67.

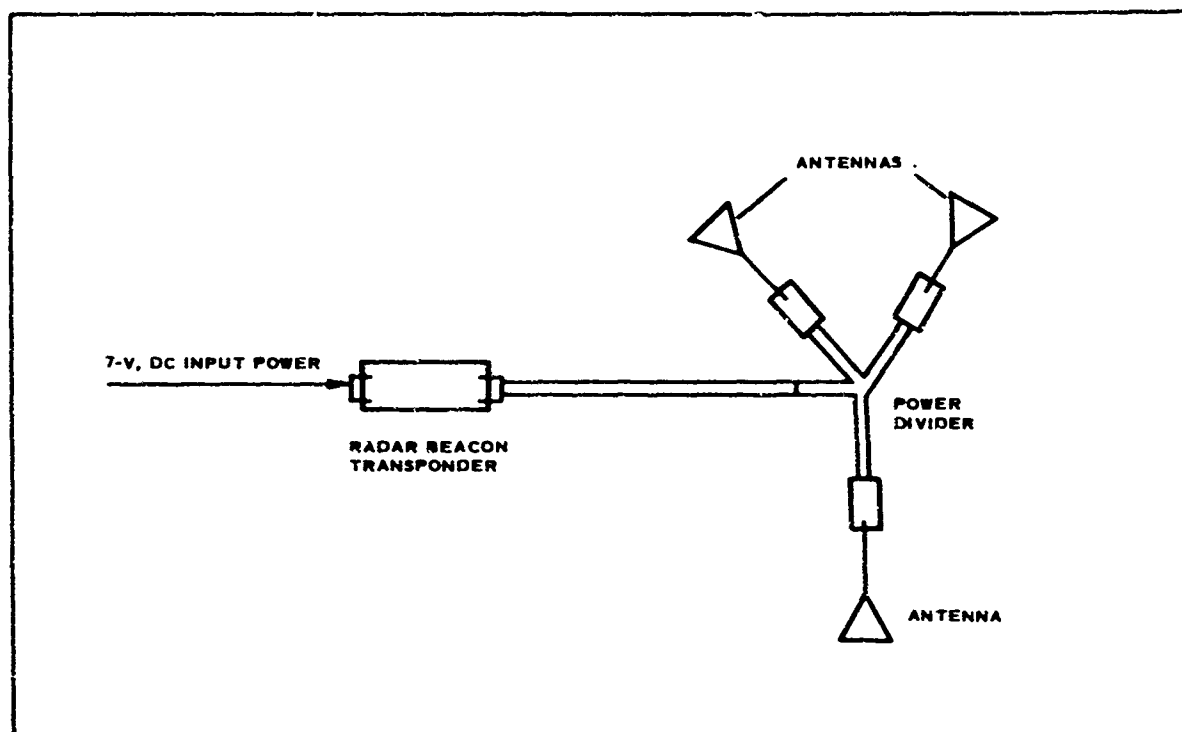


Figure 67 - Spacing of Wave-Guide Cavity Antennas

When properly interrogated by ground radar systems, the vehicle's radar beacon transponder transmits back to the ground radar system. This intercourse enables the vehicle to be tracked and eliminates the possibility of the ground radar tracking another body such as an expended booster. The radar tracking information is used to obtain vehicle altitude and range versus time for impact location and for test decelerator evaluation. The transponder's performance therefore, is critical to a meaningful free-flight test program. As a backup to the radar beacon transponder system, there are provisions for skin tracking of the vehicle. However, as the Mach number and altitudes increased, the capability to skin track the vehicle decreased.

Analysis of an automatic gain control (AGC) record of a recent high-performance flight (Mach 11 at 250,000 ft) of an Arapaho C vehicle indicated erratic behavior of the airborne radar beacon. During this flight, the AGC records exhibited a succession of momentary signal dropouts followed immediately by a 5-sec signal loss. The signal was then recovered for approximately 30 sec before being lost completely.

The shock wave influence in the region of the C-band beacon antennas has been found to be large for the blunt-nose configuration. Attenuation through this plasma region may have been severe enough to cause the momentary signal dropout. The 5-sec signal loss could be attributed to antenna detuning due to sublimation of the Teflon ablation shield over the antennas. The duration of this sublimation would have been

approximately 6 sec. The complete loss of signal appears to be due to some type of mechanical failure causing an RF disturbance.

c. Recovery

The Arapaho C recovery system has not performed during the last two ADDPEP flights and it is evident that recovery during flights that have a test point flight regime greater than Mach 4 is unlikely. The descent rate has been too great for recovery parachute deployment though measures have been taken to reduce the ballistic coefficient, $W/C_D A$, thereby reducing the descent rate. Further reduction is apparently required. Also by staging recovery parachute deployment (via reefing) and by increasing the strength of the recovery parachute, further improvement could be realized.

The overall vehicle diameter also could be increased to increase the drag area, thereby increasing the descent deceleration prior to recovery system deployment. This increase would be a tradeoff with desired boost ascent rates, which, for EUREKA, requires the capability to achieve Mach 6 at 200,000 ft. Also, the desirability to maintain the present Arapaho C test capability of Mach 10 and 250,000 ft for other test programs should be considered.

d. Pressure Measurements

The data obtained for static pressure are not accurate for the high altitude flights. The range of the static pressure transducer is 0 to 1 psia and at the higher altitudes such as 125,000 ft, 150,000 ft, and 200,000 ft, pressures of 0.0539 psi, 0.0197 psi, and 0.00287 psi are expected. These values are too close to the lower edge of the pressure range (0 to 1 psi) of the transducer to achieve usable data. It is necessary that a pressure transducer system capable of accurately measuring the low static pressures be incorporated into the basic vehicle. A pressure transducer similar to that manufactured by Hasting-Raydist, Inc. might be worth consideration.

e. Flotation

The present Arapaho C flotation system performance has been proved satisfactory when initiated in its design environment. The system consists of the main 2-ft diameter balloon mounted behind the nose probe and the auxiliary flotation BALLUTE deployed with the recovery parachute. Both flotation devices are dependent upon other operations.

1. The main BALLUTE is dependent upon nose probe separation.
2. The auxiliary BALLUTE (and recovery parachute) is dependent upon test item container ejection, tensiometer beam release, and satisfactory recovery parachute deployment.

Goodyear Aerospace recommends that consideration be given to

providing flotation that is independently activated. Possible flotation methods are described as follows.

1. Seal the existing recovery section and make it air tight.
2. Add air-tight sleeve around recovery section. Sleeve will be sized to provide buoyancy.
3. Modify existing main flotation balloon so that it is deployed from the side instead of from the forward end of the recovery section.

The flotation system again should include a radio beacon, since this is the only means to locate the recovery section precisely after water impact.

SECTION VII

CONCLUSIONS

The results of the various tests and analyses discussed in this report indicate that it is feasible to modify the Arapaho C test vehicle by addition of an inflatable appendage to provide an unsymmetrical free-flight test capability.

The preliminary design concept utilizes an inflatable Nomex membrane, which is inflated from a high-pressure nitrogen reservoir. The inflatable appendage is protected during boost conditions by metal covers that are jettisoned immediately prior to flare inflation. The flare is inflated by activating an explosive valve that allows the nitrogen gas to escape from the reservoir to the flare assembly. The design requirements given in Section I were met as follows.

1. The vehicle weight at test item deployment is estimated to be 405 lb.
2. The external geometry of the modified vehicle with the flare covers installed is identical to that of the Arapaho C vehicle.
3. The structural analysis in Section IV indicates that the structural integrity of the basic Arapaho C will be maintained.
4. The inflatable appendage will be deployed and inflated approximately 3 sec prior to test item deployment. Proper sizing of the explosive inflation valve should produce an inflation time of less than 0.3 sec.
5. The test item is deployed directly aft of the vehicle parallel to the longitudinal axis of the vehicle. The preliminary design has a test item stowage volume of 0.81 cu ft.
6. The aerodynamic analyses indicate that the vehicle will be stable from launch through test item inflation and that the despin system is sufficient to reduce the vehicle roll rate to 20 deg/sec from an initial roll rate of 4.68 rev/sec.
7. The modified vehicle utilizes a test item repositioning sequence to move the test item aft so that it will not interfere with the recovery parachute deployment. Using this repositioning technique, the test item can be retained through vehicle impact.
8. The modified vehicle retains the data acquisition and transmission, recovery, and flotation systems used on the Arapaho C vehicle. Several pyrotechnic devices were changed to comply with range safety requirements.

AFFDL-TR-67-192
Volume I

In addition to meeting design requirements, several vehicle modifications were recommended to improve vehicle performance characteristics. These recommendations are as follows.

1. Change radar beacon location and frequency to reduce shock-wave attenuation.
2. Incorporate a pressure transducer system capable of measuring low static pressures associated with high-altitude flights.
3. Improve vehicle flotation system by providing a means for positive nose-probe separation, providing a means for self-buoyancy, or modifying the existing flotation balloon to deploy from the side rather than from the front of the recovery system.
4. Improve the vehicle's recovery system by staging recovery parachute deployment (via reefing) and by increasing the strength of the recovery parachute.

APPENDIX I

SEQUENCE CIRCUIT ANALYSIS

This appendix presents the results of calculations conducted to show that the sequencing circuit on the modified Arapaho C vehicle provides sufficient current to fire all pyrotechnic squibs. The results of the calculations indicate that all electroexplosive devices will receive their recommended fire current, or more, at the time of initiation under nonshorting conditions. The results also show that under shorted conditions, where perhaps one or more squibs short out after firing, there will be at least the minimum all-fire current provided to the remaining squibs. The sequencing circuit wiring diagram is shown in Figure 68. The circuit components shown in Figure 68 have the following characteristics:

$$N = 25 \text{ (battery cells in series)}$$

$$E = N(1.25 \text{ v/cell}) = 25 \times 1.25 = 31.25 \text{ v}$$

$$R_1 = N(0.03 \text{ ohm/cell}) = 25 \times 0.03 = 0.75 \text{ ohms}$$

R_1, R_2, \dots = current limiting resistors. Resistors with 1 ohm or more have 5 percent tolerances and resistors with less than 1 ohm have 10 percent tolerance.

FR_1, FR_2, \dots = fuse resistors and have a ± 5 percent tolerance

The estimated resistance, R_L , from the source battery connections to the parallel circuit legs as shown in Figure 69 (points A and B) was arrived at as follows:

$$\text{Resistance of wire (AWG No. 20)} = 0.01 \text{ ohm/ft} \times 20 \text{ ft} = 0.20 \text{ ohm}$$

$$\text{Resistance of contacts} = 0.02 \text{ ohm/contact} \times 3 \text{ contacts} = 0.06 \text{ ohm}$$

$$\text{Resistance of terminals} = 0.01 \text{ ohm/terminal} \times 24 \text{ terminals} = 0.24 \text{ ohm}$$

$$\text{Total line resistance, } R_L = 0.50 \text{ ohm}$$

The estimated resistance R_{L1}, R_{L2}, \dots in each parallel leg of the circuit was arrived at as follows:

$$\text{Resistance of wire (AWG No. 20)} = 0.01 \text{ ohm/ft} \times 14 \text{ ft} = 0.14 \text{ ohm}$$

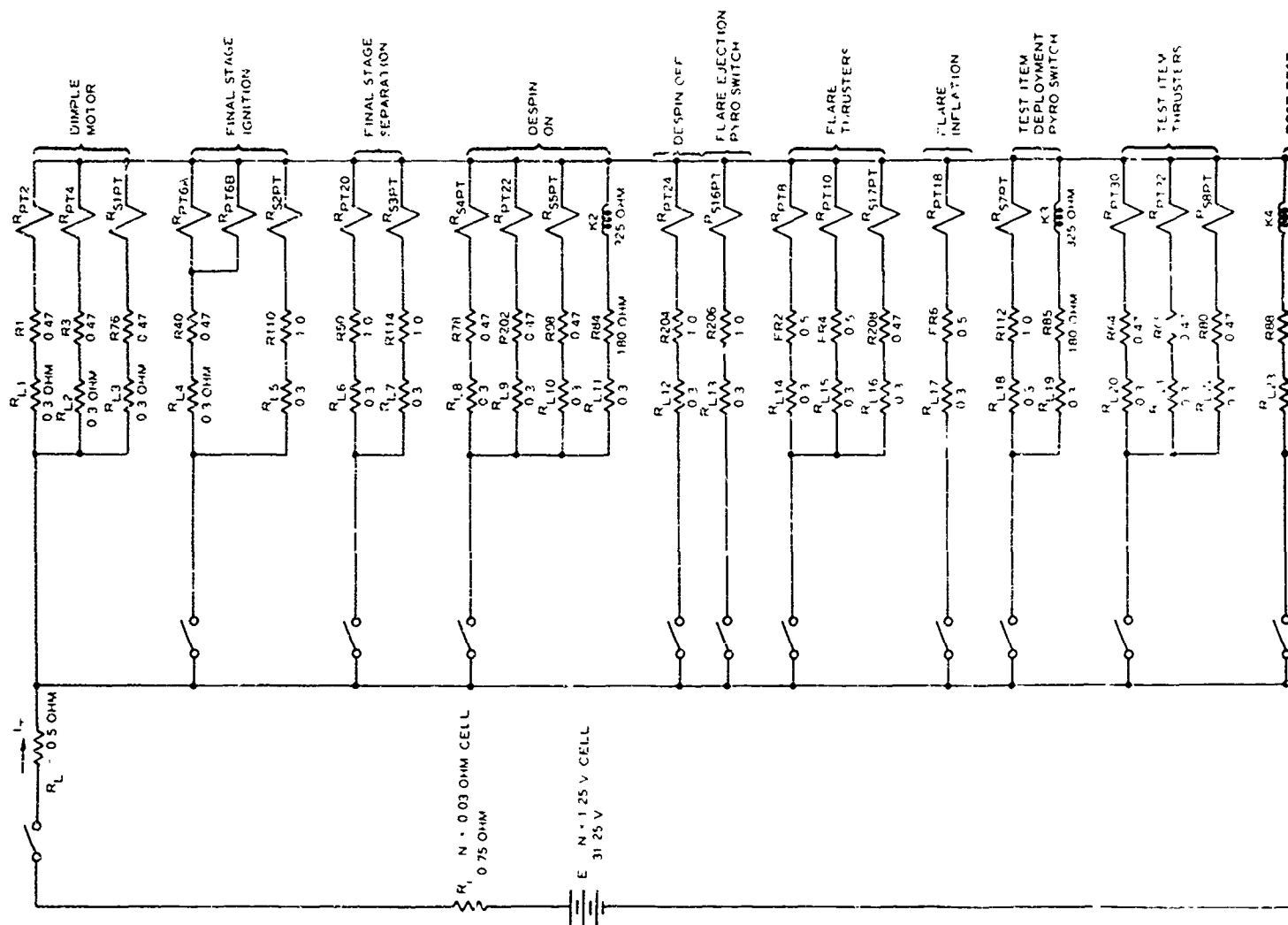
$$\text{Resistance of contacts} = 0.02 \text{ ohm/contact} \times 1 \text{ contact} = 0.02 \text{ ohm}$$

AFFDL-TR-67-192
Volume I

Resistance of terminals = $0.01 \text{ ohm/terminal} \times 14 \text{ terminals} =$
 0.14 ohms

$R_{L1} = R_{L2} = \dots = 0.30 \text{ ohm}$ (line resistance in
parallel circuit legs)

The electrical characteristics of the pyrotechnic devices along with the results of the circuit calculations are shown in Table XX.



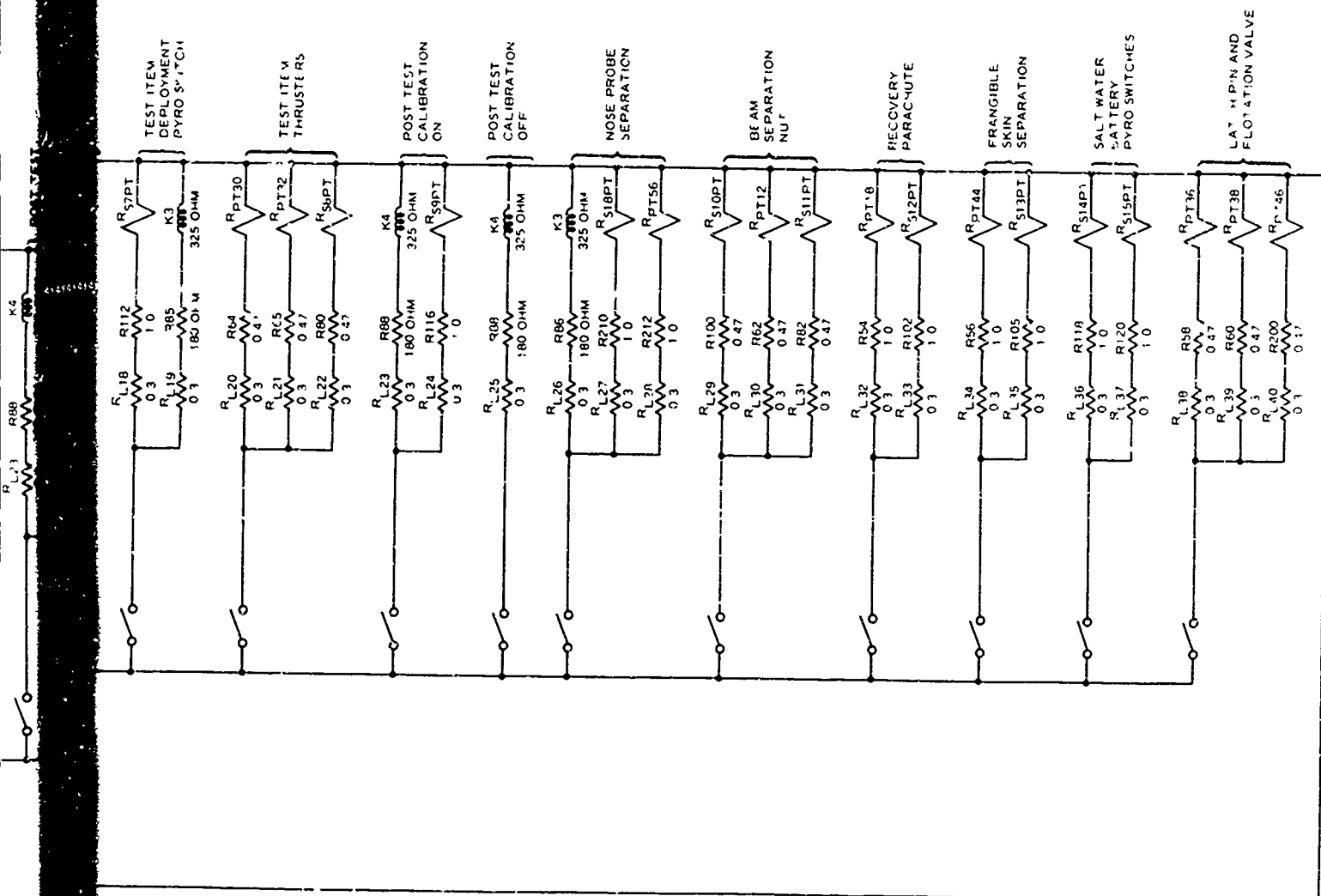


Figure 68 - Sequencing Circuit

(Reverse is blank)

B

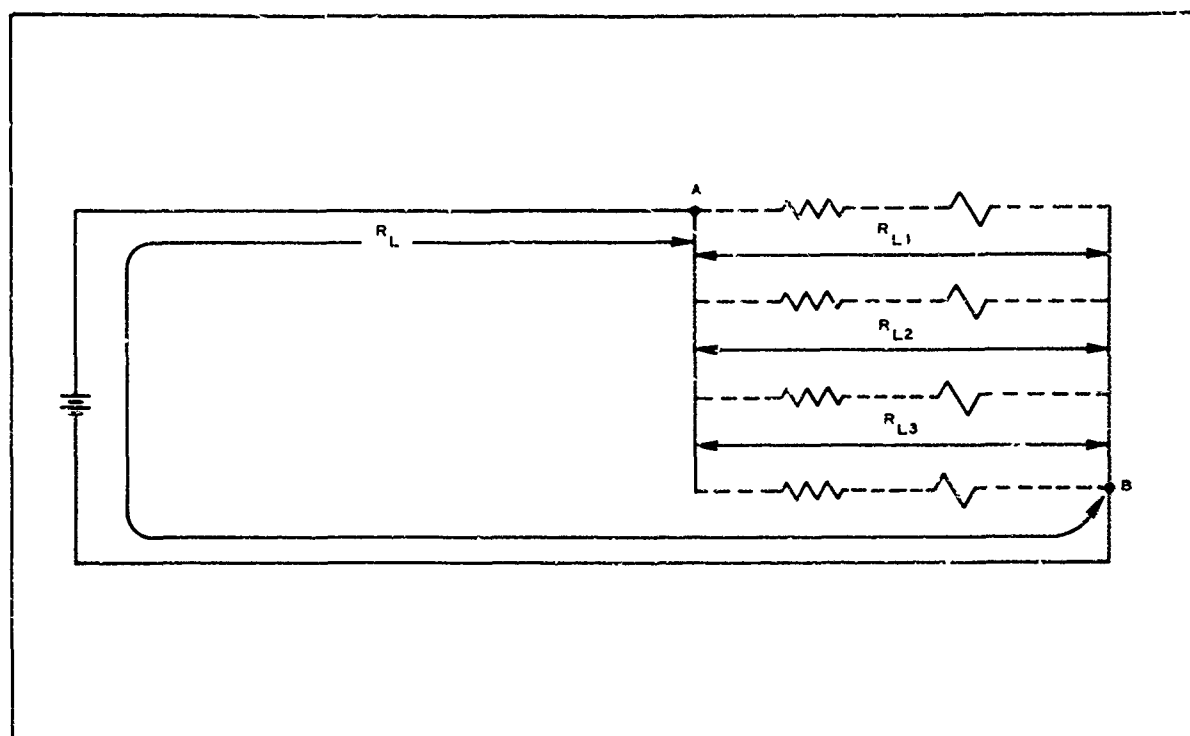


Figure 69 - Line Resistance Diagram

(Reverse is blank)

TABLE XX - PYROTECHNIC DEVICE C

Device	Part number	Application	Vendor	Circuit designation
Dimple motor	DM43BO	Timer actuation	Hercules	PT1 through 1
Despin valve	1804-013-1	Explosive valve	Conax	PT21 through
Flare thrusters	IGN116	Thruster	Atlas	PT7 through 1
Separation nut	PC-10	Separation nut	Hi-Shear	PT11 through
Recovery parachute	IGN116	Ejection charge	Atlas	PT17 through
Nose probe separation	IDT123	Separation system	Atlas	PT55, PT56
Frangible skin	SCD569A259	Separation system	Atlas	PT43, PT44
Latch pin	GDC	Pin puller	Conax	PT35, PR38
Flotation valve	1802-069-01	Explosive valve	Conax	PT45, PT46
Flare inflation valve	1802-039	Explosive valve	Conax	PT13, PT14
Test item thrusters	IGN116	Thrusters	Atlas	PT30, PT32
Pyrotechnic switches	MS-WRFTI	System control	Atlas	S1PT, S2PT,
Final stage ignition (Nike rocket motor)	IGM13	Igniter	Atlas	PT5A, PT5B,
Final stage ignition (Lance rocket motor)	A08021	Igniter	McCormick Selph	PT5A, PT5B,
Final stage separation	IDT123	Separation system	Atlas	PT19, PT20

A

AFFDL-TR-67-192
Volume I

CIRCUIT DEVICE CIRCUIT CHARACTERISTICS

Circuit reference designator indicator	Bridgewire resistance (ohms)	Firing current			
		Required		Calculated	
		Minimum all fire (amps)	Recommended fire (amps)	Shorted (amps)	Nonshorted (amps)
PT1 through PT4	0.9 - 1.2	3.5	5.0	3.90	5.40
PT21 through PT28	1.0 - 1.2	3.0	5.0	3.89	5.46
PT7 through PT10	0.9 - 1.0	3.6	4.5	4.35	5.70
PT11 through PT12	1.0 - 1.2	3.5	5.0	3.86	5.38
PT17 through PT18	0.9 - 1.0	3.6	4.5	5.25	6.56
PT55, PT56	0.85 - 1.15	3.5	5.0	5.00	6.27
PT43, PT44	0.85 - 1.15	3.5	5.0	4.70	6.30
PT35, PR38	0.9 - 1.2	3.0	5.0	3.87	5.40
PT45, PT46	1.0 - 1.2	3.0	5.0	3.04	5.40
PT13, PT14	1.0 - 1.2	3.0	5.0	...	8.20
PT30, PT32	0.85 - 1.15	3.6	4.5	4.35	5.70
S1PT, S2PT, etc.	1.0 - 1.2	3.5	5.0	3.80	5.16
PT5A, PT5B, PT6A, PT6B	1.0 - 1.2	3.5	5.0	4.70	5.00
PT5A, PT5B, PT6A, PT6B	0.85 - 1.15	3.5	4.5	3.85	4.80
PT19, PT20	0.85 - 1.15	3.5	5.0	4.70	6.30

B

(Reverse is blank)

APPENDIX II

APPENDAGE STRESS CALCULATION DATA

Tables XXI through XV shown in this appendix were used in calculation of membrane stresses in the fabric portions of the inflatable appendage.

TABLE XXI - CALCULATED FUNCTIONS OF ϕ

ϕ (deg)	$\sin \phi$	$\cos \phi$	$\sin^2 \phi$	$\cos^2 \phi$	$237 \times \sin^2 \phi$ (in. ²)	$72.2 \times \cos^2 \phi$ (in. ²)	$(r_o + a)^2$ (in. ²)	$r_o + a$ (in.)	$\tan \phi$
0	0	1.00	0	1.00	0	72.20	72.2	8.5	0
10	0.1736	0.985	0.0302	0.970	7.16	70.00	77.2	8.78	0.1763
20	0.342	0.940	0.1170	0.883	27.7	63.70	91.4	9.55	0.364
30	0.500	0.866	0.250	0.750	59.2	54.10	113.3	10.64	0.577
40	0.643	0.766	0.413	0.587	97.8	42.40	140.2	11.84	0.839
45	0.707	0.707	0.500	0.500	118.5	36.10	154.6	12.43	1.000
50	0.766	0.643	0.587	0.413	139.3	29.80	169.1	13.00	1.192
60	0.866	0.500	0.750	0.250	177.8	18.05	195.8	13.98	1.732
70	0.940	0.342	0.883	0.1170	209.0	8.45	217.5	14.74	2.748
80	0.985	0.1736	0.970	0.0302	230.0	2.18	232.2	15.24	5.671
90	1.000	0	1.000	0	237.0	0	237.0	15.40	∞

TABLE XXII - CALCULATED θ VALUES FOR CORRESPONDING ϕ 'S

ϕ (deg)	$r_0 + a = r$ (in.)	a (in.)	a^2 (in. ²)	$a^2 + d^2$ (in. ²)	$\sqrt{a^2 + d^2}$ (in.)	$\frac{a}{\sqrt{a^2 + d^2}} =$ $\sin B$	$\frac{d}{\sqrt{a^2 + d^2}} =$ $\cos B$	$\tan \theta = \frac{x}{y} =$ $\frac{b}{h} \tan \phi$	θ (deg)
0	8.50	3.05	9.30	899.1	29.98	0.1016	0.9950	0	0
10	8.78	3.33	11.10	900.9	30.02	0.1110	0.9937	0.319	17.7
20	9.55	4.10	16.80	905.6	30.09	0.1362	0.9914	0.660	33.4
30	10.64	5.19	26.9	915.7	30.26	0.1713	0.9858	1.045	46.3
40	11.84	6.39	40.8	929.6	30.49	0.209	0.9784	1.520	56.7
45	12.43	6.98	48.7	938.5	30.63	0.228	0.9739	1.812	61.6
50	13.00	7.55	57.0	945.8	30.75	0.245	0.9701	2.16	65.2
60	13.98	8.53	72.8	961.6	31.01	0.275	0.9619	3.14	72.3
70	14.74	9.29	86.3	975.1	31.23	0.297	0.9552	4.98	78.6
80	15.24	9.89	97.8	986.6	31.41	0.315	0.9497	10.27	84.4
90	15.40	9.95	99.0	987.8	31.43	0.316	0.9491	∞	90.0

TABLE XXIII - CALCULATION RESULTS OF ψ

ϕ (deg)	θ deg	Tan θ	$\frac{h^2}{b^2} \tan \theta =$ tan α	α (deg)	90 deg - $\theta + \alpha = \psi$ (deg)
0	0	0	0	0	90.0
10	17.7	0.319	0.0971	5.5	77.8
20	33.4	0.660	0.201	11.4	68.0
30	46.3	1.045	0.318	17.6	61.3
40	56.7	1.520	0.463	24.8	58.1
45	61.6	1.812	0.551	28.9	57.3
50	65.2	2.16	0.657	33.3	58.1
60	72.3	3.14	0.956	43.7	61.4
70	78.6	4.98	1.515	56.6	68.0
80	84.4	10.27	3.12	72.2	77.8
90	90.0	∞	∞	90.0	90.0

$$* \frac{(h)^2}{(b)^2} = \frac{(8.50)^2}{(15.40)^2} = 0.304$$

TABLE XXIV - HOOP STRESS CALCULATIONS

$\frac{x^*}{b}$	$\frac{y^*}{h}$	$\frac{hx}{by}$	Tan $\theta =$ $\frac{x^*}{y}$	θ (deg)	$\frac{f_h}{P_h}$
0	0.500	0	0	0	0.500
0.050	0.497	0.1006	0.182	10.4	0.4985
0.100	0.490	0.204	0.370	20.4	0.493
0.150	0.477	0.314	0.569	29.6	0.484
0.198	0.459	0.432	0.783	38.1	0.472
0.246	0.435	0.565	1.024	45.7	0.456
0.294	0.404	0.728	1.320	52.9	0.436
0.341	0.366	0.937	1.689	59.4	0.412
0.385	0.319	1.206	2.185	65.4	0.384
0.426	0.262	1.626	2.950	71.3	0.352
0.462	0.1912	2.415	4.370	77.1	0.319
0.489	0.1043	4.680	8.480	83.3	0.289
0.499	0.0316	15.790	28.600	88.0	0.276
0.500	0	∞	∞	90.0	0.275

$$* h/t = 0.5.$$




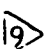


$$* h/b = 0.551.$$

TABLE XXV - HOOP STRESS CALCULATION SUMMARY

ϕ (deg)	θ (deg)	$\frac{f_h}{P_h}$
0	0	0.500
10	17.7	0.495
20	33.4	0.480
30	46.3	0.458
40	56.7	0.422
45	61.6	0.402
50	65.2	0.385
60	72.3	0.346
70	78.6	0.312
80	84.4	0.286
90	90.0	0.275

(Reverse is blank)





APPENDIX III
CHECKOFF LIST

<u>Item number</u>	<u>Description</u>	<u>Comments</u>
1.	Cameras installed	Yes
2.	Camera battery pack installed	Yes
3.	Tensiometer housing installed	Yes
4.	Recovery parachute container installed	Yes
5.	Recovery parachute riser line attached	Yes
6.	Barometric switches installed	Yes 
7.	Barometric switch plumbing installed	Yes 
8.	Inertia switch installed	Yes 
9.	Inertia switch indication provided	No  
10.	Terminal board TB-3 installed	Yes 
11.	Lanyard switch installed	Yes
12.	Lanyard switch pullaway satisfactory	(Not attempted)
13.	Safe and arm receptacle installed	Yes
14.	Safe and arm plug installable	Yes
15.	Umbilical receptacle installed	Yes
16.	Internal diameter of shell per drawing	Yes
17.	Beacon antenna assembly installed	No
18.	Beam tether cable assembly installed	Yes
19.	Beam installed	Yes
20.	Separation nut installed	Yes

AFFDL-TR-67-192
Volume I

<u>Item number</u>	<u>Description</u>	<u>Comments</u>
21.	Separation nut guard installed	Yes
22.	Beam positioning block installed	Yes
23.	Despin explosive valves (2) installed	Yes
24.	Despin nozzles installed	Yes
25.	Forward ring installed	Yes
26.	Spherical washer set installed	Yes
27.	Despin plumbing installed	Yes 2
28.	Aft can installed	Yes
29.	Test item installed	Yes
30.	Test item container installed	Yes
31.	End cap installed	Yes
32.	Aft pyro boards installed	Yes
33.	Skirt assembly installed	Yes
34.	Flare cover installed	Yes 3
35.	Aft ring installed	Yes
36.	Wiring installed	Yes 4
37.	End cap limit switch installed	Yes
38.	Flare limit switch installed	Yes 5
39.	Recovery parachute limit switch installed	Yes
40.	Parachute deployment cover installed	Yes
41.	Despin nozzle extensions installed	No 6
42.	Is accessibility available to	
	(1) Despin explosive valve cartridges	Yes 7
	Electrical plug connection	Yes 7

AFFDL-TR-67-192
Volume I

<u>Item number</u>	<u>Description</u>	<u>Comments</u>
	(2) Separation nut cartridge	Yes
	Electrical plug connection	Yes
	(3) Aft pyro board	Yes 
	(4) Test item riser line connection	Yes
	(5) Test item thrusters (2)	Yes
	Electrical plug connection	Yes
	(6) Flare cover thrusters (2)	Yes 
	Electrical plug connection	Yes 
43.	General fit	Acceptable
44.	Conflicts between events	None
45.	Skirt assembly	
	(1) General arrangement	Satisfactory (some deviation from design shape)
	(2) Packageable	Satisfactory (a light breakaway deploy- ment liner is recom- mended)
	(3) Inflation capability	Inflation was accom- plished from an ex- ternal source) 
	(4) Plumbing installed	Yes
	(5) Inflation valve assessibility	Yes

AFFDL-TR-67-192
Volume 1

<u>Item number</u>	<u>Description</u>	<u>Comments</u>
	(6) Reservoir filling capability	Yes
	Pressure monitoring	Yes 12

- 1 Barometric switches and inertia switch interchanged with terminal board TB-3 because routing of large wire bundle was not possible.
- 2 Despin plumbing was installed differently than on the mockup drawing. The method used resulted in simpler plumbing installation.
- 3 Required application of vacuum to flare in order to permit closure of covers.
- 4 Wiring to the flare cover thrusters was omitted. Two connectors, one for each flare, are required on the metallic part of the skirt assembly.
- 5 A flare cover limit switch was not installed. The final design will incorporate an event marker limit switch.
- 6 Nozzle extensions from the skirt assembly to the flare cover were not installed. Development of the nozzle extension will be incorporated in the final design.
- 7 Accessibility is excellent to these components when the flare cover and skirt assembly are removed.
- 8 An access panel in each flare cover is recommended for installation of the electrical plug connection after the flare covers are mounted on the vehicle. This will permit proper control of the wiring log from the skirt assembly to thruster cartridge.
- 9 An access panel is required on the metallic part of the skirt assembly for access to the inertia switch. The access panel also can include the parts for the barometric switches.
- 10 An access panel is also required on the flare cover for access to the skirt assembly panel described in Note 9.
- 11 The skirt assembly was not filled with the onboard inflation system. The inflation system to be employed in the final design is a standard proved method.
- 12 A means to monitor the skirt assembly inflation reservoir should be incorporated into the final design. Use of 0- to 4000-psig pressure transducer is suggested. The output of the pressure transducer

AFFDL-TR-67-192
Volume I

could be connected into the telemetry commutated channel. The signal could be used for both ground checkout and during flight as an event indication.

(Reverse is blank)

AFFDL-TR-67-192
Volume I

APPENDIX IV

VIEWS OF MOCKUP CONFIGURATION

The photographs that were taken to document the various views of the mockup configuration are presented in this appendix.

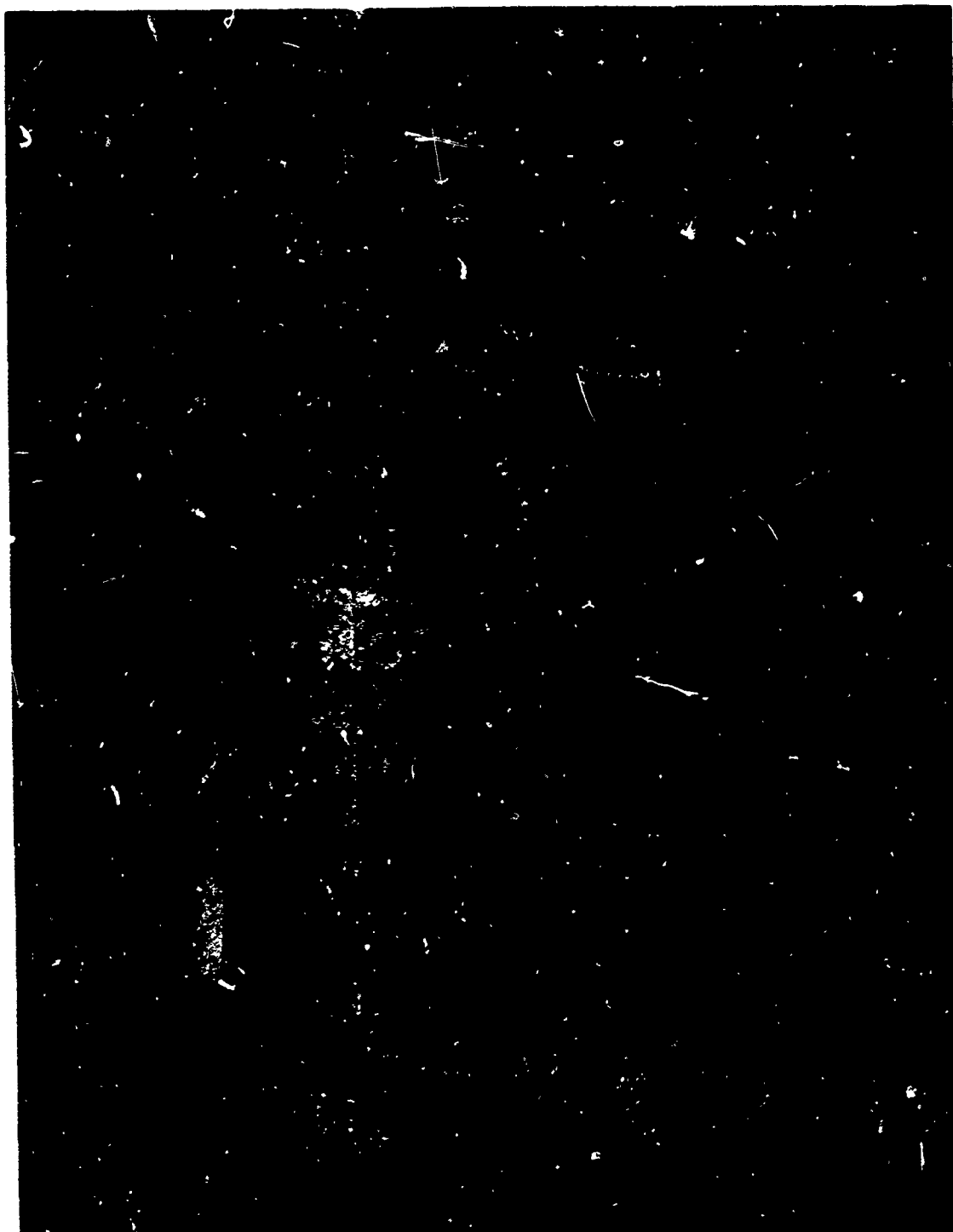


Figure 70 - Component Installation (Starboard View)



Figure 71 - Component Installation (Port View)



Figure 72 - Component Installation (Top View)



Figure 73 - Component Installation (Bottom View)



Figure 74 - Flare Module Inner Construction

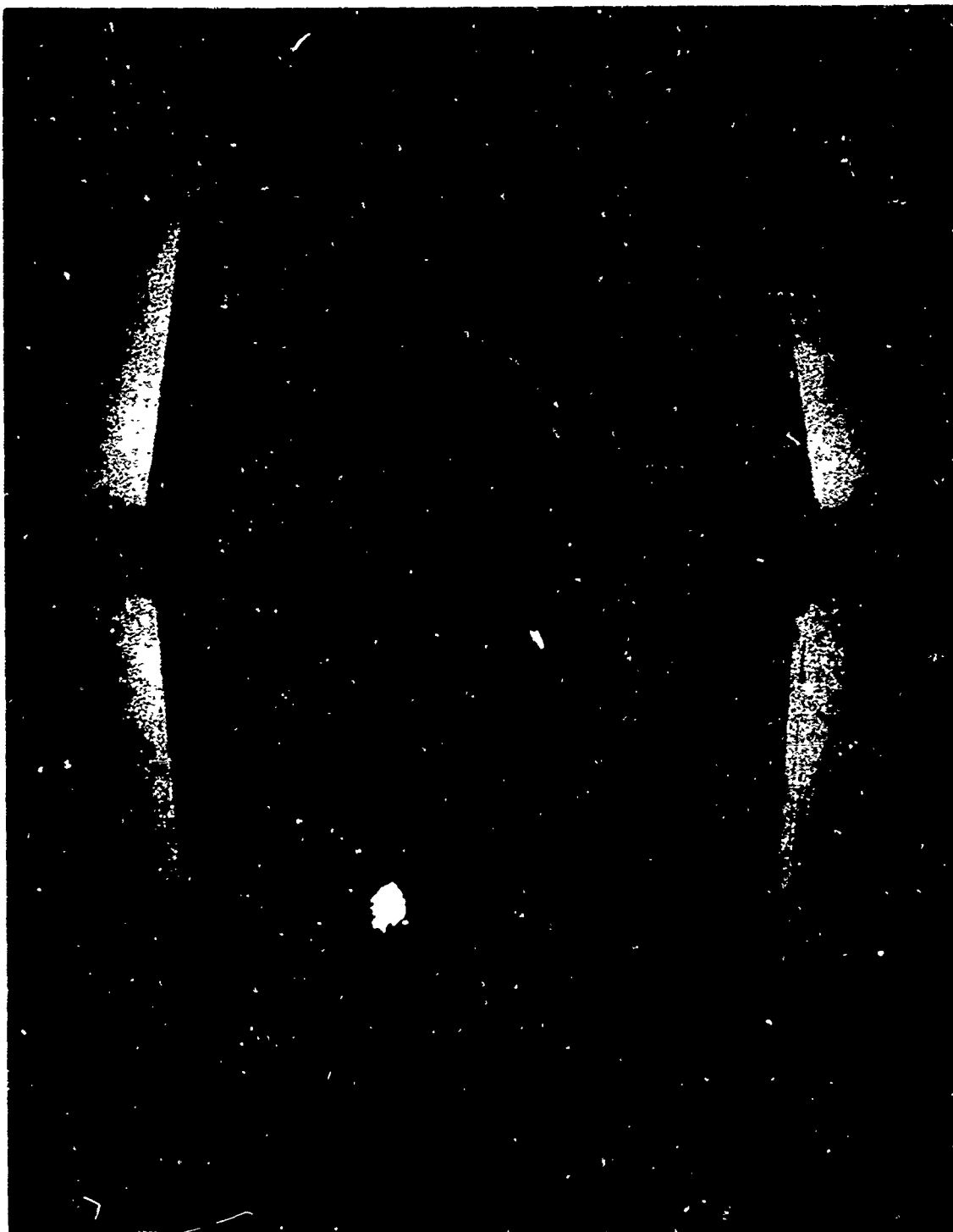


Figure 75 - Flare Cover (Aerodynamic Fairing)



Figure 76 - Mockup Assembly (Front View)

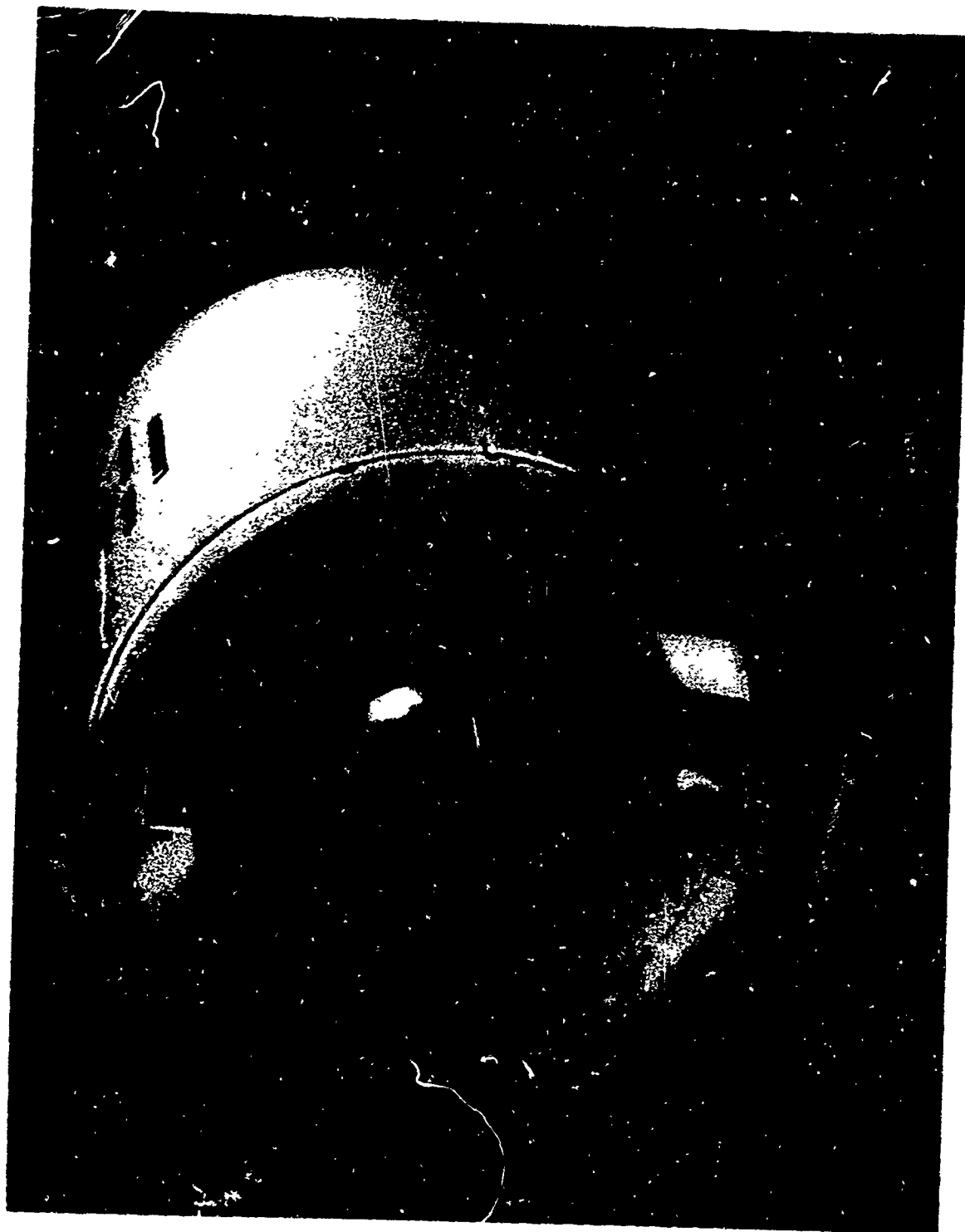


Figure 77 - Mockup Assembly (Rear View)

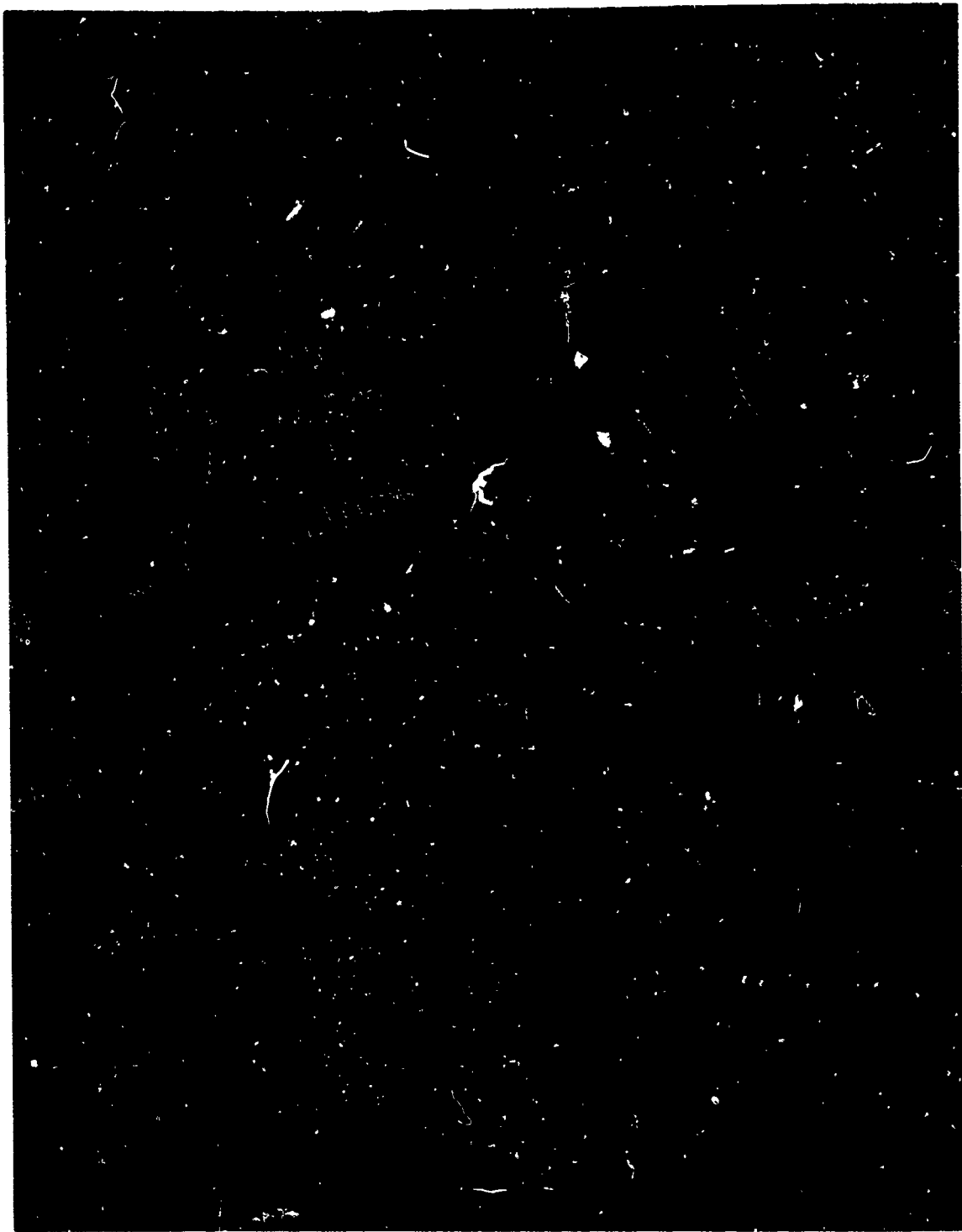


Figure 78 - Mockup Assembly (Side View)

AFFDL-TR-67-192
Volume I



Figure 79 - Flare Cover Jettison



Figure 80 - Uninflated Flare



Figure 81 - Inflated Flare (1 PSI)



Figure 82 - Test Item Deployment

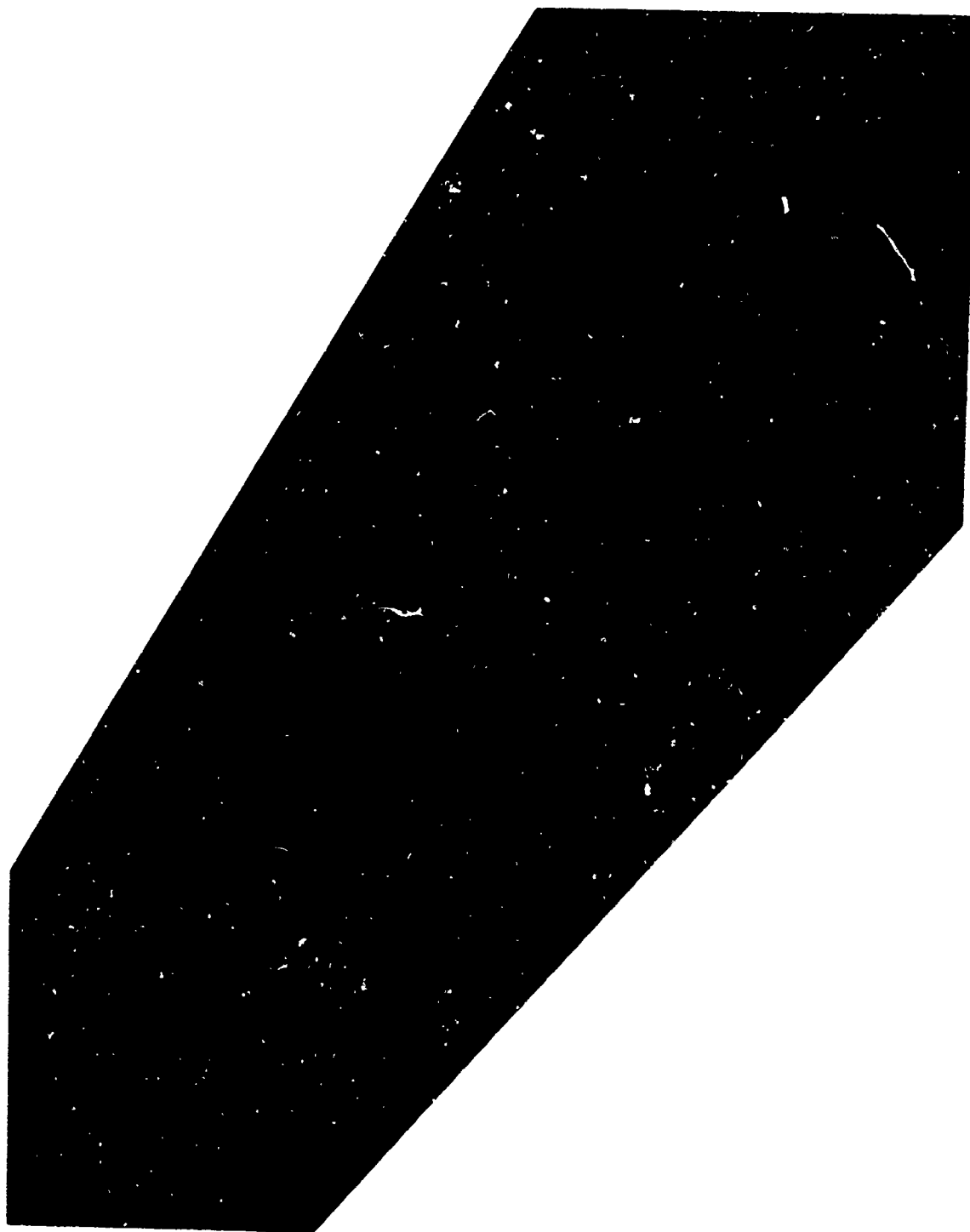


Figure 83 - Test Item Unpackaged



Figure 84 - Test Item Line Stretch



Figure 85 - Test Item Repositioning

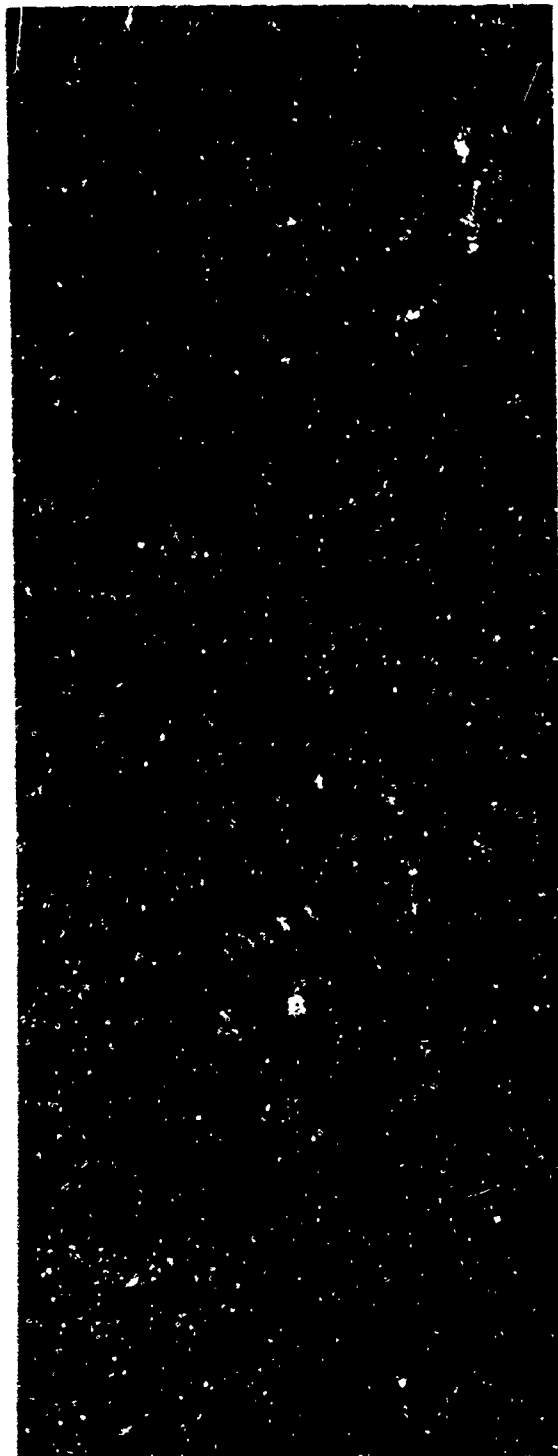


Figure 86 - Recovery Parachute
Deployment

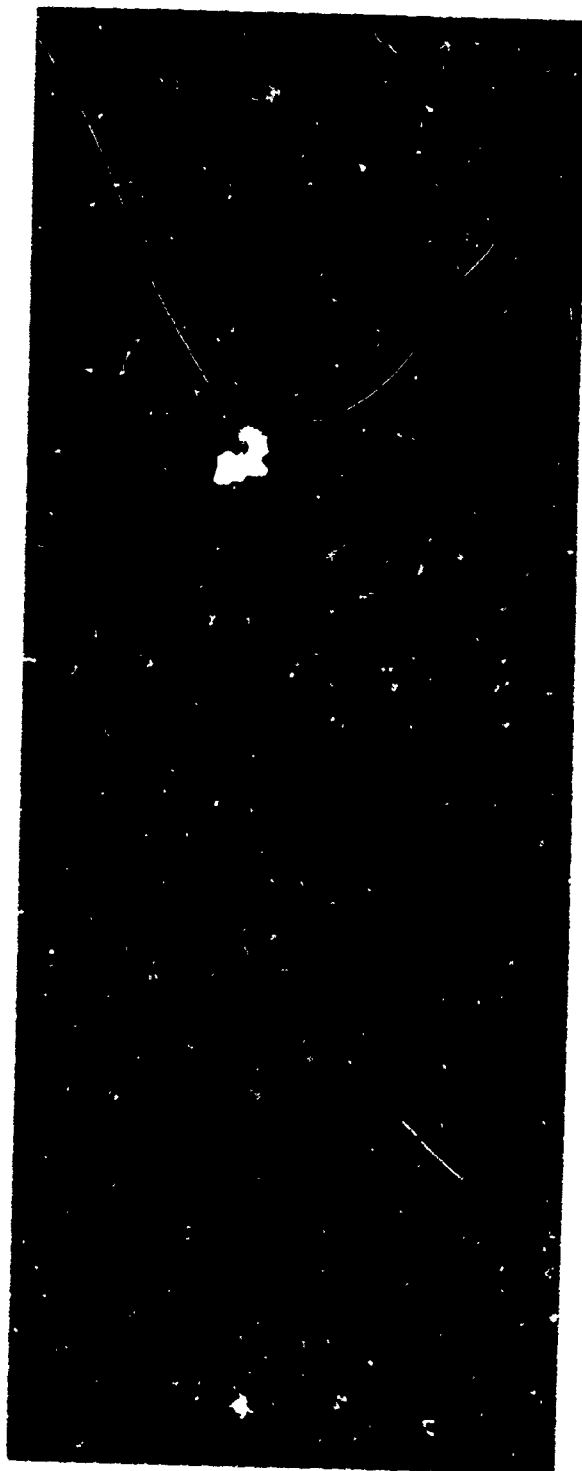


Figure 87 - Recovery Parachute
Line Stretch



Figure 88 - Internal View (Cameras Exposed)



Figure 89 - Flare with 1-psi Inflation Pressure (Top View)



Figure 90 - Flare with 2-psi Inflation Pressure (Top View)

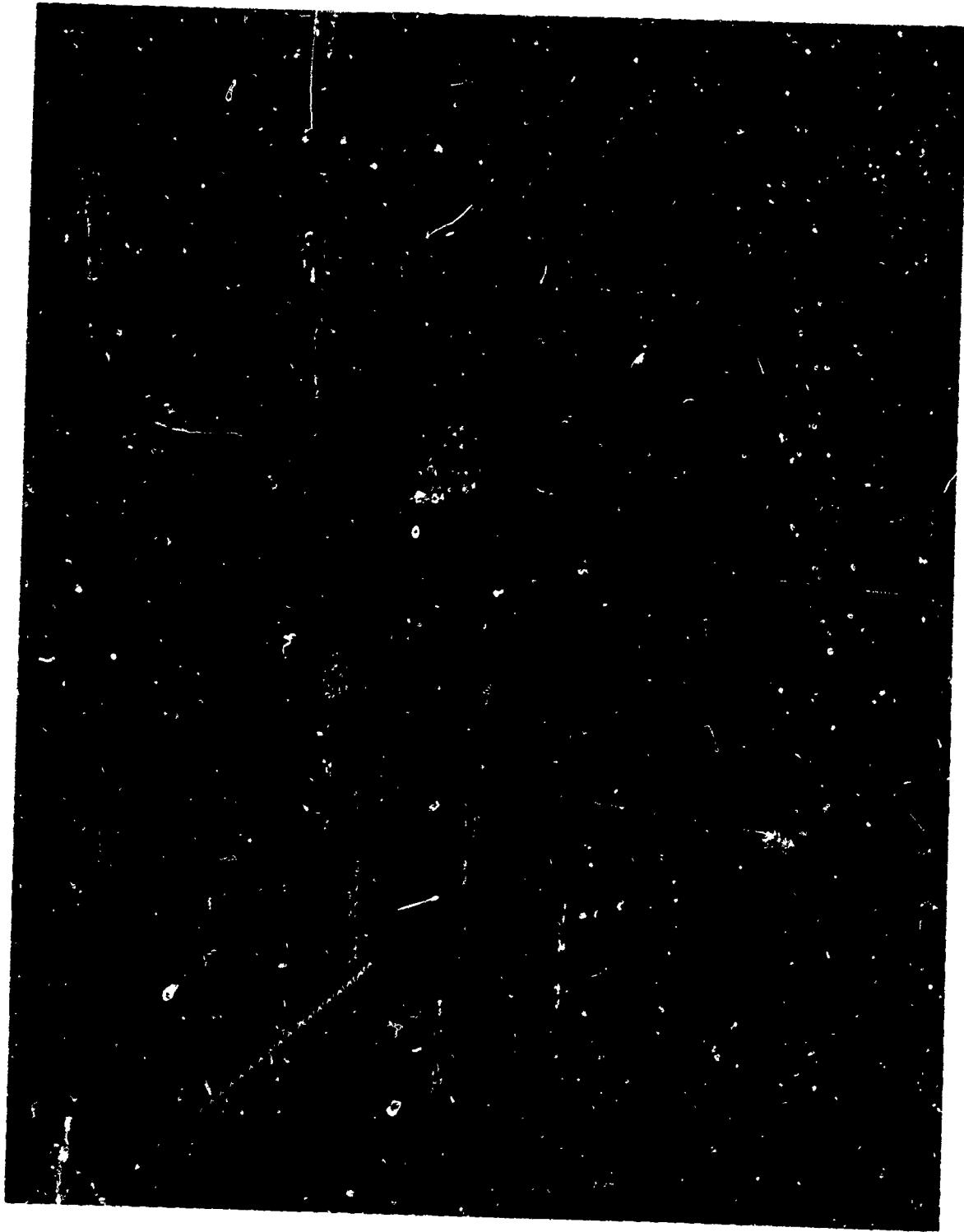


Figure 91 - Flare with 5-psi Inflation Pressure (Top View)

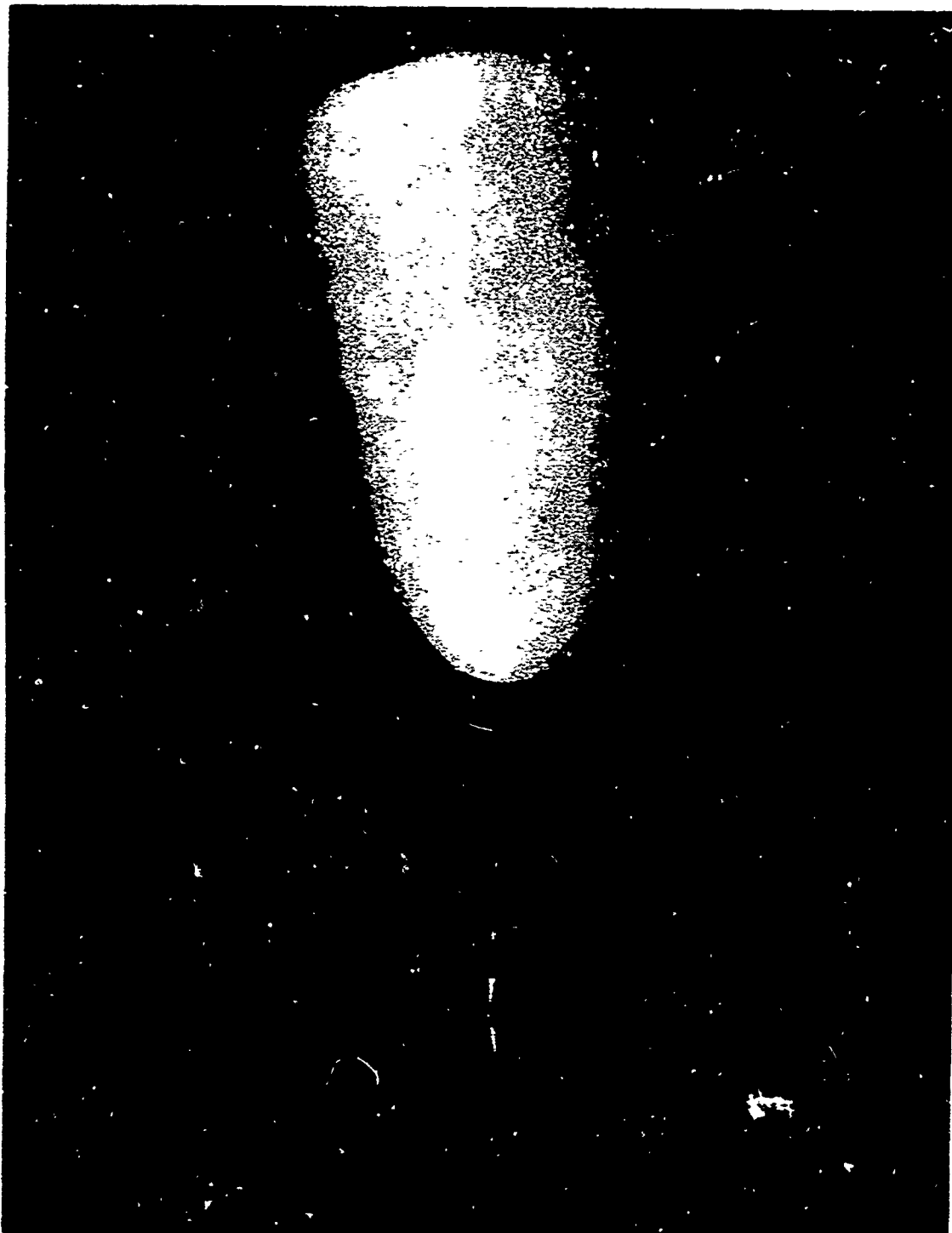


Figure 92 - Flare with 2-psi Inflation Pressure (Side View)

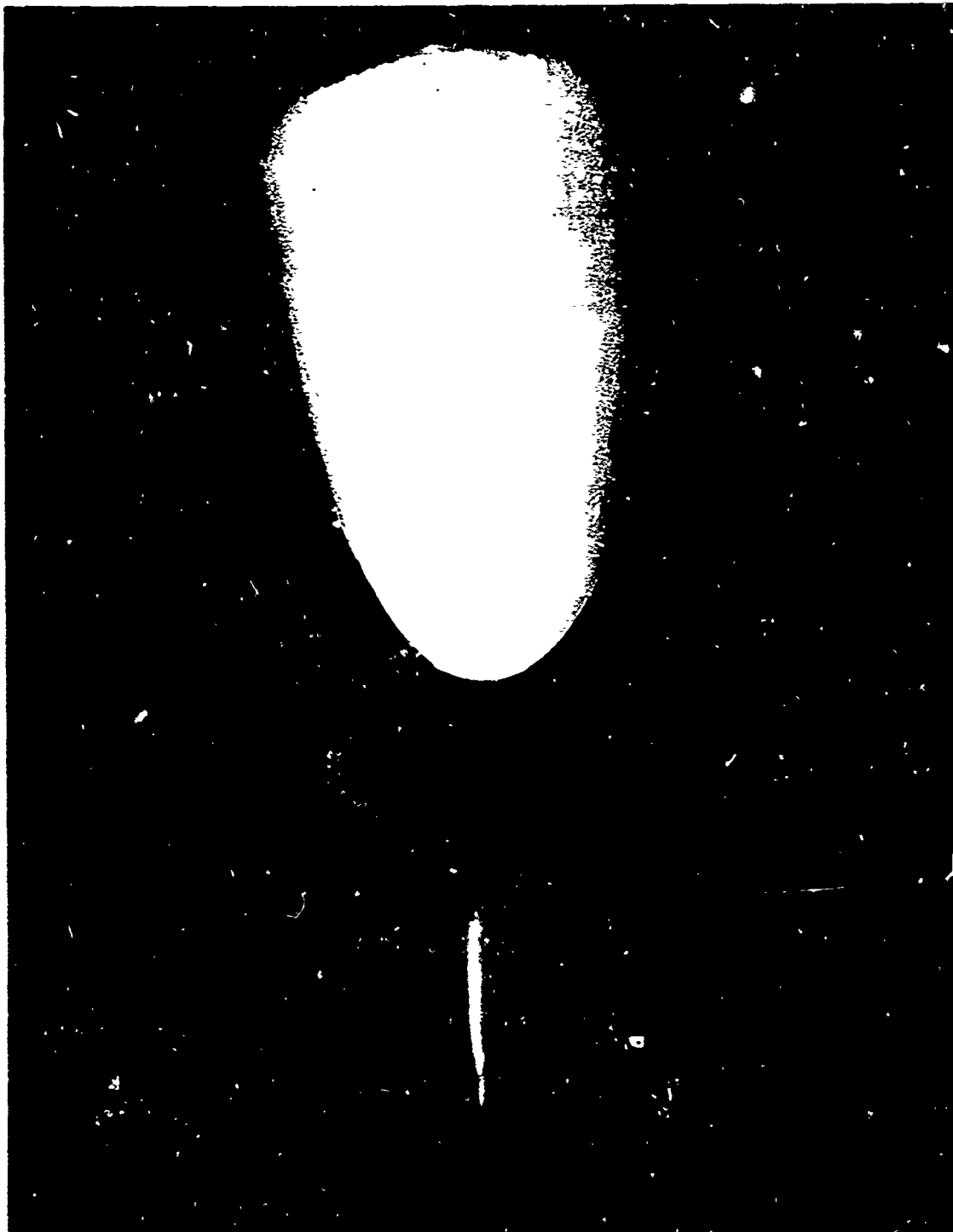


Figure 93 - Flare with 3 1/2-psi Inflation Pressure (Side View)



Figure 94 - Flare with 5-psi Inflation Pressure (Side View)



Figure 95 - Flare with 3 1/2-psi Inflation Pressure (End View)



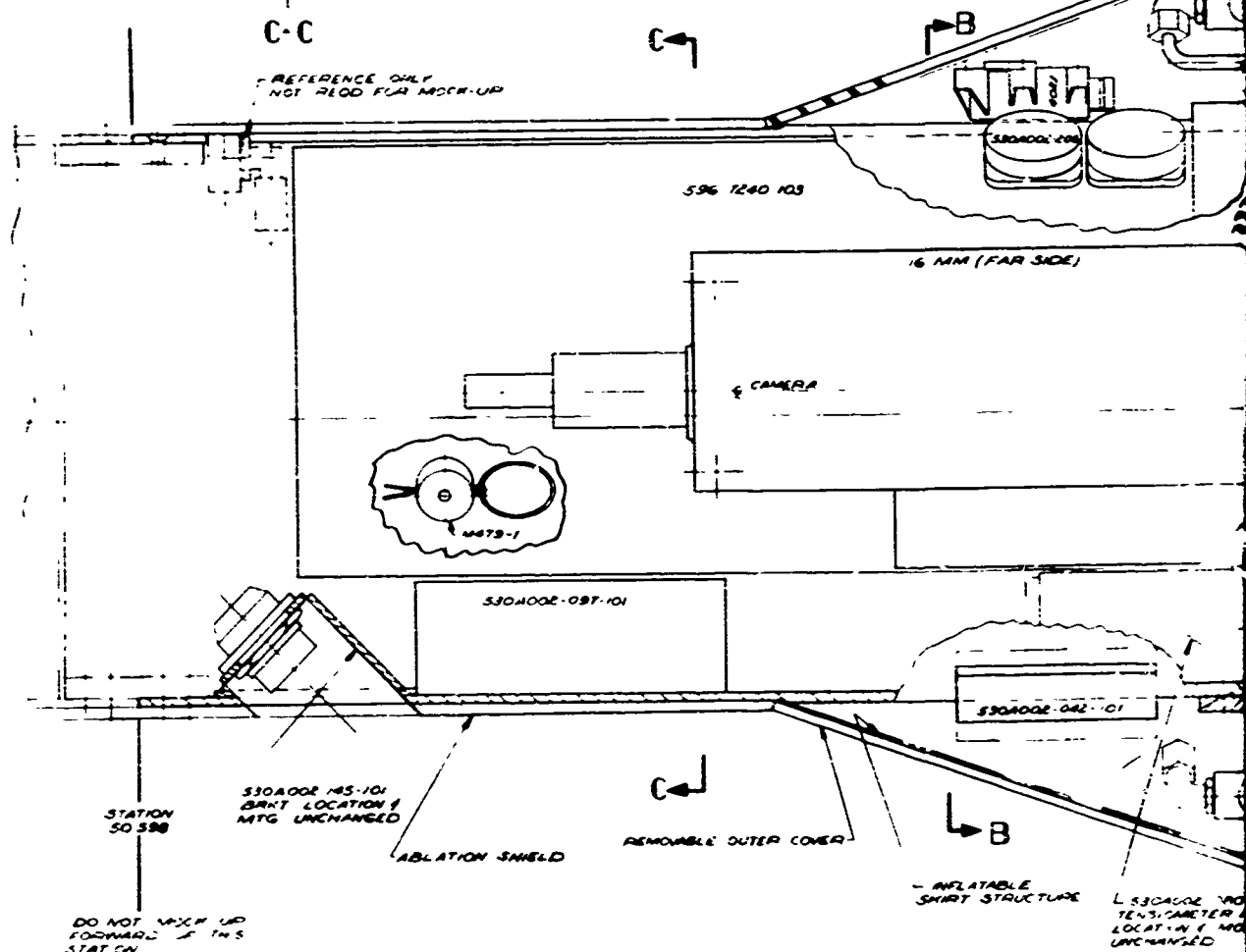
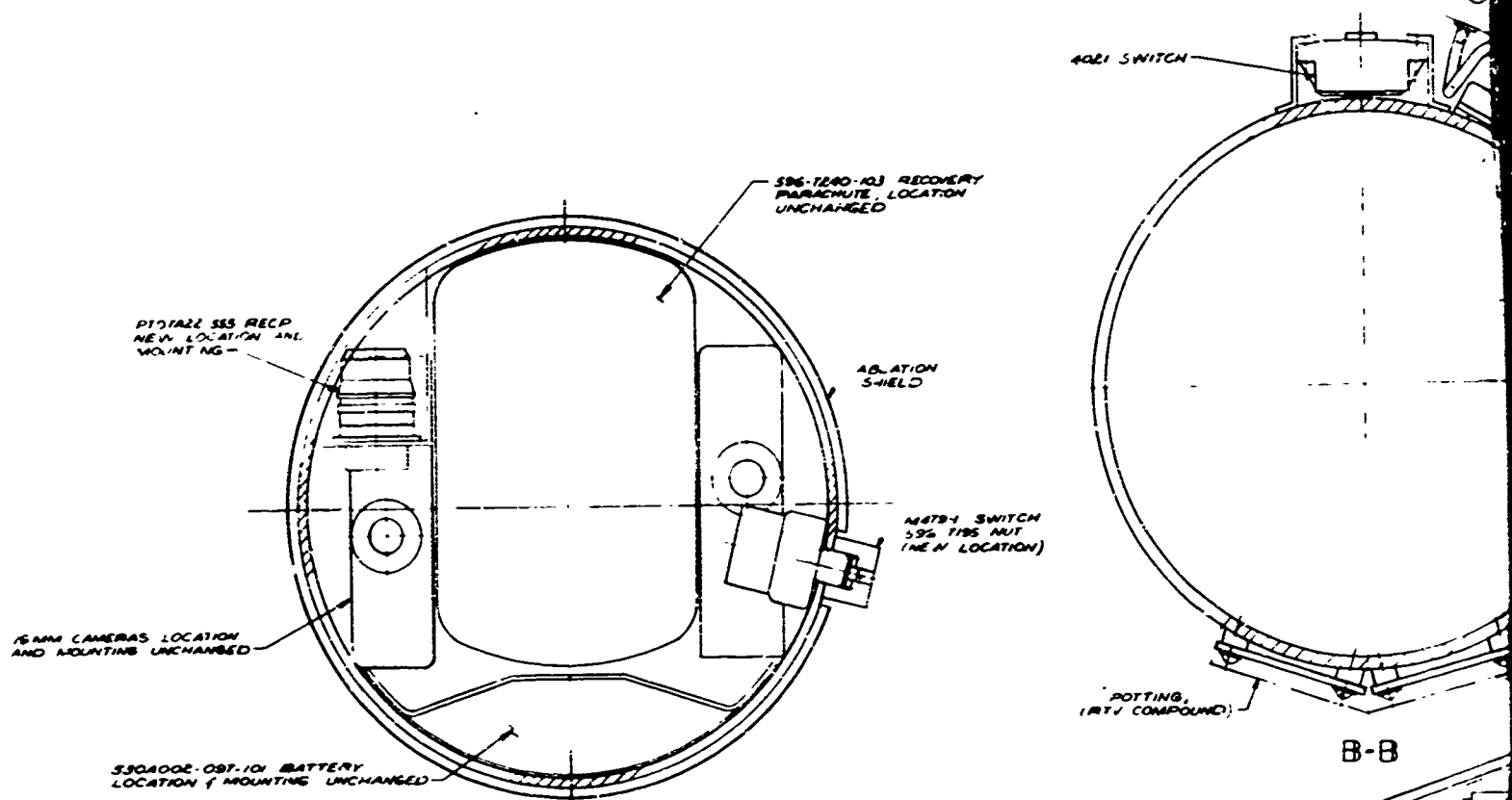
Figure 96 - Flare with 5-psi Inflation Pressure (End View)

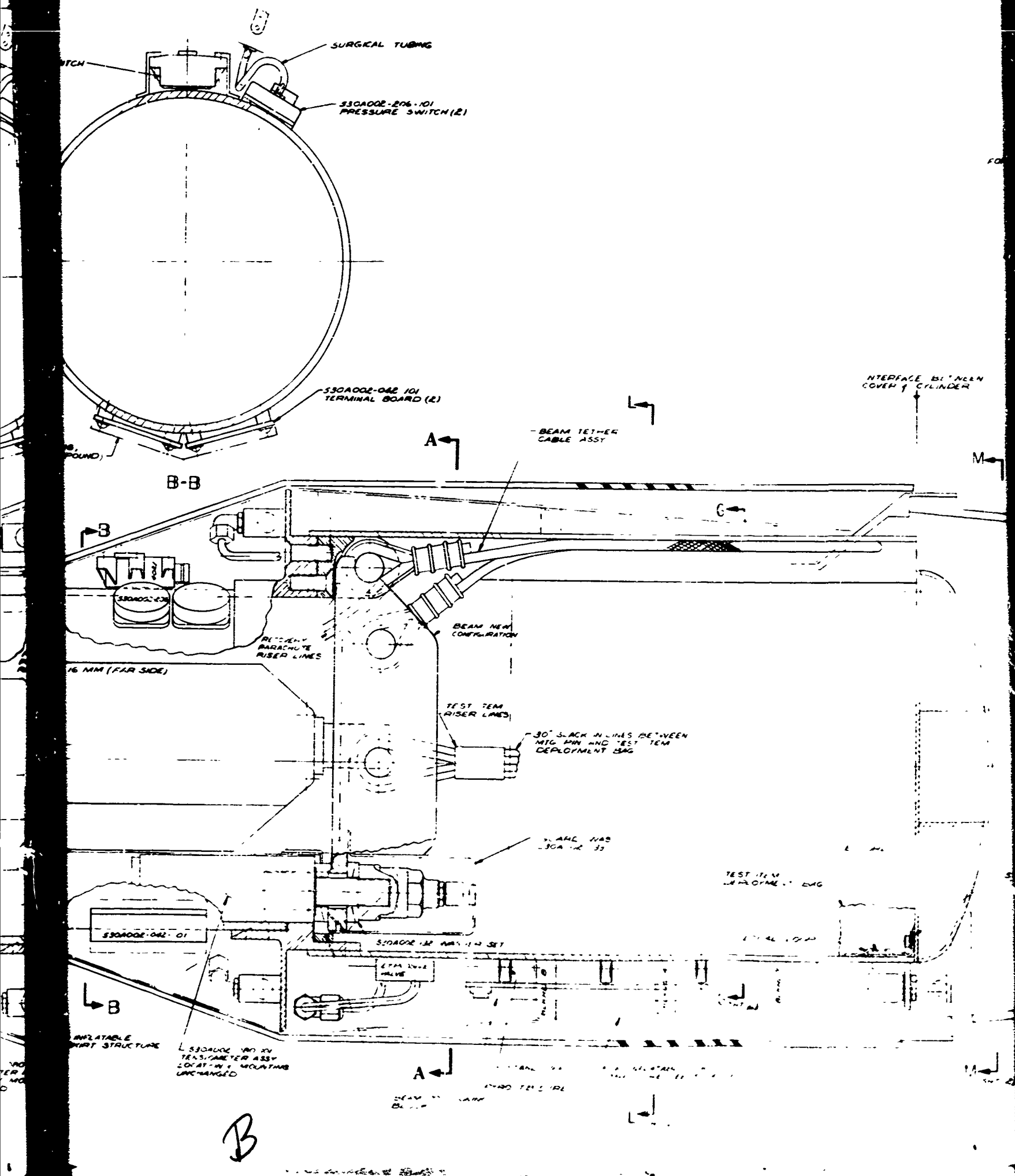
AFFDL-TR-67-192
Volume I

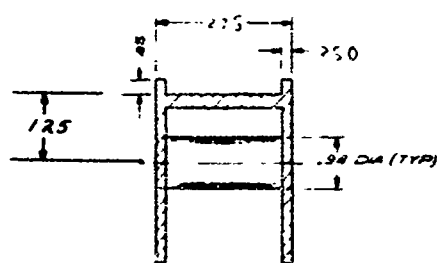
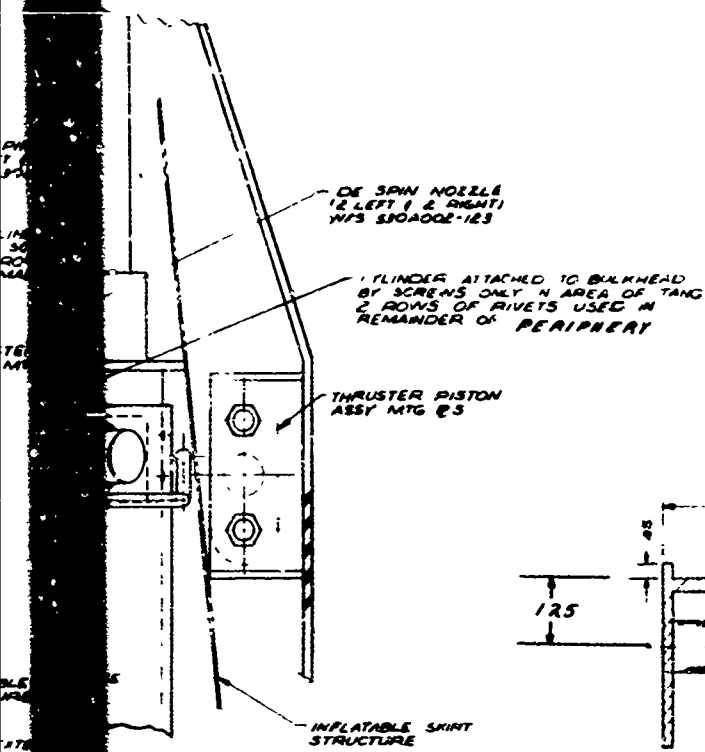
APPENDIX V
ENGINEERING DRAWINGS

Engineering Drawings 580A030 (Sheets 1 and 2) and 580A031 (Sheets 1 through 3) are included in this appendix to give a detailed description of the engineering mockup assembled during the EUREKA program. These drawings also would serve, except for minor deviations, as design drawings for any flight test hardware.

(Reverse is blank)



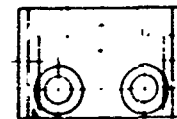




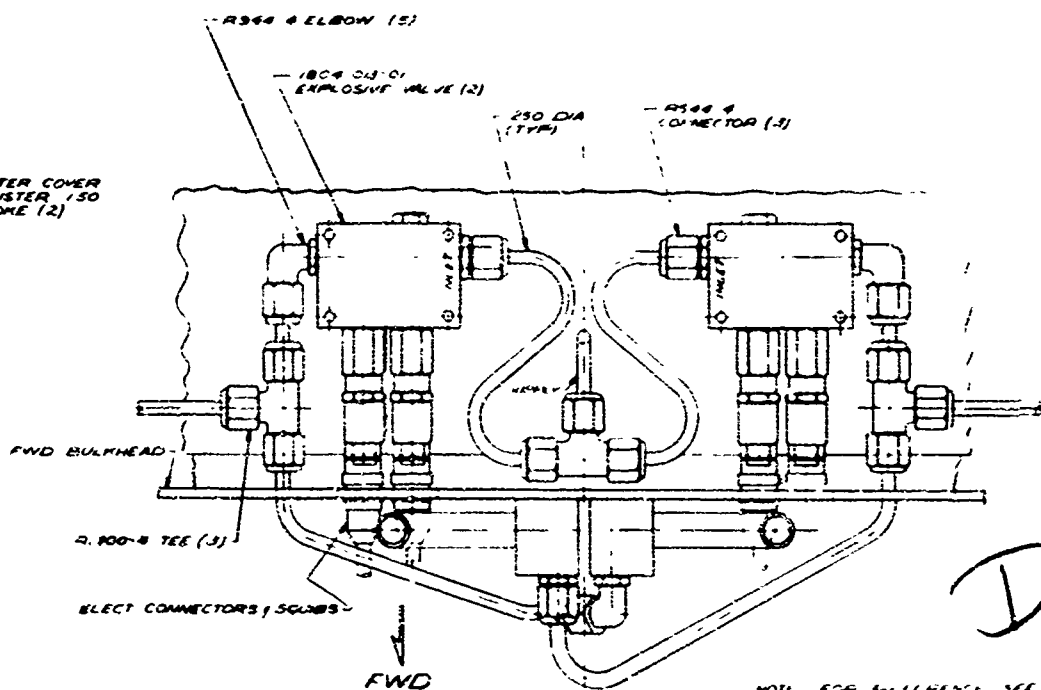
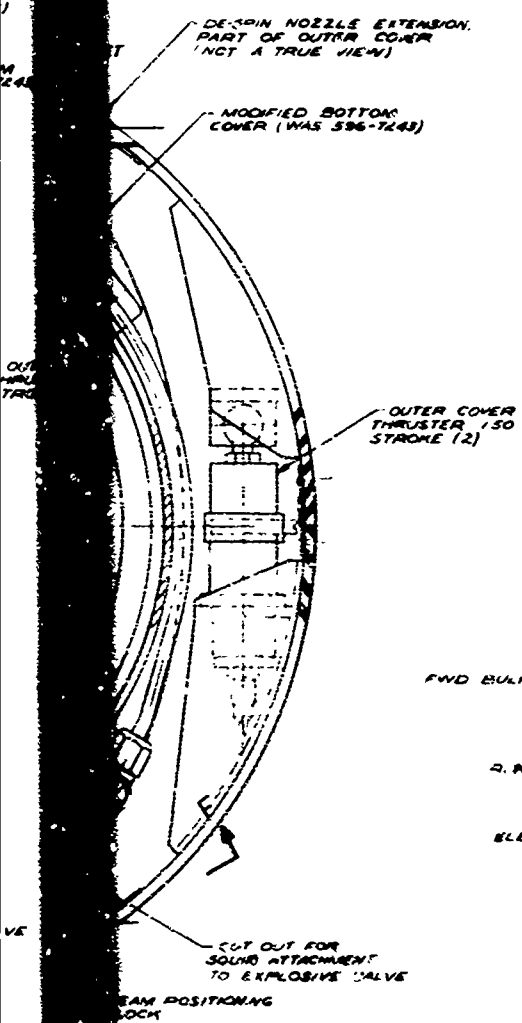
D-D
BEAM CROSS SECTION



E-E
CROSS SECTION
OF HINGE BRACKET



RELIEF
FOR BEAM
FLANGES



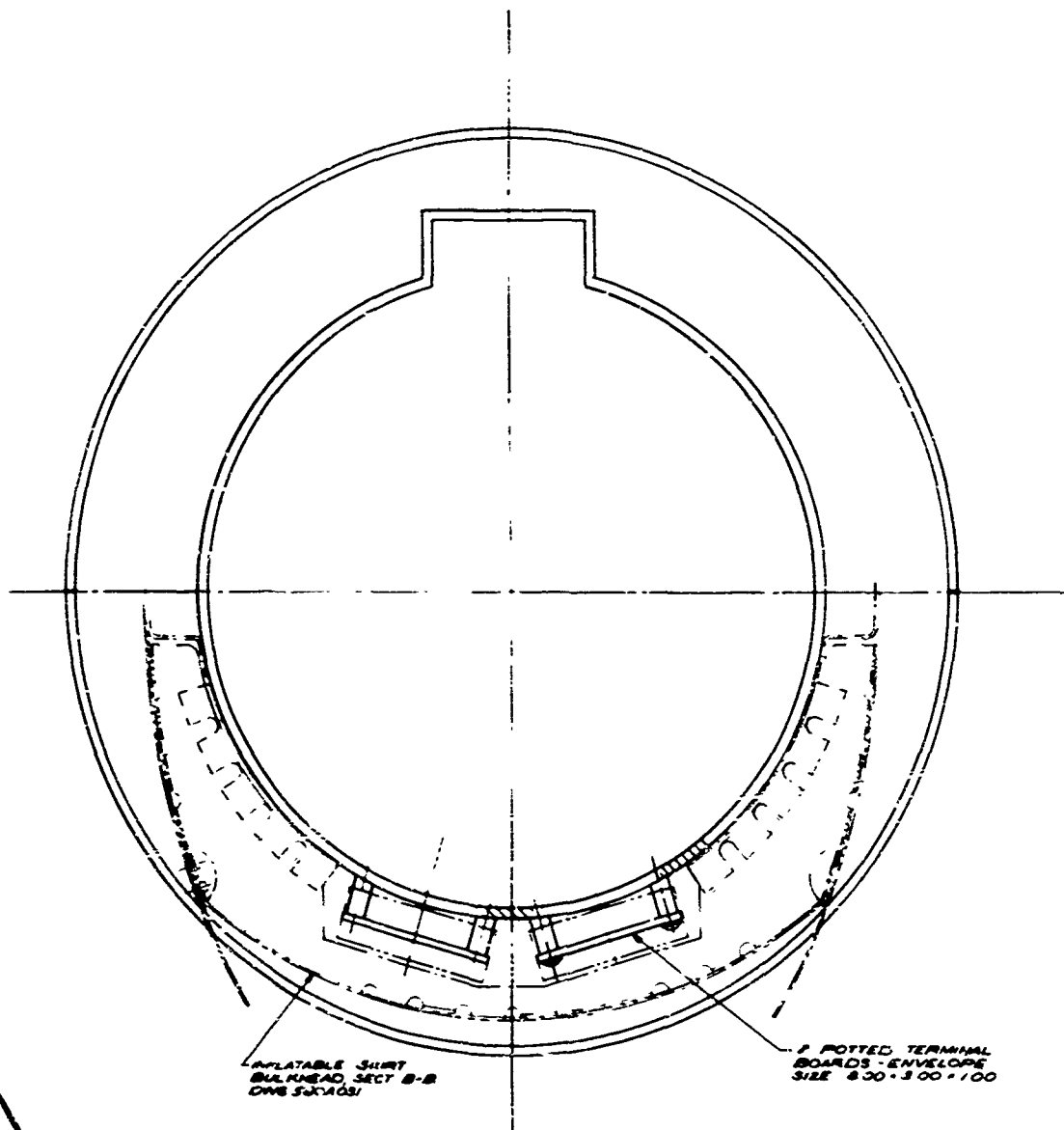
F-F

DE-SPIN VALVES & TUBING

NOTE FOR ELEMENTS SEE DRAWING
SBOACOE-010
PART NO TO BE SBOACOE-01

CONT'D	GOODYEAR AEROSPACE CORP
REV	REV
STRESS	STRESS
TECH	TECH
DATE	DATE
APPROVAL	APPROVAL
CUSTOMER APPROVAL	CUSTOMER APPROVAL
	23220
	5874030
	1000

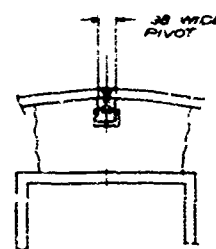
LAST SECTION F-F



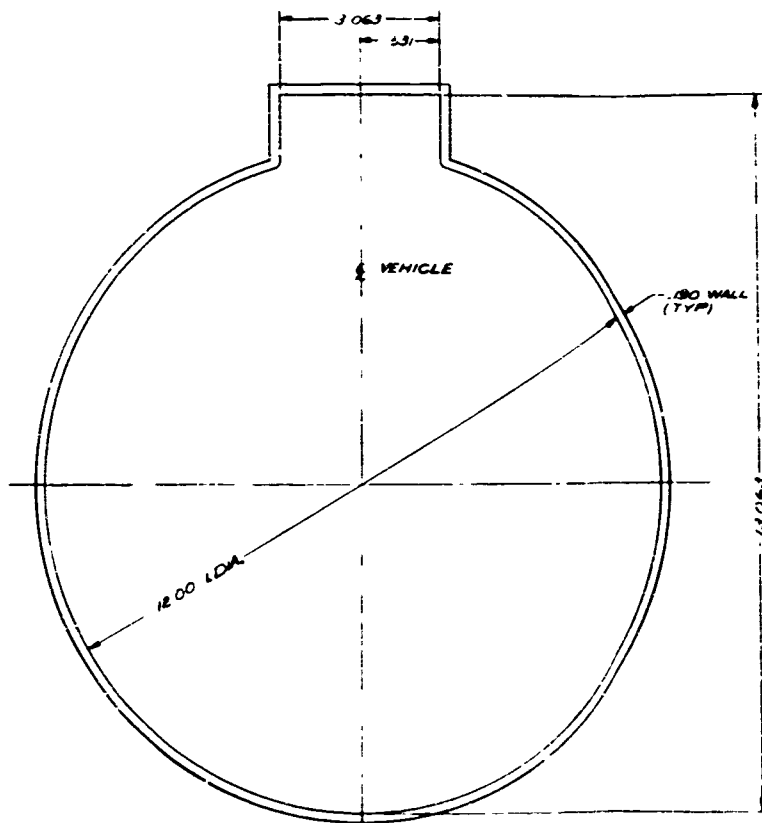
INFLATABLE SHIRT
BULKHEAD, SECT B-B
DWS 50X100

2 POTTED TERMINAL
BOARDS - ENVELOPE
SIZE 800-300-100

L=L
A/T PYROTECHNIC TERMINAL BOARD



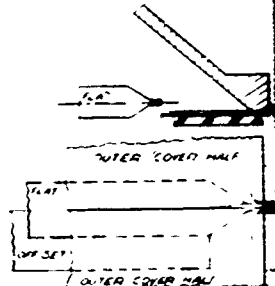
A



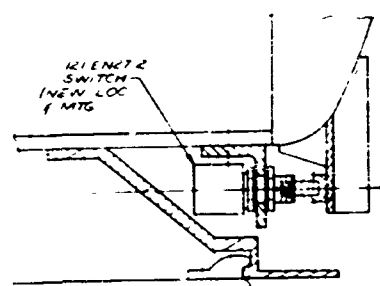
G-G
CROSS SECTION OF
INNER CYLINDER

FIBERGLAS
OUTER SHELL

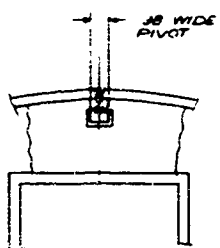
TEST ITEM CONTAINER
THRUSTERS 2 50 STROKE (2)



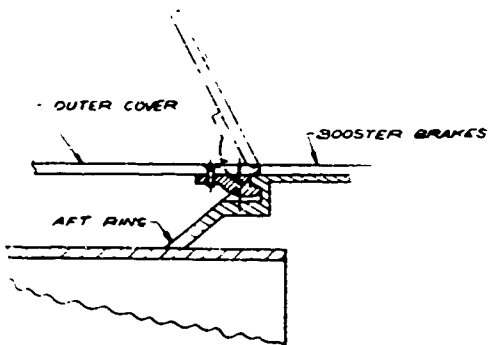
OUTER COVER RESTRAINT
PIN AT BOTH SPILT LINES



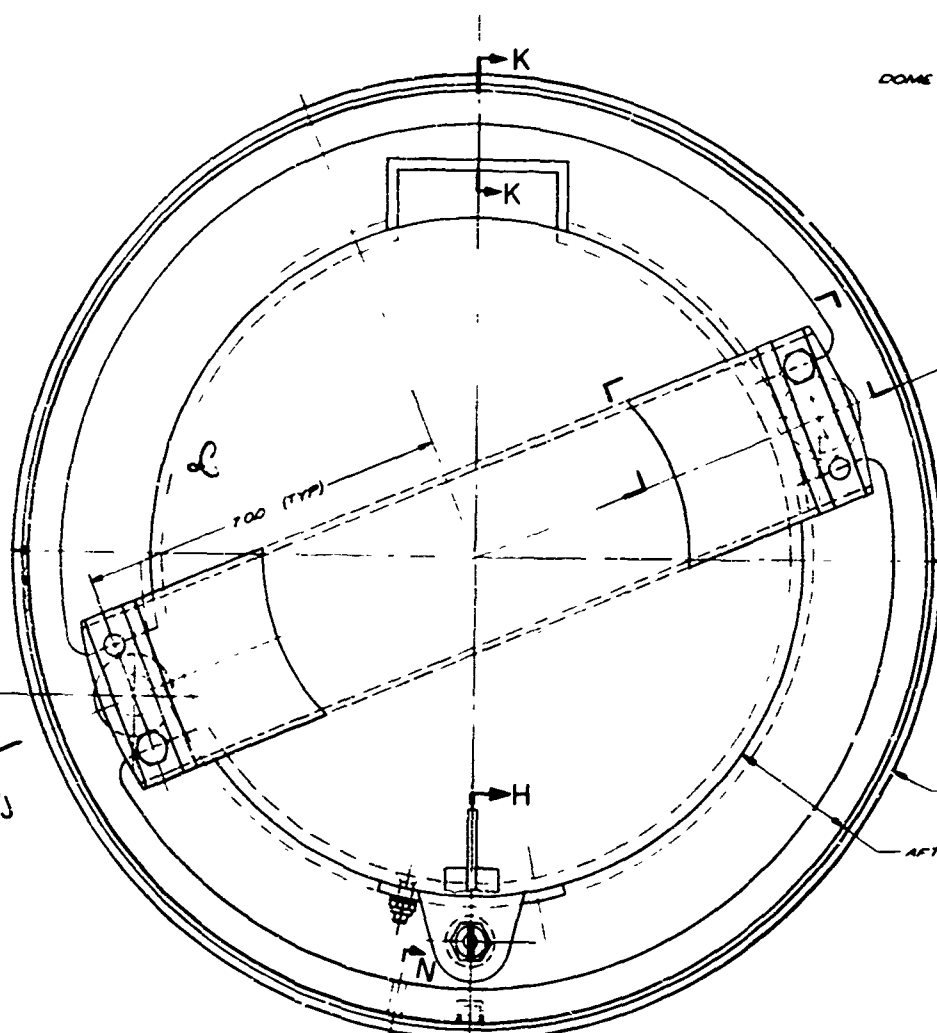
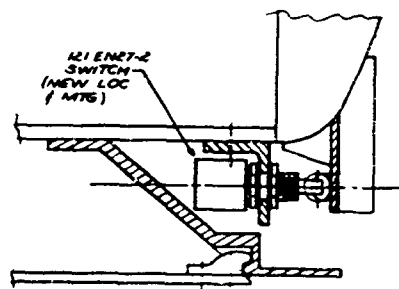
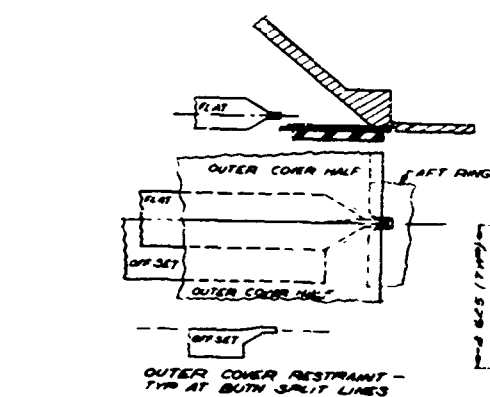
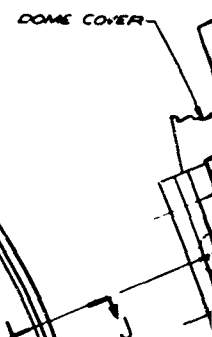
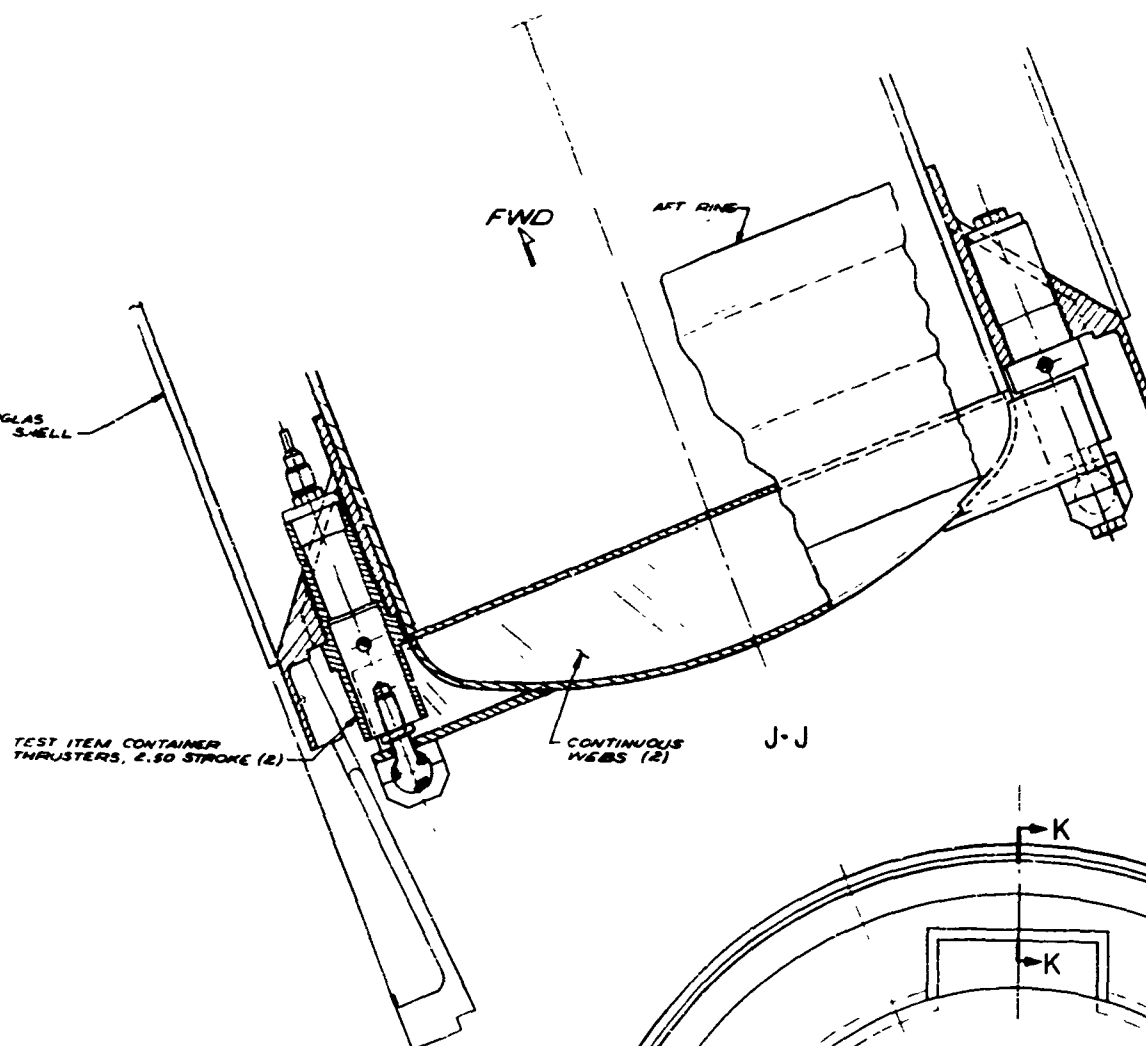
H-H
OUTER COVER PIVOT 2 0 100°



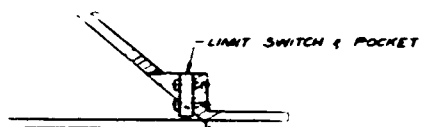
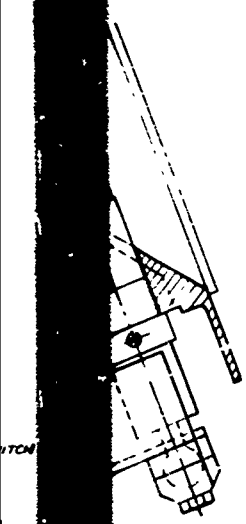
B



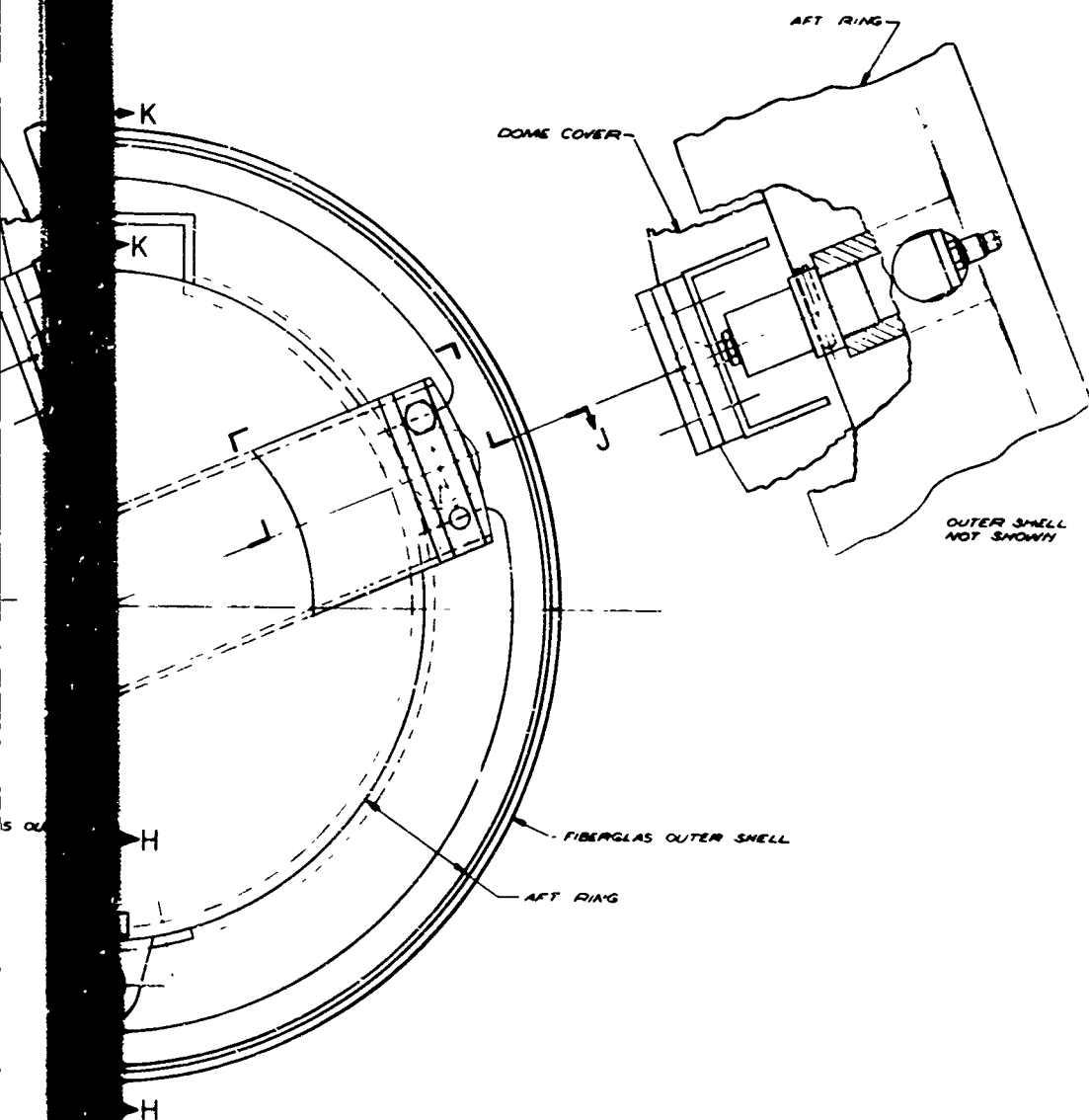
K-K
OUTER COVER PIVOT 2 0 100°



BOOSTER ADAPTER RING NOT SHOWN
THIS VIEW

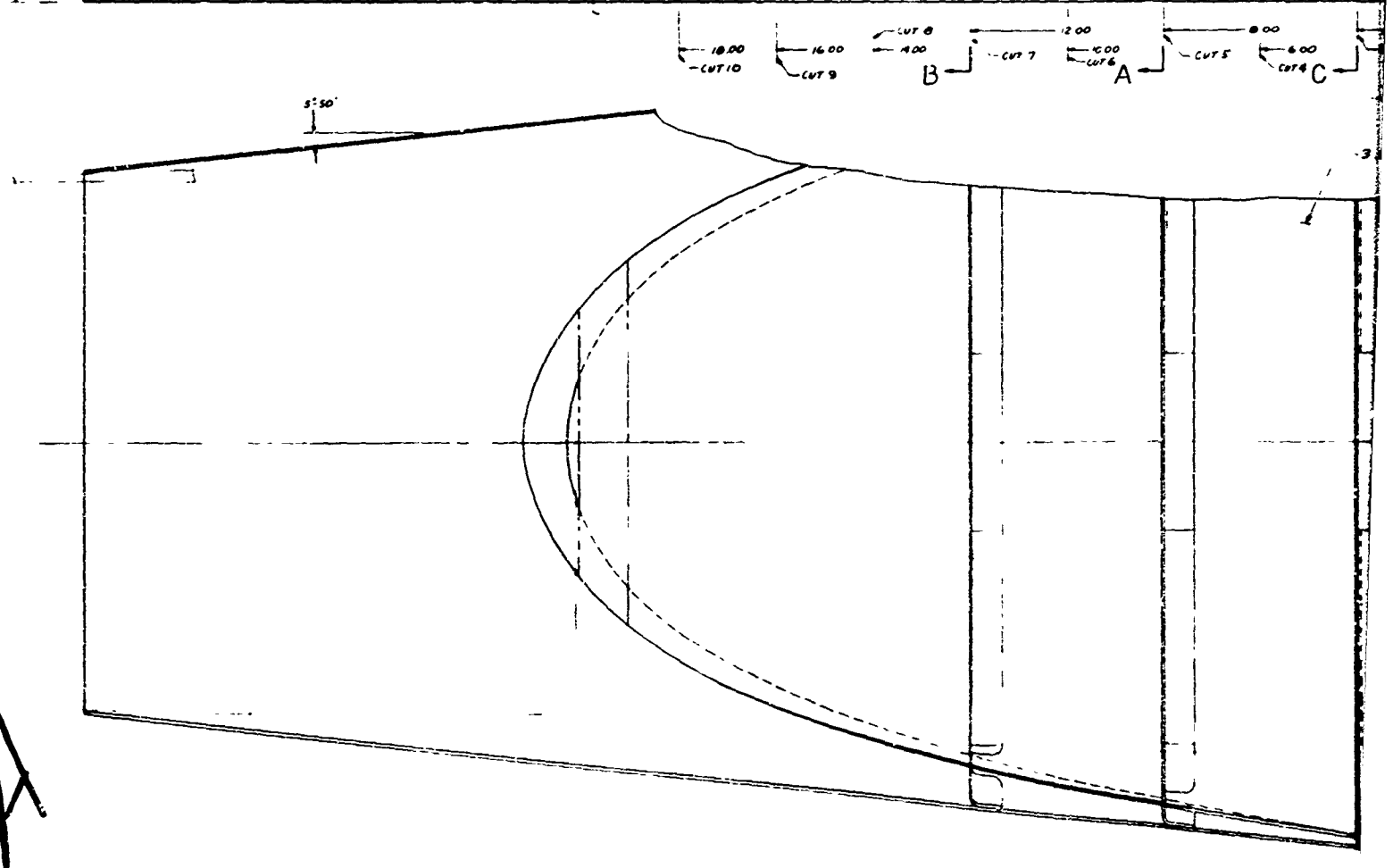
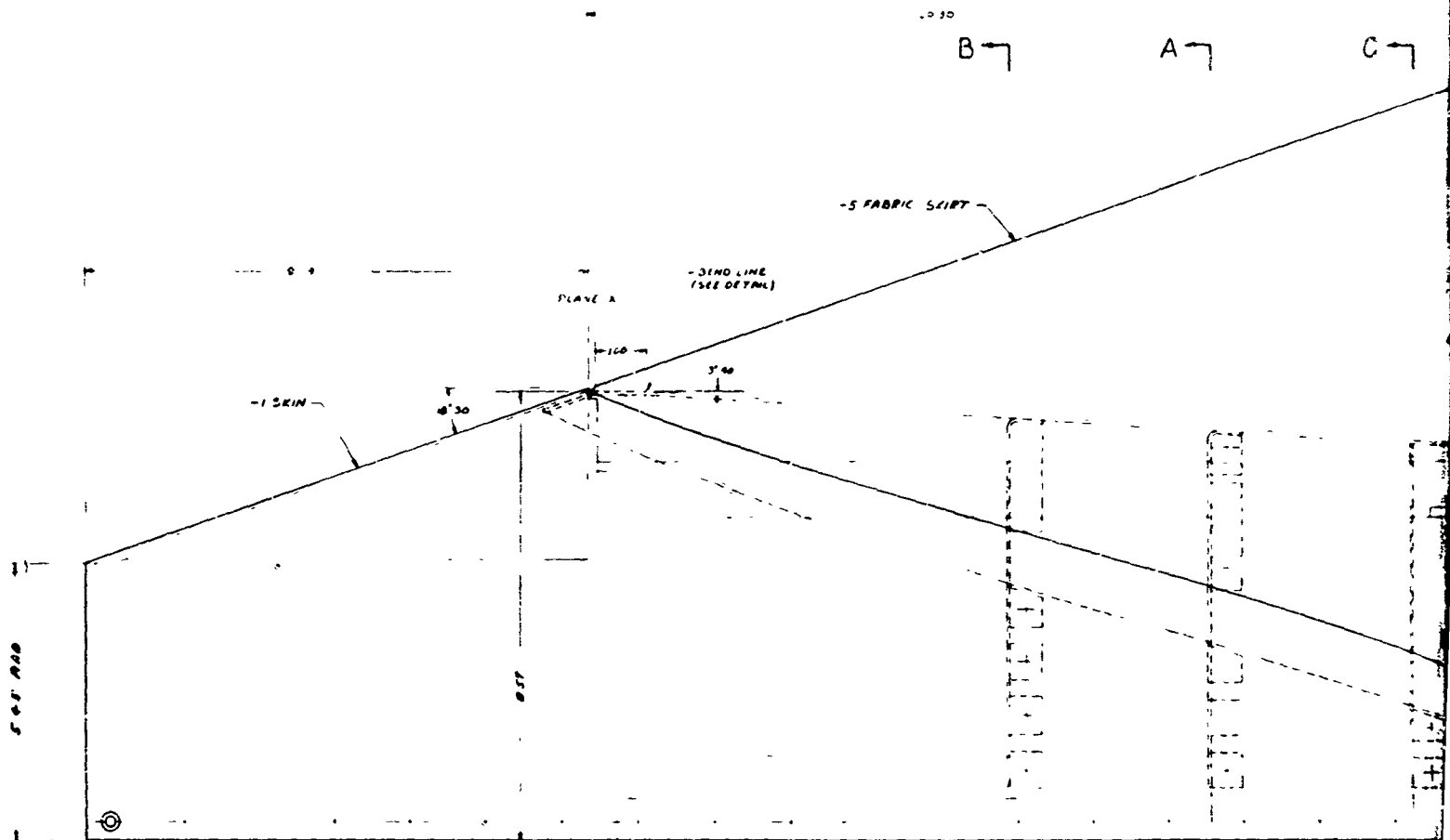


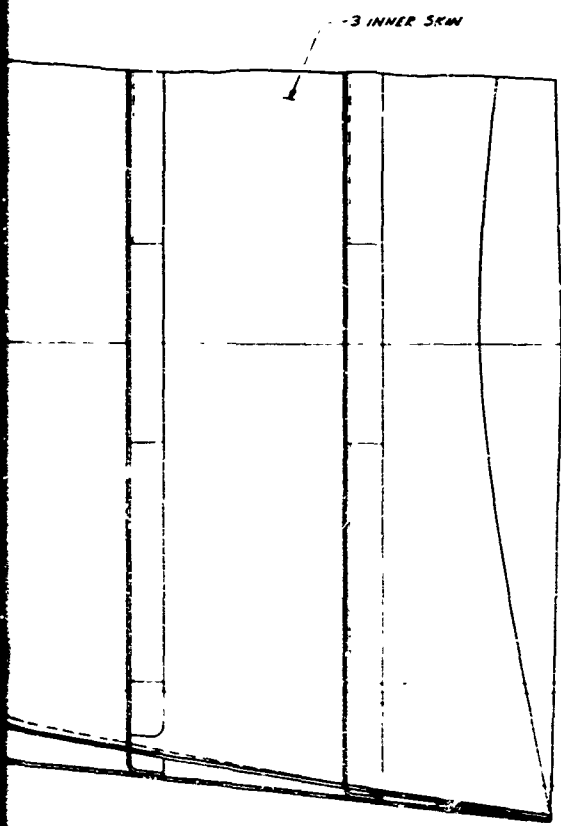
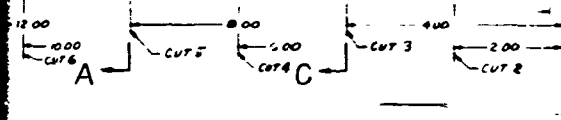
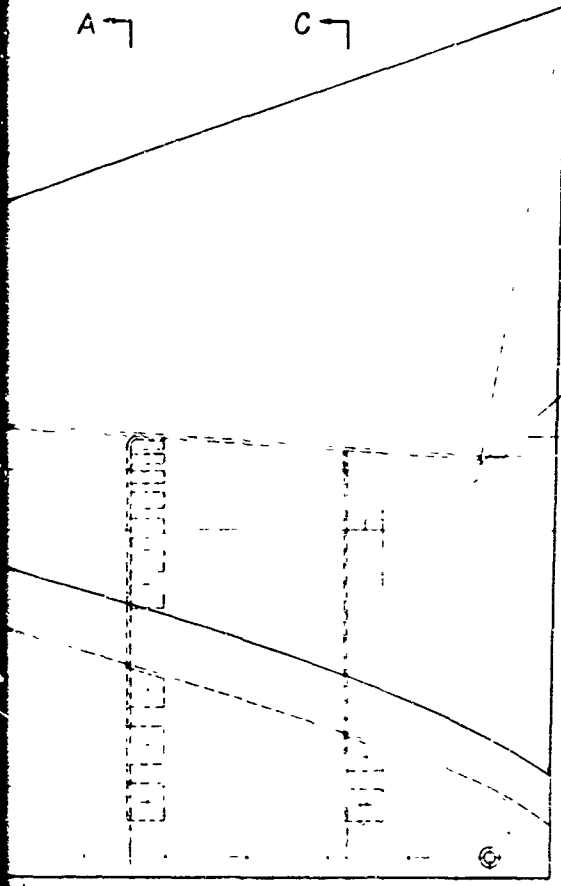
N-N
OUTER COVER LIMIT
SWITCH INSTL



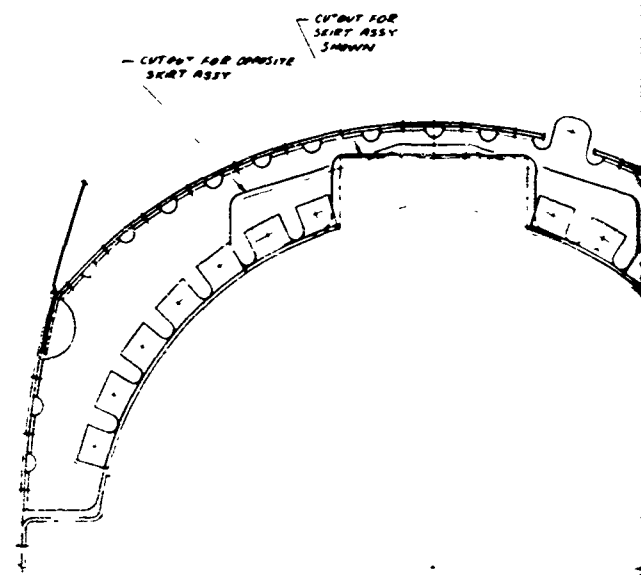
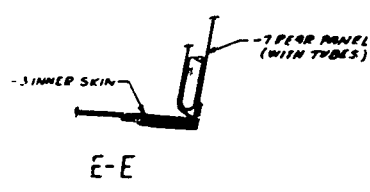
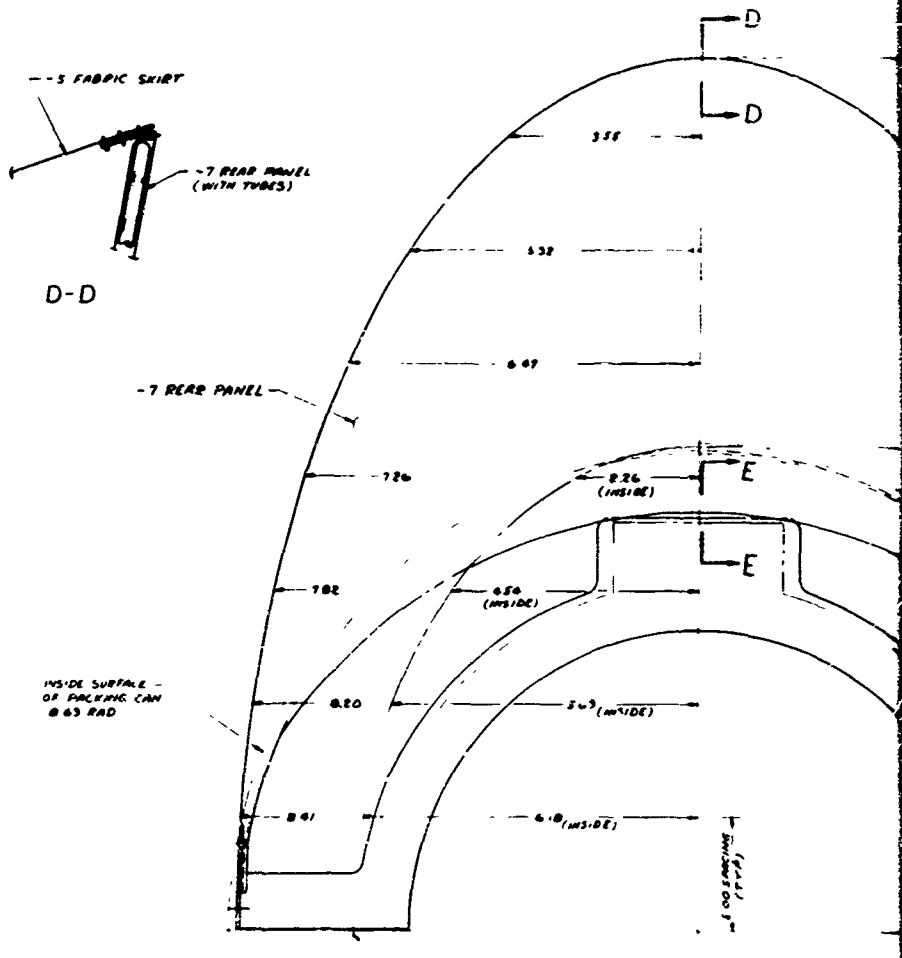
D

FILE	CODE	DRAWING NO.
	IDENT NO.	58CA030
SCALE 1/2	SHEET 2	

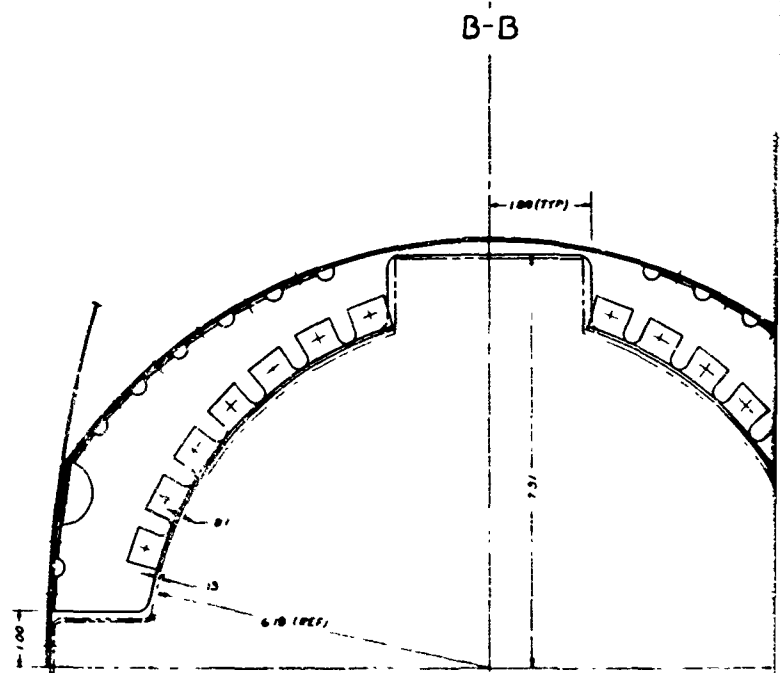
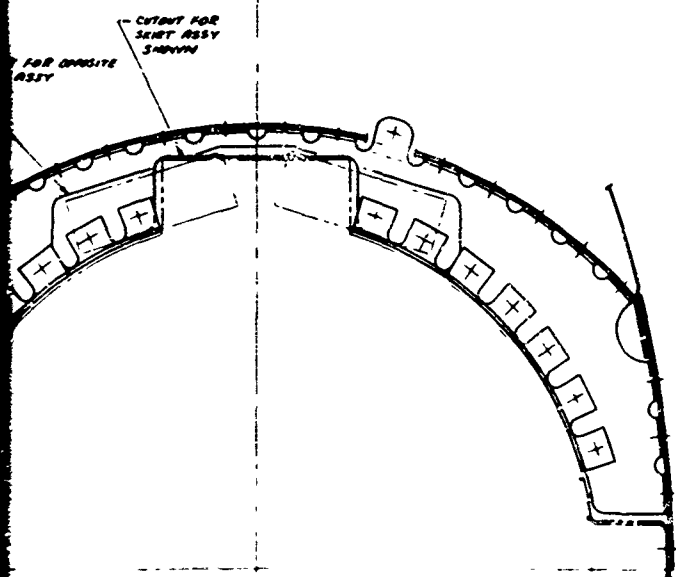
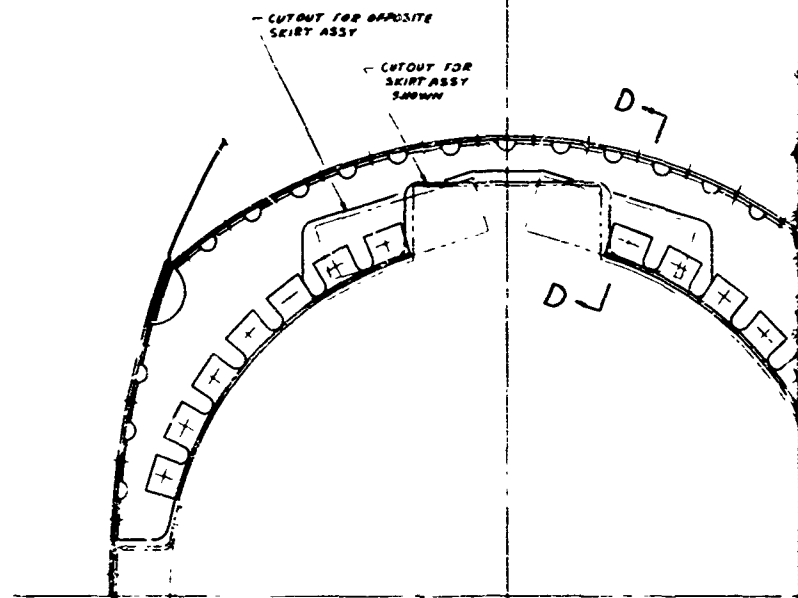
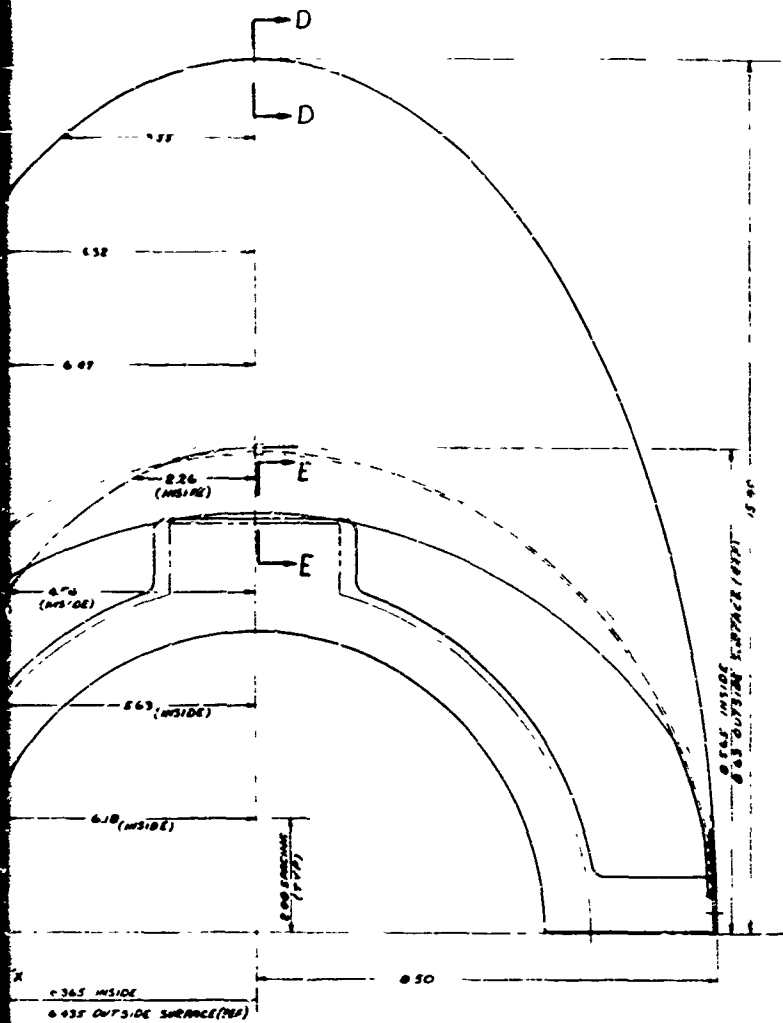




B



A-A



A-A

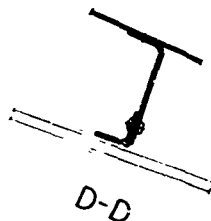
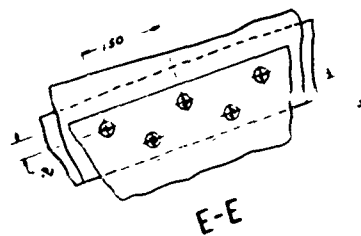
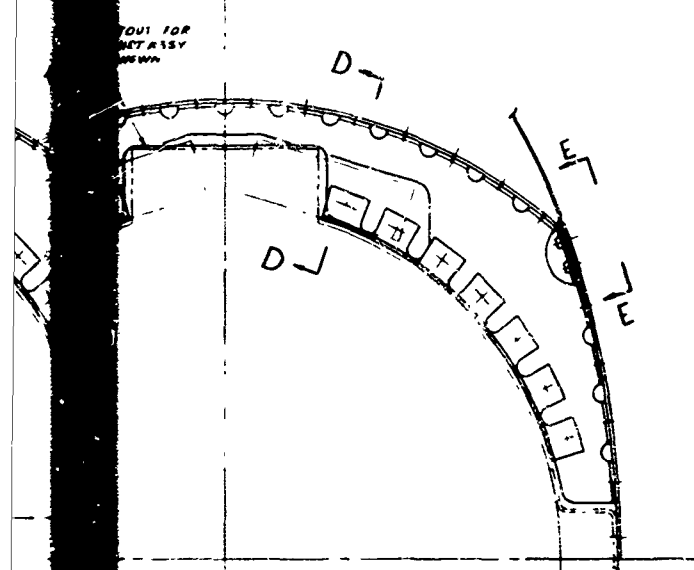
C

B-B

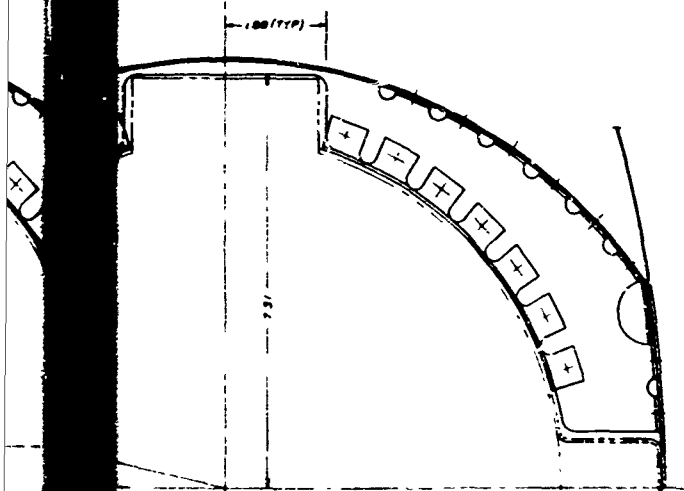
C-C

DATE

YOU FOR
NET ASSY
AND 6000



B-B

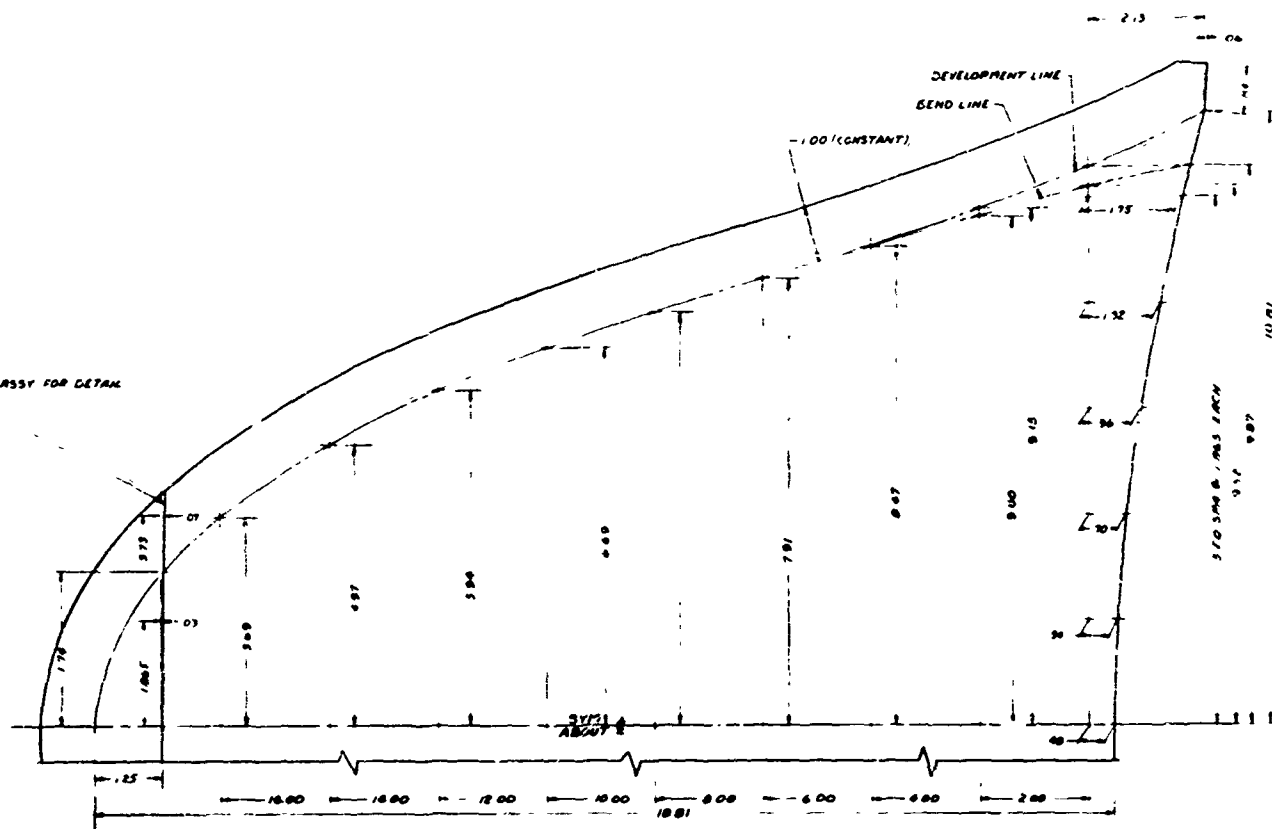


C-C

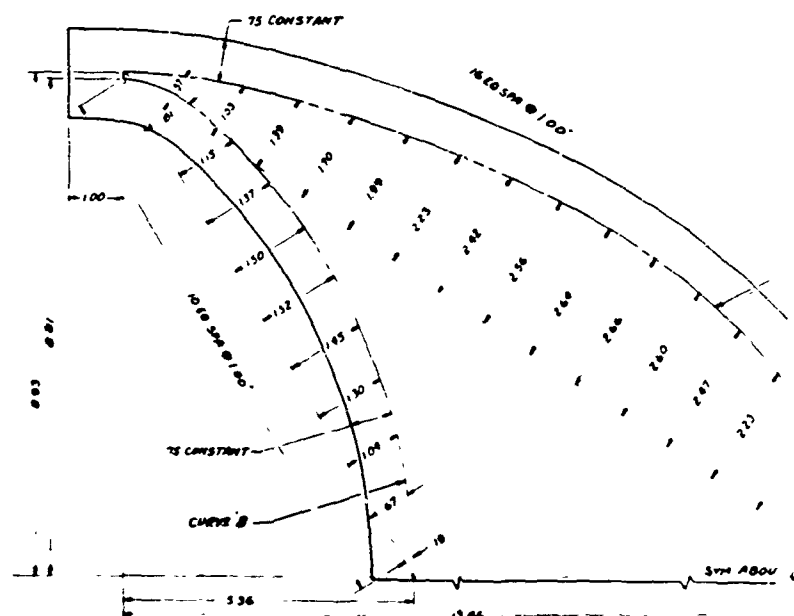
D

GOODYEAR AEROSPACE			
CORPORATION			
SKIRT ASSY			
EUREKA MOCKUP C			
PRELIMINARY DESIGN STUDY			
DATE	BY	CHKD BY	APP'D BY
10/25/70	WJL	WJL	WJL
CUSTOMER APPROVAL		DATE	7/5/70
BY		DATE	5/80A731

SEE ASSY FOR DETAIL

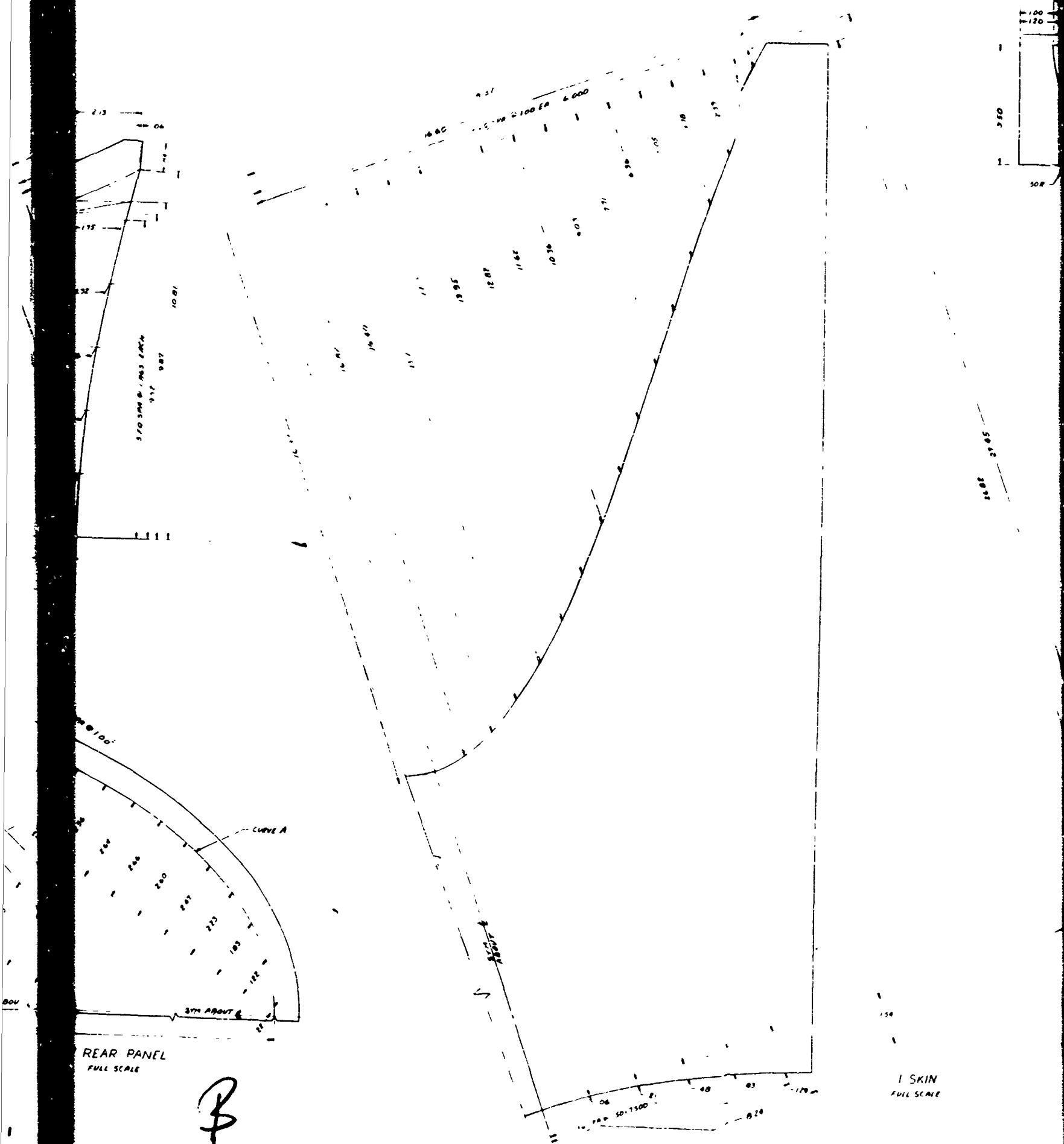


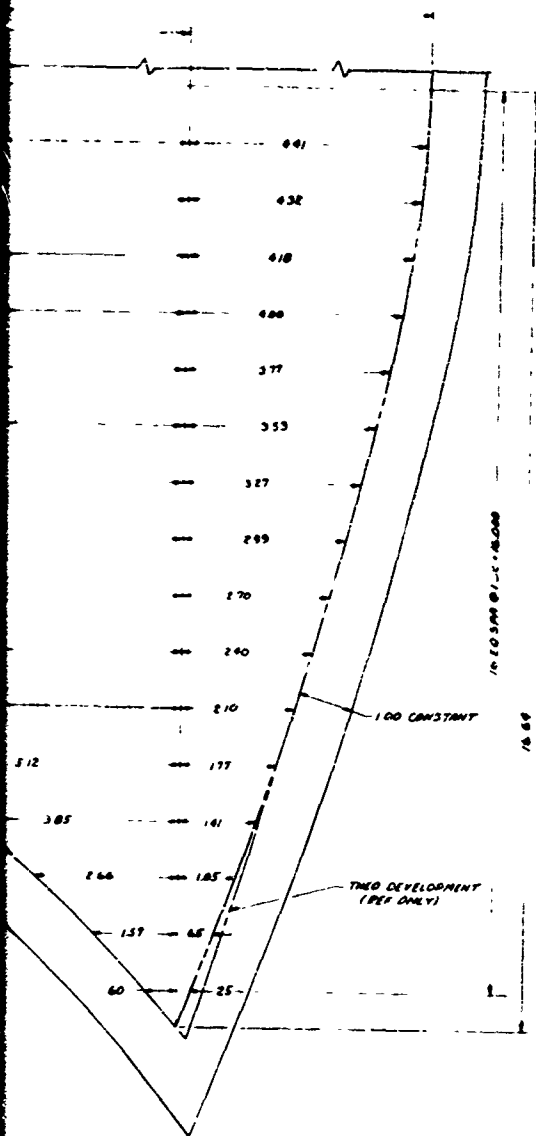
-3 INNER SKIN
FULL SCALE

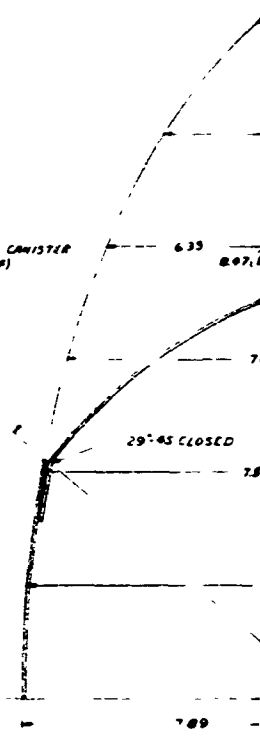
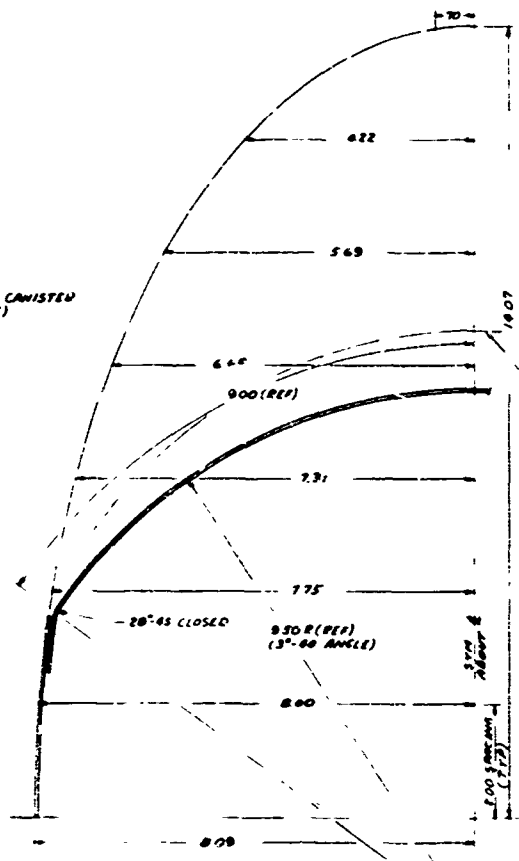
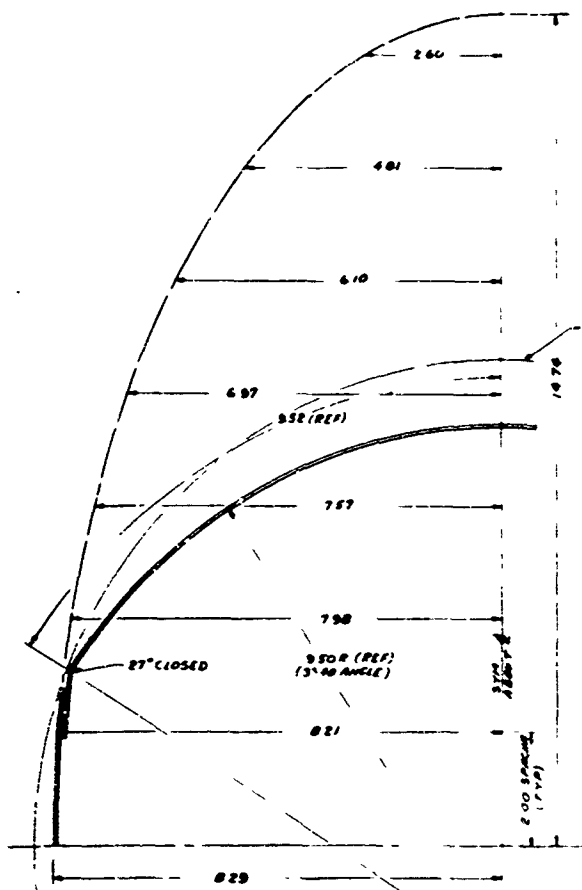
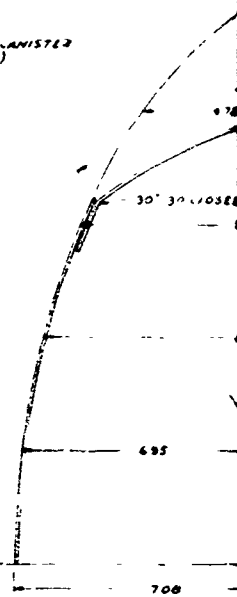
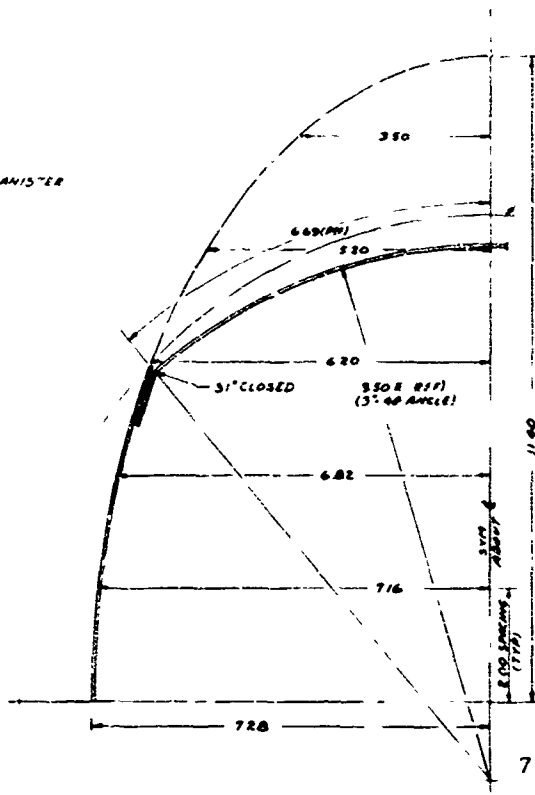
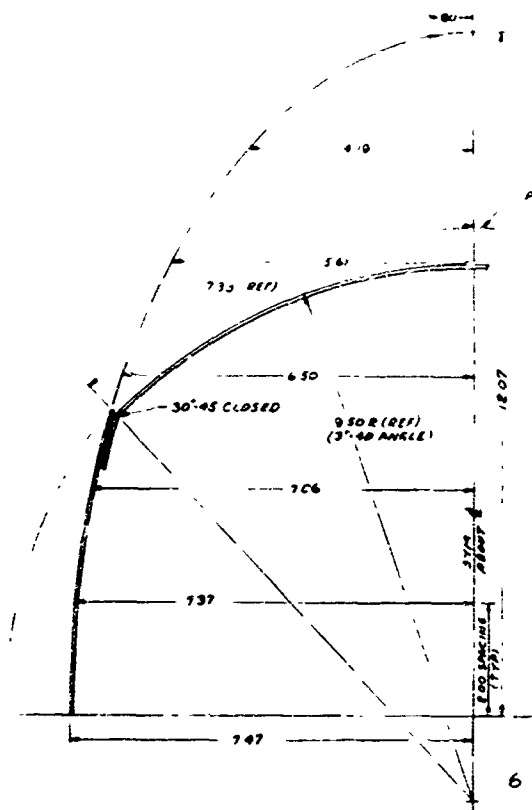


-7 REAR PANEL
FULL SCALE

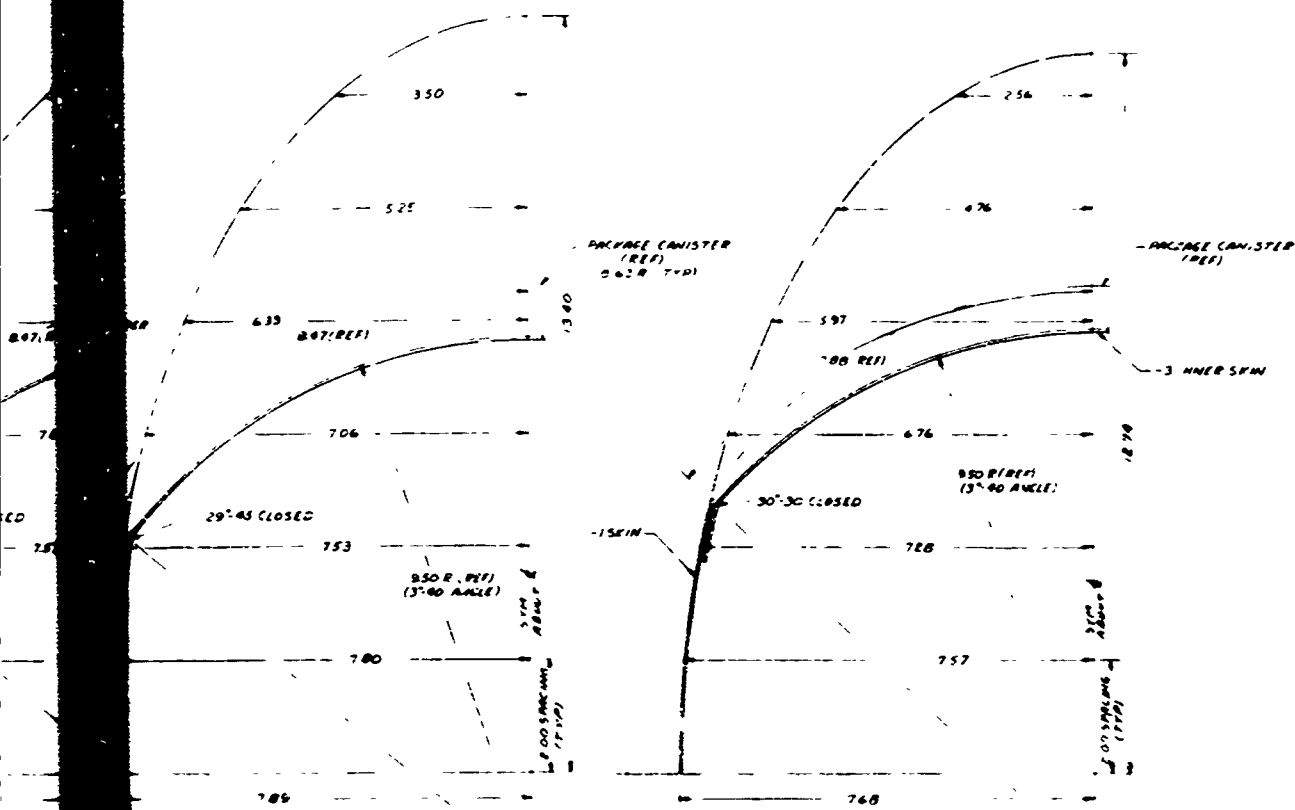
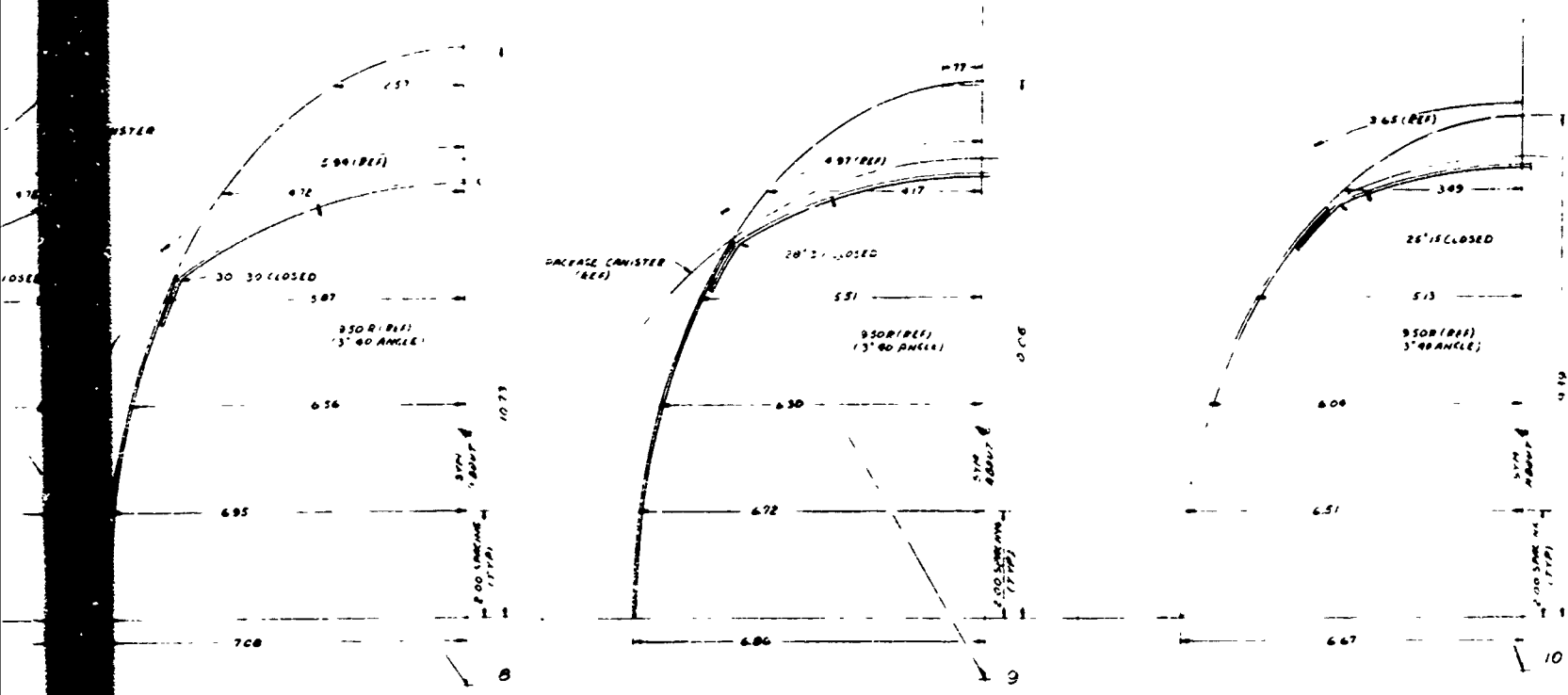
A



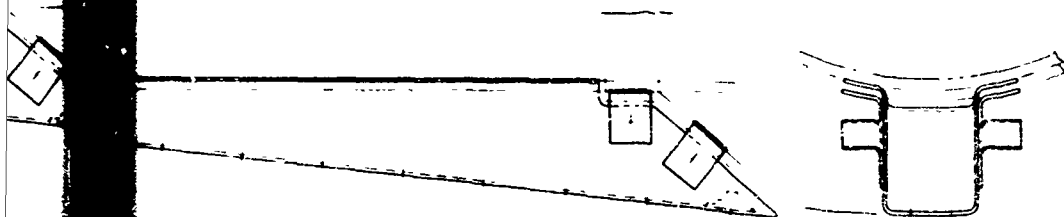




A



B



D

REFERENCES

1. Nebiker, F. R.: Aerodynamic Deployable Decelerator Performance-Evaluation Program. AFFDL-TR-65-27, Wright-Patterson AFB, Ohio, Air Force Flight Dynamics Laboratory. May 1965.
2. Jaremenko, I. M.: Wakes, Their Structure and Influence upon Aerodynamic Decelerators. NASA CR-748. Washington, D.C., Langley Research Center, NASA.
3. Hoerner, S. F.: Fluid-Dynamic Drag. Midland Park, N.J., published by author, 1965.
4. Gran, W. M.: Design and Instrumentation Testing for a Hypersonic Parachute Free-Flight Test Capability. ASD-TR-63-64. Wright-Patterson AFB, Ohio, Aeronautical System Division. 1963.
5. Stetson, K. F.: "Boundary Layer Transition on Blunt Bodies with Highly Cooled Boundary Layers," J. Aero. Sci., Vol 27, No. 2, pp 81-91.
6. GER-11497A: Detail Stress Analysis of Capabilities, "B" and "C" Test Vehicles. Akron, Ohio, Goodyear Aerospace Corporation. February 1964.
7. Stein, A. J.: Effect of Cross-Section Shape on Stress Distribution in AIRMAT Panels. GER-8860. Akron, Ohio, Goodyear Aerospace Corporation. 10 June 1958.
8. Reddick, H. W.; and Miller, F. H.: Advanced Mathematics for Engineers. 2nd ed. New York, Wiley and Sons, Inc., 1948.
9. Dwight, H. B.: Tables of Integrals and Other Mathematical Data. New York, Macmillan, 1947.
10. American Institute of Steel Construction: Steel Construction. 3rd ed. New York, 1937.
11. Niles, A. S.; and Newell, J. S.: Airplane Structures. Vol II, 3rd ed. New York, Wiley and Sons, Inc., 1943.
12. MIL-HDBK-5: Metallic Materials and Elements for Flight Vehicle Structures. Washington, D.C., Department of Defense, 1964.

Unclassified

Security Classification

DOCUMENT CONTROL DATA - R & D		
<small>(Security classification of title, body of abstract and indexing annotation must be entered when the overall report is classified)</small>		
1. ORIGINATING ACTIVITY (Corporate author) Goodyear Aerospace Corporation 1210 Massillon Road Akron, Ohio		2a. REPORT SECURITY CLASSIFICATION Unclassified
		2b. GROUP
3. REPORT TITLE ESTABLISHMENT OF AN UNSYMMETRICAL WAKE TEST CAPABILITY FOR AERODYNAMIC DECELERATORS, VOLUME I, TEST VEHICLE DESIGN MODIFICATION		
4. DESCRIPTIVE NOTES (Type of report and inclusive dates) Final Report, 1 March 1966 to 15 October 1966		
5. AUTHOR(S) (First name, middle initial, last name) Henke, Daniel W.		
6. REPORT DATE March 1968	7a. TOTAL NO OF PAGES 195	7b. NO OF PAGES 12
8a. CONTRACT OR GRANT NO AF33(615) - 3595	9a. ORIGINATOR'S REPORT NUMBER(S) GER - 13528	
b. PROJECT NO 6065		
c. Task 606507		
d.	9b. OTHER REPORT NO(S) (Any other numbers that may be assigned this report) AFFDL-TR-67-192, Volume I	
10. DISTRIBUTION STATEMENT This document has been approved for public release and sale; its distribution is unlimited.		
11. SUPPLEMENTARY NOTES		12. SPONSORING MILITARY ACTIVITY Air Force Flight Dynamics Laboratory Wright-Patterson AFB, Ohio 45433
13. ABSTRACT The results of wind tunnel investigations, analyses, and preliminary design efforts performed in order to show the feasibility of accomplishing supersonic free flight tests of deployable aerodynamic decelerators in the wake of an unsymmetrical fore- body are described in this volume. The results show that the simulation of the wake of a nonaxisymmetric lifting body is feasible and practicable by integrating inflatable aft-appendages on an Arapaho C test vehicle and that the resultant modified vehicle retains the same test capabilities as the basic Arapaho C. The modified vehicle de- sign also includes modifications required for compliance with Eglin AFB/Eglin Gulf Test Range safety criteria. Included are recommendations for further vehicle modi- fications that would improve the test capabilities of the basic Arapaho C test vehicle. A vehicle mockup was constructed to demonstrate feasibility of the approach and to preclude major assembly and actuation interference problems. The distribution of this abstract is unlimited.		

DD FORM 1 NOV 65 1473

Unclassified

Security Classification

Unclassified
Security Classification

14 KEY WORDS	LINK A		LINK B		LINK C	
	ROLE	WT	ROLE	WT	ROLE	WT
Supersonic Wake Flow Supersonic Decelerators Supersonic Decelerator Test Vehicle Aerodynamics Aerodynamic Heating Inflatable Subsystems Recovery Systems						

Unclassified
Security Classification